



University of **HUDDERSFIELD**

University of Huddersfield Repository

Gong, Cencen

The Interaction Between Railway Vehicle Dynamics And Track Lateral Alignment

Original Citation

Gong, Cencen (2013) The Interaction Between Railway Vehicle Dynamics And Track Lateral Alignment. Doctoral thesis, University of Huddersfield.

This version is available at <https://eprints.hud.ac.uk/id/eprint/19755/>

The University Repository is a digital collection of the research output of the University, available on Open Access. Copyright and Moral Rights for the items on this site are retained by the individual author and/or other copyright owners. Users may access full items free of charge; copies of full text items generally can be reproduced, displayed or performed and given to third parties in any format or medium for personal research or study, educational or not-for-profit purposes without prior permission or charge, provided:

- The authors, title and full bibliographic details is credited in any copy;
- A hyperlink and/or URL is included for the original metadata page; and
- The content is not changed in any way.

For more information, including our policy and submission procedure, please contact the Repository Team at: E.mailbox@hud.ac.uk.

<http://eprints.hud.ac.uk/>

The Interaction Between Railway Vehicle Dynamics And Track Lateral Alignment

CENCEN GONG

A thesis submitted to the University of Huddersfield in partial
fulfilment of the requirements of the degree of Doctor of
Philosophy

Institute of Railway Research
School of Computing and Engineering
The University of Huddersfield

August 2013

Acknowledgements

The author would like to express her thanks to the following people, without whose help this research would not have been possible.

Professor Simon Iwnicki for giving me the opportunity to undertake this project, and his supervision, guidance and advice was invaluable.

Dr. Yann Bezin for his supervision, careful guidance and support during the PhD research.

Sin Sin Hsu for her help with the track data during the undertaking of this research.

Prof. Felix Schmid and Dr. Charles Watson, without whose help and guidance I would not have had the opportunity to accomplish this PhD.

All of the members in the Institute of Railway Research for their help and advice.

All my friends especially Jui Yu Chang and Lu Li for for their support and encouragement during my stay in the UK.

Yunshi Zhao, who undertook his PhD alongside me, for his help both at and after work.

This work is dedicated to my family, especially my parents Hong Gong and Zhong Chen whom I love deeply. They have supported and encouraged me in my choices throughout my studies and in life. Without them I would never have been able to achieve this.

Executive Summary

This thesis examines the effect of vehicle dynamics on lateral deterioration of the track alignment. As rail traffic runs along a route, the forces imposed upon the track cause the ballast to settle, and hence the track geometry deteriorates. At a specified value of deterioration the track geometry needs to be restored by tamping or other methods. As the deterioration is mainly in the vertical direction, this aspect has been more widely studied and models have been developed to predict vertical track geometry deterioration. On the other hand, lateral track deterioration is not as well understood, and this thesis aims to fill the gap in this knowledge. However, the understanding of the lateral deterioration mechanisms becomes more important as speed and capacity increase. This thesis describes statistical studies of track lateral deterioration, as well as the development and validation of a vehicle-track lateral dynamic interaction model. This work is undertaken to contribute to the fundamental understanding of the mechanisms of track lateral deterioration, therefore making the effective control and reduction of the lateral deterioration achievable.

The statistical analysis provides a better understanding of three aspects of track lateral irregularities, namely: the relationship between vertical and lateral irregularities, the relationship between track curvature and track lateral irregularity and the change in track lateral deterioration over time. The vertical and lateral track irregularity magnitudes are clearly correlated. The track quality in the vertical direction is generally worse than in the lateral direction, however the number of track sections with lateral quality significantly worse than the vertical is non-negligible. The lateral irregularities tend to be larger on curves. It is notable that less than ten percent of the track studied has a constant lateral deterioration due to frequent maintenance activities and bidirectional lateral dynamic forces. Unlike vertical settlement, lateral deterioration develops exponentially in both magnitude and wavelength, and the major influences are found from the irregularities with wavelength longer than 10 m. The change in track lateral irregularity with different curve radii and the lateral deterioration rate are described in separate exponential power functions due to the limitation of the available track data. The parameters for these empirical equations do not remain constant due to the change in track conditions.

Current track lateral models mainly focus on lateral failures such as buckling and lateral sliding. The development of lateral track irregularities tends to be studied using representative values of net lateral forces and net L/V (Lateral/Vertical) load ratios. Unlike other track lateral deterioration models, the model developed in this thesis focuses on the development of lateral irregularities based on the dynamic interactions between the vehicles and the track system. This model makes it possible to carry out more integrations and analysis of the track lateral deterioration in a realistic dynamic simulation, using vehicle models, contact conditions, track initial irregularities, and traffic mix more close to the reality. The vehicle-track lateral dynamic interaction model was validated against track geometry data measured on the West Coast Mainline (WCML) in England. It has been found that the model gives a reasonably accurate prediction of the development of lateral track irregularities. However, it also tends to predict a short wavelength deterioration that is not seen in the actual track deterioration. Improvements to the model are suggested by either adding more factors or simplifying the model depending on specific target application. Enhancing the model by including more details, such as longitudinal forces, temperature effect, more layered track systems, uneven track bed conditions and more representative wheel-rail contact conditions etc., may help understand the reason of the additional short wavelength.

A sensitivity analysis was performed in order to identify the critical factors that influence lateral track deterioration. The track damage caused by specific vehicles can be controlled by understanding different vehicle dynamics behaviour on a particular track section or route. Vehicles with simple suspension design and heavy axle loads tend to cause more lateral track damage. Within a certain speed range, there will be a critical speed that generates the largest lateral deterioration. Vehicles with different dynamic behaviours can generate a potential offset of the lateral deterioration, so it is possible to design the traffic mix to cancel out the peak deterioration. However, it may not be very practical to redesign the traffic mix due to different traffic requirements. Subsequently, actions can be taken to effectively reduce track lateral deterioration, such as optimise the suspension design, vehicle weight, the selection of an optimal operation speed, and enhance the traffic mix design.

As the most important interface between vehicle and track, the wheel-rail contact condition has an extremely large influence on lateral deterioration. Wheel and rail profiles with different wear conditions can cause altered vehicle-track lateral dynamic interaction. It is found that increasingly worn wheel/rail profiles within an acceptable tolerance can effectively reduce the lateral deterioration.

Lateral deterioration can also be reduced by increasing all the track stiffness values, damping values and the mass of rails and sleepers, or alternatively, by decreasing the sleeper spacing. The sleeper-ballast interface is found to play the most important role in lateral deterioration. The interfaces between the sleeper and ballast shoulder, crib and base determines the non-linear characteristic such as hysteresis and sliding features. Improving the strength of the sleeper-ballast interface can improve the elastic limits and hysteresis characteristics, hence reducing the lateral deterioration.

The findings of the investigation indicate that the model provides in-depth knowledge of the mechanisms influencing lateral deterioration and provides effective solutions with consideration of vehicles, wheel-rail contact and the track system.

Further work would include track data with sufficient information in order to develop a more comprehensive empirical model that describes the lateral deterioration, inclusion of more potentially influential factors such as: temperature, ground condition, traffic etc. The model can be improved by taking into account additional factors such as the influence of longitudinal forces from the wheels to the rails, different weather and temperatures, subgrade and ground conditions, etc. The reason for the high frequency noise in the deterioration prediction is not understood yet and it should be discussed in terms of more accurate vehicle simulation results and more comprehensive rail and wheel worn profiles measured on the target track and vehicles. Furthermore, the sleeper-ballast lateral characteristics are not well understood and the previous research in this area is quite limited. To improve on the present work it would be useful to carry out laboratory tests in order to capture more accurately track lateral stiffness and damping values as well as the comprehensive non-linear characteristic of track lateral residual resistance behaviour.

Table of Contents

Acknowledgements	i
Executive Summary.....	ii
Table of Contents	iv
List of Figures.....	v
List of Tables.....	ix
Glossary of Terms	xi
Definition of Symbols Used	xii
1 INTRODUCTION	1
1.1 Brief	1
1.2 Railway track system	4
1.3 Track geometry and measurement	8
1.4 Chapter conclusion.....	13
2 LITERATURE REVIEW	14
2.1 Track settlement models	14
2.2 Track system models.....	21
2.3 Track lateral irregularity studies	23
2.4 Contemporary regulation	28
2.5 Chapter conclusion.....	29
3 STATISTICAL ANALYSIS OF TRACK QUALITY	30
3.1 The relationship between track lateral and vertical irregularities	30
3.2 The relationship between track lateral irregularities and curvature	37
3.3 Track lateral deterioration over time.....	40
3.4 Chapter conclusion.....	59
4 VEHICLE-TRACK LATERAL DETERIORATION MODEL	60
4.1 Vehicle-track dynamic model	60
4.2 Track parameters.....	66
4.3 Track lateral shift model	75
4.4 Overall track lateral model and validation	89
4.5 Model validation	92
4.6 Chapter conclusion.....	118
5 SENSITIVITY ANALYSIS	119
5.1 Effect of vehicles	119
5.2 Effect of different wheel-rail contact conditions	132
5.3 Effects of different track parameters.....	141
5.4 Chapter conclusion.....	158
6 FURTHER WORK AND RECOMMENDATIONS	160
6.1 Further work.....	160
6.2 Recommendations.....	162
7 CONCLUSIONS.....	164
8 References	167
8.1 Documents	167
8.2 Websites	174
9 Appendices	175
Appendix A	statistical analysis
Appendix B	governing equations for boef track model
Appendix C	mass, stiffness and damping matrix creation for track model
Appendix D	track model parameter selection

List of Figures

Figure 1-1 Structure of the thesis	3
Figure 1-2 Track system	4
Figure 1-3 Rail joints with fishplate (Website Reference 1)	4
Figure 1-4 Rail spike left :(Website Reference 2) and rail chair	5
Figure 1-5 Pandrol E-clip (Left: Website) and fastclip (Right: Website Reference 4)	6
Figure 1-6 Two Types of concrete sleepers [16]	6
Figure 1-7 Accelerometer installed on axle-box [25] and accelerometer position [26]	8
Figure 1-8 Standard deviation of track profile	9
Figure 1-9 Power spectral density lot	10
Figure 1-10 Geometric meaning of versine	11
Figure 1-11 Track buckle [48]	13
Figure 2-1 Track settlement process	14
Figure 2-2 Interactive dynamic settlement methodology [54]	16
Figure 2-3 Relation between velocity and settlement increment [59]	19
Figure 2-4 Research method of track settlement [60]	20
Figure 2-5 Track movement model	22
Figure 2-6 Double Layer Elastic Track Model	22
Figure 2-7 Double layer discretely supported track model	23
Figure 2-8 Initial lateral misalignment effected by longitudinal force	24
Figure 2-9 Track lateral shift parameters [2]	26
Figure 2-10 Modelling approach [2]	27
Figure 2-11 Track buckling analysis approach [83]	28
Figure 2-12 Track lateral irregularity limits for different speeds [85]	28
Figure 3-1 Vertical and lateral irregularities SD results of combined track data	32
Figure 3-2 Statistical results of lateral to vertical irregularity ratios	33
Figure 3-3 Example of rough line deviation pattern	34
Figure 3-4 Relationship between fractal dimension and standard deviation	35
Figure 3-5 SD and Dr values for different signal inputs	36
Figure 3-6 Dynamic wheel-rail forces at the leading left wheel	37
Figure 3-7 SD value against different curve radius ranges	38
Figure 3-8 Median SD growth plotting against different curvature ranges	39
Figure 3-9 Best curve fitting result	40
Figure 3-10 Curve profile	41
Figure 3-11 Maintenance dates and information	42
Figure 3-12 Locations of track sections with reasonable lateral deterioration	43
Figure 3-13 Tamping and stone blowing maintenance activities	44
Figure 3-14 Average daily growth of selected track sections SD value	46
Figure 3-15 SD growth over time	46
Figure 3-16 PSD result of long wavelength track irregularities	51
Figure 3-17 PSD results of short wavelength track irregularities	54
Figure 3-18 Summary of average peak power density growth per month	56
Figure 3-19 Summary of growth of irregularity wavelength per month	56
Figure 3-20 Fractal dimension and SD value change over time	57
Figure 3-21 Fractal dimension value and SD value for selected track sections	58
Figure 4-1 Rolling radius difference of new and worn wheel rail profiles	61
Figure 4-2 Class 390 (Website Reference 6) and 221 vehicles (Website Reference 7)	61
Figure 4-3 FEAB (Website Reference 8) and FSAO (Website Reference 9) wagons	62
Figure 4-4 IPAV (Website Reference 9) wagons	62
Figure 4-5 Dynamic properties of VAMPIRE® suspension elements	63
Figure 4-6 Basic axis system for VAMPIRE® simulation	64

Figure 4-7 Wheel-rail axis to wheelset axis	65
Figure 4-8 Force-deflection diagram of track with quasi-static excitation	67
Figure 4-9 Structure of track stiffness	68
Figure 4-10 Rail fastener lateral stiffness against different vertical load	69
Figure 4-11 Characteristic of lateral resistance measurement	73
Figure 4-12 Friction coefficient varies with vertical force [93]	74
Figure 4-13 Friction coefficient reduction over loading passes	75
Figure 4-14 FE track model	76
Figure 4-15 Rail element load and displacement condition	77
Figure 4-16 Centre rail node displacement and input vertical forces	80
Figure 4-17 Dynamic response of the centre of rail and lateral force input from VAMPIRE80	
Figure 4-18 Simulation results with different number of nodes	81
Figure 4-19 Residual deflection of sleepers versus number of passes	82
Figure 4-20 Lateral resistance load deflection characteristics	82
Figure 4-21 Force-displacement relationship in pre-sliding and sliding	83
Figure 4-22 Track lateral resistance characteristic	83
Figure 4-23 Dynamic lateral resistance influenced by vertical load	84
Figure 4-24 Definition of track lateral pre-sliding behaviour	85
Figure 4-25 Iwan friction element	86
Figure 4-26 Single sleeper simulation result	88
Figure 4-27 Scheme of vehicle-track dynamic model	89
Figure 4-28 Distribution of freight vehicle loading condition [147]	91
Figure 4-29 Measured and predicted track irregularity comparison	93
Figure 4-30 Deterioration comparison and precision measurement	95
Figure 4-31 Measured and predicted track irregularity comparison	96
Figure 4-32 Deterioration comparison and precision measurement	98
Figure 4-33 Measured and predicted track irregularity comparison	99
Figure 4-34 Deterioration comparison and precision measurement	101
Figure 4-35 Measured and predicted track irregularity comparison	102
Figure 4-36 Deterioration comparison and precision measurement	104
Figure 4-37 Comparison between measured and predicted lateral deterioration PSD	105
Figure 4-38 Measured and filtered predicted track irregularity comparison	106
Figure 4-39 Deterioration comparison and filtered precision measurement	108
Figure 4-40 Measured and filtered predicted track irregularity comparison	109
Figure 4-41 Deterioration comparison and filtered precision measurement	111
Figure 4-42 Measured and filtered predicted track irregularity comparison	112
Figure 4-43 Deterioration comparison and filtered precision measurement	114
Figure 4-44 Measured and filtered predicted track irregularity comparison	115
Figure 4-45 Deterioration comparison and filtered precision measurement	117
Figure 5-1 Leading left wheel lateral and vertical wheel-rail dynamic forces of passenger and freight vehicles	121
Figure 5-2 Track residual deflection caused by one pass of different vehicles	122
Figure 5-3 Lateral to vertical loading ratio delivered from vehicles to rail	123
Figure 5-4 Summary of average lateral forces and L/V ratio of different vehicles	124
Figure 5-5 Residual deflection calculation	125
Figure 5-6 Residual deflection at different speed	126
Figure 5-7 Peak and average residual deflection at different speed	127
Figure 5-8 PSD of residual deflections resulted by different speeds	127
Figure 5-9 Two peak power densities change	128
Figure 5-10 Residual deflection caused by different vehicles	129
Figure 5-11 Track deterioration under actual traffic and designed traffic scenario	131

Figure 5-12 Track lateral deterioration with different worn rails	133
Figure 5-13 Leading left wheel lateral forces with different rail profiles	134
Figure 5-14 PSD of track lateral deterioration with different rail profiles	135
Figure 5-15 Track lateral deterioration with different worn wheels	136
Figure 5-16 Leading left wheel lateral forces with different wheel profiles	137
Figure 5-17 PSD of track lateral deterioration with different wheel profiles	137
Figure 5-18 Track lateral deterioration with different level of worn wheels	138
Figure 5-19 Rolling radius difference of five contact files	139
Figure 5-20 PSD and RMS of track lateral deterioration with different level of worn wheel profiles	140
Figure 5-21 Track lateral deflection with different rail-sleeper vertical stiffness values	143
Figure 5-22 Residual deflection change of every 5% increase of stiffness values	144
Figure 5-23 Average change per unit increase of stiffness value	145
Figure 5-24 Track lateral deflection with different rail-sleeper vertical damping values	146
Figure 5-25 Residual deflection change for every 5% increase of damping values	147
Figure 5-26 Average change per unit increase of damping value	147
Figure 5-27 Track lateral deflection with different rail and sleeper masses	148
Figure 5-28 Residual deflection amplitude change of every 5% increase of masses	149
Figure 5-29 Average change per unit increase of rail and sleeper masses	150
Figure 5-30 Change of softening factor	150
Figure 5-31 Track lateral deflection with softening factors	151
Figure 5-32 Residual deflection change of every 0.5% increase in softening factor	152
Figure 5-33 Dynamic elastic breaking limit	153
Figure 5-34 Track lateral deflection with different elastic breaking limits	154
Figure 5-35 Residual deflection change by elastic breaking limits	155
Figure 5-36 Track lateral deflection with different sleeper spacing	156
Figure 5-37 Residual deflection change of every 5% increase of sleeper spacing	157
Figure 9-1 Vertical and lateral SD values in freight lines of Network A	177
Figure 9-2 Vertical and lateral SD values in regional lines of Network A	177
Figure 9-3 Vertical and lateral SD values in upgraded lines of Network A	178
Figure 9-4 Vertical and lateral SD values in high speed lines of Network A	178
Figure 9-5 Vertical and lateral SD values in regional lines of Network B	179
Figure 9-6 Vertical and lateral SD values in upgraded lines of Network B	179
Figure 9-7 Vertical and lateral SD values in high speed lines of Network B	180
Figure 9-8 Vertical and lateral SD values in freight lines of Network C	180
Figure 9-9 Vertical and lateral SD values in regional lines of Network C	181
Figure 9-10 Vertical and lateral SD values in upgraded lines of Network C	181
Figure 9-11 Vertical and lateral SD values in freight lines of Network A	182
Figure 9-12 Vertical and lateral SD values in regional lines of Network A	183
Figure 9-13 Vertical and lateral SD values in upgraded lines of Network A	183
Figure 9-14 Vertical and lateral SD values in high speed lines of Network A	184
Figure 9-15 Vertical and lateral SD values in regional lines of Network B	184
Figure 9-16 Vertical and lateral SD values in upgraded lines of Network B	185
Figure 9-17 Vertical and lateral SD values in high speed lines of Network B	185
Figure 9-18 Vertical and lateral SD values in freight lines of Network C	186
Figure 9-19 Vertical and lateral SD values in regional lines of Network C	186
Figure 9-20 Vertical and lateral SD values in upgraded lines of Network C	187
Figure 9-21 MSC between track lateral and vertical irregularities of Network A	188
Figure 9-22 MSC between track lateral and vertical irregularities of Network B	188
Figure 9-23 MSC between track lateral and vertical irregularities of Network C	189
Figure 9-24 SD value box plot result of freight lines in Network A	189

Figure 9-25 SD value box plot result of regional lines in Network A	190
Figure 9-26 SD value box plot result of upgraded lines in Network A	190
Figure 9-27 SD value box plot result of high speed lines in Network A	190
Figure 9-28 SD value box plot result of regional lines in Network B	191
Figure 9-29 SD value box plot result of upgraded lines in Network B	191
Figure 9-30 SD value box plot result of high speed lines in Network B	191
Figure 9-31 SD value box plot result of freight lines in Network C	192
Figure 9-32 SD value box plot result of regional lines in Network C	192
Figure 9-33 SD value box plot result of upgraded lines in Network C	192
Figure 9-34 Vertical and lateral fractal dimension values in freight lines of Network A	193
Figure 9-35 Vertical and lateral fractal dimension values in regional lines of Network A	193
Figure 9-36 Vertical and lateral fractal dimension values in upgraded lines of Network A	194
Figure 9-37 Vertical and lateral fractal dimension values in high speed lines of Network A	194
Figure 9-38 Vertical and lateral fractal dimension values in regional lines of Network B	195
Figure 9-39 Vertical and lateral fractal dimension values in upgraded lines of Network B	195
Figure 9-40 Vertical and lateral fractal dimension values in high speed lines of Network B	196
Figure 9-41 Vertical and lateral fractal dimension values in freight lines of Network C	196
Figure 9-42 Vertical and lateral fractal dimension values in regional lines of Network C	197
Figure 9-43 Vertical and lateral fractal dimension values in upgraded lines of Network C	197
Figure 9-44 Beam Element Model	198

List of Tables

Table 2-1 Proposed net axle L/V limits _____	29
Table 3-1 Track categories _____	30
Table 3-2 Correlation coefficient of track lateral and vertical irregularities _____	31
Table 3-3 Percentage of sections for which the lateral irregularities are larger than the vertical ones [%] _____	32
Table 3-4 MSC results of the track lateral and vertical irregularities _____	34
Table 3-5 Correlation coefficient of vertical and lateral irregularity fractal dimensions ____	36
Table 3-6 Median SD value in different curvature range _____	39
Table 3-7 Curve fitting results _____	40
Table 3-8 Track recording dates and dataset numbers _____	41
Table 3-9 Track recording dates and dataset numbers _____	42
Table 3-10 Selected track sections _____	43
Table 3-11 Selected lateral deterioration data sets _____	45
Table 3-12 Curve fitting parameters and evaluations for three types of track sections ____	47
Table 3-13 Curve fitting parameters and evaluations for three types of track sections ____	48
Table 3-14 Curve fitting parameters and evaluations for three types of track sections ____	50
Table 3-15 Summaries of the long wavelength PSD results _____	52
Table 3-16 Summarise of short wavelength PSD results _____	55
Table 3-17 Selected track sections for lateral deterioration analysis _____	57
Table 4-1 General vehicle models _____	63
Table 4-2 Transient simulation inputs and outputs _____	65
Table 4-3 Parameters of CEN60 rail _____	68
Table 4-4 G44 sleeper parameters _____	69
Table 4-5 Vertical stiffness published by Pandrol company [kN/mm] _____	69
Table 4-6 Rail fastening system vertical stiffness in Chinese standard [kN/mm] _____	70
Table 4-7 Quasi-static CEN60-rail fastening system-half G44 sleeper assembly test under 60kN preload [kN/mm] _____	70
Table 4-8 Summary of Pandrol report [kN/mm] _____	70
Table 4-9 Summarised rail pad parameters _____	70
Table 4-10 Rail pad parameters _____	71
Table 4-11 Summary of track bed stiffness per sleeper _____	71
Table 4-12 Quasi-static stiffness measurements at various sites _____	71
Table 4-13 Sleeper support parameter in four different researches _____	71
Table 4-14 Track bed parameters _____	72
Table 4-15 Lateral Resistance Characteristic Values per Sleeper _____	72
Table 4-16 Summary of ballast lateral stiffness in different studies _____	72
Table 4-17 Values of constants for wood and concrete sleepers [93] _____	73
Table 4-18 Possible residual and friction coefficient values for simulation _____	74
Table 4-19 Selected track parameters for linear simulation _____	79
Table 4-20 Simulation time for a 30 m section of track _____	81
Table 4-21 Track parameters _____	87
Table 4-22 Summarise of traffic information _____	90
Table 4-23 Traffic scenario between measured track datasets _____	90
Table 4-24 Traffic scenario for later simulation _____	91
Table 5-1 Different vehicle running speed _____	126
Table 5-2 Summary of two peaks in PSD of residual deflections _____	128
Table 5-3 Axle passages for each vehicle _____	129
Table 5-4 Rail-wheel profile combination 1 _____	132
Table 5-5 Peak PSD of track lateral deterioration with different rail profiles _____	135

Table 5-6 Rail-wheel profile combination 2_____	135
Table 5-7 Peak PSD of track lateral deterioration with different wheel profiles _____	138
Table 5-8 Rail-wheel profile combination 3_____	138
Table 5-9 Peak PSD of track lateral deterioration with different level of worn wheel profiles _____	141
Table 5-10 Original parameters _____	141
Table 5-11 Stiffness variation_____	142
Table 5-12 Peak residual deflection under different rail-sleeper vertical stiffness _____	143
Table 5-13 Damping variation [kN.s/m] _____	145
Table 5-14 Peak residual deflection under different damping values _____	146
Table 5-15 Rail and sleeper masses variation [kg]_____	148
Table 5-16 Peak residual deflection under different rail and sleeper masses [mm]_____	148
Table 5-17 Softening factor variation_____	151
Table 5-18 Peak residual deflection under different softening factors [mm]_____	151
Table 5-19 Elastic breaking limit variation _____	153
Table 5-20 Average residual deflection under different elastic breaking limits _____	154
Table 5-21 Sleeper spacing variation [m]_____	155
Table 5-22 Peak residual deflection under different sleeper spacing [mm]_____	156
Table 9-1 Meaning of the numbers on x axis in box-plot figures _____	189
Table 9-2 ACTRAFF data for the route _____	203
Table 9-3 Track lateral resistance parameters _____	204
Table 9-4 Lateral resistance characteristic values per sleeper _____	204
Table 9-5 Summary of lateral resistance test on unloaded track, concrete sleepers _____	204

Glossary of Terms

Term	Meaning / Definition
ABA	Axle Box Acceleration
ADIF	Administrator of Railway Infrastructures
BOEF	Beam on Elastic Foundation Model
CWR	Continuous Welded Rail
DEMU	Diesel Multiple Unit
ECML	East Coast Main Line
EMU	Electric Multiple Unit
ERRI	European Rail Research Institute
FE	Finite Element
GPR	Ground Penetrating Radar
HTRC	High-Speed Track Recording Coach
IQR	Interquartile Range
L/V	Ratio of Lateral force over Vertical force
MSC	Magnitude Squared Coherence
ORE	Office for Research and Experiments of the International Union of Railways
PSD	Power Spectral Density
RMS	Root Mean Square
RMSE	Root Mean Squared Error
RSMV	Rolling Stiffness Measurement Vehicle
RLD	Resistance to Lateral Displacement
S&C	Switch and Crossings
SD	Standard Deviation
SSE	Sum of Squared Errors of prediction
TLV	Track Loading Vehicle
TQI	Track Quality Index
TRC	Track Recording Coach

Definition of Symbols Used

Term	Unit	Meaning / Definition
σ	mm	Standard deviation
$\Delta\sigma$	mm	Change of standard deviation
D_r	-	Fractal dimension
r	-	Correlation coefficient
A	m^2	Cross section area of the rail
c	N. s/m	Damping assuming a linear response to load
ρ	kg/m	Mass density of the rail
E	N/m ²	Young's modulus
EI	N · m ²	Bending stiffness
F	N	Force on the beam
I	m^4	Second moment of inertia
I_{yy}	m^4	Lateral second moment of inertia of the rail
k	N/m	Stiffness assuming a linear response to load
k_b	N/m	Beam bending stiffness
k_l	N/m	Load distribution linear coefficient
L	N	Lateral forces on the rail
m_r	kg/m	Distribution mass of the rail
m_s	kg	Mass of the sleeper
P	N	Concentrated load on the beam
w	mm	Beam deflection
x	m	Longitudinal distance along the rail from the load
y	mm	Lateral displacement
y_{r1}, y_{r2}	mm	Lateral displacement of two rails respectively
y_s	mm	Lateral displacement of the sleeper
s	m	Sleeper spacing
I_{yy}	m^4	Section moment of area about vertical axis
I_{zz}	m^4	Section moment of area about horizontal axis
k_{ry}	N/m	Rail pad lateral stiffness
c_{ry}	N. s/m	Rail pad lateral damping
k_{rz}	N/m	Rail pad vertical stiffness
c_{rz}	N. s/m	Rail pad vertical damping
k_{sy}	N/m	Sleeper-ballast lateral stiffness
c_{sy}	N. s/m	Sleeper-ballast lateral damping
k_{sz}	N/m	Sleeper-ballast vertical stiffness
c_{sz}	N. s/m	Sleeper-ballast vertical damping
w_e	mm	Elastic breaking displacement
F_e	N	Elastic breaking force
w_p	mm	Peak resistance displacement
F_p	N	Peak resistance force

Term	Unit	Meaning / Definition
w_i	mm	Displacement at failure
F_i	N	Sliding force for track
μ_r	-	Residual deflection coefficient
μ_s	-	Friction coefficient
θ	-	Softening factor

1 INTRODUCTION

Track condition has a big influence on the behaviour of the train-track system in terms of ride safety, maintenance and passenger comfort. However, it is physically impossible to eliminate track irregularities in practice. It is therefore important to understand the mechanism of track deterioration and predict the development of track irregularities to reduce the life-cycle cost of the railway system [1]. The deterioration of track alignment can be measured by railway infrastructure managers using a Track Recording Coach (TRC). The limit of track lateral resistance still used today was defined relatively early by Prud'homme in 1967. Therefore it is sensible to develop a model that describes the evolution of the track lateral misalignment based on the understanding of existing vertical models. A better understanding of the relationship between influencing factors and the growth of lateral misalignment can be determined, which helps to better understand the vehicle-track interaction. This thesis presents an in-depth investigation into track lateral irregularities and the development of a vehicle-track dynamic lateral deterioration model.

1.1 Brief

This research is about the interaction between railway vehicle dynamics and track lateral misalignment. The aim of the research is to develop a novel method for analysing and predicting railway track lateral deterioration caused by traffic, and determine the triggering limits in terms of track loading and running condition.

The objectives are defined as follows:

- To form an understanding of vehicle-track interaction dynamics and identify the key factors in the development of lateral misalignment.
- To form an understanding of the relationship between the deterioration of vertical and lateral track geometry.

To form an understanding of the relationship between curvature and the deterioration of lateral track geometry.

To form an understanding of the development of track lateral irregularities.

- To analyse the sleeper-ballast interaction and establish a track lateral deterioration model.
- To build a complete lateral deterioration model by coupling the vehicle-track dynamic model and the track lateral deterioration model.
- To validate the model against measured site data.
- To analyse the influential factors and determine their relationship with track lateral deterioration.

1.1.1 Methodology

A dynamic vehicle-track lateral interaction model has been developed. The data relating to track deterioration was captured by site measurement using Track Recording Coach (TRC) data. The track data has been analysed statistically at the first stage using MATLAB¹, in order to establish the empirical curve that describes the track lateral deterioration evolution over time. Various interfaces in the vehicle-track system and different types of track systems were studied to capture the key parameters in the model. It is essential to identify all of the factors that impact the whole dynamic system, and one of the most critical factors is the sleeper-ballast interface [2]. The vehicle-track lateral interaction can be modelled by considering two main interactions: the interaction between the sleeper and ballast and the interaction between the vehicle and track. Computer simulation has been backed up by data from site measurements, the sleeper-ballast interface has been analysed and mathematically transcribed into a detailed vehicle-track interaction model. The output of the track lateral deterioration model, which is the predicted track lateral irregularity growth, can be used as an input as the irregularity data into the vehicle-track model. Therefore, the interaction between the track and the vehicle was comprehensively modelled. The dynamics of the complete system has been analysed including lateral and vertical loadings to increase knowledge of the limiting values.

1.1.2 Structure

The structure of this thesis is illustrated in Figure 1-1.

The research background, aims and objectives are given in Chapter 1.1. The railway track subsystems and the different ways of describing the track geometry and methods that can be used to measure them are described in Chapter 1.2 and Chapter 1.3 respectively.

Chapter 2 is a review of the research literature, which demonstrates all the related statistical and numerical research into track lateral and vertical deterioration.

The results of the statistical analysis, which are the relationship between the vertical and lateral irregularities, the relationship between track lateral irregularities and curvature and the track lateral deterioration over time, are presented and analysed in Chapter 3 in both time and spatial domains.

Chapter 4 describes the development of the vehicle-track lateral dynamic interaction model. The vehicle dynamic model and track Finite Element (FE) model are explained in detail, as well as the track parameters.

A sensitivity analysis is carried out in Chapter 5 in order to establish the impact of the model's parameters on track lateral deterioration.

Chapter 6 gives recommendations and some ideas of further work.

Chapter 7 concludes the thesis and gives a review of the methodology the author used in undertaking the research.

¹ MATLAB is copyright 1984-2013, The MathWorks inc., Natick, Massachusetts

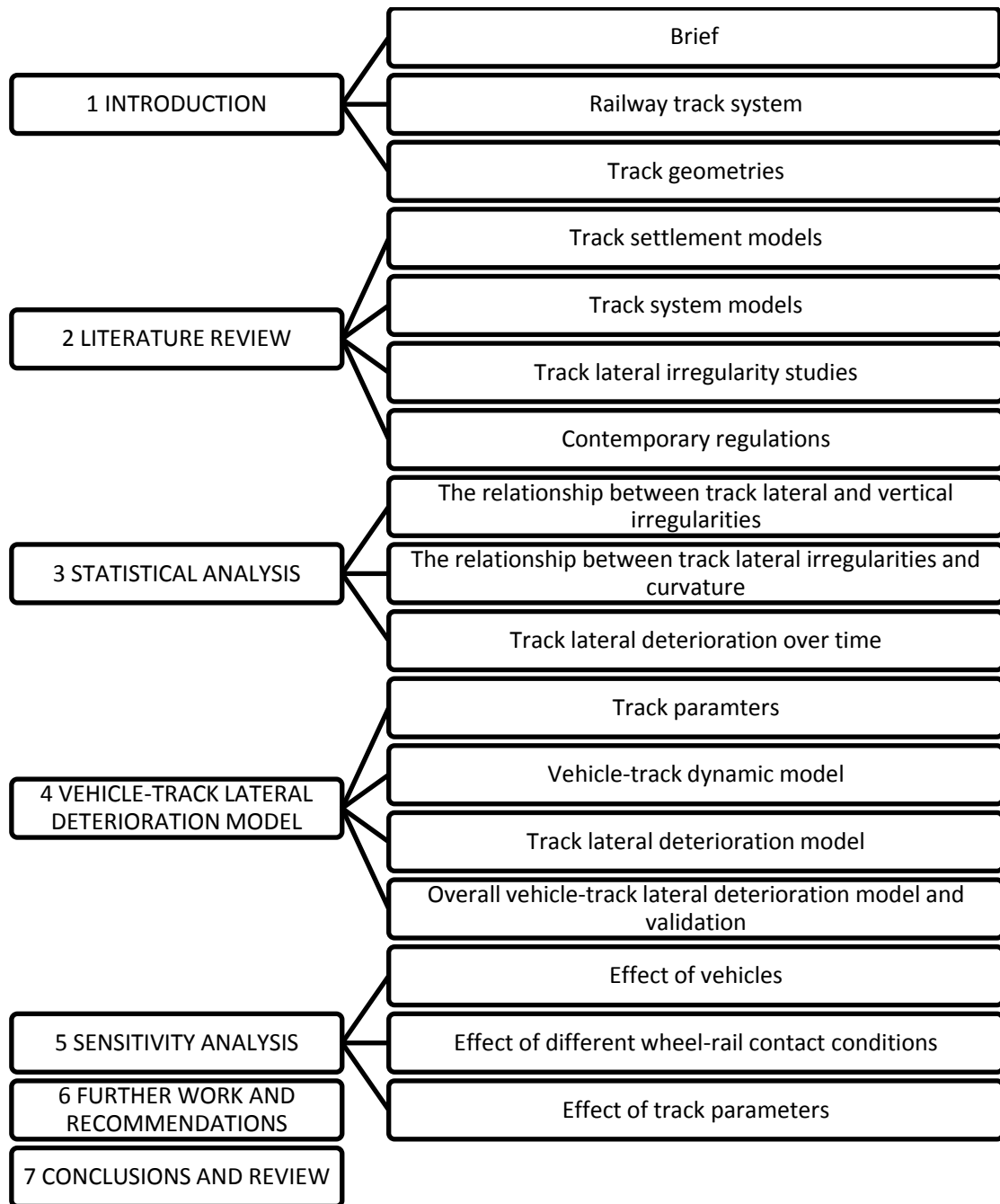


Figure 1-1 Structure of the thesis

1.2 Railway track system

The track system supports the loads due to the passage of vehicles, spreads the load into the ground, provides guidance to the traffic and resists traction and braking forces. It generally consists of the subgrade, ballast, sleepers, rail fastenings and the rail, as shown in Figure 1-2. The function of the rail is to guide and support the vehicle. The rail fastenings secure the rail to the sleepers to maintain the gauge, transfer the dynamic load from the wheel-rail interface to the sleeper and provide electrical isolation between the rail and the sleeper. The ballast layer holds the sleepers in position, distributes the forces from sleepers to subgrade, provides some resilience to the system and aids drainage. The subgrade, which is the original ground that the track system is constructed on, absorbs all the forces from the ballast. There may also be a geotextile layer and or a capping layer between the ballast and the subgrade depending on the properties of the subgrade.

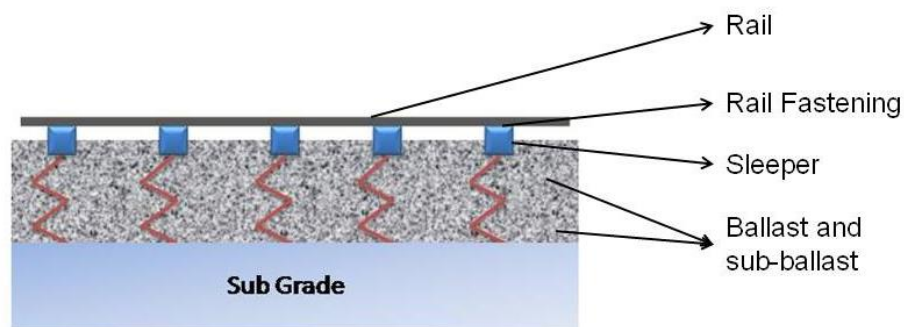


Figure 1-2 Track system

1.2.1 Rails

The steel rail has the function of supporting and guiding the vehicles running on it. Originally, the rails were short in length, 18 m was common, and were joined using bolts and fishplates at the ends (Figure 1-3). Over a large number of loading cycles, it was found that the joints developed dips due to the inherent weakness of the joint. As the joint dip increases, so-called P2 forces, which are a relatively low frequency dynamic forces, occur when the wheel and rail vibrate on the ballast [3]. P2 forces cause rapid deterioration of the track quality. Continuously Welded Rail (CWR) eliminates the joints by welding the rail ends together into much longer lengths. CWR substantially reduces rail maintenance, in that the damage occurring to the rail ends and misalignment of the rails are minimised [4]. Thus, an improved ride quality is provided and the life of all track components is extended.



Figure 1-3 Rail joints with fishplate (Website Reference 1)

There are many different rail cross-section profiles, and different wheel and rail profiles generate different conicity that in turn influences the vehicle hunting stability [5], and wheel and rail wear [6]. It is generally considered essential to achieve an optimal combination of wheel and rail profiles [7]. The dynamic performance of the vehicles is largely determined by the interaction between the wheel and rail, which has been extensively studied, e.g. [8, 9]. Grinding is a typical maintenance method used to control surface fatigue [10] and keep the rail surface in good condition. The interface between rail and wheel connects the railway vehicles with the track system, thus the understanding of it is important in the study of vehicle dynamics and track lateral alignment.

1.2.2 Rail fastenings

Rail fastening systems fix the rail to the sleeper, restraining the rail against longitudinal movement and preventing it from overturning [11]. The rail fastening systems also transfer the vertical, horizontal and longitudinal forces from the rail to the sleeper. Different types of rail fastenings may be selected based on a number of aspects such as: cost, installation requirements and behaviour. Although there are numerous types of modern rail fastening systems, they have similar fundamental functions:

- To secure the rails to the sleepers and maintain the gauge
- To maintain the lateral, vertical and longitudinal position of the rail, thereby preventing it from overturning and creeping longitudinally
- To transfer the wheel load from the rail to the sleeper
- To provide electrical isolation between rail and the sleeper
- To provide vibration isolation

With the development of the railways, the fastening system has been through significant changes. In the early years, fastenings were mainly non-resilient, known as direct fastenings. Rail spikes and rail chairs (Figure 1-4) are widely used where the rails are rigidly fixed to the sleeper. Non-resilient rail fastenings have the advantages of low cost and easy replacement in case of failure. However, the fastening, sleeper and ballast are all subject to vibration forces which may give rise to fatigue problems. The operating speed of trains on track laid with non-resilient fastenings tends to be relatively slow, and maintenance is more expensive due to the increased forces transmitted to the track system [12]. Direct contact between the rail foot and sleeper can also cause severe damage to timber sleepers [13]. An increasing requirement for higher operating speeds and lower maintenance costs means that these systems are no longer installed in modern track.



Figure 1-4 Rail spike left :(Website Reference 2) and rail chair

Resilient rail fastening systems, also known as elastic rail fastening systems, have been developed in order to reduce the track forces and to reduce the likelihood of fatigue. The screw-type elastic fastening was first introduced to the rail industry, quickly followed by the elastic spring clip. Pandrol's E-clip and Fastclip (Figure 1-5) are now the most common types of fastening used in Britain. These fastenings can be used with concrete, steel and timber sleepers. The common elements of this type of fastening are the baseplates, spring steel components, rail pads and insulators.

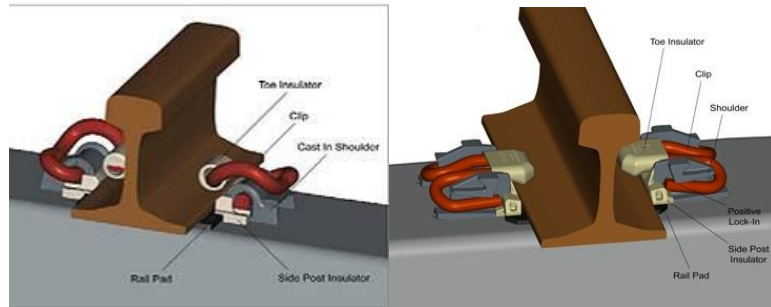


Figure 1-5 Pandrol E-clip (Left: Website) and fastclip (Right: Website Reference 4)

In the past few years, urban railways have gone through an increasingly fast development. Many railway lines are constructed beside, or under, residential areas. Therefore, it is essential to minimise the noise and vibration associated with railway operations. Highly resilient fastenings with low stiffness and the ability to reduce vibration have been developed. Pandrol Vanguard, Pandrol VIPA and the Delkor 'Egg', are designed to fulfil these requirements by using large rubber elements. However, the low stiffness results in larger rail deflections than other fastenings, which can increase the dynamic envelope of trains using this type of track.

1.2.3 Sleepers

Originally, timber sleepers were used as this was the only viable material available at the time. Pre-stressed concrete sleepers were developed and introduced during the Second World War due to a shortage of timber. Since that time, concrete sleepers have become the standard sleeper used today. Timber sleepers are still used in certain applications due to their greater flexibility, which provides superior load spreading over concrete. Steel sleepers have also been developed as an alternative to concrete, as they are lighter in weight, easy to transport due to their stackability and the fact that they allow a lower track form height, which makes them suitable for use in loading gauge enhancement projects. Both sleepers and rail fastenings hold the rail at an angle to match the wheel and rail contact angle, such as 1:20 and 1:40 [14]. Two types of typical concrete sleepers are twin-block sleeper and mono-block sleeper [15], as shown in Figure 1-6.

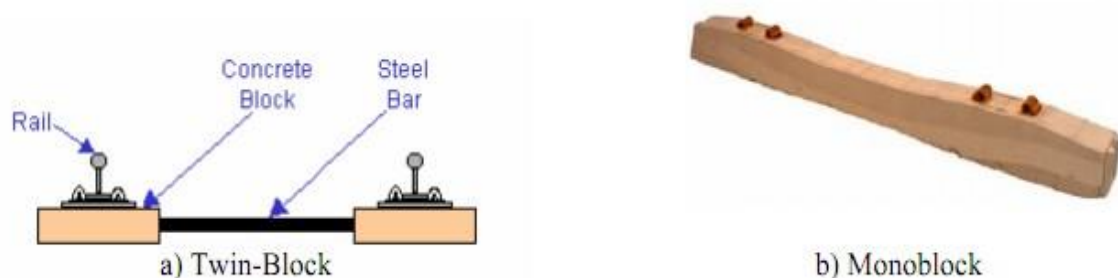


Figure 1-6 Two Types of concrete sleepers [16]

Sleepers support the rails vertically, laterally and longitudinally by sitting inside the ballast layer. There are three contact surfaces between the sleeper and ballast: the sleeper base, the sides of the sleepers and the sleeper ends. It is understandable that the more friction force is provided by the ballast, the more stable the track system will be. Therefore, the shape and mass of the sleeper are significant contributors to the stability of the track system.

1.2.4 **Ballast**

Ballast is a permeable, granular and angular shaped material, and the selection of ballast type usually depends on the material that can be found locally. However the material must be robust enough to withstand the loads from passing traffic without disintegrating, hence granite is the most popular ballast material used in the UK on mainline railways. The ballast material, to some extent, determines the drainage capability, stability and maintenance requirement of the track [17]. Most railway authorities allow 400 to 500 kPa pressure on the ballast [18]. Ballast is classified into four types by function and location [19]:

- Crib ballast is located between sleepers, providing mainly longitudinal resistance and some lateral resistance.
- Shoulder ballast is positioned at the end of the sleepers, giving sufficient lateral resistance to the sleepers.
- Top and sub ballast, also known as load bearing ballast, mainly support the sleepers vertically. The sub-ballast has a smaller size than the top ballast, and lies between the top ballast layer and the subgrade. It can provide a more stable and drained support to the top ballast. The thickness of top and sub ballast is an important factor in the ballast design.

The important functions of ballast are:

- The ballast distributes the load from the sleepers to the subgrade at an acceptable level.
- Ballast provides sufficient drainage.
- The ballast holds the sleepers in place by resisting the vertical, lateral and longitudinal forces caused by the wheel loads.
- The ballast also provides some resilience to the track system.

1.2.5 **Subgrade and Geo-textile**

The requirement for a geotextile layer or a capping layer depends on properties of the subgrade. Since all the loads are distributed into the subgrade eventually, the bearing capacity of the subgrade is extremely important. The deformation of the subgrade can lead to track irregularities and ballast settlement. Therefore the stiffness of the subgrade strongly influences the whole track system design, such as the thickness of the ballast layer and the usage of geotextiles or a capping layer. Geotextiles can be used to either reinforce the subgrade or provide a moisture barrier between the subgrade and track system. Geo-grid reinforcement is used to improve weak subgrades where a capping layer would result in an excessively high trackform. The capping layer, which is generally a layer of compacted clay or granular fill, can be applied in especially soft soil conditions in order to improve the bearing capacity of the native soil [20].

1.3 Track geometry and measurement

Good track condition is important in ensuring a more efficient train-track system in terms of the safe running, low maintenance and good passenger comfort. However, it is physically impossible to completely eliminate all track irregularities in practice. Track irregularities can be characterised in different ways and described by their different wavelengths.

1.3.1 Track geometry and measurement

To achieve a quantitative assessment of the condition of the track system, it is necessary to be able to describe the track by measureable parameters. The fundamental track geometry parameters are the track alignment in vertical, horizontal and twist directions, track gauge, cant, curvature, gradient, and rail profile. The track geometry plays an essential role in the ride quality and safety of operations, and it degrades under repeated dynamic loading from the passing traffic [21]. Different countries have their own standards when it comes to describing track geometry. The track quality in China is described using a Track Quality Index (TQI), which is the sum of standard deviations of seven track irregularity parameters [22]. These seven parameters are left rail vertical profile, right rail vertical profile, left rail alignment, right rail alignment, gauge, cross level and track twist. Portable, manually driven devices can give information on a relatively short length of track [23]. Axle Box Acceleration (ABA) measurement uses the accelerations due to the wheel-rail interaction, as shown in Figure 1-7, and converts the accelerations to displacements by double integration. The mid-chord offset method is currently the mainstream method to measure vertical and horizontal track displacements, which uses three measuring axes arranged in line [24]. The centre axis measures the offset of the rail from the chord that connects to the two end axes. Compared to the manual measurements, there is a significant saving in time and labour by using a TRC. It can measure the track geometry while running at a higher speed, and modern systems are capable of operating at line speed. An additional benefit of using a TRC is that they are usually full scale vehicles and give measurements that show the track in its loaded condition.

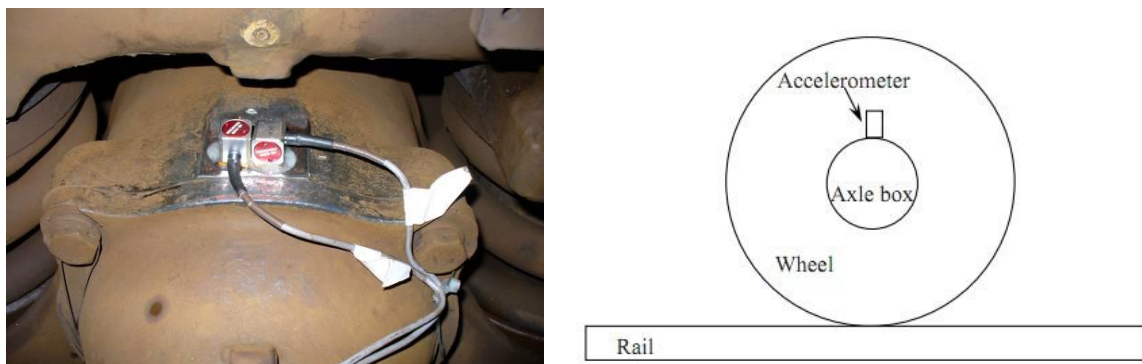


Figure 1-7 Accelerometer installed on axle-box [25] and accelerometer position [26]

The High-Speed Track Recording Coach (HSTRC) was designed by British Rail in order to get accurate and regular maintenance data on railway-track quality [27]. It is a single-point system that uses inertial techniques, including: accelerometers, rate gyroscopes and displacement transducers. The track geometry is calculated by an on board computer system and the data recorded digitally.

While a TRC measures the spatial position of the rails relative to an imaginary track datum line, other types of measurement can provide further information regarding the condition of supporting layers of the track under the rails. Ground Penetrating Radar (GPR) can be used to determine the thickness of the different track layers, and the Swedish Rolling Stiffness Measurement Vehicle (RSMV) can measure the dynamic track stiffness at rail level for various frequencies up to 50 Hz [28]. The track is dynamically excited through two oscillating masses above an ordinary wheel axle of a freight wagon. The latter two measurement methods are able to highlight defects like ballast fouling, ballast settlement, subgrade failure and problems related to embankments.

1.3.2 Description of track quality based on measured irregularities

Measuring the size of track irregularities can be used to characterise the quality of the track with respect to different requirements such as the speed category or engineering maintenance activities. This section describes the various mathematical tools used to characterise track quality.

1.3.2.1 Standard Deviation (SD)

SD is the most common way to describe the smoothness of the track, which shows the amount of track variation from its mean value. Network Rail defines it as:

“Standard deviation is a universally used scientific measure of the variation of a random process. Track profiles have been found to be sufficiently similar statistical properties to random processes to enable a measure of the magnitude of track irregularities to be obtained from the standard deviation of the vertical and horizontal profile data. This form of analysis provides track quality indices.[29]”

SD can be calculated using the equation shown below:

$$\sigma = \sqrt{\frac{1}{m} \sum (a_1 - a)^2} \quad \text{Equation 1}$$

Where,

a...mean value

a₁...sample value

m...total number of values.

Figure 1-8 shows the ideal SD of the track profile assuming a normal distribution.

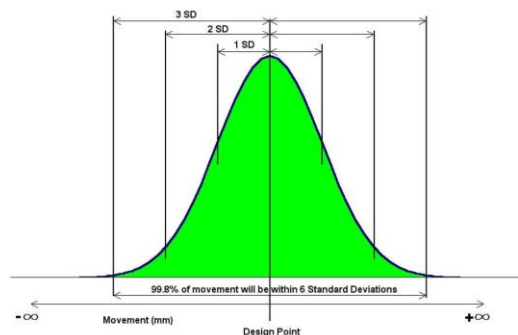


Figure 1-8 Standard deviation of track profile

There are two drawbacks in using the SD to describe track irregularities. Firstly, there will be a difference between the ideal SD curve and reality. Also, although a single large discrete defect can lead to derailment, it will not significantly affect the SD of the total track profile. This is why the current UK and EN standard also specify limits on maximum values.

1.3.2.2 Power Spectral Density (PSD) plot

The distribution of track irregularities can be shown in the form of PSD plot, which shows the distribution of the power over different frequencies. The vertical axis represents the power in each frequency band, while the horizontal axis represents a spatial frequency which is always described by cycle/m. The ideal power spectrum of the track is shown in Figure 1-9.

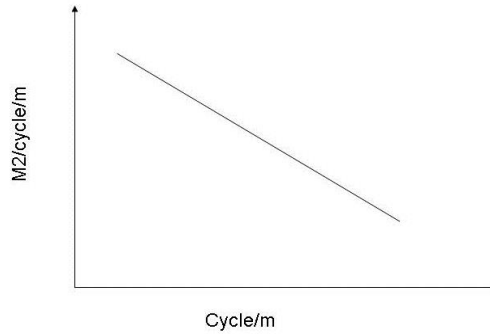


Figure 1-9 Power spectral density lot

Track vertical irregularities are defined by using a PSD function in the track irregularity model which predicts the value of peak amplitudes for a given track length [30]. The PSD method is widely used in different countries to analyse track irregularities. The American Federal Railroad Administration (FRA) collected a large amount of data in order to summarise the track irregularities PSD, the equations for which are below [31].

Track vertical irregularity PSD:

$$S_v(\Omega) = \frac{kA_v\Omega_c^2}{\Omega^2(\Omega^2 + \Omega_c^2)} \quad \text{Equation 2}$$

Track lateral irregularity PSD:

$$S_s(\Omega) = \frac{kA_s\Omega_c^2}{\Omega^2(\Omega^2 + \Omega_c^2)} \quad \text{Equation 3}$$

Where,

$S(\Omega)$...track irregularity PSD ($\text{mm}^2 \cdot \text{m} \cdot \text{cycle}$),

A ...roughness constant ($\text{m}^2 \cdot \text{rad} \cdot \text{m}^{-1}$),

Ω ...irregularity frequencies ($\text{rad} \cdot \text{m}^{-1}$),

k ...constant parameter, usually is 0.25.

Similar track irregularity PSD equations were developed by different countries based on the American research with respect to different characteristics of their particular railways [32] [33].

1.3.2.3 Versine

A versine is the distance of the mid-chord offset from a curvature [34], as shown in Figure 1-10. It is easy to measure and calculate, and is sometimes used to describe track irregularities.

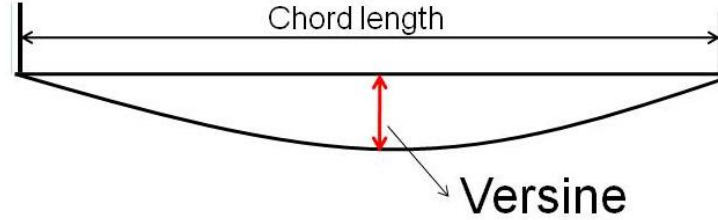


Figure 1-10 Geometric meaning of versine

1.3.2.4 Root Mean Square (RMS) value

The RMS value has been used to describe track irregularities in a rail surface corrugation study [35]. The vertical unsprung-mass acceleration of an axle box induced by the track irregularities is measured. The RMS value is calculated from Equation 4. It is a good way of measuring quantities varying both positively and negatively from the mean value, such as track irregularities. RMS value of the unsprung mass acceleration describes the track irregularity indirectly.

$$\psi_a = \sqrt{\frac{1}{t_2 - t_1} \int_{t_1}^{t_2} a^2(t) dt} \quad \text{Equation 4}$$

Where,

t_1 ...starting time of the test

t_2 ...ending time of the test

$a(t)$...time series of acceleration.

1.3.3 Track vertical irregularity

Track measurement contains irregularities of varying wavelengths, typically ranging from approximately 30 mm to over 70 m (or 150 m in case of high speed measurement). The distribution of track irregularities can be periodic, random or discrete. Railhead corrugations or cross-beam and sleeper effects are considered as periodic irregularities, which can cause significant vehicle vibrations [36]. Random irregularities tend to be located in a mixture of frequency bands and usually described statistically by using a one-sided PSD function. Discrete irregularities are usually caused by dipped rail joints or impacts due to wheel flats, and a solution model with respect to this was developed by Lyon [37]. Knothe and Grassie [38] claimed that five different wave propagation modes occur on railway track, including lateral bending, vertical bending and three torsional modes. Track irregularities are classified in different ways by different authors, Dahlberg [39] stated that irregularities can be divided into three categories: irregularities due to corrugations (30 to 80 mm), short wavelength irregularities (80 to 300mm) and long wavelength irregularities (0.3 to 2m).

TRC vehicles measure a point every 0.2 to 0.3m, therefore the TRC data measurement and derived quality assessment are not valid for the wavelength ranges mentioned above. Therefore, corrugations and short wavelength irregularities cannot be measured by a TRC and are not typically modelled using vehicle dynamics.

The first study of rail corrugations took place in the late 19th Century [40]. Rail corrugations can lead to a number of serious issues under many load cycles, such as the track settlement resulting in a loss of vertical track profile, ballast degradation and fastening deterioration. Massel [35], Fastenrath [41] and Dahlberg [39] have all stated that the development of corrugations is not fully understood. According to Lichberger [42], Grassie and Kalousek [43] and Sato, Matsumoto et al. [44], there are six types of corrugations:

- Heavy haul corrugation (200-300mm),
- Light rail corrugation (500-1500mm),
- Rolling contact fatigue corrugation (150-450mm)
- Booted sleeper corrugation (45-60mm),
- Rutting corrugation (50mm for trams),
- Roaring rail corrugation on high speed lines (25-80mm).

A detailed study of corrugations using numerical methods was undertaken by Jin, Wen et al. [45], which illustrates three factors: the periodically varying of rail profile, the stochastic varying of rail profile and the sleeper pitch, have a strong impact on the formation of rail corrugations. A series of measurements and tests were undertaken in Britain [46], showing that grinding new rail can delay the formation of rail corrugations by 2.5 years, and grinding corrugated rail can significantly reduce the railhead roughness. With increasing train speed, long wave length track irregularities in the range from 20 m to 120 m have a large effect on comfort [47]. Long wavelength track irregularities can be caused by various factors. The manufacturing process of the rail explains some long wave irregularities. Meanwhile, the variation of the stiffness and geometry of the track support system leads to long wavelength track irregularities.

1.3.4 Track lateral irregularity

Track lateral irregularities are usually corrected before they have a big influence on ride comfort or safety mainly because the vertical irregularities are much bigger and grow much faster, and hence need maintenance operations more frequently. The growth of lateral misalignments may be caused by a high L/V loading ratio, an increase in longitudinal forces, track dynamic uplift due to high vertical loads, etc. The growth may become stable after many loading cycles or keep increasing until there is a risk of buckling, which can cause derailment. The initial lateral misalignment tolerance for high speed newly installed track is between 1 and 4 mm, and the maximum allowable before maintenance required is 4 mm for high speed lines, according to SNCF [2]. The recorded track lateral irregularities are low pass filtered either at 35 m or 70 m wavelength, and any longer wavelength irregularity may be obtained from the curvature measurement.



Figure 1-11 Track buckle [48]

1.4 Chapter conclusion

This chapter helps build a better fundamental understanding of the track system and its geometry. The components of the railway track system were explained in details, namely: the rails, the fastenings, the sleepers, the ballast layer and subgrade layers and geotextiles. The definition of track geometry and its measurement were described, and the current methods used to determine the quality of the track geometry based on these measurements were explained. This introduction and further literature review allows the research aims and objectives to be described, in order to define a systemetric research approach and methodologies.

2 LITERATURE REVIEW

A large part of a railway infrastructure owner's budget is devoted to maintenance [49]. Nowadays, there is a clear trend towards increasing speeds and capacity, meaning that possession time is reduced and the window for maintenance activities becomes highly constrained. More efforts therefore required to understand the mechanisms of track deterioration and to design suitable maintenance strategies. It is important to understand the mechanism of the track deterioration and be able to predict the growth of track irregularities in order to reduce the life-cycle cost of the railway system and help designing new track structures [1]. Various models of track settlement have been developed to predict the development of vertical track irregularities. However, there are not many studies related to the growth of track lateral misalignments. In Section 2.1, empirical track vertical settlement models are studied in order to help better understand track settlement. In Section 2.2, models simulating the dynamic behaviour of railway track are explained. In Section 2.3, research related to track lateral irregularities is reviewed.

2.1 Track settlement models

It is recognised that track irregularities are largely caused by uneven track settlement, and uneven track settlement is largely influenced by the bending stiffness of the rail, ballast layer and subgrade deformation and initial track misalignment [50]. Track settlement is closely related to consolidation of the ballast and the inelastic behaviour of the subgrade [51]. The ballast transfers the load into the subgrade via the friction and shear forces between the individual ballast stones. Different magnitudes of track stiffness and ballast layer thickness cause irregular ballast settlement. The subsoil settlement is generated under rail joints and due to irregular stiffness of the ballast layer or the subgrade itself [52]. Generally, there are two phases of track settlement. Firstly, there is a period of rapid settlement directly after tamping. After that, a slower settlement occurs as shown in Figure 2-1.

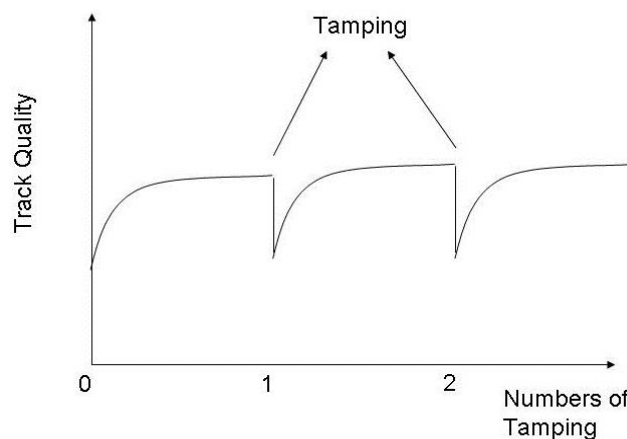


Figure 2-1 Track settlement process

It is important to understand the mechanism of track settlement in order to develop a suitable settlement model.

2.1.1 Sato's Track settlement model

Sato [53] claims that the settlement of tamped track under many loading cycles can be expressed as

$$y = \tau(1 - e^{-\alpha x}) + \beta x \quad \text{Equation 5}$$

Where,

y...settlement [mm]

x...repeated number of loading or tonnage carried by track

τ , α and β ... coefficients

The two phases of track settlement are taken into account in this equation. The first part of the equation: $\tau(1 - e^{-\alpha x})$, represents the initial settlement of the track directly after tamping, while βx describes the long term settlement. The parameter α describes the rate of the initial settlement and τ indicates the severity of the settlement. Sato explained that the parameter β depends on several factors, such as the velocity of the repeated loading, the amount of ballast contamination, the sleeper pressure and the ballast vertical acceleration. Ideally, the parameter β should be small to minimise settlement. Therefore, the change of the impact factors of β can be useful in the design process.

Sato has also defined the rate of the deterioration D as

$$D = L \times M \times N \quad \text{Equation 6}$$

- ❖ L is the influence of the axle load, vehicle factor and the speed, and can be determined by:

$$L = \sum 2Q_i \times C_i \times v_i \quad \text{Equation 7}$$

Where,

$2Q_i$...static axle loads [kN]

C_i ...vehicle factor

v_i ...speed [m/s]

The calculation of C_i is shown below

$$C_i = \frac{1}{1 - \xi\eta} \quad \text{Equation 8}$$

$$\eta = \frac{M_b}{m} \quad \text{Equation 9}$$

Where,

ξ ...constant expressing the spring characteristic of the vehicle suspension, which is taken as 0.5 for freight vehicles and 0.9 for passenger coaches

M_b ...sprung mass (kg)

m ...unsprung mass (kg)

- ❖ M is the track structure factor, which is proportional to the maximum sleeper pressure, maximum ballast acceleration and the coefficient of impact.

$$M = P_b \times \ddot{y} \times s \quad \text{Equation 10}$$

$$M = \frac{P_b \sqrt{k_1}}{\sqrt{mElk}} \quad \text{Equation 11}$$

Where,

P_b ...maximum load on sleeper [kN]

\ddot{y} ...maximum ballast acceleration [m/s^2]

s ...impact factor

k_1 ...spring constant between rail and sleeper

E ...constant of elasticity of rail steel [N/m^2]

I ...moment of inertia of the rail [m^4]

k ... stiffness per length of rail supporting [kN/mm]

- ❖ N is the level of irregularity of the rail, sleeper, ballast and subsoil or the contamination of the ballast. N has not yet been expressed well numerically.

A model of the growth of track irregularities is presented by Sato, which is influenced by five factors.

$$S = 2.09 \times 10^{-3} T^{-0.31} V^{0.98} M^{1.1} L^{0.21} P^{0.26} \quad \text{Equation 12}$$

Where,

S ...average irregularity growth rate [mm/100 days]

T ...traffic tonnage [million tons/year]

V ...average running speed [km/h]

M ...structure factor

L ...influence factor of CWR (Continuous Welded Rail) or jointed rail, 1 for CWR and 10 for jointed

P ...influence factor for subgrade (1 for good and 10 for bad)

It can be found that the growth of irregularities is almost proportional to the running speed and the repeated loading. Improvement of the track structure can effectively reduce irregularity growth.

2.1.2 Frohling's track settlement model

Frohling [54] analysed the differential track settlement in relation to dynamic wheel loading and track support condition. The methodology of the dynamic settlement model is described in detail in Figure 2-2.

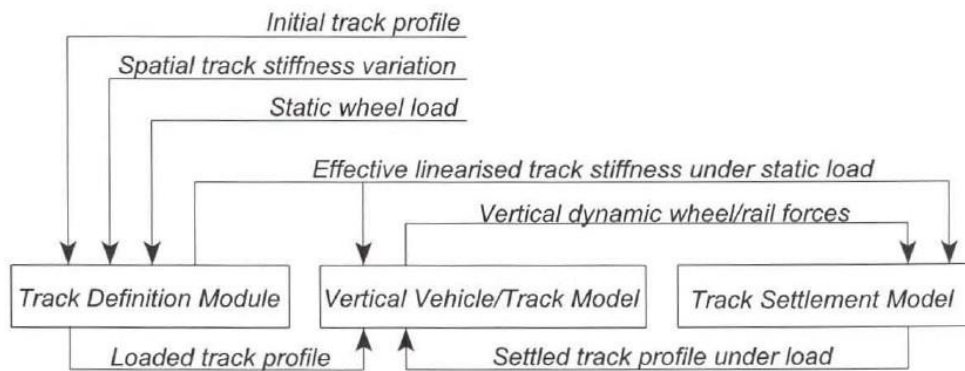


Figure 2-2 Interactive dynamic settlement methodology [54]

The settlement, in mm, after N load alternations e_N is defined in Equation 13.

$$e_N = \left[\left[k_1 + k_2 \left(\frac{k_{2mi}}{k_3} \right) \right] \times \frac{P_{dyn}}{P_{ref}} \right]^w \times \log N \quad \text{Equation 13}$$

Where,

k_{2mi} ...measured average track stiffness of an individual sleeper, after the consolidation phase [N/m]

k_{1-3} ...constant factors

P_{dyn} ...dynamic wheel load [kN]

P_{ref} ...reference wheel load [kN]

N...number of load cycles

w...coefficient of track settlement

The process of the accumulated ballast deterioration can be used to account for a mix of cyclic loadings at a particular sleeper. However, only ballast settlement is considered, and no ballast degradation is taken into consideration in this model.

2.1.3 Shenton's Track Settlement Model

Shenton [52] investigated several major factors related to track degradation, the dynamic forces, rail irregularities, sleeper spacing, sleeper support, ballast settlement and substructure. A numerical settlement model was developed to forecast the settlements after N load cycles:

$$e_N = K \frac{F_e}{10[(0.69 + 0.028h)^5 \sqrt[5]{N} + 2.7 \times 10^{-6}N]} \quad \text{Equation 14}$$

Where,

K...track structure factor, a value of K=1.1 is typical for track in Britain

F_e ...equivalent wheelset load [t]

h...lifting value [mm]

The equivalent wheelset load is calculated according to the Equation 15, which considers the fact that high wheelset loads are dominant in settlement. It ensures a more rational model for the different axle loads F_i .

$$F_e = \sqrt[5]{\frac{\sum_{i=1} F_i^5 N_i}{\sum_{i=1} N_i}} \quad \text{Equation 15}$$

According to Dahlberg [51], Equation 13 can be simplified as

$$e_N = K_1 N^{0.2} + K_2 N \quad \text{Equation 16}$$

Shenton considers the number of load cycles in the settlement model. The coefficient K_1 and K_2 depend on the major factors, and are selected to ensure that the second term becomes significant only if the number of load cycles, N, is larger than 10^6 . This model emphasises the relationship between settlement and number of load cycles.

2.1.4 Track settlement study from ORE

According to ORE (Office for Research and Experiments of the International Union of Railways, UIC) studies by Alva-Hurtado and Selig [55], the ballast strain after N identical load cycles e_N [mm] can be calculated by Equation 17.

$$e_N = e_1 \times (1 + b \times \log N) \quad \text{Equation 17}$$

Where,

N ...number of load cycles

b ...constant, approximately 0.2 for an individual sleeper, and around 0.43 for the track grid

e_1 ...settlement after the first load cycle [mm]

In the ORE track settlement model [56], the settlement after a certain period of operational load T is described in Equation 18.

$$E_T = a_1 + a_0 \times \log\left(\frac{T}{2 \times 10^6}\right) \quad \text{Equation 18}$$

Where,

a_0, a_1 ... coefficients of settlement depending on the quality of the permanent way

T ...period of operation load [t]

Like Sato's model, this model also consists of two parts: the first part e_1 describes the settlement directly after tamping, and the second part $e_1 \cdot b \cdot \log N$ represents the track settlement coupled with the traffic volume. However, an Australian study by Lonescu et al. [57] has shown that the ORE settlement model is inaccurate under a large number of load cycles. The track settlement under a large number of load cycles is stated as:

$$e_N = e_1 N^b \quad \text{Equation 19}$$

Where,

b ...empirical coefficient

The conclusion of the study is that the trains with high axle loads or high wheel dynamic forces increase track settlement.

2.1.5 Ford's track settlement model

One limitation of the ORE model is that there is a precondition of identical loading. Ford [58] has modified Equation 17 to investigate the varying load cycles. e_1 is redefined as e'_1 which is a curve against the applied stress Δq and failure stress q_f . A new value for N , which is N_e , is determined by inverting Equation 17.

$$N_e = 10^{\frac{\left[\frac{e_N}{e'_1} - 1\right]}{b}} \quad \text{Equation 20}$$

Where,

e'_1 ...initial permanent strain corresponding to the new load

e ...the current value of permanent strain

Therefore, the ballast settlement is determined from Equation 21.

$$E_N = e'_1(1 + \log(N_e + 1)) \quad \text{Equation 21}$$

Unlike Sato's model, the long-term settlement grows logarithmically. There are some limitations to this model. Some assumptions in the modelling process are not strictly valid. The confining stress of the ballast and the ballast failure stress are assumed to be constant, therefore the ballast strain is assumed constant throughout the ballast layer.

2.1.6 Al Shaer's settlement study

Al Shaer, Duhamel et al. [59] tried to link the settlement with the acceleration for high load velocities based on experimental results. A reduced scale (1/3) ballasted railway track is represented by three sleepers, and these sleepers are loaded with the help of three hydraulic jacks that provide signals having the shape of the letter M. A moving load is therefore simulated at different rolling velocities, and the relationship between the load velocity and the increment of the settlement is shown in Figure 2-3.

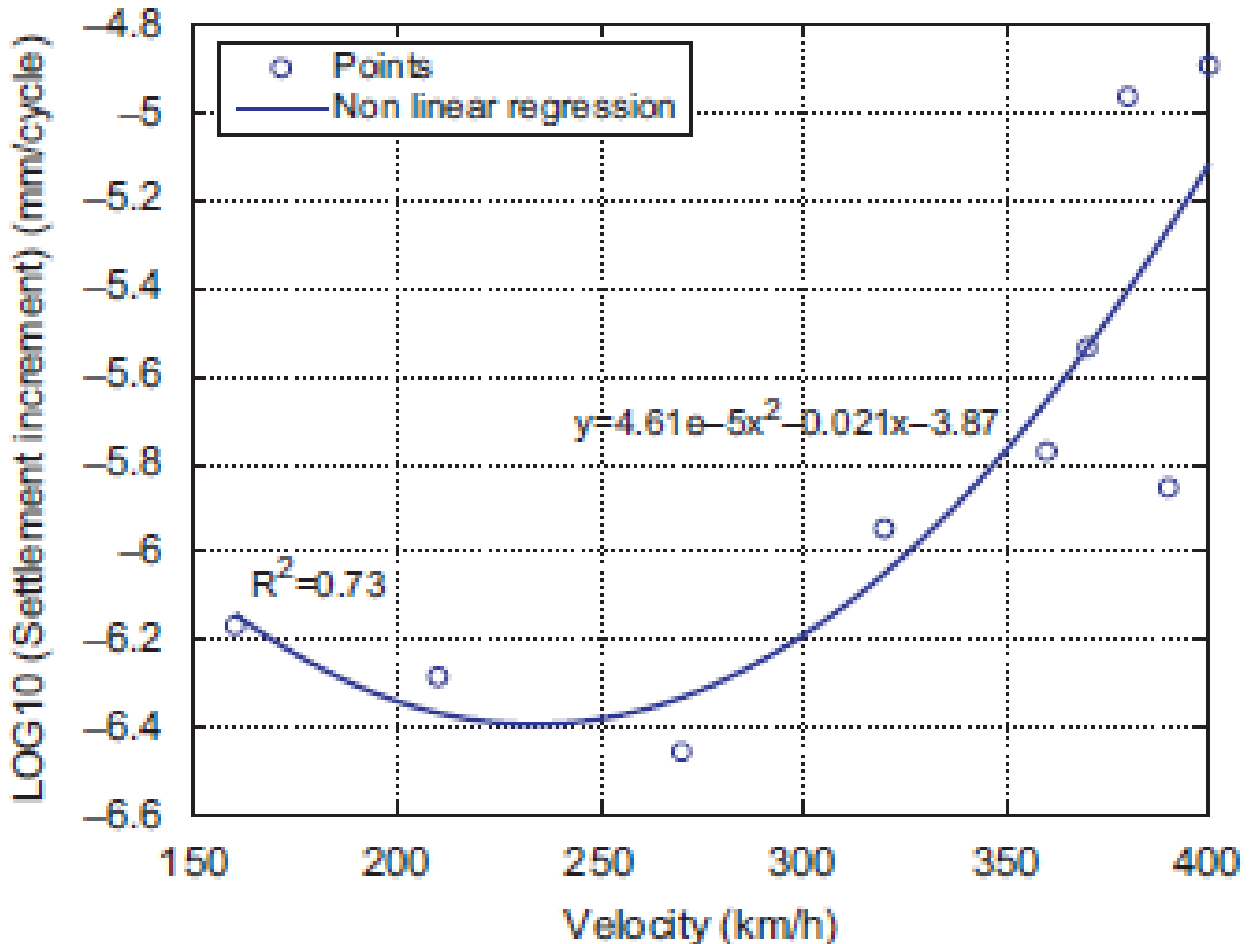


Figure 2-3 Relation between velocity and settlement increment [59]

Furthermore, the relationship between increment of the standard deviation caused by the settlement and the average accelerations of the sleeper in the upward and downward directions is studied, and a linear relationship is found between them. However, the linear relationship is only accurate when the speed is below 360 km/h.

2.1.7 Gao and Zhai's track settlement model

Gao and Zhai [60] investigated track settlement by combining the vehicle-track coupling vibration model and the track settlement model. The dynamic response and the irregularities of the track are taken as a feedback to the model, as shown in Figure 2-4.

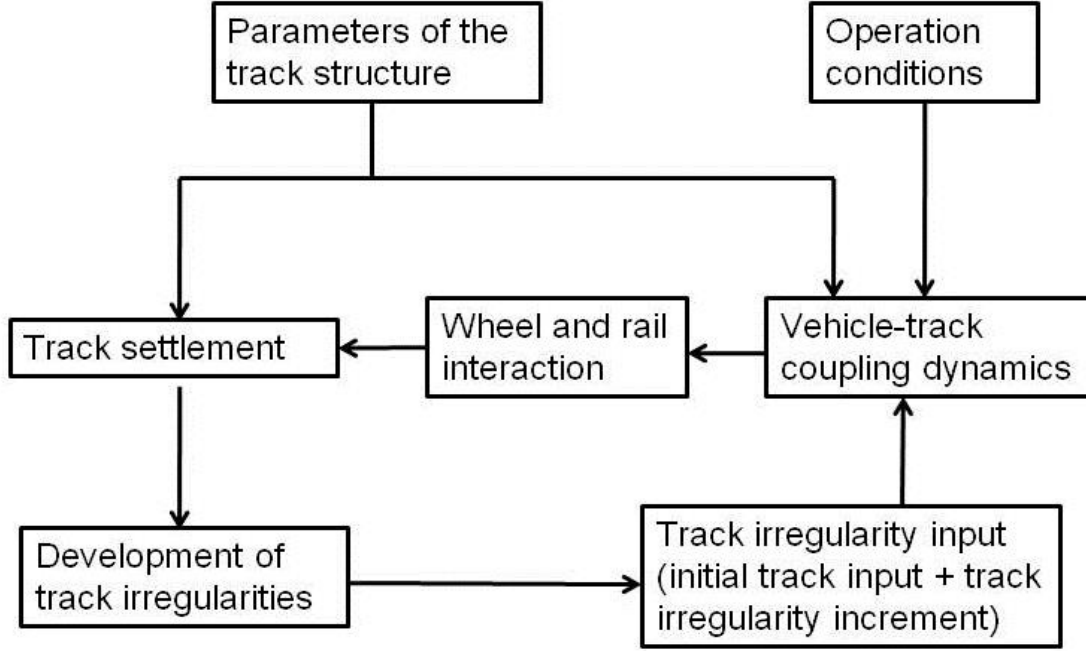


Figure 2-4 Research method of track settlement [60]

The numerical track settlement model is shown in the Equation 22 and Equation 23.

$$e_t = \sum_{i=1}^N e_{bi} \quad \text{Equation 22}$$

$$e_{bi} = c_1(\sigma_b - c_2)^2 c_{ba} \quad \text{Equation 23}$$

Where,

e_t ...track settlement [mm]

e_{bi} ...track settlement under i load cycles [mm]

N ...number of load cycles

c_1 and c_2 ... experimental coefficient

c_{ba} ...ballast acceleration [m/s^2]

σ_b ... ballast stress [N/m^2]

The interaction between vehicle dynamics and dynamic track performance are considered in the study. Different types of track structure and operational factors can be used as the input in this model. It is found that the roughness of the surface of the wheel and rail has a strong impact on track settlement behaviour.

2.1.8 Track vertical deterioration study from BRR (British Rail Research)

In the track deterioration study by BRR [61], the effects of track bed stiffness variation on track geometry deterioration are identified. A number of basic contributors to track geometry deterioration have been determined in order to predict:

- Dynamic forces due to unsprung mass response to weld dips and the resulting track quality
- Dynamic forces due to unsprung mass response to general track roughness and the resulting track quality
- Track quality due to vehicle body response to general track roughness

These three aspects are combined together to calculate the total track SD, and the equation is shown below.

$$\begin{aligned}
 \text{Total Track SD} &= \left[\left(\text{Track SD due to unsprung mass response to weld dips} \right)^2 \right. \\
 &\quad + \left(\text{Track SD due to unsprung mass response to general track roughness} \right)^2 \\
 &\quad \left. + \left(\text{Track SD due to vehicle body response to general track roughness} \right)^2 \right]^{1/2}
 \end{aligned}
 \tag{Equation 24}$$

However, further equations derived in the track geometry model have not yet been validated. Additionally, the model was only used to analyse a limited number of test cases as part of the Eurobalt project.

2.2 Track system models

Track system dynamics has been extensively studied, and various mathematical models have been developed for design and maintenance purposes. Most track models assume that the track system is excited by a single wheel or a single bogie with two wheelsets [62]. The track system is most commonly modelled either in the frequency or the distance domain. Spatial domain methods use variable frequencies to excite the track at a fixed point along the track, while distance domain methods use variably moving loads applied along the track during a certain time period. Most spatial domain track studies are based on the infinite Euler-Bernoulli and Timoshenko beam models [63, 64]. In general, there are two methods that simulate the vibration behaviour of the rail, which are the Finite Element Analysis (FEA) and Vibration Modal method. The vibration modal method effectively reduces the number of Degrees of Freedom (DOF), and hence, the calculation time, while the FEA is better at dealing with nonlinear factors in the track system [65]. Track models are also classified as rails resting on a continuous support or on discrete supports, which are discussed in detail in [66].

2.2.1 BOEF model

Beam on elastic foundation models (BOEF) are relatively simple track models, in which the track foundation modulus is based on experimental tests [66, 67]. BOEF can be considered for track behaviour at rail level, but the track foundation beneath the rail is oversimplified as a foundation modulus. Therefore, BOEF models are not ideal for track lateral movement modelling. Figure 2-5 shows an early model that describes the railway track system, in which the infinite beam is continuously supported by an elastic foundation. A fourth order partial differential equation (PDE) describes the BOEF model, as shown in Appendix B. It is a simple model that ignores the dynamic behaviour of the sleepers and ballast, and the discrete support at the sleepers is also simplified. The model is useful to understand the basic dynamics of the track system, and can solve some low frequency dynamic problems.

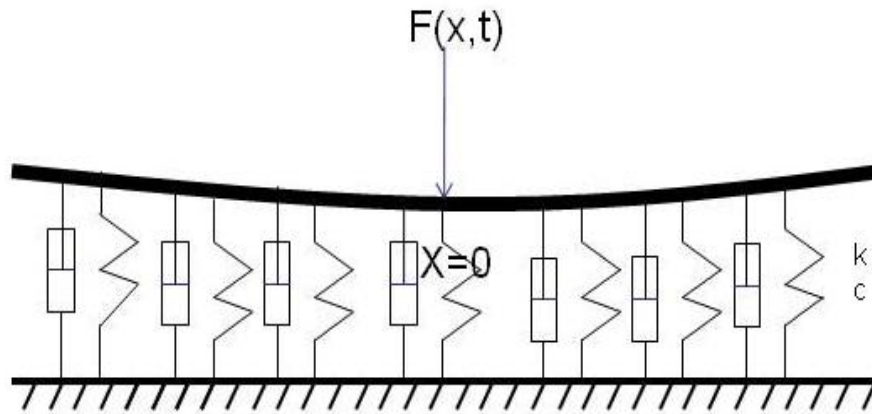


Figure 2-5 Track movement model

2.2.2 Layered elastic models

Based on a BOEF model, layered elastic models [68, 69] can be used, which give a more realistic dynamic behaviour. Layered elastic models are mainly static track system models, in which the average modulus of each layer of the track is used, and the pressure distribution at different track system layers can be found.

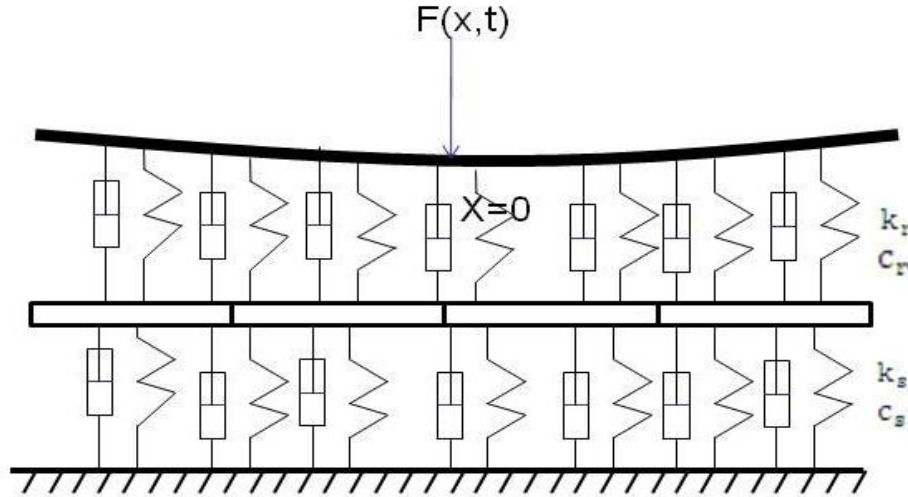


Figure 2-6 Double Layer Elastic Track Model

For a double layer elastic model (Figure 2-6), a fourth order PDE can be built for the rail, and a second order PDE can be established for each track bed layer. For both BOEF and layered elastic models, the vibrational behaviour of the track can be analysed, however, it is difficult to add a moving load and non-linear behaviour of the interfaces between different track subsystems to these models.

Finite Element (FE) models [70, 71] and layered elastic models [68, 69] are both quasi-static track system models. In layered elastic models, the average modulus of each layer of the track is used, and the pressure distribution at different track system layers can be found.

2.2.3 Discrete supported track model

BOEF and layered elastic models all assume that the rail is continuously supported, however, in reality, the track is supported discretely. Consequently, discrete supported models have been developed, as shown in Figure 2-7.

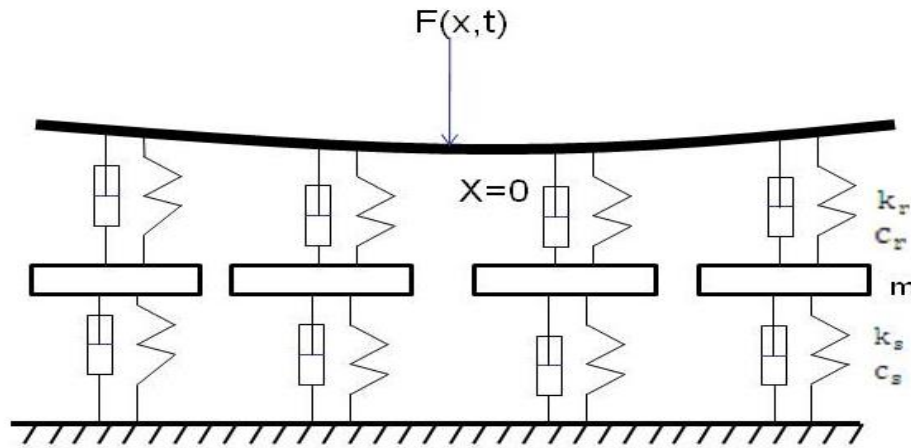


Figure 2-7 Double layer discretely supported track model

Two methods are widely used to describe and solve a discretely supported track model, which are the Finite Element Analysis and modal analysis. The vibration modal analysis effectively reduces the number of Degrees of Freedom (DOF), and hence, the computation time, while the FE model is better at dealing with the nonlinear factors in the track system [65]. Advanced vehicle dynamics analysis tools exist, such as VAMPIRE®² and SIMPACK³ (Website 5). These vehicle dynamics packages can use track geometry data obtained from a Track Recording Coach (TRC). However, this tool cannot simulate the loading in the track bed or easily allow representative variations of the vertical and lateral track stiffness [72]. Furthermore, these software systems do not allow multiple layer track models and relative force connection between track elements underneath adjacent axles.

2.3 Track lateral irregularity studies

Track lateral stability is a key requirement to ensure safety and passenger comfort. Track lateral shift and buckling can cause serious running stability problems or even derailment. Therefore, it is important to identify the mechanism of track lateral movement under dynamic wheel loads. Lateral displacement resistance plays an essential role in stabilising the track, and it is mainly influenced by the lateral sleeper support, stress free temperature, condition of joints, friction between sleeper and ballast, and the effect of tamping [73].

Unlike the vertical displacement, track lateral displacement is affected by vertical, lateral and longitudinal forces. If the vertical force is high, the resistance between the ballast and the sleeper is high. Therefore, the L/V load ratio is a critical parameter in track lateral movement. The longitudinal force can lead to track uplift or exert a lateral misalignment, shown in Figure 2-8. The black line represents the rail, and the orange line shows the longitudinal force and the decomposition of this force along the track and perpendicular to the track.

² Vampire is copyright 2013 and registered trademark of DeltaRail Group pc. Derby

³ Simpack is copyright 2013 of Simpack AG. Gilching Germany.

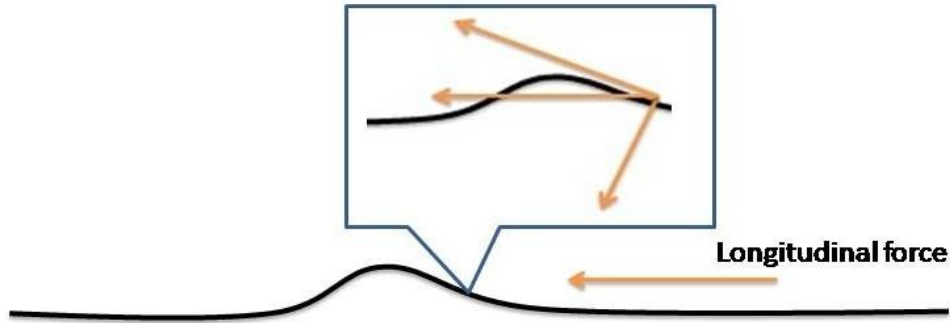


Figure 2-8 Initial lateral misalignment effected by longitudinal force

There have not been many studies about the development of the track lateral misalignment by dynamic load cycles. One model was developed in France following track buckling studies.

2.3.1 Prud'homme studies

One of the earliest studies of track lateral misalignment was undertaken by Prud'homme [74]. The lateral resistance of wooden sleeper track under a moving lateral load was experimentally evaluated. The vertical load remained constant while the lateral load incremented after every Track Loading Vehicle (TLV) pass. The first empirical equation for the lateral resistance of track with timber sleepers was developed, and is given in Equation 25.

$$L_p = 10 + \frac{V}{3} \quad \text{Equation 25}$$

Where,

L_p ...track lateral resistance [kN]

V ...vertical axle load [kN]

The Prud'homme limit provides a good guideline to following lateral track movement studies, but some important factors, such as curvature and rail thermal load effects, were not considered in this equation. In the following study [75], Equation 25 is improved to reflect the rail temperature, track curvature, track stiffness and rail profile properties.

$$L_p = \rho \left(10 + \frac{V}{3} \right) \quad \text{Equation 26}$$

$$\rho = \left[1 - 0.125AT \left(1 + \frac{800}{R} \right) \right] \left(\frac{K_v}{2 * 10^7} \right)^{1/8} 0.225 \frac{(EI_{xx})^{1/4}}{(EI_{zz})^{1/8}} \quad \text{Equation 27}$$

Where,

R ... curve radius (m)

T ... temperature of the rails above the neutral temperature (C)

EI_{xx} ...bending rigidity of both rails in the lateral direction (Nm²)

EI_{zz} ...bending rigidity of both rails in the vertical direction (Nm²)

A ... rail cross sectional area (m²)

K_v ...foundation modulus of the track (N/m²)

2.3.2 Kabo's track lateral resistance studies

After Prud'homme's study, a three-dimensional FE model [76] was developed to study ballast resistance under vertical and lateral loading against various influencing factors. The sleeper is modelled as an elastic body with material properties of concrete, and the ballast is modelled using an elastoplastic constitutive continuum model of a granular material that accounts for non-linear hardening and compaction. Four different geometries of ballast shoulder have been analysed against different vertical loads and friction, and it shows that either widening the ballast shoulder or increasing the shoulder height can increase the lateral resistance significantly.

The results show that the peak lateral ballast resistance for a single concrete sleeper varies from 5 to 18 kN as the ballast compaction increases. The results also show that the deterioration is not closely related to subgrade stiffness, while the top ballast layer suffers the most strain and is the leading contributor to the settlement.

2.3.3 Lateral sliding track resistance study at the University of Southampton

The resistance of the railway track is more complex than the lateral resistance defined by Prud'homme. Three contact areas between the ballast and sleeper, which are the sleeper base, ballast crib and shoulder, are analysed in a recent experimental study [77] at the University of Southampton. The sleeper base study is based on an empirical relationship [78] of normal, lateral and moment loads at failure.

The maximum bearing capacity of the base resistance can be calculated by

$$V_{\max} = N_{\gamma} s_{\gamma} (0.5\gamma B - \Delta u) BL \quad \text{Equation 28}$$

In which,

$$\begin{cases} N_q = K_p e^{\pi \tan \phi'} \\ K_p = \left(\frac{1 + \sin \phi'}{1 - \sin \phi'} \right) \\ N_{\gamma} = (N_q - 1) \tan(1.4\phi') \\ s_{\gamma} = 1 + 0.1 K_p \left(\frac{B}{L} \right) \end{cases} \quad \text{Equation 29}$$

Where,

N_q ...bearing capacity factor

N_{γ} ...analogous to the bearing capacity factor found in the Meyerhof formula [79]

K_p ...passive pressure coefficient

s_{γ} ...shape factor from Meyerhof formula

ϕ' ...angle of effective shearing resistance [rad]

B ...foundation width [m]

L ...foundation length [m]

γ ...bulk unit weight of ballast [kN/m³]

u ...pore water pressure

The crib resistance can be determined using

$$R_{\text{crib}} = (s - b)lh'\tan\phi' \quad \text{Equation 30}$$

Where,

s...sleeper spacing or stable slope angle for ballast [rad]

b...sleeper width in the direction of the track [m]

l...sleeper length [m]

The result of the ballast shoulder tests is compared and considered consistent with the ERRI (European Rail Research Institute) report [80], ORE (Office for Research and Experiments of the International Union of Railways) report [81] and Kabo's study [76]. It shows that a change in shoulder width can largely influence the lateral resistance over a certain range of lateral displacements. There is a wide degree of uncertainty in calculating the shoulder resistance because of the difficulties of quantifying the effective angle of shearing resistance for the ballast.

2.3.4 SNCF Studies

Kish, Samavedam et al. [2] investigated the mechanism of track lateral misalignment growth, and developed a model to predict track lateral shift. As shown in Figure 2-9, the parameters used in the track shift analysis are vehicle characteristics, foundation modulus, rail mass, axle vertical and lateral load, rail thermal load, track curvature, and so on.

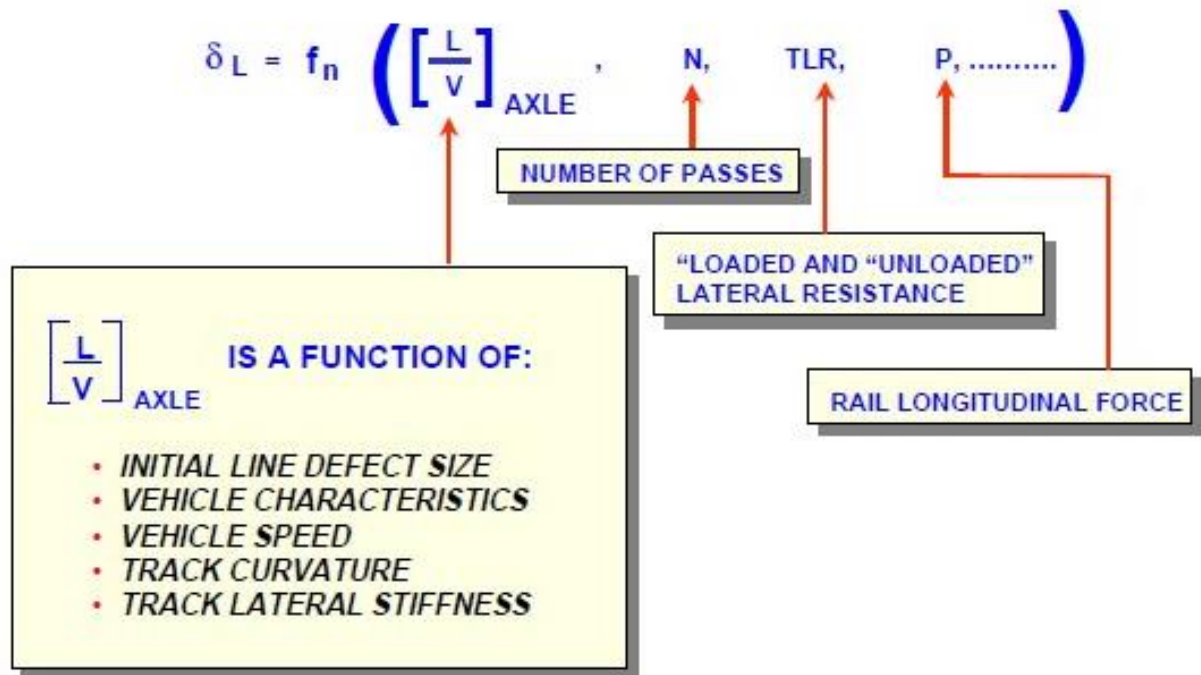


Figure 2-9 Track lateral shift parameters [2]

Two fundamental models were coupled to analyse the problem: the track residual deflection model and the vehicle dynamics model (Figure 2-10). In the track residual deflection model, the track is considered as a beam on springs with nonlinear elastoplastic characteristics, and the moving lateral loads are characterised as quasi-static. The vehicle dynamic model utilises the OMNISIM code [82], which assesses wheel climb more accurately.

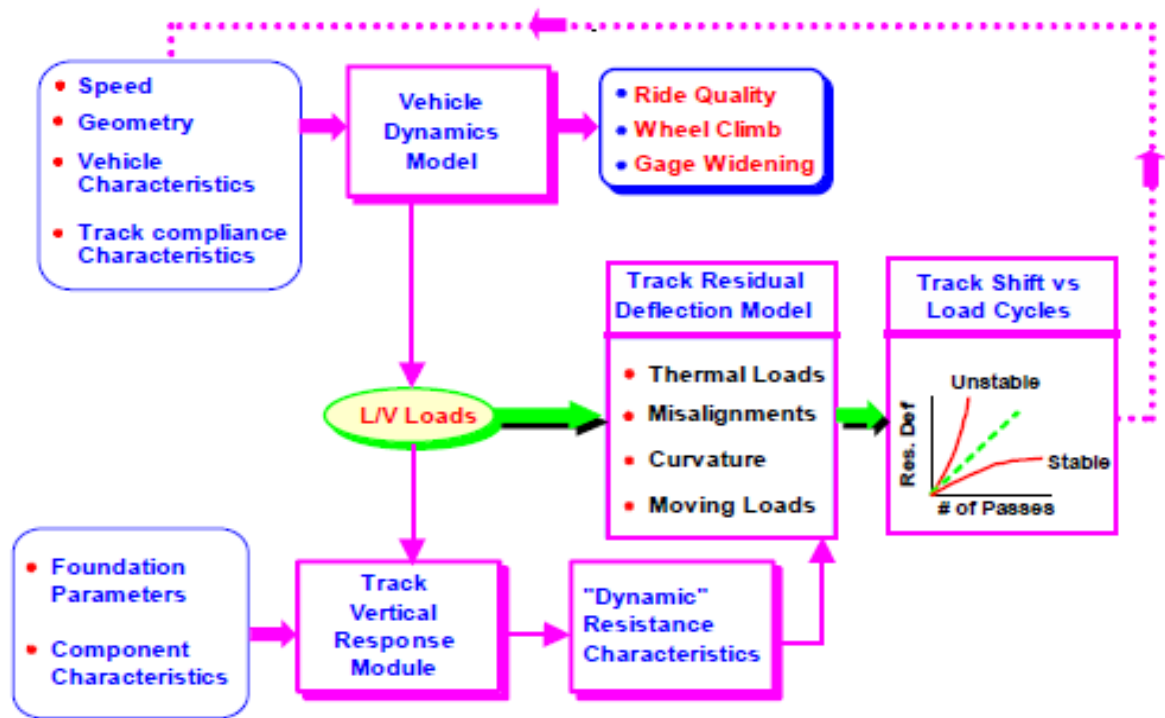


Figure 2-10 Modelling approach [2]

The validation shows that the model can predict relatively accurate track lateral misalignment within a certain number of TLV passes. The effect of a few factors, which are the track curvature, temperature (thermal force), lateral resistance, sleeper-ballast friction, net-axle lateral load and the number of passes, on the track lateral shift is analysed. Two limits are determined with respect to elastic deflection and stable residual deflection. These limits are more suitable for modern concrete sleeper track compared with the limits determined by Prud'homme based on wooden sleeper track.

2.3.5 Track Buckling Studies

Kish and Samavedam [83] analysed track buckling development to predict the probable number of buckles on a given track. There are two primary track parameters used in the research – lateral resistance and initial lateral displacement. Some other parameters with less impact on track buckling are also considered, such as the torsional resistance, longitudinal resistance, dynamic vehicle loads, etc. The load and strength of the track structure are expressed in terms of temperature in the track buckling growth process.

The overall approach is shown in Figure 2-11.

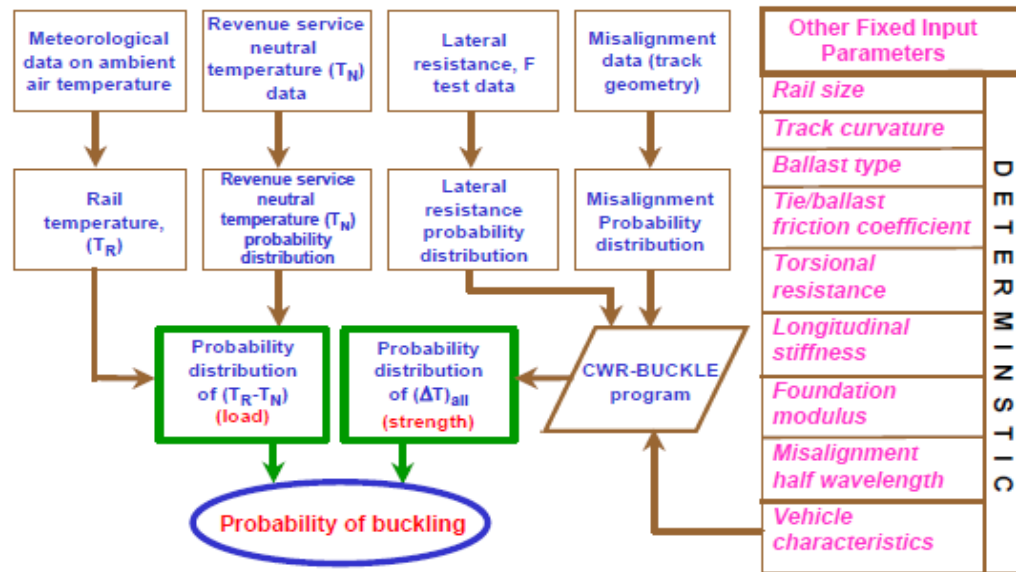


Figure 2-11 Track buckling analysis approach [83]

However, this model does not consider the effect of the non-uniformly distributed ballast resistance along the track, missing sleepers and fasteners, the variation of track gauge, and differing neutral temperatures between two rails. Lim and Sung [84] developed a more accurate three dimensional track buckling model taking into account more impact factors.

2.4 Contemporary regulation

The limit of track lateral irregularities depends on different train speeds, and Figure 2-12 shows the peak values of lateral irregularities with wavelength from 3 m to 25 m according to various standards [85].

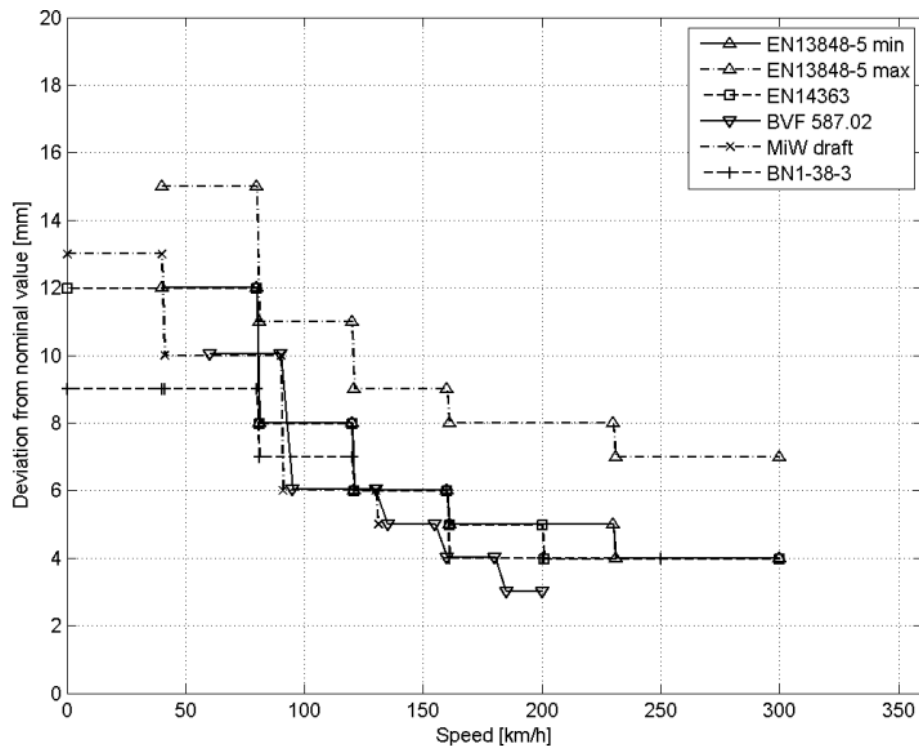


Figure 2-12 Track lateral irregularity limits for different speeds [85]

Resistance to Lateral Displacement (RLD) is the value of the resistance to lateral track irregularities which is important in the geometric stability to withstand buckling.

Different forms of the Prud'homme equation are used as a vehicle acceptance criterion in many countries [86-91]. However, it is considered over simplified to describe the mechanism of lateral track movement. Additionally, the experiment was based on track with timber sleeper and lighter rail sections, while the track system and traffic scenario have significantly changed with the development of the concrete sleepers amongst other things.

The current SNCF practice on misalignment tolerances and load limits for high-speed trains is given in a recent SNCF paper [92]. In this paper, the critical misalignment at which operations are impacted and safety is potentially compromised is indicated as a 12mm peak to peak value with a wavelength range of 20-40m. The maximum allowable misalignment before maintenance should be smaller. Concrete sleepers on granite ballast must be designed such that the minimum lateral resistance should be around 13.3-17.8 kN/sleeper.

The current US high speed standard, defined by the Federal Railroad Administration (FRA), indicates an L/V load ratio of around 0.5 for different values of vertical axle loads. It gives higher allowable values than given by the Prud'homme limit [93]. Furthermore, the limit in this study also varies with the change of vertical load, as shown in Table 2-1.

Table 2-1 Proposed net axle L/V limits

V (kN)	L/V limit	
	$L/V=0.28+4.46/V$ (no alignment defect)	$L/V=0.28+3.97/V$ (with alignment defect)
89	0.50	0.48
133	0.43	0.41
178	0.39	0.38
245	0.36	0.35

2.5 Chapter conclusion

It is important to understand the mechanisms behind the development of track irregularities, and many studies have been carried out to model track vertical irregularities. A comparison study of different settlement models [94] shows that there are considerable differences between the models, and it is necessary to consider various parameters in order to choose a suitable model. Most of the numerical models are empirical and based on duplicate experiments. However, lateral track misalignment development is not well understood, because little research has been carried within this area. Contemporary regulations are mostly based on the Prud'homme limit, which is a simple function with two parts involving the L/V loading ratio and static lateral resistance. This model may be improved by considering dynamic influences rather than just the net L/V ratio and lateral forces. A limit for the size of lateral track irregularities for different speeds is defined, yet without considering many other influencing factors. All of these limits may not be efficient from the maintenance point of view, which can be increased by having an accurate prediction of a particular railway line.

3 STATISTICAL ANALYSIS OF TRACK QUALITY

This chapter contains a series of statistical analysis studies about the relationship between lateral and vertical irregularities, between track lateral irregularities and curvature, and about the track lateral deterioration over time. For the first two relationships, it is better to have lots of track data covering long sections of different types of track. For track deterioration over time, it is better to have data covering the same section of track measured at different time intervals. Therefore, track data from the European project DynoTrain has been chosen for the first two studies, while the West Coast Main Line (WCML) and East Coast Main Line (ECML) data sets have been used for studying lateral track deterioration over time. The standard deviation of track alignment low pass filtered below 35m wavelength is generally considered to be a good overall indicator of track quality [95]. Therefore, the irregularity data filtered at 35m is selected in the statistical analysis.

3.1 The relationship between track lateral and vertical irregularities

In order to obtain representative results, the input data to the statistical analysis should be representative of a wide range of track conditions. A large amount of track data produced by the EU project DynoTrain was chosen for this research because it covers track representative of different countries and different running speeds. This track database contains measured track data from 6 European railway networks and 3 of them were selected for this work. Each network database consists of track categories with different operational speeds shown in Table 3-1. There is a lot of track information with a total length more than 5800 km.

Table 3-1 Track categories

Freight lines	$0 < v \leq 120 \text{ km/h}$
Regional lines	$120 < v \leq 160 \text{ km/h}$
Upgraded lines	$160 < v \leq 200 \text{ km/h}$
High speed lines	$200 < v \leq 300 \text{ km/h}$

There are many more studies into vertical track deterioration than lateral track deterioration. One of the most important reasons is that the changes in the lateral alignment are slower than the changes in vertical alignment under typical loading cycles [96]. Therefore, the maintenance of lateral misalignment is usually considered to be less important. Most track settlement models only include the vertical influence factors and ignore the lateral parameters. The deterioration in the lateral direction is a nonlinear phenomenon because of the highly nonlinear behaviour of vehicles in curves or on straight track due to possible hunting behaviour, and is related to forces on both vertical and lateral direction. On the contrary, the vertical settlement of track is very much governed by vertical axle load and vehicle speed only.

However, as an indivisible load supporting system, it is possible that the track lateral alignment has an impact on the vertical track settlement behaviour. Reduced horizontal residual stresses that confine the ballast layer can decrease the stability of the track [97]. Therefore, it is sensible to analyse the relationship between the lateral and vertical track settlement.

3.1.1 Distance domain analysis

Firstly, a correlation coefficient is used to see if there is a strong linear relationship between track lateral and vertical irregularities. For data sets $X = (x_1, x_2, x_3, \dots, x_n)$ and $Y = (y_1, y_2, y_3, \dots, y_n)$, the level of scatter of the data set around the best-fit line can be measured by the correlation coefficient r , as defined in Equation 31. The detailed linear regression description is shown in Appendix A.1. The correlation coefficient takes a value between -1 and 1. The data is completely correlated positively when r equals 1 (-1 means correlated negatively), while the data is not linearly related at all when r equals 0. There are three level of correlation: $|r| < 0.4$ shows the data sets are not correlated, $0.4 \leq |r| < 0.7$ shows some degree of correlation, and $0.7 \leq |r| \leq 1$ indicates a high correlation [98].

$$r = \frac{n \sum x_i y_i - \sum x_i \sum y_i}{\sqrt{n \sum x_i^2 - (\sum x_i)^2} \sqrt{n \sum y_i^2 - (\sum y_i)^2}} \quad \text{Equation 31}$$

The SD values of 200, 600 and 1000 m track irregularities in both vertical and lateral directions are calculated and are compared. The calculation results are shown in Appendix A.1., and it is found that results calculated using different track length show similar trends. Therefore, the typical 200 m SD results are chosen to describe the relationship between vertical and lateral irregularities in this section.

The correlations between the vertical and lateral irregularity SD results of tangent and curved track are separately calculated and the coefficients are listed in Table 3-2. For Network C, the track sections are relatively shorter so the result may not be as accurate as the results from Network A and B. In order to find more representative results, all track sections of different types of tracks from all networks are combined together, and the overall results are shown in the last column in the table. Generally speaking, the correlation coefficients are bigger than 0.4 which indicates a reasonable relationship between vertical and lateral irregularities, in the sense that decreasing quality in the vertical direction generally coincides with decreasing quality in lateral direction.

Table 3-2 Correlation coefficient of track lateral and vertical irregularities

	Types Networks	Freight lines	Regional lines	Upgraded lines	High speed lines	Total track
Tangent track	Network A	0.8222	0.5947	0.5690	0.2667	0.4926
	Network B	-	0.4610	0.4884	0.4779	
	Network C	-0.0688	0.0283	0.2843	-	
Curved track	Network A	0.7280	0.6637	0.6196	0.2722	0.5562
	Network B	-	0.4630	0.4474	0.3806	
	Network C	0.2482	-0.0533	0.3565	-	

Figure 3-1 shows the linear regression of the overall combined track data results for tangent and curved track respectively. The pink dashed line represents the limit when lateral irregularity SD equals the vertical SD. There are a few points with lateral SD bigger than the lateral limit provided by the standard in Section 2.4. However, the number of these points are smaller than 4 in both plots, so the influence of these points on the statistical analysis result can be ignored.

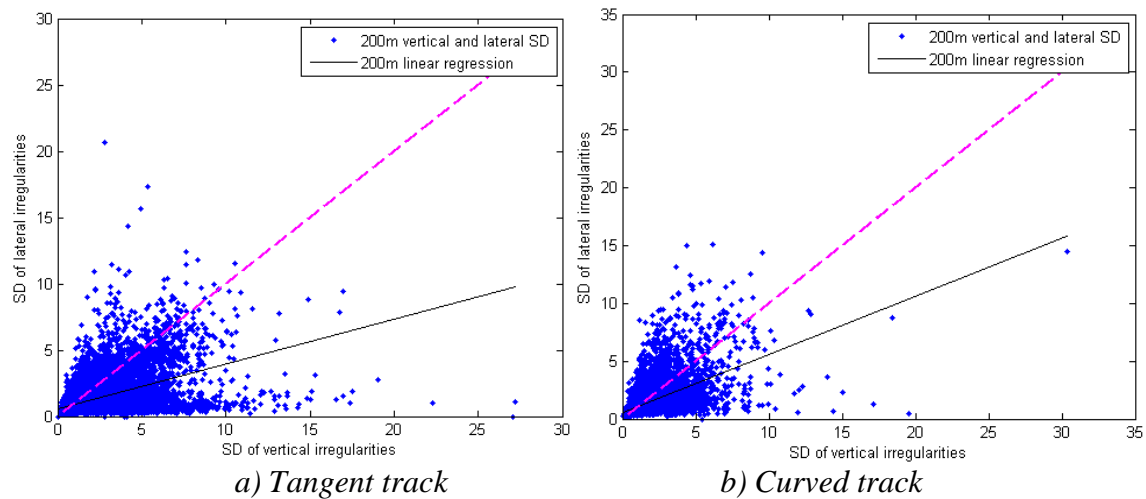


Figure 3-1 Vertical and lateral irregularities SD results of combined track data

The linear regression line in Figure 3-1 shows a slope smaller than 1, which indicates that the vertical irregularities are generally larger than the lateral irregularities. The percentages of lateral irregularity SD larger than the vertical SD are listed in Table 3-3.

Table 3-3 Percentage of sections for which the lateral irregularities are larger than the vertical ones [%]

	Types Networks	Freight lines	Regional lines	Upgraded lines	High speed lines	Total track
Tangent track	Network A	14.63	14.58	16.13	55.98	22.52
	Network B	-	23.02	38.77	30.50	
	Network C	23.61	11.06	0.98	-	
Curved track	Network A	29.59	22.75	41.55	48.69	33.15
	Network B	-	31.46	87.58	45.89	
	Network C	52.35	43.2	2.53	-	

In order to understand more about the relationship between lateral and vertical irregularities, the ratio between each section lateral SD and vertical irregularity SD is calculated using the overall combined track data, and the distributions of these ratios and a very good generalized extreme value curve fit are shown in Figure 3-2. The mean values of the lateral to vertical irregularity SD ratios are 0.78 for tangent track and 0.93 for curved track. From Table 3-3 and Figure 3-2, it can be concluded that track quality in the lateral direction is generally better than in the vertical direction. On straight track less than 23% of lateral SDs are bigger than the vertical SDs, but on curved track this proportion increases to around 33%. From the probability plot and the generalized extreme value curve fit, it becomes clear that a non-negligible number of sections have a lateral quality significantly worse than the vertical with a twofold increase for 3% and 5% of all cases for the tangent and curved track respectively.

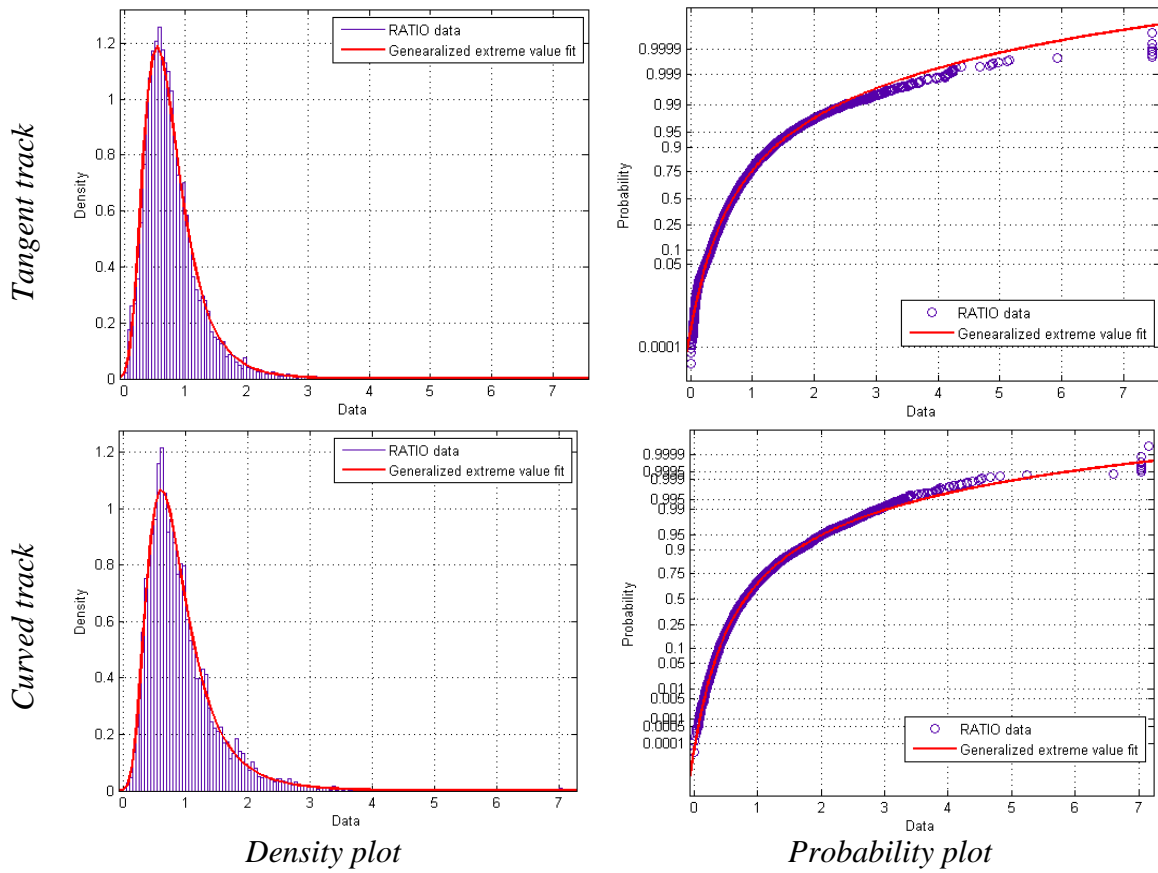


Figure 3-2 Statistical results of lateral to vertical irregularity ratios

3.1.2 Spatial domain analysis

3.1.2.1 Magnitude squared coherence

The formation and development of track irregularities is the result of a number of random factors. The data recorded by a TRC usually covers a long distance of a route and contains various frequency ranges. A Power Spectral Density (PSD) method is good at gaining an understanding of data in the spatial domain. A PSD analysis treats the track alignment data as a random signal and measures the typical power per unit of frequency in order to understand the characteristic of the irregularities distributed on the track. Typical wavelengths will be chosen for further statistical analysis.

Magnitude Squared Coherence (MSC) is the cross coherence of PSD results, which shows the level of coherence between two sets of data in the spatial domain with the unit of 1/m. The Welch method is the most commonly used algorithm in track irregularity analysis. In the calculation process, the length of the segment analysed should be more than twice the maximum wavelength in order to avoid negligence in the calculation [99]. The maximum wavelength of the collected data is 35m and the track data is taken every 0.25 meter, so it is sensible to take between 512 and 4096 points to calculate the PSD. The calculation segment should be between 0.128 and 1.024km, which is roughly 3.6 to 29.2 times longer than the longest wavelength. An MSC results in values from 0 to 1. The data is completely correlated if the MSC value is 1, while there is no coherence between the data sets if the MSC value is 0. Table 3-4 shows the MSC results for the track data sets used in previous PSD analysis. The detailed results of the MSC analysis between lateral and vertical track irregularities are shown in Appendix A.2.

Table 3-4 MSC results of the track lateral and vertical irregularities

Types Networks	Freight lines		Regional lines		Upgraded lines		High speed lines	
	Frequency (Hz)	Magnitude	Frequency (Hz)	Magnitude	Frequency (Hz)	Magnitude	Frequency (Hz)	Magnitude
Network A	0.188	0.0712	0.0313	0.0191	0.250	0.0168	0.254	0.00721
Network B	-	-	0.328	0.0218	0.258	0.00484	0.152	0.00893
Network C	0.231	0.0250	0.277	0.0235	0.270	0.152	-	-

The results show that the maximum magnitudes of the MSC are all less than 0.2, which indicates weak correlation between vertical and lateral irregularities at different wavelengths. The peak MSC occurs at different frequencies, and shows no clear regularity of correlations in major vertical and lateral irregularity wavelength.

3.1.2.2 Line divider fractal analysis

Fractal analysis is used to deal with objects that seem highly chaotic and random, and is widely used in many area of science [100] such as: complex 1 dimensional lines, 2 dimensional shapes and 3 dimensional objects. Nowadays, the applications of fractal analysis cover a wide range, such as landscape or coastline complexity [101], heart rate analysis [102], diagnostic imaging [103], solid studies [104], etc. Railway track irregularities contain random characteristics, therefore, fractal analysis can be used to characterise track geometry data and provide unique numerical values that can quantify geometry signatures [105]. A variety of algorithms are available to calculate the fractal dimension, counting the line divider, box counting, variogram and triangular prism method [106]. The divider method, which is also called the yardstick method, is used to analyse the track irregularities. The length of the rough line measured by each ruler length, λ , can be calculated by simply multiplying the number of ruler lengths, n , as shown in Equation 32.

$$L(\lambda) = n\lambda \quad \text{Equation 32}$$

An example of the deviation of a rough line for the computer simulation is shown in Figure 3-3. The closer the ruler length is to the smallest detail of the rough line, the more accurate the measured length is.

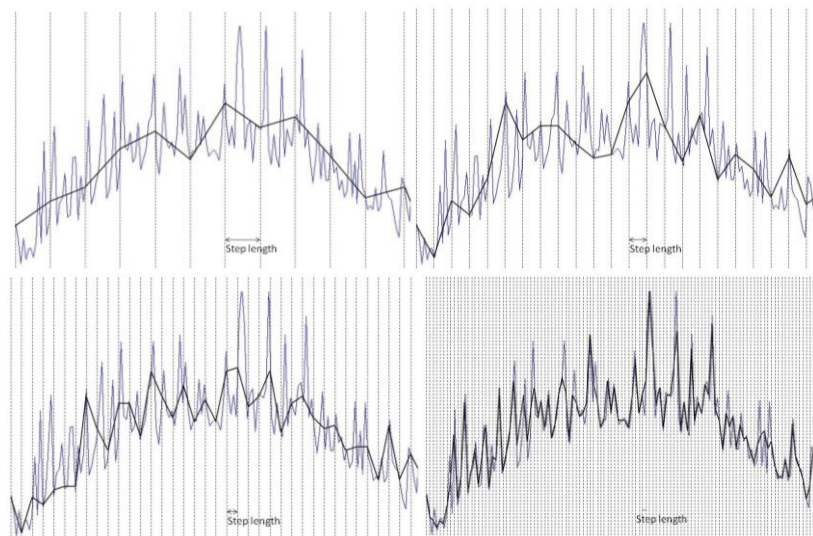


Figure 3-3 Example of rough line deviation pattern

An empirical equation expresses the constant increase in measured length as the ruler length decreases using Equation 33.

$$L(\lambda) = n\lambda^{1-D_r} \quad \text{Equation 33}$$

Where,

λ ...length of unit measurement

$L(\lambda)$...length of the rough line by unit measurement length λ

n ... number of steps of length λ

D_r ...fractal dimension of the rough line

Taking the logarithm of both sides of Equation 34 gives

$$\log L(\lambda) = (1 - D_r)\log \lambda + \log n \quad \text{Equation 34}$$

This gives a linear relationship between λ and $\log L(\lambda)$ on a log-log scale, and the slope of the linear line is $1 - D_r$.

Figure 3-4 shows the comparison between the general fractal dimension values and the traditional SD values for different track sections of Network A. The relationship between SD and the fractal dimension values are different because the SD relies on magnitude whereas fractal dimension value is pattern based.

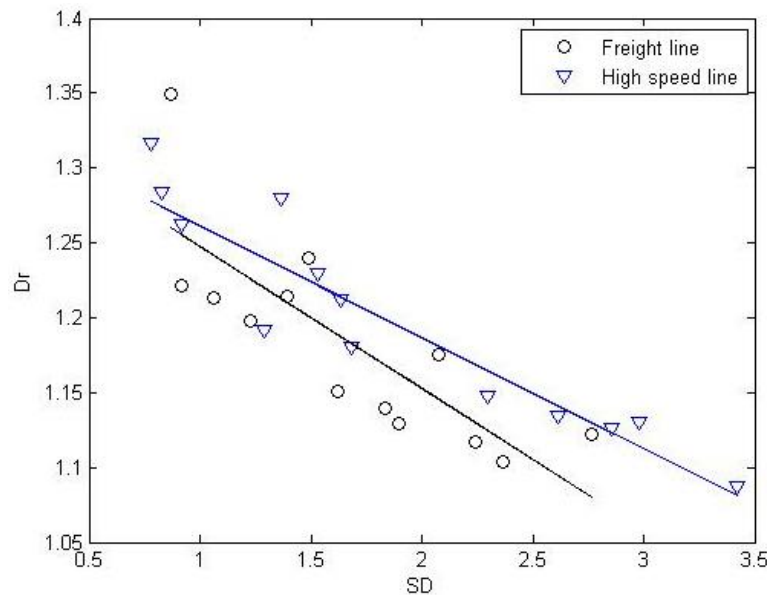


Figure 3-4 Relationship between fractal dimension and standard deviation

Figure 3-5 shows the SD and fractal dimension values for different types of signal input, which have different frequency or magnitude. The 1st and 2nd signals have the same frequency but different magnitude, while the 1st and 3rd signals have the same magnitude but different frequency. On one hand, it can be found that the SD values are almost the same when the signals have different frequencies as long as the magnitudes are the same. On the other hand, the fractal dimensions are the same for the same frequency signal inputs despite the signal magnitude. This may be due to the SD value depending mainly on the distribution of the signal while the fractal dimension is pattern based.

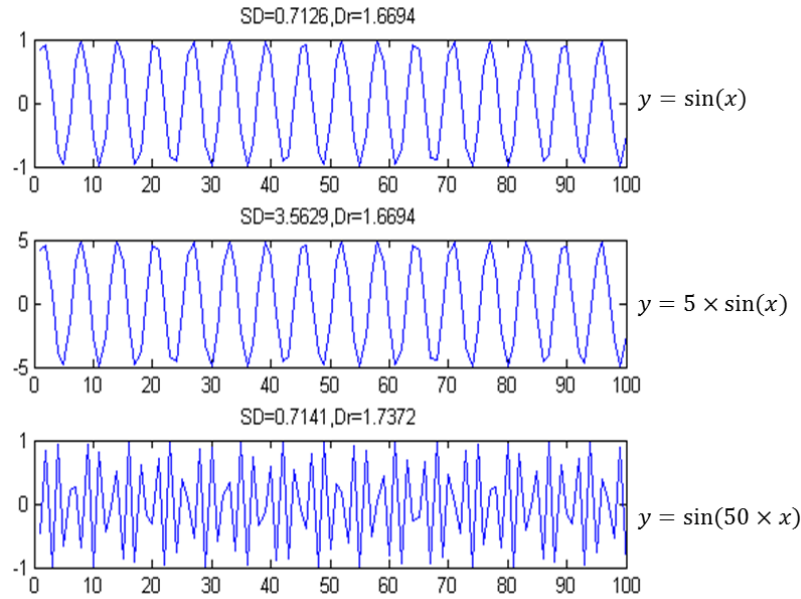


Figure 3-5 SD and Dr values for different signal inputs

Therefore, SD is a good tool to evaluate the growth of the irregularity in size while the fractal dimension is good to analyse the change in irregularity wavelengths. The selection of the band pass frequency value of the irregularity data has a strong influence on the fractal dimension value of the track. It is important to use the same band pass processing in all the original track data sets for a fractal analysis.

The fractal dimensions of each 1km vertical and lateral irregularities were calculated for all DynoTrain track datasets. All of the calculation results and figures are shown in Appendix A.4. The correlation coefficient between both vertical and lateral fractal dimensions are shown in Table 3-5. It was found that the track vertical and lateral irregularities have an obvious correlation between each other in the spatial domain with correlation coefficient around 0.4.

Table 3-5 Correlation coefficient of vertical and lateral irregularity fractal dimensions

Types Networks	Freight lines	Regional lines	Upgraded lines	High speed lines
Network A	0.4323	0.3218	0.3984	0.3613
Network B	-	0.3854	0.4356	0.3824
Network C	0.1495	0.1678	0.4098	-

3.1.3 Conclusion

Comparing both the distance domain and spatial domain results, it is noted that the vertical and lateral irregularity magnitudes are clearly correlated with correlation coefficient mostly bigger than 0.4. However, peak MSC occurs at different frequencies, and shows no clear regularity of the correlations of the vertical and lateral major irregularity wavelength. In conclusion, the relationship between vertical and lateral irregularities is obvious in both the distance domain and spatial domain. The track quality in the vertical direction is generally worse than in the lateral direction, however some track sections with a lateral quality significantly worse than the vertical are non-negligible.

3.2 The relationship between track lateral irregularities and curvature

A moving vehicle causes forces between the wheel and rail at the contact patch, which can stress the rail laterally. The lateral force acting on the rails varies with different track curvature, cant and speed. The lateral forces on the high rail of curved track whose radius of curvature is small are much bigger than those on a large curve radius on account of the lateral forces [107]. Track lateral irregularities are created by the forces acting on the track. Therefore, it is necessary to understand the relationship between track lateral irregularities and curvature. To gain a general understanding of the lateral and vertical track forces, the vertical and lateral forces resulting from a vehicle running through a section of track with both tangent and curved elements are shown in Figure 3-6. It is shown that the lateral forces on the curves are much bigger than on the tangent elements, and the static vertical force is much larger than the dynamic vertical forces.

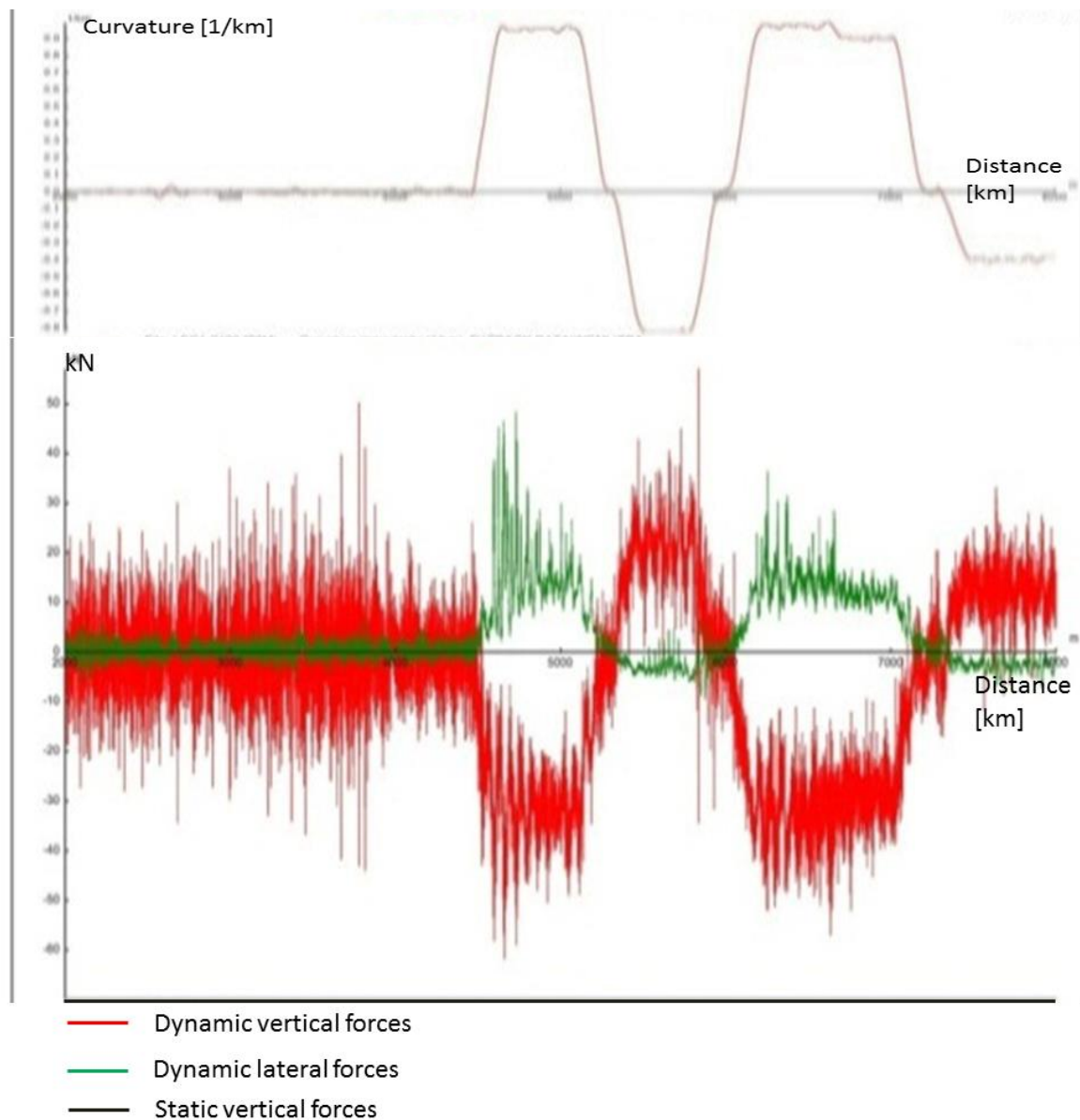


Figure 3-6 Dynamic wheel-rail forces at the leading left wheel

A MATLAB program written for the EU project DynoTrain is used to select different track elements, such as tangent track, curved track, switch and crossings, and transitions. For each network, the curved track sections are selected and divided into six ranges of curve radius shown in Table 3-6 and the tangent track elements are also selected. The value of these curve ranges of all data from four networks and different types of lines are box plotted in Figure 3-7. The box plotting results for each type of line on each network are also shown in Appendix A.3. The width of the box is defined by Interquartile Range (IQR), that is, $IQR = Q3 - Q1$, where $Q1$ and $Q3$ are the lower quartile and upper quartile. The box contains 50% of the total values. The red line in the box is the median value of the data, or 50th percentile, or $Q2$. An outlier is any value that lays more than 1.5 times the length of the box from either end of the box. The red points represent the whisker outliers in the data sample, which are defined if they are larger than the greatest value: $Q3 + 1.5IQR$ or smaller than least value: $Q1 - 1.5IQR$.

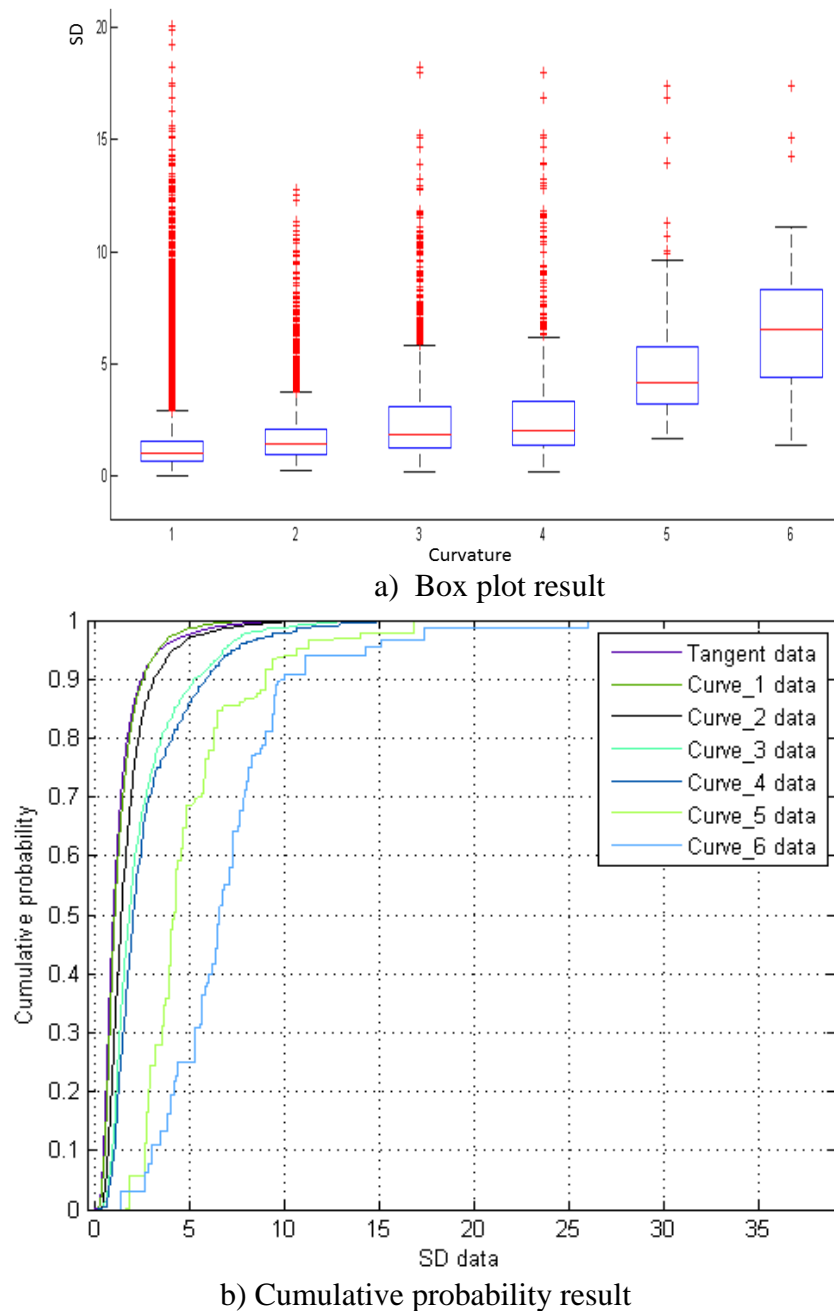


Figure 3-7 SD value against different curve radius ranges

The figures show that there is a clear trend towards a worsening lateral track quality as the curves get sharper. This result can be quite representative because it contains a comprehensive amount of track data, equivalent to 4545.3km of track, including freight, original, upgraded and high speed lines. A clear trend can be found that the track quality deteriorates as curve radius reduces. The median values of SD for all of the curvature ranges are shown in Table 3-6.

Table 3-6 Median SD value in different curvature range

	1	2	3	4	5	6	7
Curve radius range [1/km]	0-0.2	0.2-0.5751	0.5751-1.1501	1.1501-1.7253	1.7253-2.3004	2.3004-2.8752	2.8752-3.4506
Curve radius range [m]	Straight line	5000-1739	870-1739	580-870	435-580	348-435	290-348
Median SD σ [mm]	0.9974	1.0760	1.4192	1.8590	2.0566	4.1725	6.5404
$\Delta\sigma$ [mm]	0	0.0786	0.4218	0.8616	1.0592	3.1751	5.543

By plotting the $\Delta\sigma$ values, which are the differences between the median SD values, an exponential growth characteristic can be found, as shown in Figure 3-8.

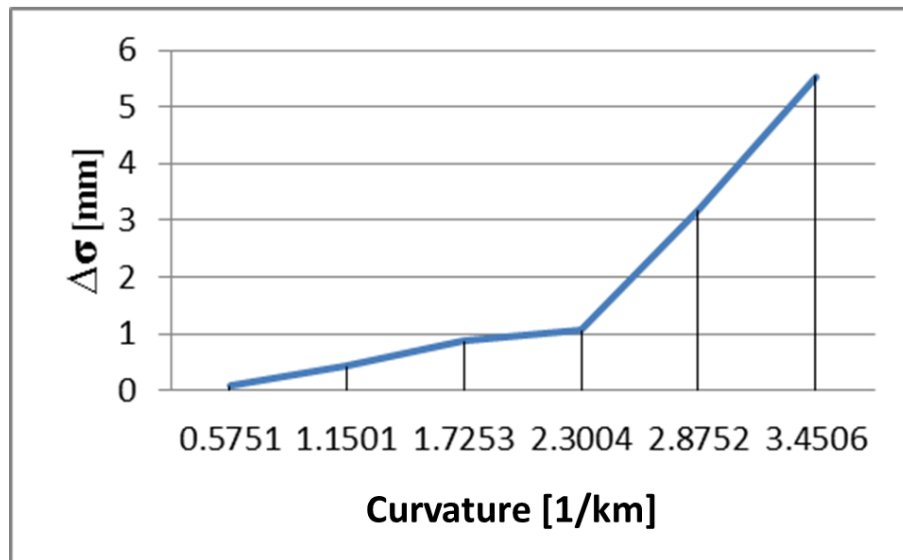


Figure 3-8 Median SD growth plotting against different curvature ranges

Two different types of curve fitting were applied to the median lateral irregularity SD value against the curve radius range. The $a \cdot e^{b \cdot r}$ exponential curve gives a better fit to the data than the $a \cdot e^{b \cdot r} + c \cdot e^{d \cdot r}$ equation, while an $a \cdot r^b + c$ power curve gives a better fit than $a \cdot r^b$. So the $a \cdot e^{b \cdot r}$ exponential equation and the $a \cdot r^b + c$ power curve equation results are shown in Table 3-7. The best curve fitting result using data set 2 with a power curve fitting equation is shown in Figure 3-9. A Sum of Squared Errors of prediction (SSE), R^2 , adjusted R^2 and a Root Mean Squared Errors (RMSE) are all measures of the discrepancy between the data and the estimation model. A small SSE and RMSE value indicates a close correlation between the curve fitting equation and the data, while the closer R^2 and adjusted R^2 are to 1 the better the curve fits the data. Data set 1 and 2 represents the whole set of data, and data without the curve range number 4.

Table 3-7 Curve fitting results

	Exponential		Power	
	$Median\ SD = a \cdot e^{b \cdot r}$		$Median\ SD = a \cdot r^b + c$	
	Data set 1	Data set 2	Data set 1	Data set 2
	a=0.09719 b=1.176	a=0.1414 b=1.066	a=0.05761 b=3.662 c=0.2101	a=0.1269 b=3.023 c=0.1494
SSE	0.2923	0.06317	0.2655	0.02293
R^2	0.9868	0.9971	0.988	0.9989
Adjust R^2	0.9835	0.9962	0.98	0.9979
RMSE	0.2703	0.143	0.2975	0.1071

Although data set 2 gives a more accurate curve fitting result as shown in Figure 3-9, there is no strong evidence that indicates curve range number 4 is a bad sample. Meanwhile, the shaper the curvature is, the less data points will be in the curve range. Therefore, it would be sensible to collect more data that sufficient in all curve ranges to provide a more accurate curve fitting result.

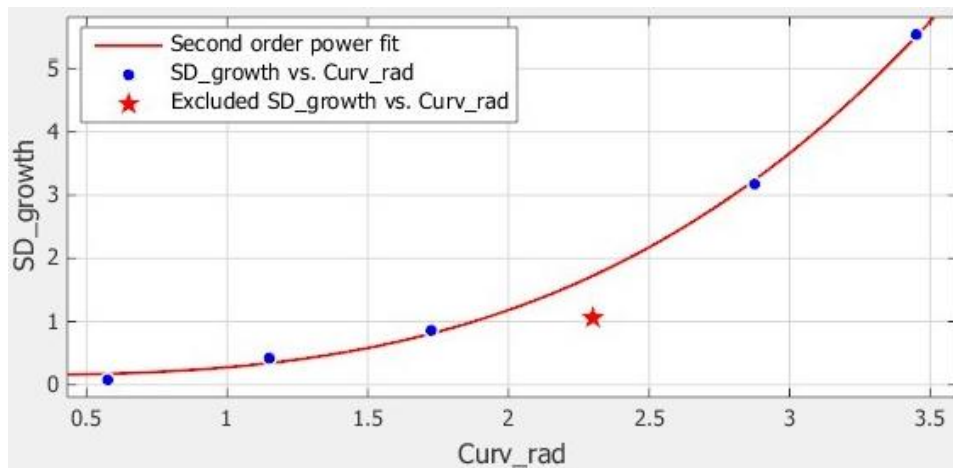
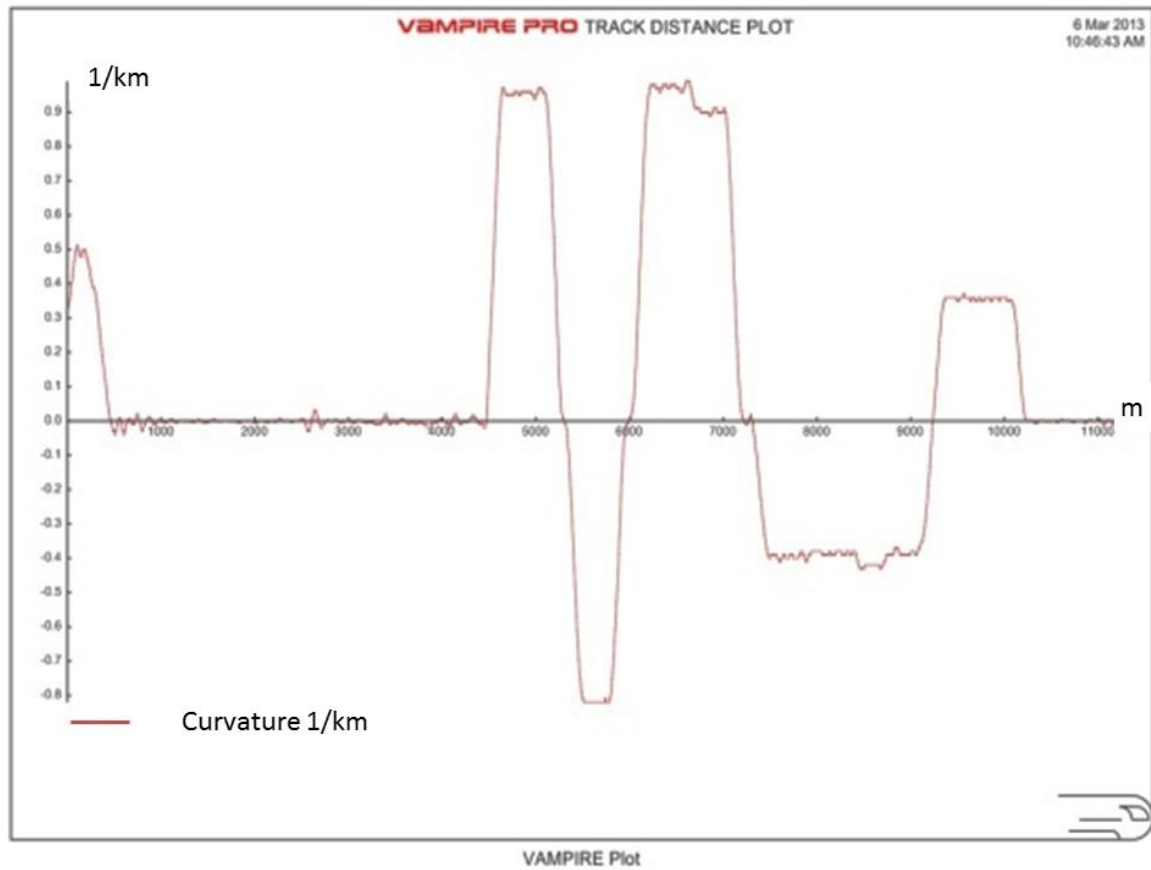


Figure 3-9 Best curve fitting result

In conclusion, the lateral forces are directed in both directions on tangent track which counteract each other, while there is always a large static vertical force due to the vehicle weight. This explains why the deterioration of railway track in the vertical direction is greater than in the lateral direction. On curves, railway track tends to deteriorate faster due to the larger lateral forces as a result of vehicle running with cant deficiency or cant excess. The track irregularity SD generally tends to show an exponential growth with decreasing curve radius when considering all track types. This power exponential characteristic may vary when considering a particular type of railway line, such as freight lines, regional lines and high speed lines.

3.3 Track lateral deterioration over time

The track data used in this section was recorded by Network Rail over a time interval of 1 to 3 months between Wolverton and Rugby on the West Coast Main Line which has a line speed of 125mph. The total length of this data set is 7 miles, and contains 6 elements of curved track and 2 elements of tangent track. All of the curves are numbered and their radius shown beneath Figure 3-10.



$Rc_1=2$ km, $Rc_2=1.05$ km, $Rc_3=1.21$ km, $Rc_4=1.08$ km, $Rc_5=-2.56$ km, $Rc_6=2.78$ km

Figure 3-10 Curve profile

The dates that the track data was recorded is shown in Table 3-8.

Table 3-8 Track recording dates and dataset numbers

Date set	Date	Period between two measurement dates (Day)
D1	14/04/2010	
D2	09/06/2010	56
D3	14/07/2010	35
D4	11/08/2010	28
D5	13/10/2010	63
D6	08/12/2010	56
D7	19/01/2011	42
D8	16/03/2011	56
D9	18/05/2011	63
D10	15/06/2011	28
D11	20/07/2011	35
D12	17/08/2011	28
D13	14/09/2011	28
D14	16/11/2011	63
D15	18/01/2012	63
D16	15/02/2012	28
D17	18/04/2012	63
D18	18/07/2012	91

Another set of track data taken from the ECML is also used in the analysis to give more comprehensive understanding of lateral track deterioration. It is worth noting that the ECML datasets are taken from parallel track lines at the same location.

Table 3-9 Track recording dates and dataset numbers

Description	Data set	Date	Period between two measurement dates (Day)
Down slow line	D19	2010/01/25	210
	D20	2010/08/23	
Up slow line	D21	2009/08/24	154
	D22	2010/01/25	
Up fast line	D23	2008/07/28	406
	D24	2009/09/07	
Down fast line	D25	2009/08/10	182
	D26	2010/02/08	

3.3.1 SD values change over time

During the WCML measurement intervals, maintenance activities were carried out on the track. It is worth mentioning that different types of maintenance activities took place on the track. Any maintenance that may have influenced the lateral track irregularities, such as tamping, stone blowing and track renewal, have been selected, and shown in Figure 3-11. The data was supplied by Network Rail from their track maintenance records.

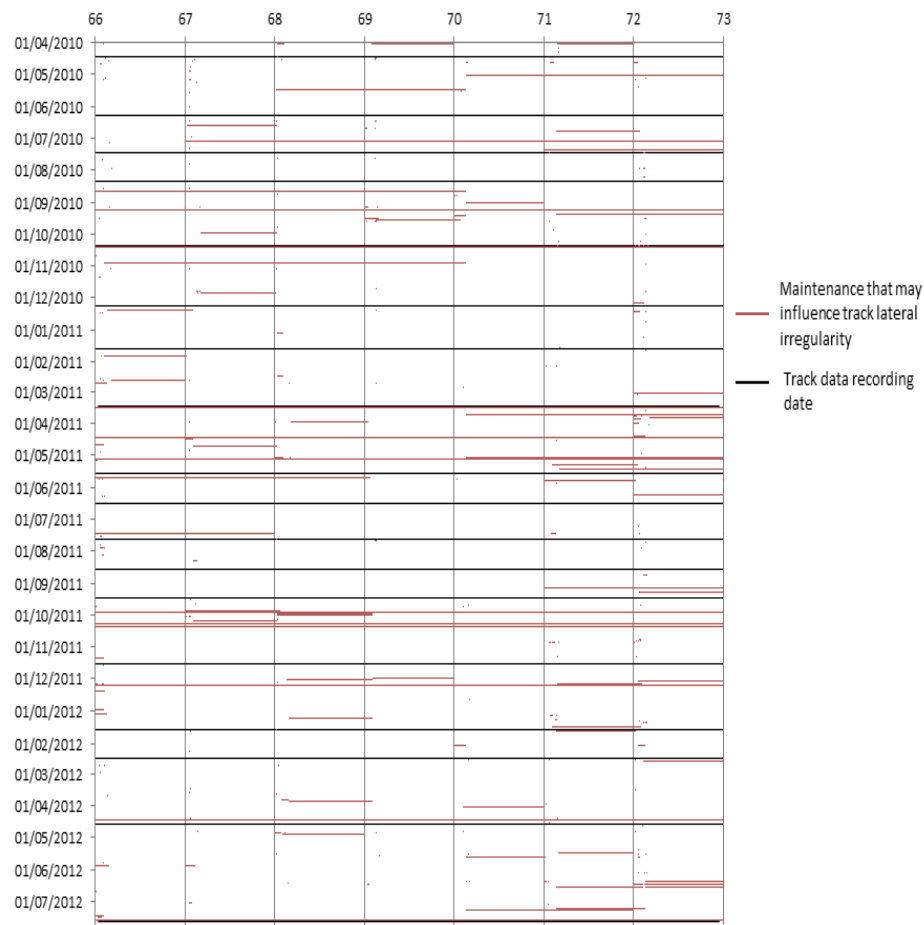


Figure 3-11 Maintenance dates and information

Due to the fact that the lateral forces between the vehicle and track occur in both directions, it is difficult for the track to develop a constantly increasing track lateral deterioration. In addition, the influence of maintenance on the track cannot be ignored. Consequently, it is hard to find track sections with growing irregularities. The length of track for the SD value calculation also has a strong influence on the results. SD values of 30m, 50m, 60m, 90m, 100m and 200m long track sections are used to discover track sections with increasing lateral irregularities. The location of these sections is shown in Figure 3-12. It can be found that different measurement lengths lead to quite different locations of the track sections. In order to get more accurate results, it is sensible to select the overlapped locations of track sections for the following study.

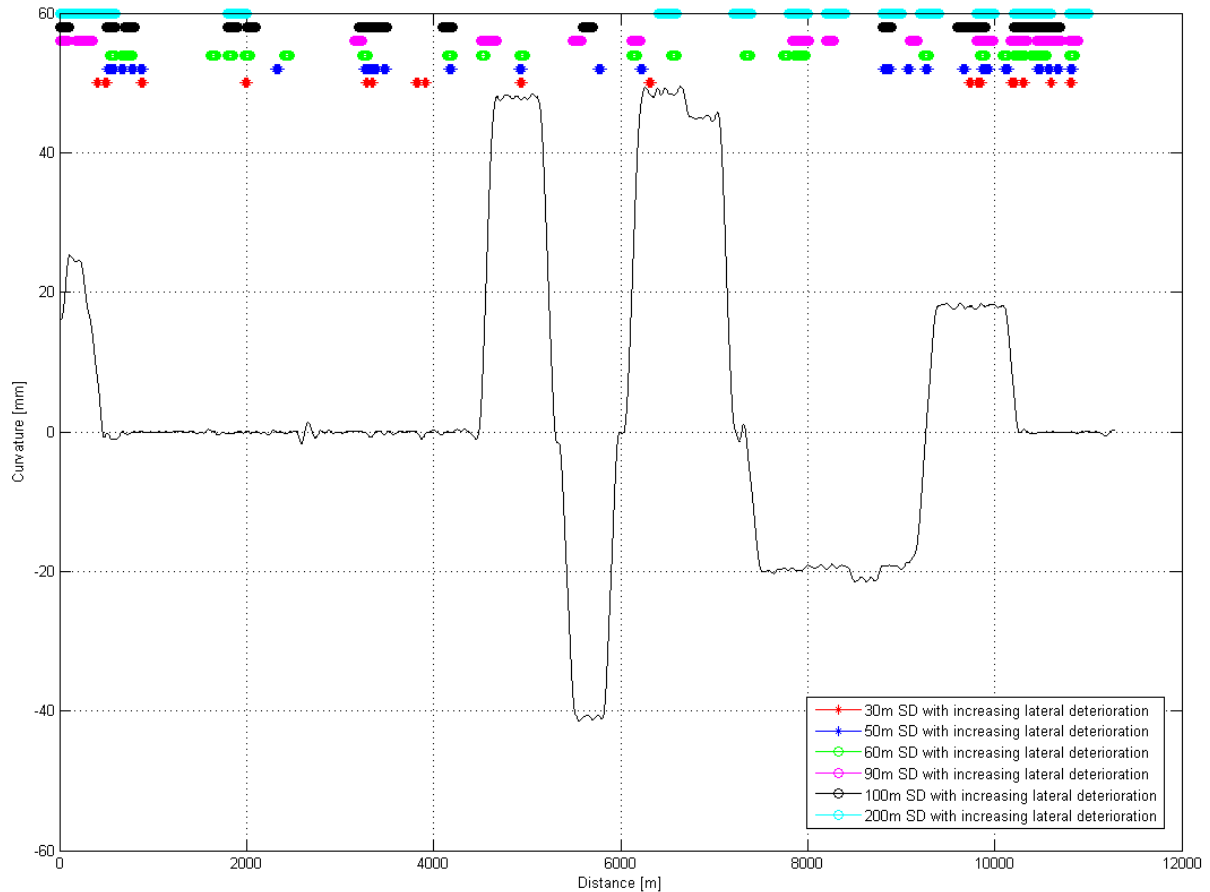


Figure 3-12 Locations of track sections with reasonable lateral deterioration

Taking the track model into consideration, the length for the calculation of SD values is chosen to be 60m for the convenience of calculation due to the 0.6m sleeper spacing used in the track model. Consequently, 18 track sections are selected with at least 6 sets of recorded track data showing an increasing SD.

Table 3-10 Selected track sections

Track sections	Location of selected sections [m]	Lateral irregularity increasing data sets	Curvature of selected section [mm]
S1	540 -600	D2-D8	0
S2	660-720	D9-D14	0
S3	720-780	D9-D14	0
S4	1800-1860	D8-D13	0
S5	1980-2040	D10-D15	0
S6	2400-2460	D7-D13	0

S7	3240-3300	D6-D12	0
S8	4140-5200	D6-D12	0
S9	7320-7380	D8-D13	Transition c_4 to c_5
S10	7860-7920	D8-D14	c_5
S11	7920-7980	D8-D13	c_5
S12	9840-9900	D3-D13	c_6
S13	10200-10260	D8-D13	Transition c_6 to t_2
S14	10260-10320	D8-D13	Transition c_6 to t_2
S15	10380-10440	D8-D14	0
S16	10440-10500	D8-D13	0
S17	10500-10560	D8-D14	0
S18	10800-10860	D8-D13	0

Among the maintenance activities, tamping and stone blowing have the largest influence on lateral geometry correction. Therefore, they are selected to be considered in the research. The dates that these two maintenance activities were undertaken and the track sections with increasing lateral deterioration are shown in Figure 3-13. It can be found that most of the selected track sections are not influenced by tamping or stone blowing. The sections that were influenced by maintenance activities are not considered in the following research.

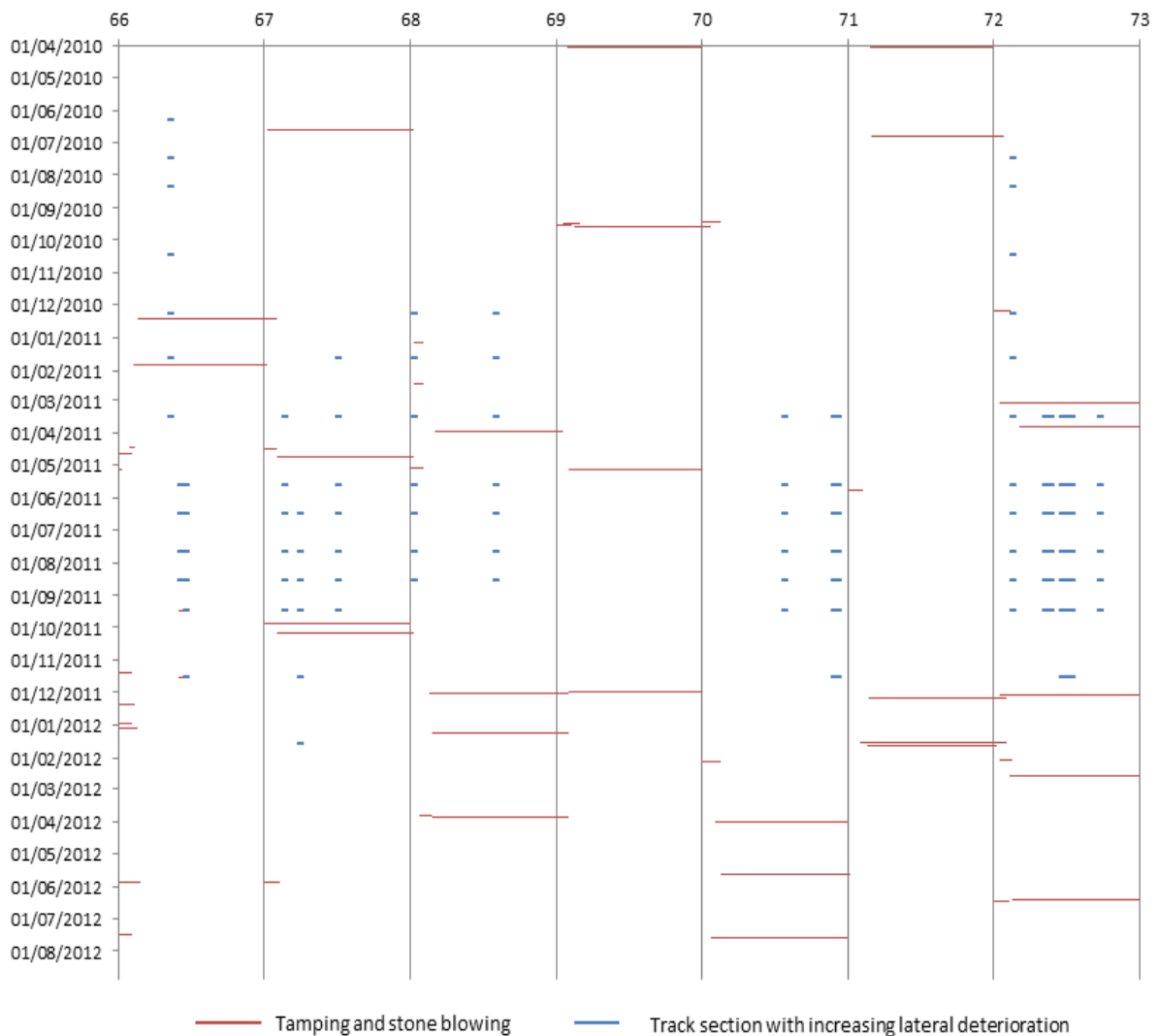


Figure 3-13 Tamping and stone blowing maintenance activities

The final selected datasets for the lateral deterioration analysis are shown in Table 3-11.

Table 3-11 Selected lateral deterioration data sets

60m SD	S1	S2	S3	S4	S5	S6	S7	S8	S9
	66.336	66.41	66.448	67.119	67.23	67.491	68.013	68.573	70.549
14/04/2010									
09/06/2010	0.8196								
14/07/2010	1.0145								
11/08/2010	1.1661								
13/10/2010	1.2874								
08/12/2010	1.5481								
19/01/2011									
16/03/2011									1.3357
18/05/2011		0.5036	0.8921	0.2721		0.296	0.7742	1.2145	1.3968
15/06/2011		0.5149	0.9457	0.3267	0.3899	0.3067	0.8252	1.2657	1.5348
20/07/2011		0.562	1.0645	0.3479	0.4267	0.3338	0.8665	1.2812	1.5924
17/08/2011		0.8396	1.1292	0.3611	0.4347	0.3376	0.8823	1.4363	2.0135
14/09/2011		0.987	1.3707	0.4156	0.5232	0.343			2.4245
16/11/2011		1.265	1.5636						
18/01/2012									
15/02/2012									
18/04/2012									
18/07/2012									
	S10	S11	S12	S13	S14	S15	S16	S17	S18
	70.884	70.921	72.114	72.338	72.375	72.45	72.487	72.525	72.711
14/04/2010									
09/06/2010									
14/07/2010									
11/08/2010									
13/10/2010									
08/12/2010									
19/01/2011									
16/03/2011	1.2907	0.4005	0.7819	0.4605	0.4108	0.2446	0.3245	0.3656	0.3196
18/05/2011	1.4154	0.4197	0.8983	0.5361	0.4211	0.2983	0.3452	0.4213	0.421
15/06/2011	1.516	0.4406	0.9053	0.6105	0.4218	0.2991	0.3693	0.4702	0.5307
20/07/2011	1.7194	0.4514	0.9325	0.8278	0.5808	0.4274	0.4703	0.4754	0.5489
17/08/2011	2.9094	0.5302	1.2207	1.0183	0.8846	0.7259	0.5566	0.5728	0.7704
14/09/2011	3.4214	1.2578	1.3932	1.4992	1.0832	0.8659	0.6143	0.7387	0.921
16/11/2011	3.4298					0.9337		1.1549	
18/01/2012									
15/02/2012									
18/04/2012									
18/07/2012									

The average daily growth of the SD value for each section is then found and shown in Figure 3-14. It can be found that the track lateral deterioration generally increases faster on curves and transitions.

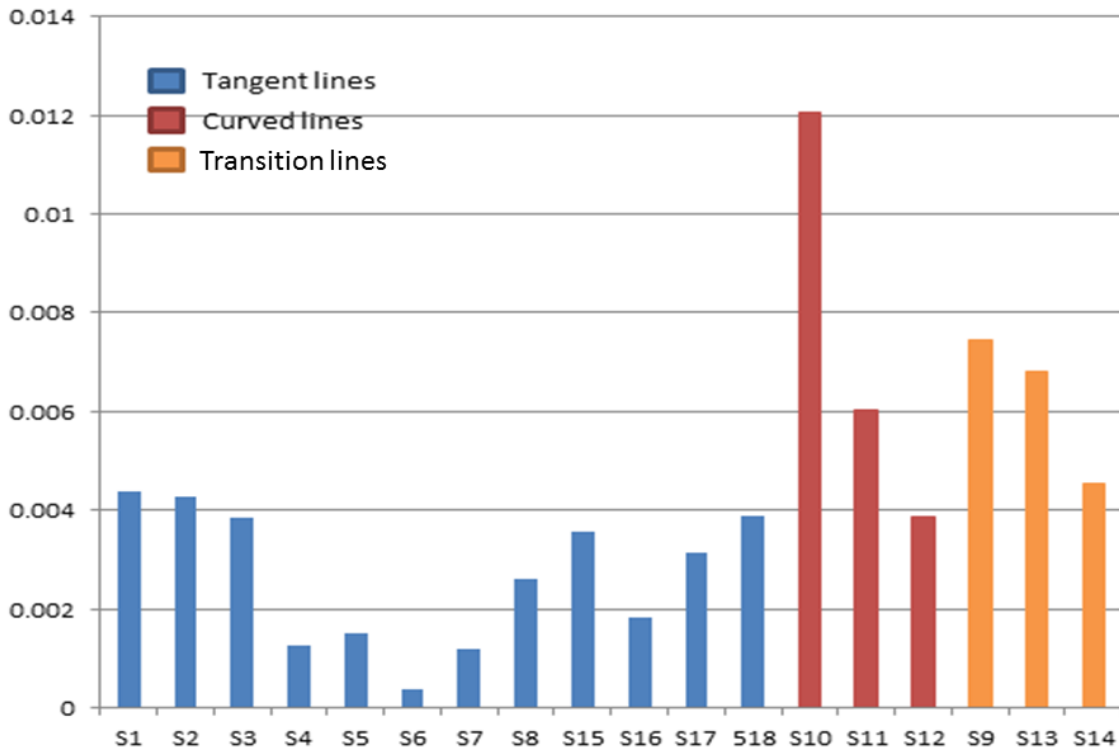


Figure 3-14 Average daily growth of selected track sections SD value

It is difficult to determine the original date of tamping or stone blowing, so the growth of lateral irregularities shown in Table 3-11 may be any part of the deterioration line shown in Figure 3-15.

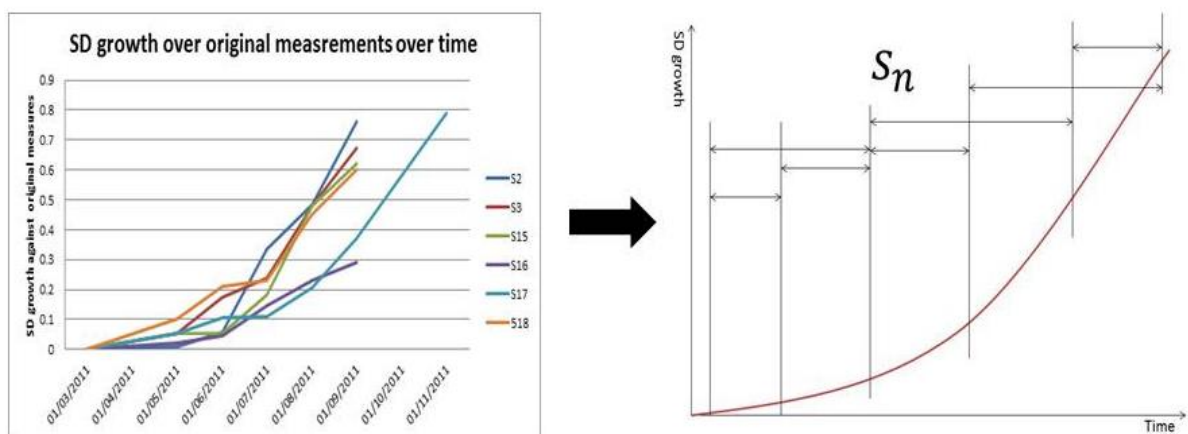


Figure 3-15 SD growth over time

All data sets can be shifted in time in order to describe the track irregularity growth characteristics. According to the shape of all SD growth shapes, it can be deduced that the curve is likely to be nonlinear, which is likely to be either quadratic or exponential. Three different functions are used to estimate the track lateral deterioration and the results are compared.

3.3.1.1 Quadratic function

The estimation function is assumed to be

$$\Delta\sigma = a \cdot t^2 + b \cdot t \quad \text{Equation 35}$$

Where,

$\Delta\sigma$...SD growth [mm]

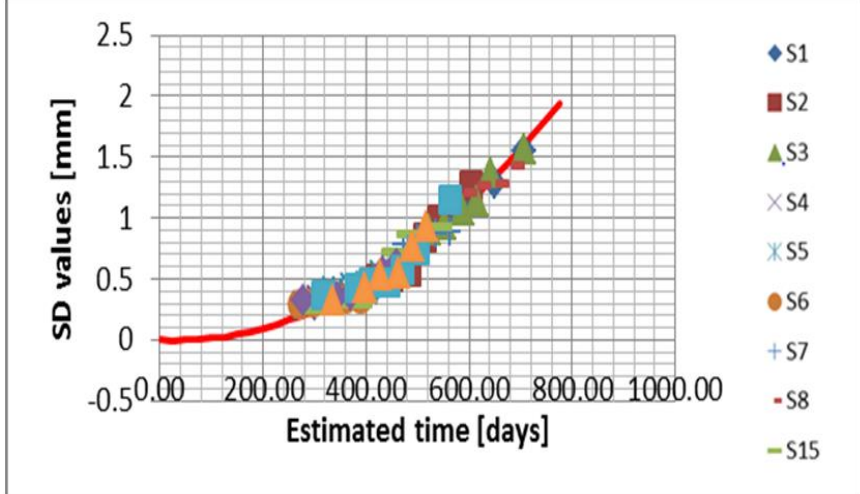
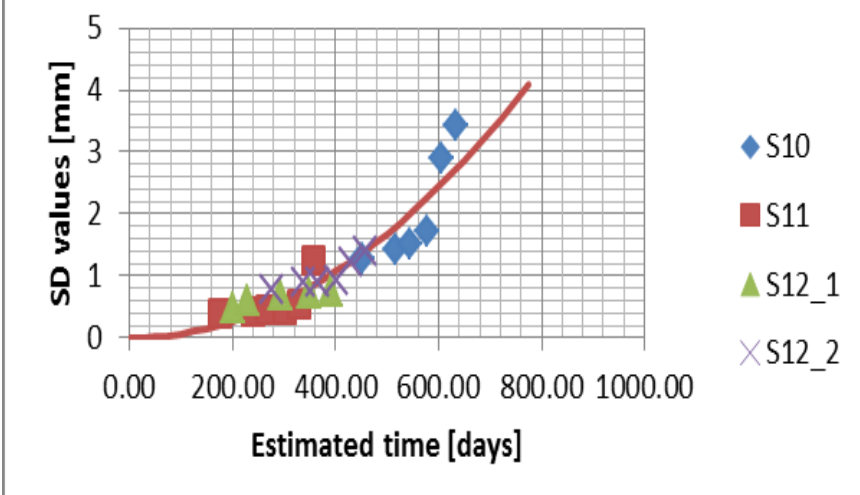
t...time [days]

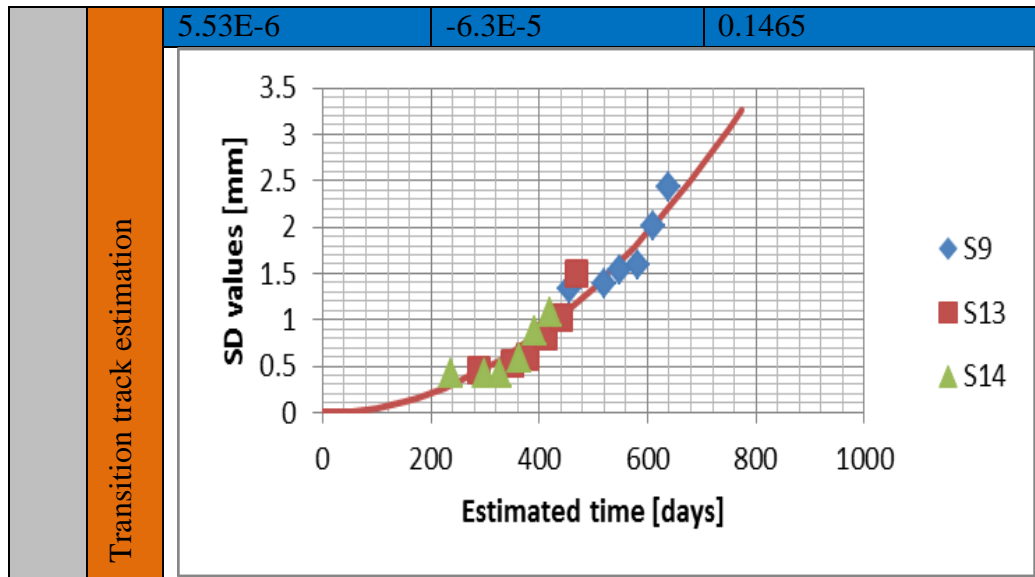
a,b...parameters

The estimated quadratic curve fitting results for tangent, curved and transition elements are shown in Table 3-12.

For track consisting mainly of straight track, parameter a is the smallest at roughly 2.91×10^{-6} which indicates a small slope and slower lateral deterioration, while for curved and transition track it is around 5 to 6×10^{-6} .

Table 3-12 Curve fitting parameters and evaluations for three types of track sections

		a	b	RMSE
$\Delta\sigma = a \cdot t^2 + b \cdot t + c$	Tangent track estimation	2.91E-6	9.05E-5	0.0801
				
	Curved track estimation	6.87E-6	-6.3E-5	0.2899
				



3.3.1.2 Power function

The estimation function is assumed to be

$$\Delta\sigma = a \cdot t^b + c \cdot t^d \quad \text{Equation 36}$$

Where,

$\Delta\sigma$...SD growth [mm]

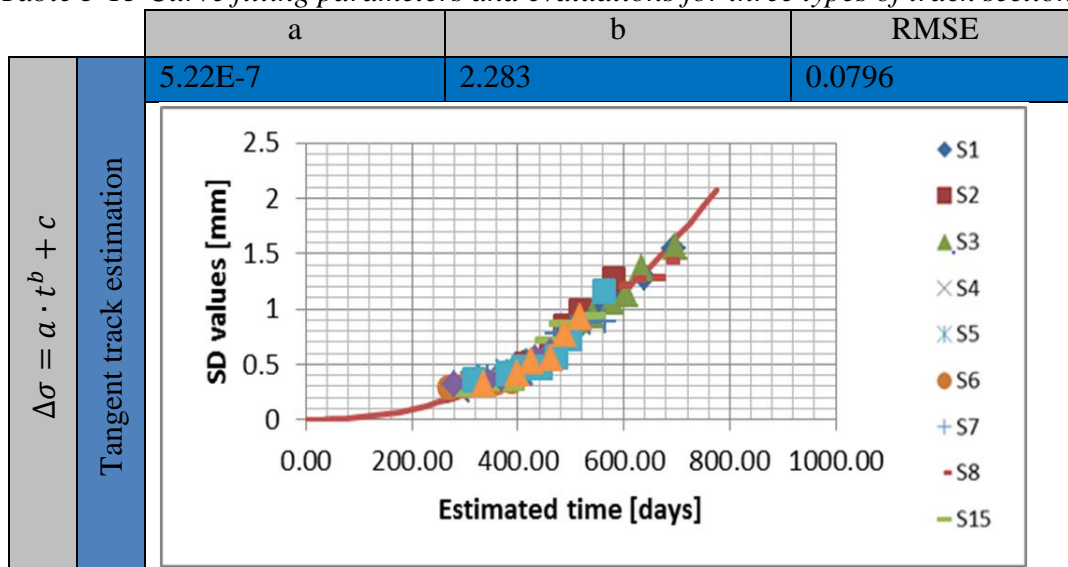
t...time [days]

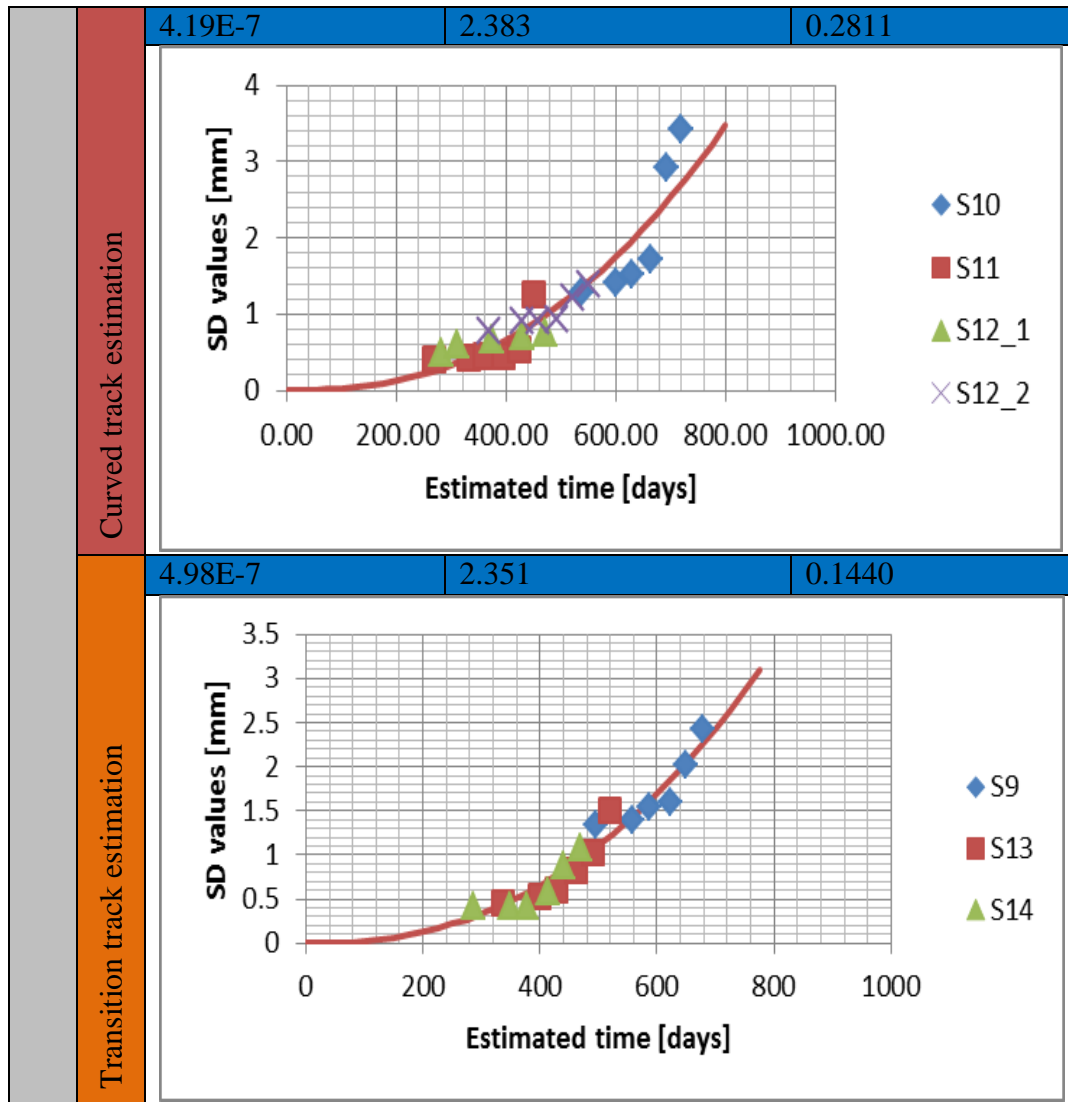
a,b,c,d...parameters

It is found that when there are two parts in the function the estimation results are not as accurate as when it is only $\Delta\sigma = a \cdot t^b$.

The estimated power function curve fitting results for tangent, curved and transition elements are shown in Table 3-12.

Table 3-13 Curve fitting parameters and evaluations for three types of track sections





3.3.1.3 Exponential function

The estimation function is assumed to be

$$\Delta\sigma = a \cdot e^{bt} + c \cdot e^{td} \quad \text{Equation 37}$$

Where,

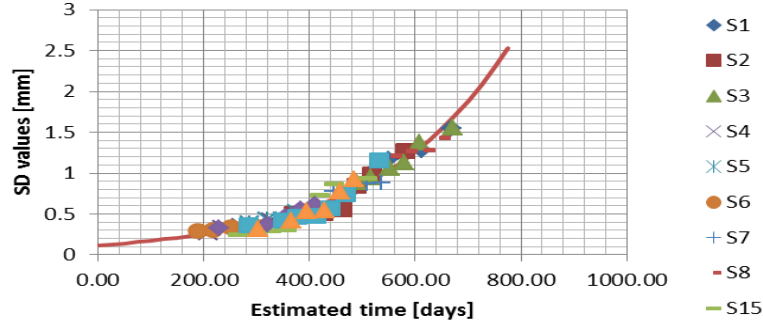
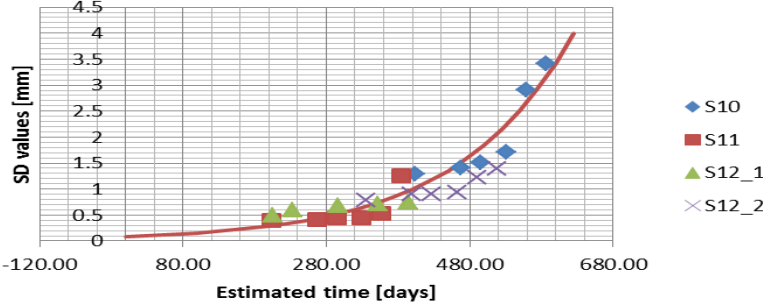
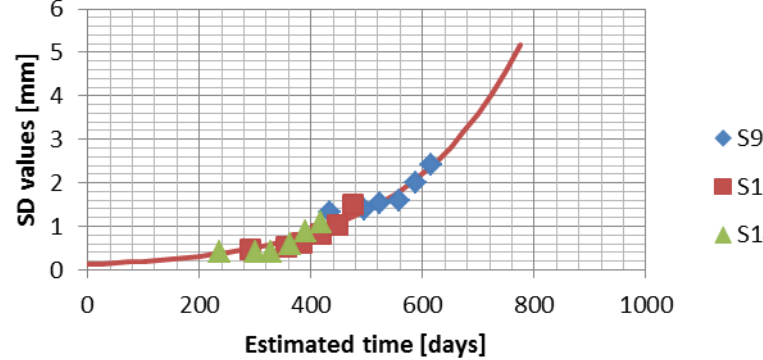
$\Delta\sigma$...SD growth [mm]

t...time [days]

a,b,c,d...parameters

It is found that when there are two parts in the function the estimation results are not as accurate as when it is only $\Delta\sigma = a \cdot e^{bt}$. The estimated exponential function curve fitting results for tangent, curved and transition elements are shown in Table 3-14.

Table 3-14 Curve fitting parameters and evaluations for three types of track sections

		a	b	RMSE
$\Delta\sigma = a \cdot t^b + c$	Tangent track estimation	0.1159	0.0040	0.0811
				
	Curved track estimation	0.084	0.00618	0.2811
				
	Transition track estimation	0.012	0.004857	0.1515
				

Between the quadratic, power and exponential functions, the power function provides the most accurate fit to lateral deterioration.

3.3.2 PSD values change over time

The PSD presents an understanding of the track in the spatial domain. It can be found in Chapter 3.3.1 that datasets D8 to D13 from the WCML are least influenced by maintenance activities. Therefore, D8 to D13 from the WCML and D19 to D26 from the ECML were used for the PSD analysis; this is to exclude measurements which have been influenced by maintenance. The analysis is undertaken in two parts, a long wavelength analysis and a short wavelength analysis.

3.3.2.1 Long wavelength analysis

In terms of long wavelength, a linear scale of the PSD on both the x and y axis gives a better representation of the data. Figure 3-16 shows the long wavelength PSD results for the D8 to D13 datasets from the WCML and D19 to D26 datasets for the ECML. It can be seen that the power density is more clearly shown when the wavelength is longer than 10m in spatial frequency 0.1 cycle/m; therefore, the long wavelength analysis is defined in the range between 10 to 35 m.

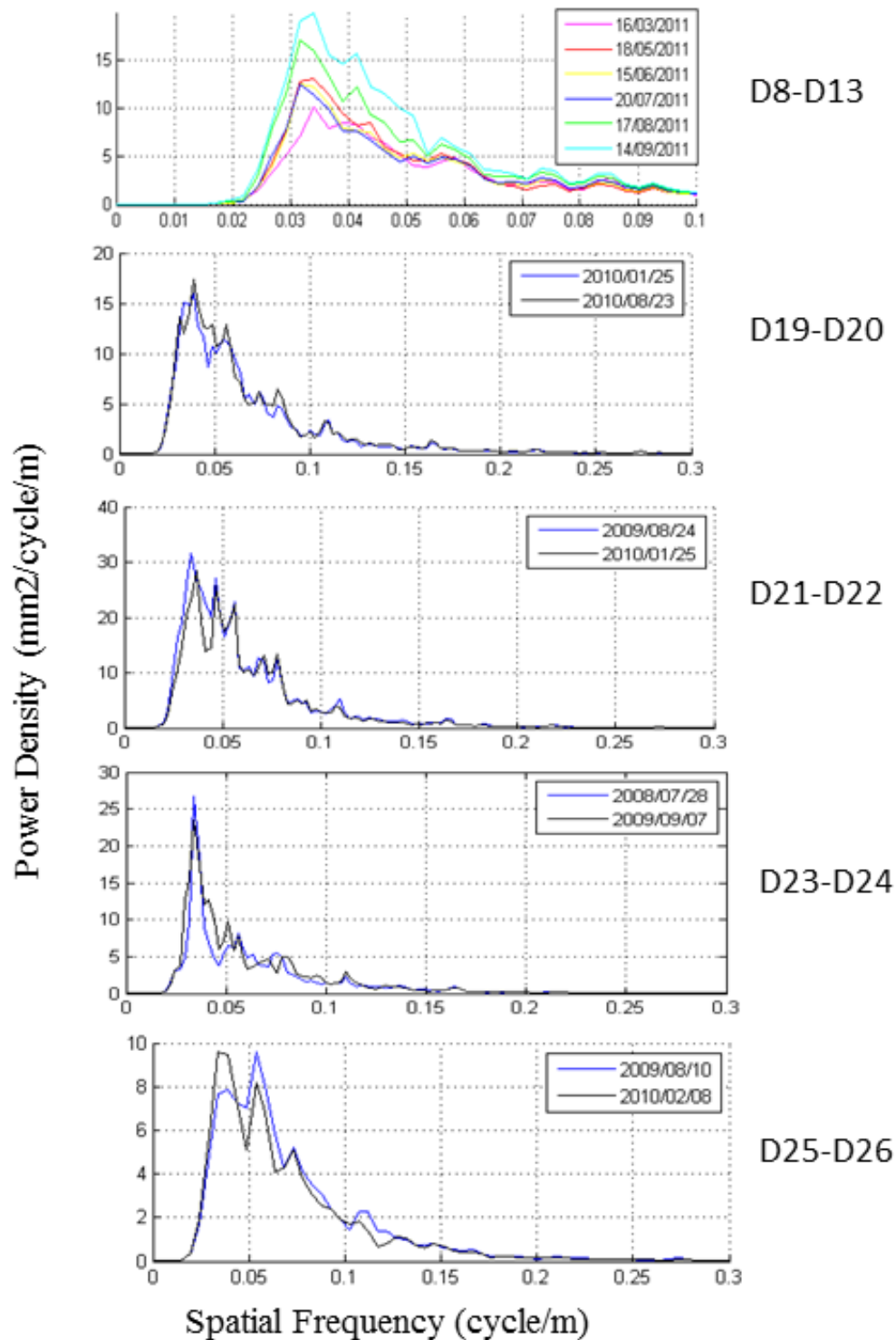


Figure 3-16 PSD result of long wavelength track irregularities

The peak power density points in the figures are summarised from Figure 3-16 in Table 3-15. It can be found that the peak power densities occur within the spatial frequency range from 0.03418 to 0.03906 cycle/m which is equivalent to a wavelength of 25.6 to 29.2 m. Moreover, it is notable that many long wavelength irregularities grow only in size, not wavelength. Generally, the growth of the irregularity size is quite small and the growth rates of the power density of these defects are different for different track sections. The average growth of peak power density per month is around 7-16% of the original power density.

Table 3-15 Summaries of the long wavelength PSD results

		Period between data sets [days]	Data taken time [yy/mm/dd]	Peak power density [mm ² /cycle/m]	Average growth of peak power density [mm ² /cycle/m/month]	Spatial frequency at peak [cycle/m]	Average growth of irregularity wavelength [mm/month]	Frequency for line speed of 125mph [Hz]	Percentage of decrease of frequency [%]
1 st peak power density	D8	63	16/03/2011	10.150	1.6071	0.03418	0	1.9100	0
	D9		18/05/2011	13.020		0.03418		1.9100	
	D10		15/06/2011	12.500		0.03174		1.7736	
	D11		20/07/2011	12.540		0.03174		1.7736	
	D12		17/08/2011	17.090		0.03174		1.7736	
	D13		14/09/2011	19.900		0.03418		1.9100	
	D19	210	2010/01/25	16.020	0.1886	0.03906	0	2.1827	0
	D20		2010/08/23	17.340		0.03906		2.1827	
	D21	154	2009/08/24	28.490	0.624	0.03662	389.88	2.0463	6.66
	D22		2010/01/25	31.610		0.03418		1.9100	
	D23	406	2008/07/28	26.670	0.2446	0.03418	0	1.9100	0
	D24		2009/09/07	23.490		0.03418		1.9100	
	D25	182	2009/08/10	7.879	0.2835	0.03906	609.21	2.1827	12.49
	D26		2010/02/08	9.580		0.03418		1.9100	
2 nd peak power density	D8	63	16/03/2011	8.469	1.1886	0.03906	-0.4022	2.1827	-6.25
	D9		18/05/2011	8.519		0.04395		2.4559	
	D10		15/06/2011	7.480		0.04395		2.4559	
	D11		20/07/2011	7.667		0.04150		2.3190	
	D12		17/08/2011	12.180		0.04150		2.3190	
	D13		14/09/2011	15.680		0.04150		2.3190	
	D19	210	2010/01/25	11.310	0.2271	0.05371	265.82	3.0013	9.09
	D20		2010/08/23	12.900		0.04883		2.7286	
	D21	154	2009/08/24	25.640	0.3020	0.04639	0	2.5923	0
	D22		2010/01/25	27.150		0.04639		2.5923	
	D23	406	2008/07/28	6.454	0.2445	0.05127	0	2.8649	0
	D24		2009/09/07	9.633		0.05127		2.8649	
	D25	182	2009/08/10	9.601	-0.2330	0.05371	0	3.0013	0
	D26		2010/02/08	8.203		0.05371		3.0013	

3 rd peak power density	D8		16/03/2011	4.819		0.05859		3.274	
	D9	63	18/05/2011	5.251		0.05615		3.1377	
	D10	28	15/06/2011	4.806	0.3447	0.05615	0.4022	3.1377	4.16
	D11	35	20/07/2011	4.795		0.05615		3.1377	
	D12	28	17/08/2011	6.163		0.05615		3.1377	
	D13	28	14/09/2011	6.910		0.05615		3.1377	
	D19	210	2010/01/25	4.831	0.2289	0.08301	0	4.6386	0
	D20		2010/08/23	6.433		0.08301		4.6386	
	D21	154	2009/08/24	12.240	0.2260	0.07813	0	4.3659	0
	D22		2010/01/25	13.370		0.07813		4.3659	
	D23	406	2008/07/28	8.240	-0.0289	0.05615	0	3.1377	0
	D24		2009/09/07	7.864		0.05615		3.1377	
	D25	182	2009/08/10	5.242	-0.0225	0.07324	0	4.0927	0
	D26		2010/02/08	5.107		0.07324		4.0927	

3.3.2.2 Short wavelength analysis

A log-log scale of the x and y axis gives a better understanding of the PSD results. The sample rate of the track data measurement is 5 points per meter, so the results will not be accurate when the spectral wavelength is smaller than 0.8 m, which is 4 data points. This means the results with a spectral density larger than $10^{0.1}$ cycle/m can be ignored. The log-log scale results for wavelengths between 0.8 and 10 m are shown in Figure 3-17, which shows that the power density peaks for short wavelength irregularities have different spatial frequency ranges for different networks. For the WCML, the peaks exist near spatial frequencies between $10^{-0.24}$ and $10^{-0.16}$ which is in the 1.45 to 1.74 m wavelength range, while for the ECML the peak appears between spatial frequencies of $10^{-0.3}$ and $10^{0.06}$ which is a wavelength between 2.00 and 0.87 m.

There are two peaks in some of the data sets. One is with a longer wavelength between 1.46 and 1.87 m, while the other one is between 0.85 and 1.19 m, and, as mentioned before, all other peaks with a wavelength shorter than 0.8 m can be ignored. It is noted that the power density unit is 1000 times smaller than in the previous long wavelength irregularity analysis. The average growth of the peak power density per month is around 3-4% of the original irregularity power density. With the small magnitude of the short wavelength irregularities, this growth of peak power density can be almost ignored.

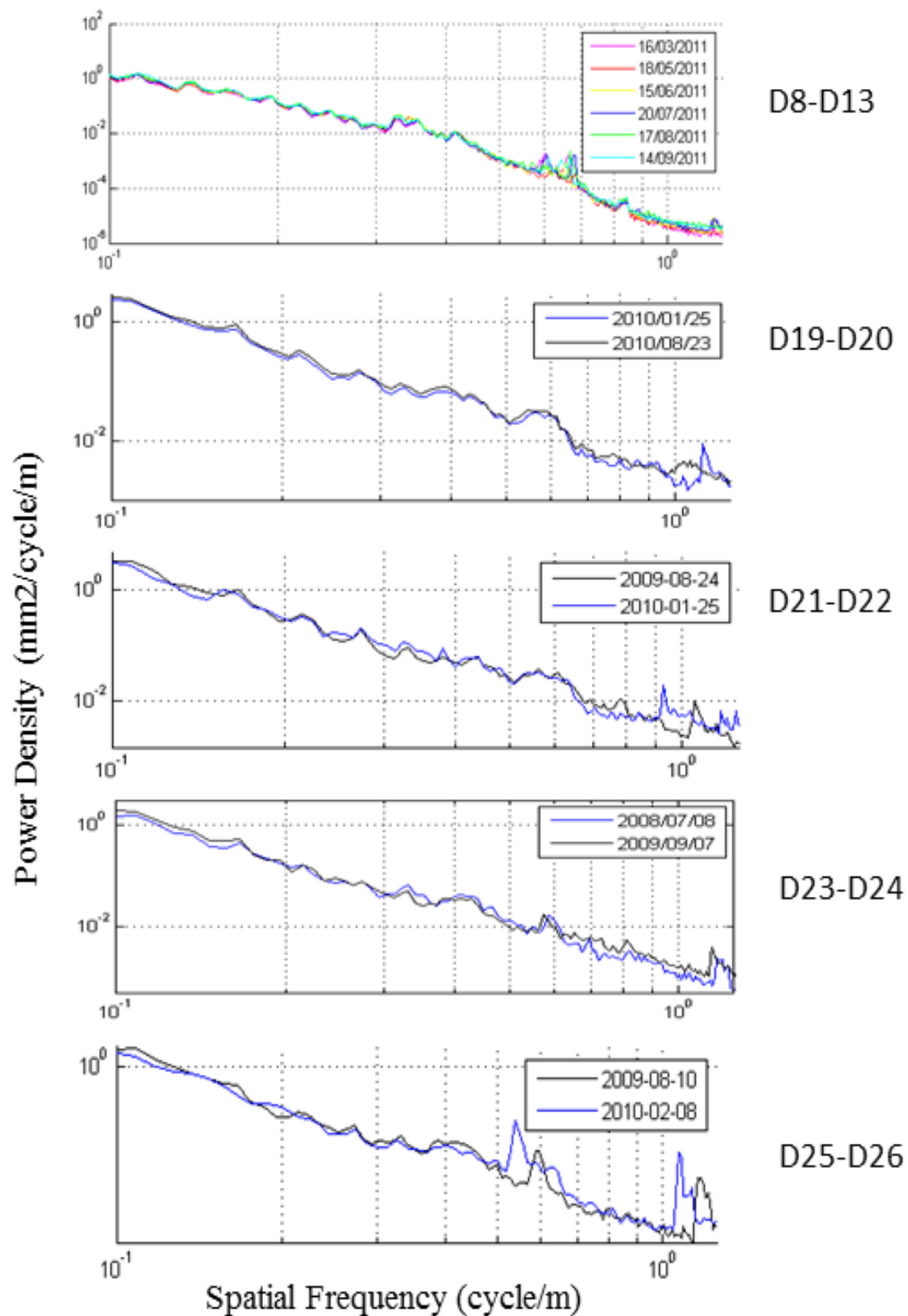


Figure 3-17 PSD results of short wavelength track irregularities

Table 3-16 Summarise of short wavelength PSD results

		Period between data sets [days]	Data taken time [yy/mm/dd]	Peak power density [mm ² /cycle/mm]	Average growth of peak power density [mm ² /cycle/mm/month]	Spatial frequency at peak [cycle/m]	Average growth of irregularity wavelength [mm/month]	Frequency for line speed of 125mph [Hz]	Percentage of decrease of frequency [%]
Spatial frequency $10^{-1} - 10^{-0.1}$	D8	63 28	16/03/2011	1.9000	- 0.0887	0.6006	-1.6154	33.562	-1.63
	D9		18/05/2011	0.4997		0.6152		34.377	
	D10		15/06/2011	0.8085		0.6006		33.562	
	D11		20/07/2011	1.8960		0.6055		33.835	
	D12		17/08/2011	0.6336		0.6104		34.109	
	D13		14/09/2011	1.3600		0.6104		34.109	
	D19	210	2010/01/25	29.4600	0.4057	0.5664	8.9930	31.650	3.44
	D20		2020/08/23	32.3000		0.5469		30.561	
	D21	154	2009/08/24	-	-	-	-	-	
	D22		2010/01/25	-		-		-	
	D23	406	2008/07/28	16.3900	0.0223	0.5859	2.2102	32.740	1.66
	D24		2009/09/07	16.6800		0.5762		32.198	
	D25	182	2009/08/10	37.9600	14.256 7	0.5859	25.8458	32.740	8.33
	D26		2010/02/08	123.5000		0.5371		30.013	
Spatial frequency $10^{-0.1} - 10^{0.1}$	D8	63 28	16/03/2011	1.6670	- 0.0641	0.6641	-0.7912	37.11	-0.72
	D9		18/05/2011	0.3908		0.6836		38.2	
	D10		15/06/2011	0.8024		0.6592		36.836	
	D11		20/07/2011	1.6350		0.6787		37.926	
	D12		17/08/2011	2.2370		0.6689		37.378	
	D13		14/09/2011	1.2780		0.6689		37.378	
	D19	210	2010/01/25	8.9570	- 0.6223	1.123	7.0540	62.753	5.25
	D20		2020/08/23	4.6010		1.064		59.456	
	D21	154	2009/08/24	9.7370	1.7066	1.055	26.0135	58.953	12.07
	D22		2010/01/25	18.2700		0.9277		51.840	
	D23	406	2008/07/28	2.2850	0.1258	1.1720	1.1395	65.491	1.71
	D24		2009/09/07	3.9210		1.1520		64.374	
	D25	182	2009/08/10	13.0000	3.6283	1.1820	14.1792	66.050	9.14
	D26		2010/02/08	34.7700		1.0740		60.015	

3.3.2.3 Comparison between long and short wavelength PSD results

Figure 3-18 summarises the average growth of peak power density results from Table 3-15 and Table 3-16. The shorter the irregularity wavelength is, the slower the power density growth. When the irregularity wavelength is below a certain length, the growth of irregularity size can be neglected. However, from a growth rate point of view, short wavelength lateral irregularities grow much faster than long wavelength ones.

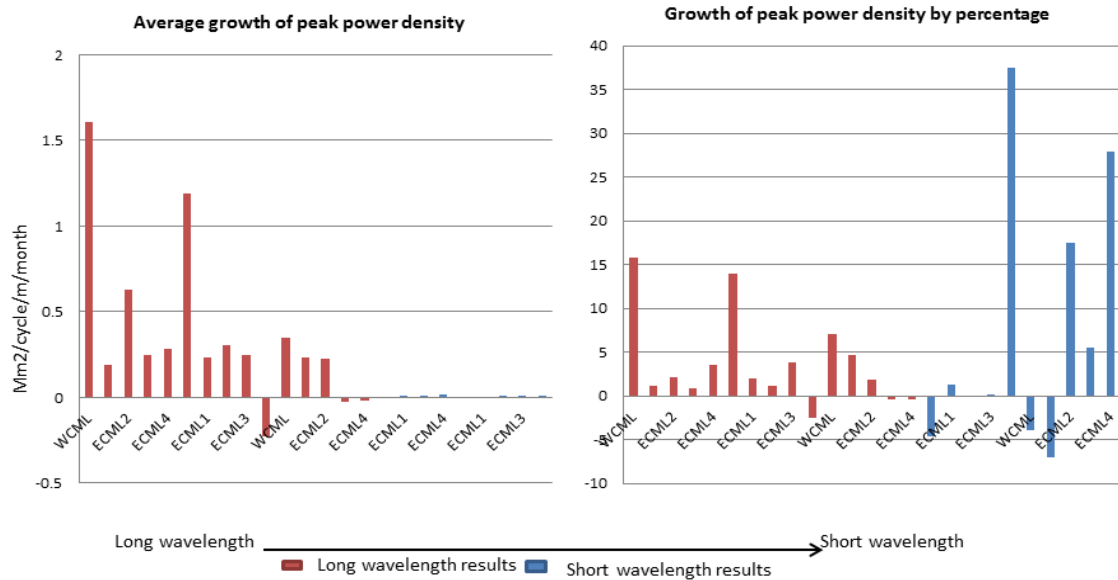


Figure 3-18 Summary of average peak power density growth per month

Figure 3-19 shows a summary of the irregularity wavelength growth results from Table 3-15 and Table 3-16. A conclusion can be made that most track irregularities grow in length, but the long wavelength irregularities appear to be more stable than the short ones, as it can be seen in the figure that many of the long wavelength irregularities settles and the wave length does not change. The growth of irregularities does not follow a set pattern for all data sets regardless of size or length, which may be due to different subgrade conditions, traffic mix and types of track subsystems. However, a specific section of track can be studied in order to find the pattern of irregularity growth.

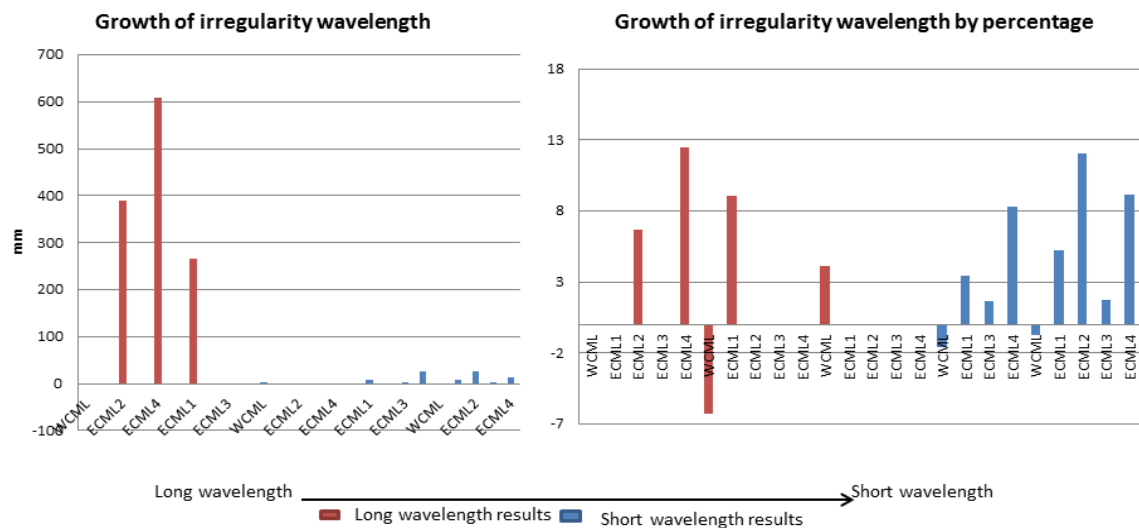


Figure 3-19 Summary of growth of irregularity wavelength per month

3.3.3 Fractal dimensions change over time

Unlike a PSD analysis, an FD analysis does not require a long length of track section to get enough information. As discussed in section 3.1.2.2, fractal dimension and SD can both describe the lateral track quality yet in different ways. The overall fractal dimension and SD are calculated for a section of track, and shown in Figure 3-20.

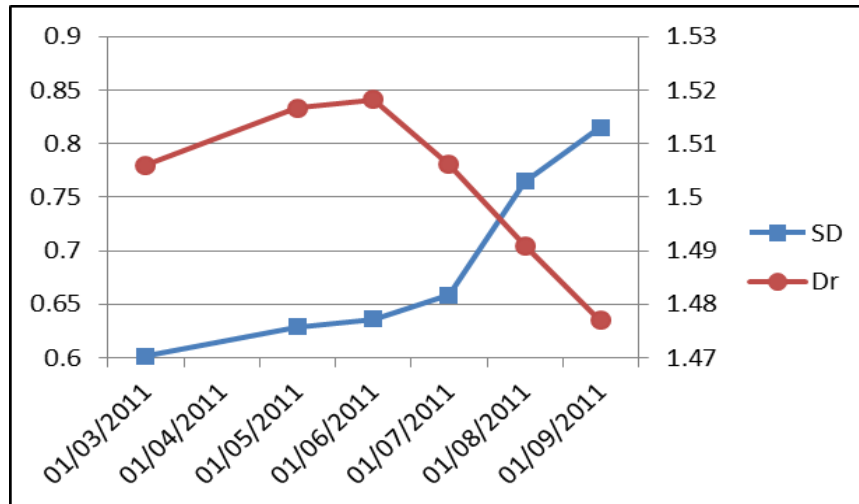


Figure 3-20 Fractal dimension and SD value change over time

The fractal dimension has a general trend of dropping over time, which describes the irregularity wavelength growth. However, although the fractal dimension describes the overall frequency change to some extent, it is easily influenced by the length of track that is chosen, as for a longer length track there will be a variety of frequency bands. Therefore, it is sensible to choose some particular sections for the following study.

There are 3 sets of 120m track sections chosen for the analysis, as shown in Table 3-17. These are used for the following track deterioration analysis and fractal analysis.

Table 3-17 Selected track sections for lateral deterioration analysis

Track type	Tangent track	Transition track	Curved track
Selected sections	S15 – S16	S13 – S14	S10 – S11
Mileage	72.450 – 72.525	72.338 – 72.413	70.884 – 70.959
Meter	10380-10500	10200-10320	7860-7980
Datasets	D8 – D13 measured datasets		

The results of the fractal dimension calculations and SD over time are shown in Figure 3-21.

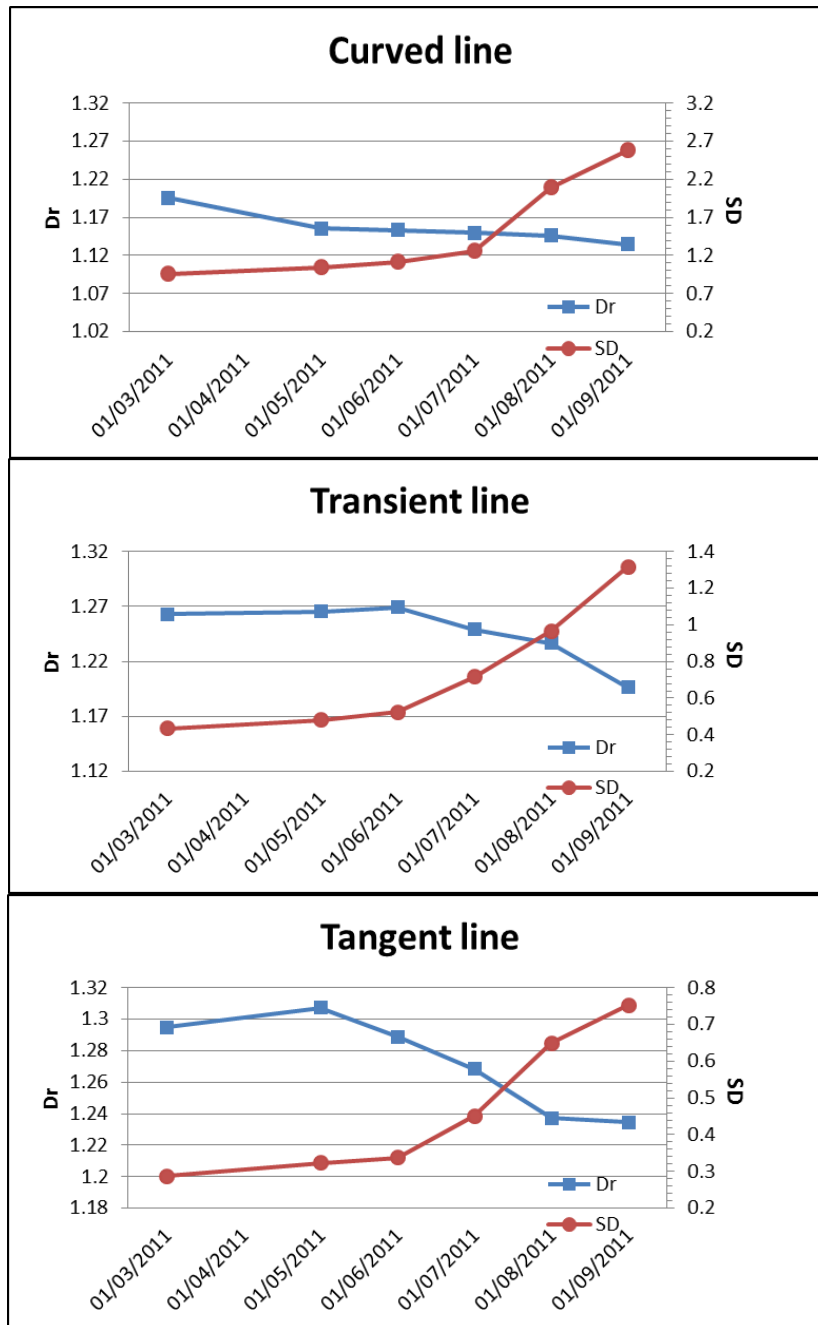


Figure 3-21 Fractal dimension value and SD value for selected track sections

In order to examine the correlation between wavelength and magnitude changes over time, the correlation coefficient between Dr and SD values is calculated and found to be -0.8098 which is near -1. This indicates that the increase in frequency and magnitude of the track irregularities are correlated negatively, which means that the wavelength and magnitude of the track irregularity are correlated positively. This result shows the same regularity for the change of lateral track irregularities as the results in Section 3.3.2, that is, the lateral track irregularities grow in size and length at the same time.

3.3.4 Conclusion

It can be quite rare for a section of operational track to have a constant lateral deterioration due to the large number of maintenance activities, especially on curves. For around 10% of the total track length studied (around 1 km selected over 11 km track), a recognisable growth pattern of lateral irregularities can be identified, while for the rest, there is no specific growth pattern. If there is no disruption in the growth of the lateral irregularities due to maintenance interventions, the lateral irregularities grow exponentially. The average daily deterioration rate of curves and transitions track is generally larger than on tangent track. Three power curve fitting equations are found to describe the growth of irregularities on tangent, transition and curved track, and the parameters should be determined for different types of the track and traffic pattern.

According to the PSD results, lateral track irregularities grow both in size and length. The short wavelength lateral irregularities do not make a big impact on the track lateral deterioration due to their small amplitude. The long wavelength irregularities appear to be more stable than the short ones, as a large proportion of the long wavelength irregularities stabilise and do not change. The growing long wavelength irregularities, which make up a small proportion, are the main feature impacting the lateral track deterioration. Short wavelength irregularities do not make a big impact on lateral deterioration, yet may develop into a medium or long wavelength irregularity in the future.

For track sections with constant growth of lateral irregularity SD values, the fractal dimension drops. The increase of the frequency and magnitude of the lateral track irregularities are correlated negatively, which means the lateral track irregularities grow in both size and length. This result agrees with the result from the PSD analysis.

3.4 Chapter conclusion

The relationship between vertical and lateral irregularities is obvious in both the distance domain and spatial domain. However, no clear regularity of the correlations of the vertical and lateral major irregularity wavelength are found between lateral and vertical irregularities. The track quality in the vertical direction is generally worse than in the lateral direction, but some track sections with a lateral quality significantly worse than the vertical are non-negligible.

On curves, railway track tends to deteriorate faster due to the larger lateral forces that result from the vehicle running with cant deficiency or cant excess. The track irregularity SD generally tends to have an exponential growth with increasing curve radius. This exponential characteristic may vary by considering a particular type of railway line, such as freight lines, regional lines and high speed lines.

For track sections with constantly developing lateral deteriorations, the lateral irregularity is found to grow both in size and length when subject to both time and spatial domain analysis. The major influences are from the long wavelength track irregularities, while the small wavelength irregularities can be neglected as they have a small amplitude growth rate. However, the short wavelength irregularities are not as stable as the lateral irregularities, and they may grow into longer wavelength irregularities, and hence could not be neglected in the lateral deterioration. Beside they may have an impact on the safe operation of the railway.

4 VEHICLE-TRACK LATERAL DETERIORATION MODEL

In modelling railway vehicle dynamic behaviour and depending on the focus of the research, it is normal for either the vehicle or track model to be simplified. For example, the vehicle can be modelled as a mass resting on a simple parallel spring and damper, or the track can be modelled as a single layer elastically supported beam. There are complex models that describe the vehicle and track coupling mechanism which are difficult to use and require lengthy computation time in order to obtain the simulation results [108]. In order to build a nonlinear vehicle-track dynamic interaction model in this work, a vehicle dynamics model in VAMPIRE® and a non-linear track model built in MATLAB were coupled together. Selected track sections from the WCML mentioned in Chapter 3.3 were used in this research.

4.1 Vehicle-track dynamic model

VAMPIRE® software allows the user to build a dynamic model of any rail vehicle and study the response of the vehicle to real measured track geometry or user specified inputs in the form of track displacements and external force inputs. Rail vehicles can be modelled with simulated instrumentation allowing almost any aspect of the vehicle's behaviour to be studied (Website Reference 5). This software is used to build dynamic multi-body models of rail vehicles and to capture the forces between the wheels and rails.

4.1.1 Track irregularity file

The track data measured by a Track Recording Coach, which in the UK commonly includes 70 and 35 m low pass filtered vertical profile, and lateral alignment, as well as curvature, gauge, and crosslevel filtered at 3 and 5 m, can be used to create a track irregularity input file. The data is typically measured at intervals of 0.2 or 0.25 m. The irregularity file in VAMPIRE® normally consist of 6 data fields: the distance along the track (m), cross level irregularity (mm), curvature irregularity (1/km), lateral irregularity (mm), vertical irregularity (mm) and gauge variation (mm). If there are switches and crossings present in a track section, flange way irregularity to left and right check rails (mm) may also be included.

4.1.2 Wheel-rail contact model

The wheel-rail contact model includes both wheel and rail profiles, and a non-linear creep law, as used in this research. The friction coefficient between the wheel and rail is chosen to be 0.3 as this is generally considered to be the most prevalent value in the UK. The selection of the rail and wheel profiles is highly dependent on the actual situation. The WCML used for this work is now mainly CEN60 rail – inclined at 1 in 20, and passenger vehicle wheels tend to have a BR-P8 profile, while freight vehicles use either BR-P5 or BR-P10 wheel profile. The CEN60-20_P8 contact model was chosen for simulation of passenger vehicles and the CEN60-20_BR-P10 and CEN60-20_BR-P5 contact model were used for freight vehicles.

The rolling radius difference for both new and worn CEN60-20_BR-P8 is shown in Figure 4-1. A very small difference occurs when using different rail profiles. It is noted that the wheel and rail profiles on an operational railway line will not be new profiles, so a worn CEN60-20 rail profile measured on the WCML was also used in conjunction with worn BR-P8 wheels measured from Class390 vehicles, which operate the majority of services on the WCML.

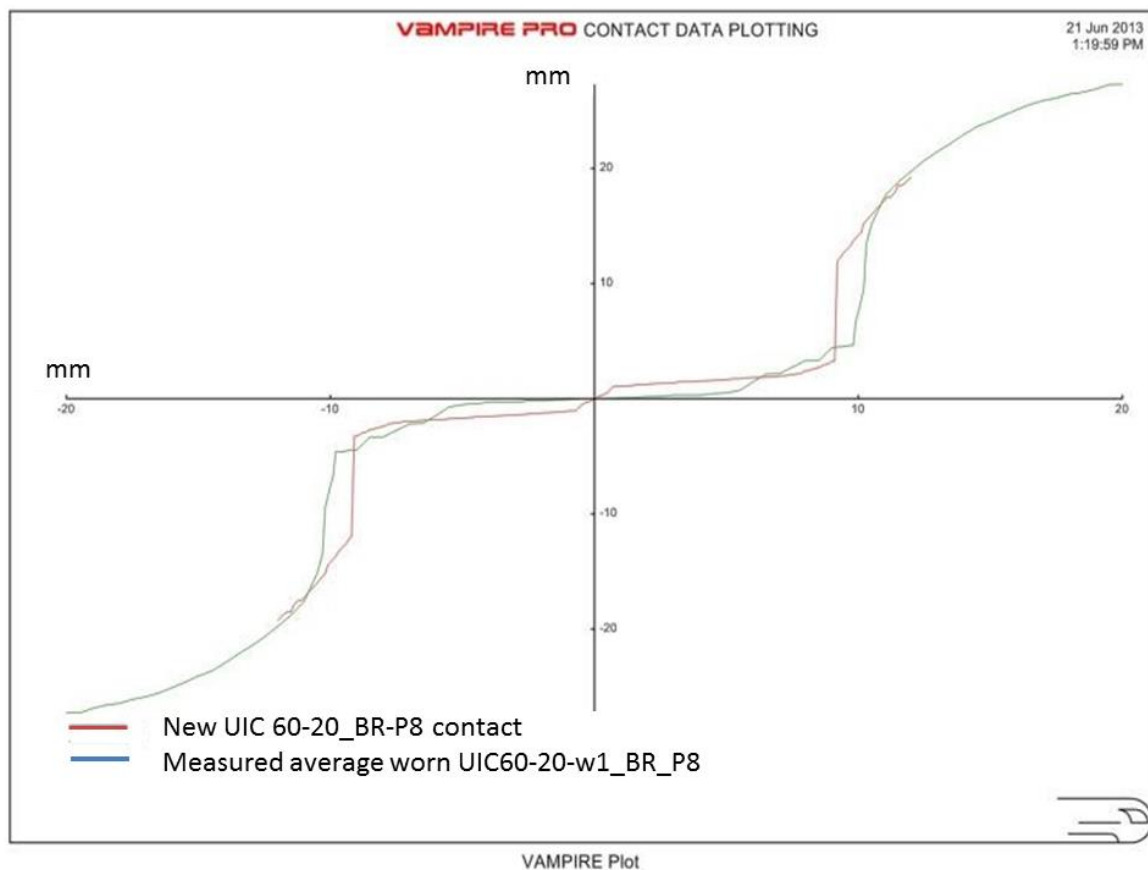


Figure 4-1 Rolling radius difference of new and worn wheel rail profiles

The rolling radius difference of new and worn profile can be quite different, and therefore are critical to the simulation.

4.1.3 Vehicle models

The detailed traffic information data for this section of the WCML is shown in Appendix D.1. There are 11 types of vehicles that operate over the relevant section of the WCML: Class 390, Class 221, FEAB, FSAO, MKIII, FTAI, IPAV, KFAF, MKII and Class 66. The Class 390, commonly known as the Pendolino Electric Multiple Unit (EMU), makes up to 80.82% of the traffic on the section under study, followed by Class 221 SuperVoyager Diesel Multiple Unit (DMU), which makes up 6.02% of the traffic.



a) Class 390 Pendolino



b) Class 221 SuperVoyager

Figure 4-2 Class 390 (Website Reference 6) and 221 vehicles (Website Reference 7)

The FEAB and FSAO, shown in Figure 4-3, are flat wagons used for transporting containers. The FTAI and KFAF freight vehicles are also similar to the FEAB and FSAO, having similar suspension structure and dynamic behaviour. Therefore, it is possible to represent these freight vehicles using one vehicle model.



a) FEAB



b) FSAO

Figure 4-3 FEAB (Website Reference 8) and FSAO (Website Reference 9) wagons

Unlike the other wagons, the IPAV wagons are two axle wagons which are mainly used to carry cars. Figure 4-4 shows this type of freight vehicle.



Figure 4-4 IPAV (Website Reference 9) wagons

The multi-body approach is used in establishing the vehicle model in the VAMPIRE® software. The vehicles are idealised as a collection of masses representing the body, bogie frames, wheelsets, etc. These masses are connected together by various suspension elements. Therefore, the modelling of suspension elements plays an essential role in the vehicle models. The dynamic properties of VAMPIRE® suspension elements have been categorised into stiffness and damping properties, as shown in Figure 4-5 [109].

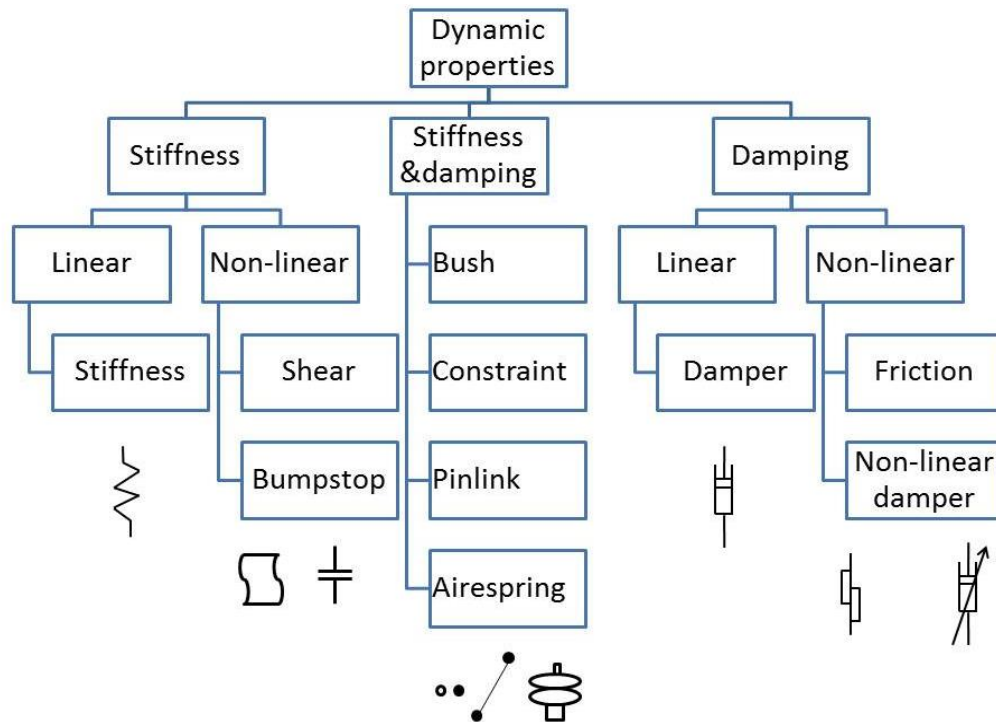
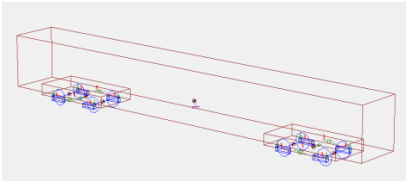
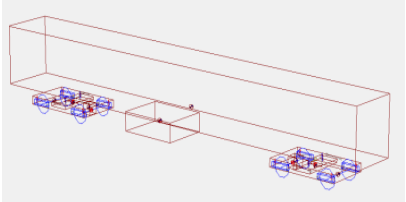
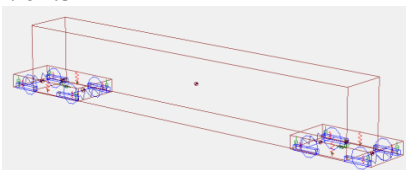
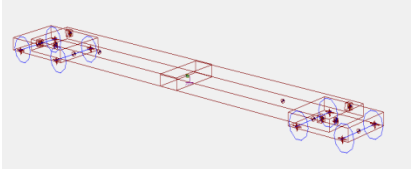
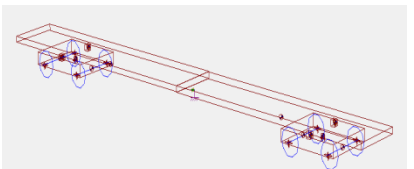
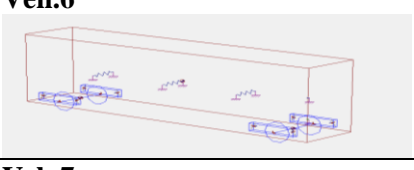
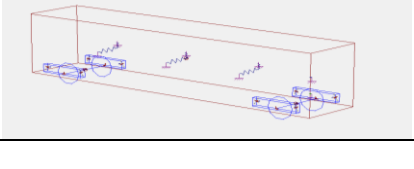


Figure 4-5 Dynamic properties of VAMPIRE® suspension elements

The vehicles will be modelled in VAMPIRE® based on the real vehicle, but it would be too time consuming to model all of the vehicles. Therefore, only the main passenger vehicles, such as the Class 390, Class 221 and MKIII are modelled. The four different 4-axle freight vehicles mentioned previously in both laden and tare conditions are represented by two freight vehicle models. Vehicles which make up a small percentage of the total are omitted in the simulation. The models for Veh.1 to Veh.7 are shown Table 4-1.

Table 4-1 General vehicle models

Vehicle models	Type of vehicle	Weight [ton]	Speed [m/s]	Suspension elements
Veh.1 	Class390	56.0	44.70	Stiffness, shear, bumpstop Bush Damper
Veh.2 	Class221	59.8	44.70	Stiffness, shear, bumpstop Bush, constraints, pinlink, airspring Damper,
Veh.3 	MKII & MKIII	39.6	44.70	Stiffness, shear, bumpstop Bush, Damper, friction

Veh.4 	FEAB FSAO FTAI KFAF laden	79.6	33.53	Stiffness, bumpstop Bush Damper, friction
Veh.5 	FEAB FSAO FTAI KFAF tare	19.7	33.53	Stiffness, bumpstop Bush Damper, friction
Veh.6 	IPAV laden	109.9	20.12	Stiffness, bumstop Pinlink Damper, friction
Veh.7 	IPAV tare	40.7	20.12	Stiffness, bumstop Pinlink Damper, friction

4.1.4 Transient response analysis

Once the track irregularity, contact and vehicle files are selected, a transient analysis is used to carry out the non-linear calculations that compute the response of the vehicle to discrete track inputs. The basic axis system for the simulation is shown in Figure 4-6.

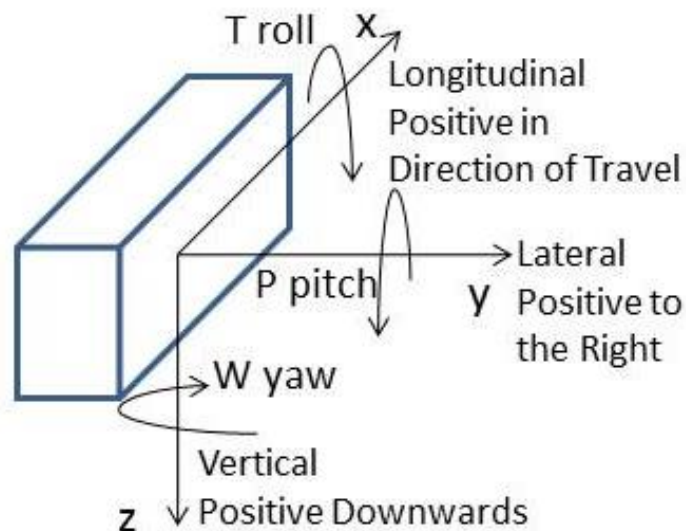


Figure 4-6 Basic axis system for VAMPIRE® simulation

In a transient analysis, a moving coordinate system is employed, in which the vehicle axis systems, wheelset axis systems and contact axis systems move along the track at the speed of the vehicle. The inputs and outputs are shown in Table 4-2.

Table 4-2 Transient simulation inputs and outputs

Track irregularity data	WCML measured track data D8-D13 from 0 to 11000m
Vehicles	Veh.1 to Veh.7
Calculation time step	0.001 s
Output time step	0.004s for passenger vehicles 0.005s for 4-axle freight vehicles 0.009s for 2-axle freight vehicles
Speed	100mph (44.70 m/s) for passenger vehicles 75mph (33.528m/s) for 4 axle freight vehicles 45mph(20.117m/s) for 2 axle freight vehicles
Coefficient of friction	0.3 for all vehicles
Contact file	CEN60-20-worn_br-p8-worn for passenger vehicles CEN60-20-worn_br-p10 for 4-axle freight vehicles CEN60-20-worn_br-p5 for 2-axle freight vehicles
Creep law	Friction coefficient 0.3 Nonlinear creep law
Outputs	Vertical and lateral forces from each wheel to the rail

The running speed for different vehicles can be found in details of running lines [110]. An average worn CEN60-20 rail profile measured on the sections of the WCML and an average worn BR-P8 wheel profile measured from Class 390 vehicles are selected for the passenger vehicle simulation. The determination of the running speeds of different vehicles depends on the line speed indicated on the WCML combined with the maximum cant deficiency allowed. The determination of calculation and output time step is to fulfil both accuracy and time consumption requirements. As the distance between two nodes of the track model is 0.2 m. A reasonable output time step was chosen to be 0.004 s, 0.005 s or 0.009 s depending on the running speed, which results in a force input onto the rails of each 0.1788 m, 0.1676 m or 0.1811 m for passenger vehicles and 0.1006 m for freight vehicles. The wheel lateral force output is obtained by adding the wheel tread creep forces and the flange contact forces. The wheel vertical forces are the sum of the static wheel load and the dynamic wheel vertical force.

The total wheel-rail forces output from VAMPIRE® are shown in Equation 38 and Equation 39. Figure 4-7 shows the different axis systems used in VAMPIRE® and how the lateral forces in the wheel-rail axis system convert to the wheelset axis system.

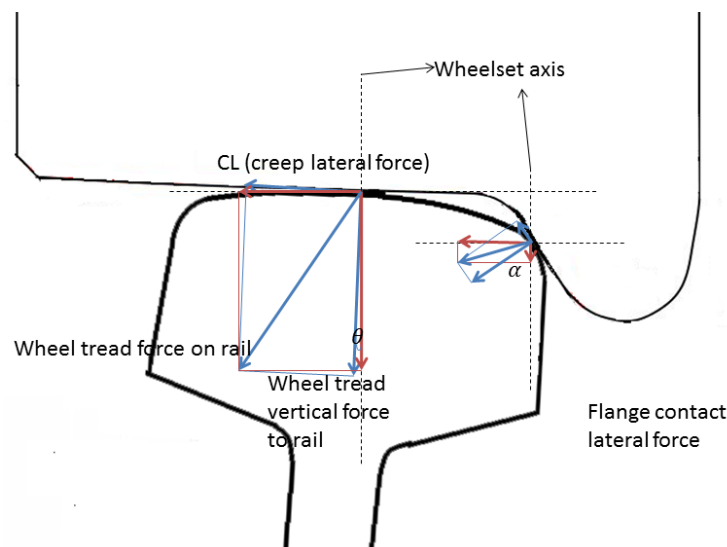


Figure 4-7 Wheel-rail axis to wheelset axis

$$F_v = W + F_z \quad \text{Equation 38}$$

$$F_y = CL_y \cdot \cos \theta + F_v \cdot \sin \theta + CF_y \cdot \cos \alpha + CF_z \cdot \sin \alpha \quad \text{Equation 39}$$

Where,

F_v and F_y ... total wheel-rail vertical and lateral force

W ... static vertical force

F_z ... dynamic vertical force

θ ... angle of wheel/rail tread contact from horizontal

α ... angle of flange contact from horizontal

CL_y ... lateral creep force on wheel-rail axis system

CF_y ... flange creep force on wheel-rail axis system

CF_z ... flange normal force on wheel-rail axis system

4.1.5 Conclusion

The VAMPIRE® simulation tool has been explained in detail in terms of its inputs and outputs. Firstly, the parameters of the track irregularity input file were described, and track sections S15-S17 and S10 of D8-D13 from Chapter 3.3 were selected for the analysis. Secondly, different wheel-rail contact conditions were compared and the measured worn rail and wheel profiles were selected for the simulation. Then, seven models of vehicles which run on the particular section of track of the WCML were developed. Finally, the calculation step and running speeds are determined according to the different vehicle types, and the resultant vertical and lateral dynamic forces between the wheels and rails are described.

4.2 Track parameters

Track parameters describe the characteristics of the track, and track in different conditions and locations may have different representative parameter values. The development of different track parameters is based on many studies which involve complicated measurement and lab tests. Accurate track parameters give a better understanding of the track system and the selection of track parameters plays an essential role in track model development. In this section, all the important track parameters that are used in the lateral track deterioration model will be presented and described in detail. For validation purpose the track parameters are selected to represent as best as possible the WCML track condition.

4.2.1 Track stiffness and damping

In the track model, the sleeper is considered rigid and the ballast, sub-ballast and geotextile layers are considered as a whole subsystem in order to reduce the complexity. Track stiffness and damping are the fundamental track parameters, which describe the elastic characteristics of the track. These play an important role in vehicle-track dynamic behaviour. Many studies have pointed out that the track stiffness has a significant influence on track dynamic performance. Esveld [111] claimed that track stiffness has been found to be useful for determining the cause of certain subgrade problems. Sussmann et al. [112] stated that track stiffness can be used to provide an additional indicator of track condition to inspectors and to guide maintenance planning and execution. It is also asserted by Fröhling [113] that spatial variation of the track stiffness contributes significantly to track deterioration, both in terms of differential track settlement and increased dynamic vehicle loading. Relatively high track stiffness is beneficial in that it provides sufficient track resistance to loads, however, track stiffness that is too high can cause increased dynamic forces in the wheel-rail interface as well as on sleepers and ballast, which may lead to wear and fatigue of track components [114]. The damping of the track has a large impact on the dynamic reactions, and an increase in damping can effectively reduce rolling noise [115]. Consequently it is important to have a good understanding of the track in order to select the right stiffness value in the model development process.

The stiffness values between two adjacent components should be determined. As it is a triple layered track model, the stiffness values considered are the rails, rail pads and fastenings stiffness, as well as the track bed stiffness. The stiffness of different track layers can be measured from laboratory tests. Normally, the force-deflection relationship has the nonlinear characteristic shown in Figure 4-8 [116] and also includes some degree of hysteresis.

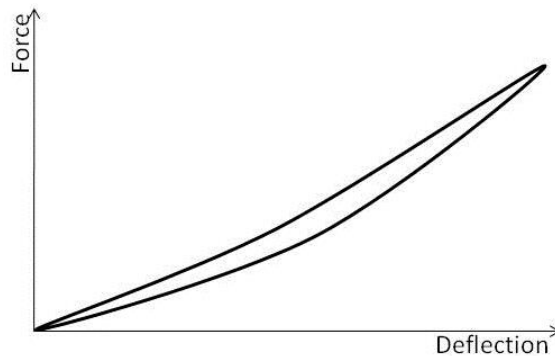


Figure 4-8 Force-deflection diagram of track with quasi-static excitation

However, the track stiffness (k) is most commonly approximated as a linear relationship shown in Equation 40, where the track stiffness is the ratio of applied load on the track (F) and the track deflection (z) at a certain force level.

$$k(t) = \frac{F(t)}{z(t)} \quad \text{Equation 40}$$

The global stiffness takes the whole track structure into account, and can be measured by several existing methods. Liu and Wang [117] claimed that a reasonable range of global stiffness is between 62 kN/mm and 87 kN/mm per rail for ballast track. For the track system, the series of stiffnesses in different layers is shown in Figure 4-9.

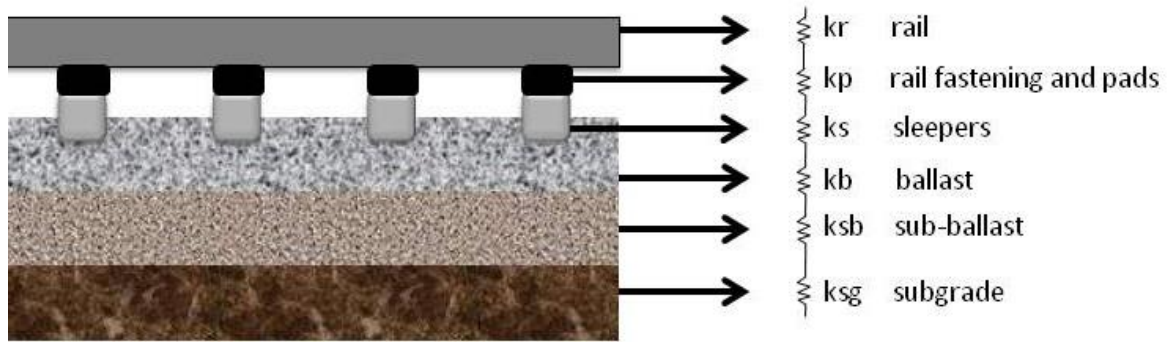


Figure 4-9 Structure of track stiffness

Various pieces of equipment exist to measure and estimate the track stiffness. A rolling Stiffness Measurement Vehicle (RSMV) is a rebuilt two-axle freight wagon equipped with loading and measuring equipment, which can estimate the dynamic stiffness up to 50 Hz [114]. The railway Portancemetre is basically a vibrating wheelset to measure the dynamic stiffness of railway track, and can measure the stiffness by exciting the track at a maximum of 35 Hz. The track instrumentation stiffness measurement methods, which are commissioned by the Administrator of Railway Infrastructures (ADIF) of Spain, are based on the use of sensors external to the track mounted on the rails. Furthermore, a light dynamic penetrometer with variable energy (Panda) has been developed at the Blaise Pascal University in Clermont-Ferrand, which can measure the stiffness of different track layers.

4.2.2 Rail parameters

The parameters of rails are relatively easy to find since they are quantified by the manufacturer. Tata Steel produces most of the commonly used types of rails and their brochure contains all the necessary parameters. The parameters of a CEN60 rail that is widely used in Europe is shown in Table 4-3 [118].

Table 4-3 Parameters of CEN60 rail

Parameters	Unit	Value
Section weight	kg/m	60.21
Moment of inertia I_{yy}	cm^4	3038
Moment of inertia I_{zz}	cm^4	512.3
Section modulus Z_{xx}	cm^3	333.6
Section modulus Z_{yy}	cm^3	68.3
Distance of neutral axis from top of rail	mm	91.08

4.2.3 Sleeper parameters

The sleeper material, weight and sleeper spacing impact the distribution of the load and the dynamic behaviour of the whole track system, while the sleeper shape and weight can have a large influence on the track lateral resistance. The sleeper spacing is determined according to British standard [119], which is normally 650 mm. G44 sleepers are widely used in UK mainline track and its parameters are shown in Table 4-4.

Table 4-4 G44 sleeper parameters

	Units	Symbol	Values
Mass	kg	m	308
Overall length	mm	l	2500
Base width under rail centre	mm	w	285
Height at rail centre	mm	d1	200
Height at sleeper centre	mm	d2	175

4.2.4 Rail fastening and pad parameters

The stiffness of the rail fastening system is the sum of the rail pad stiffness and the stiffness of the rail clips. The stiffness of different types of rail fastenings varies to a large extent as shown in test results. Different types of railway lines, such as freight lines, passenger lines, high speed lines and metros, have diverse requirements for the fastener system behaviour in terms of noise, maintenance, stiffness, etc. Thompson and Verheij [120] carried out a large amount of laboratory work and showed that the static and dynamic stiffness of rail fastener systems varies with the preload and loading frequencies. The fastener lateral stiffness is more complicated, because it varies with the vertical load as shown in Figure 4-10 [121]. Therefore, the lateral fastening system stiffness taken in the models are almost average values from the measurements. Research [122] has shown that the choice of damping value does not influence the track displacement much, therefore, the damping values can be determined by reasonable damping ratios which range from 1% to 4% of the stiffness value.

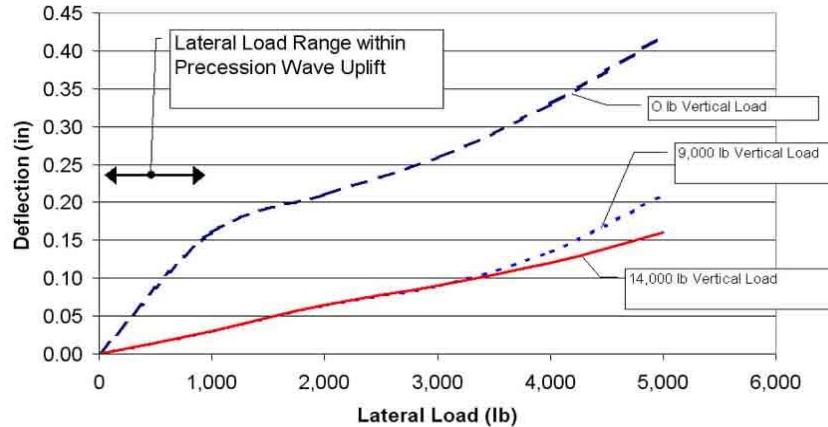


Figure 4-10 Rail fastener lateral stiffness against different vertical load

Table 4-5 shows the vertical stiffness of three types of Pandrol fastening systems which are published on the Pandrol website.

Table 4-5 Vertical stiffness published by Pandrol company [kN/mm]

	Static	Dynamic
Pandrol SFC	45	63
Pandrol VIPA	17	20
Pandrol Vanguard	5	8

According to the Chinese standard [117], different values for rail fastening system stiffness are given in Table 4-6. The dynamic stiffness is also studied in China, and the results indicate that the dynamic stiffness is roughly 1.2 to 1.5 times higher than the static stiffness.

Table 4-6 Rail fastening system vertical stiffness in Chinese standard [kN/mm]

Freight lines	70 ~ 90
Freight and passenger mix lines	50 ~ 80
Passenger lines	50 ~ 70
Slab track lines	30 ~ 50

These two tables give a general idea of the rail fastening system stiffness range. The stiffness value used in the track model is usually the stiffness of rail-fastening-sleeper assembly system. 5 types of commonly used rail fastening systems assembled with CEN 60 rail and half G44 sleeper were tested at the University of Birmingham [123] for the Crossrail project, and Table 4-7 shows the measured stiffness of these tests under 60 kN preload. It shows a large difference between the different rail fastening systems.

Table 4-7 Quasi-static CEN60-rail fastening system-half G44 sleeper assembly test under 60kN preload [kN/mm]

	Pandrol E-clip	Pandrol SFC	Pandrol VIPA	Pandrol Vanguard	DELKOR
	60 kN preload				
Vertical	120.7	108.5	12.3	7.4	12.2
Lateral	41.4	54.4	10.1	62.7	10.8

The dynamic stiffness of two assemblies, which are widely used on British mainline railways, can be found in Pandrol test reports. The parameters of the 60E1 and 56E1 assemblies are summarised from Pandrol test reports No.41174 and No.45111 and the average value of the test results are shown in Table 4-8. The results were not always consistent in the lateral direction. The reason may be the fact that the effective stiffness at the rail head is different because of the contribution of rail roll.

Table 4-8 Summary of Pandrol report [kN/mm]

Properties	60E1 assembly	56E1 assembly
Vertical	270	200
Lateral	400	250
Equivalent lateral head stiffness	398	250
60E1 assembly: G44 sleepers - clips FC1504 – CEN60		
56E1 assembly: G44 sleepers – clips FC1504 – BS113A		

Bezin [124] selected and summarised both the quasi-static and dynamic parameters of the rail pads, and are shown in Table 4-9.

Table 4-9 Summarised rail pad parameters

	Quasi-static	Dynamic	
	Stiffness [kN/mm]	Stiffness [kN/mm]	Damping [kN.s/m]
Soft rail pad	75	150	20
Typical rail pad	150	300	30
Stiff rail pad	500	1000	50

The rail pad vertical parameters are summarised from receptance tests [125], and are shown in Table 4-10.

Table 4-10 Rail pad parameters

	Pad section	Stiffness [kN/mm]	Damping [kN.s/m]
Railtrack	FC584	480	49
DB AG	ZW900	196	32
SNCF	9mm rubber	500	30

4.2.5 Track bed parameters

The subgrade modulus is the most variable quantity among all of the track parameters due to change of soil type, environmental conditions and stress state. Therefore, the track bed stiffness of the same type of track can be different in different locations. In the lateral direction, the sleeper tends to behave in a highly nonlinear manner. The sleeper behaves relatively linearly below a certain force limit, above which it slides. Furthermore, it is difficult to measure the lateral properties. An indicative value of the ballast lateral stiffness was measured by Clark et al. and the typical track bed stiffness is summarised in Table 4-11 [126].

Table 4-11 Summary of track bed stiffness per sleeper

	Vertical			Lateral	
	Quasi-static	Dynamic		Quasi-static	
	Stiffness kN/mm	Stiffness kN/mm	Damping kN.s/m	Stiffness kN/mm	Damping kN.s/m
Soft track bed	10	20	50	-	-
Typical track bed	40	80	100	40	240
Stiff track bed	100	200	150	-	-

The sleeper vertical support stiffness on the East Coast Main Line (ECML) is measured in four different locations and summarised in Table 4-12 [127].

Table 4-12 Quasi-static stiffness measurements at various sites

Site name (all on ECML)	Sleeper support stiffness kN/mm per sleeper
Dry Doddington	43
Gamston	35
Retford	51
Noblethorpe	28

Sun and Dhanasekar [62] outlined the track parameters from four different track studies and the sleeper stiffness and damping coefficients are shown in Table 4-13.

Table 4-13 Sleeper support parameter in four different researches

	Dong et al.	Newton and Clark	Fermé and Nielsen	Zhai
Sleeper stiffness (kN/mm)	31.6	79	98	98
Sleeper damping (kN.s/m)	21.8	50	130	130

The track bed parameters are also summarised in a Chinese report [65] shown in Table 4-14. These parameters represent the entire track bed including ballast, sub-ballast and subgrade, so it is larger than the actual sleeper-ballast interface properties.

Table 4-14 Track bed parameters

	Vertical	Lateral
Stiffness [kN/mm]	100-400	40-60
Damping [$kN \cdot s/m$]	80-150	25-30

There are a few laboratory tests that have looked at these non-linear relationships between sleeper and ballast listed in Appendix D, and these are summarised in Table 4-15. It is found that the lateral stiffness is around 4kN/mm in the unloaded condition.

Table 4-15 Lateral Resistance Characteristic Values per Sleeper

	Elastic resistance Fe (kN)	Elastic displacement we (mm)	Break-away force Fp (kN)	Break-away displacement wp (mm)	Sliding resistance Fl (kN)	Sliding displacement wl (mm)
Loose Tamped/Relay (Weak)	2.4	0.6	8	3	5.2	40
Just Tamped/Undisturbed (Medium)	2.8	0.8	9.8	3.5	6.2	40
Trafficked (Strong)	4.0	1.0	13.3	4.8	6.7	40

Lateral ballast stiffness is considered to be 4000 kN per square metre; when the lateral resistance of the ballast is reduced to 800 kN per square metre the lateral displacements become large [128]. Field test results [129] give a lateral ballast resistance value of 95.2 kN per centimetre per sleeper spacing. The ballast lateral stiffness is considered to be $133 \times 10^6 N$ per square metre in a high frequency wheel-rail interaction model in both the vertical and lateral directions [130]. The units of these stiffness values are transformed into consistent values as shown in Table 4-16.

Table 4-16 Summary of ballast lateral stiffness in different studies

Original value in different units to uniformed unit $kN/mm/m$	
4000 $kN/m/m$	4
95.2 $N/cm/tie$	15.87
$133 \times 10^6 N/m/m$	133

It can be seen that the ballast lateral stiffness values varies by a large amount. The reason may be that the different studies have different track bed properties. It is difficult to find any research that studied or tested the ballast lateral stiffness and damping in detail. Another reason may be that the highly non-linear characteristic of the sleeper-ballast interface makes it difficult to obtain reliable test results. In this study, the interface between the sleeper and ballast is more important, therefore the sub-ballast and subgrade layers can be considered rigid supporting the ballast layer. Single Tie Push Tests (STPT) were carried out by Sussmann et al. [131] to investigate the lateral resistance of concrete sleepers, and the average peak lateral resistance range of a concrete tie was between 8.4kN to 16.1kN with strong condition within a displacement of 25mm. Figure 4-11 shows the load-displacement relationship of a concrete sleeper and the stiffness of the single tie can be estimated at around 4-8kN/mm.

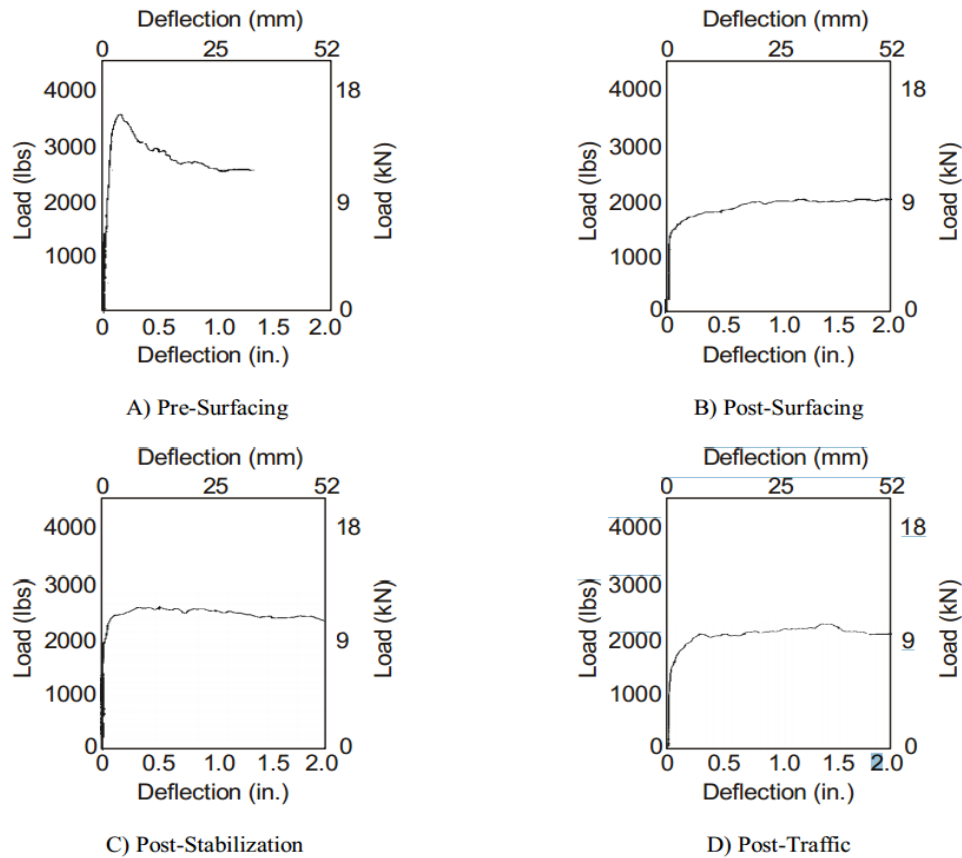


Figure 4-11 Characteristic of lateral resistance measurement

4.2.6 Friction coefficient

This is the friction coefficient defined by the ratio of sleeper lateral force resistance to vertical loading force. In most analyses the friction coefficient is taken at a constant value of around 0.8 for concrete sleepers. However, the friction value varies with the different vertical load Kish et al. [93] describe the change of friction coefficient with the dynamic vertical load in an analytical equation as shown below.

$$\mu = \mu_2 + (\mu_1 - \mu_2)e^{-\beta F_v} \quad \text{Equation 41}$$

Where,

F_v ...the vertical load

μ_1 ...the friction coefficient at zero vertical load

μ_2 ...the coefficient at large vertical load

β ...constant parameter

Table 4-17 shows the value of the constants in the friction coefficient equation for both wooden and concrete sleepers.

Table 4-17 Values of constants for wood and concrete sleepers [93]

	μ_1	μ_2	β (1/kN)
Concrete sleeper	0.9	0.75	0.71
Wooden sleeper	1.15	0.68	0.49

Figure 4-12 shows the resulting tie-ballast friction coefficient as a function of vertical sleeper force for both wooden and concrete.

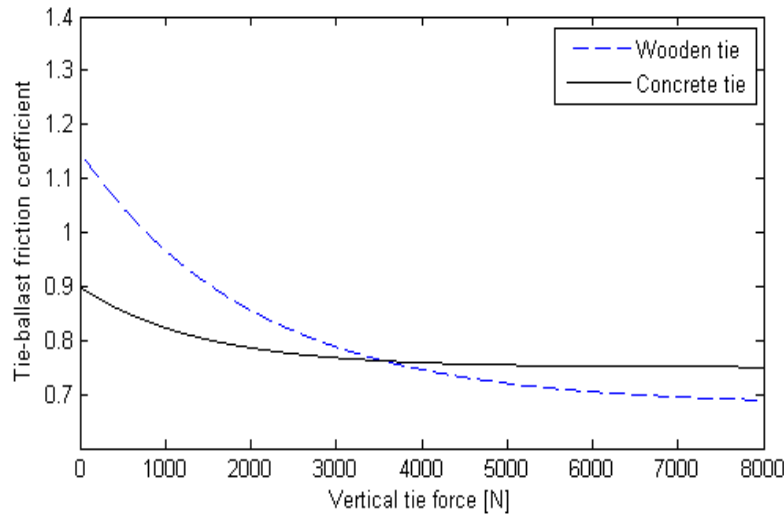


Figure 4-12 Friction coefficient varies with vertical force [93]

These ‘friction’ parameters are tested based on the sleeper-ballast interface, which includes the bending forces from the rails. In the track shift model, only the interface between an individual sleeper and the ballast is considered.

The lateral resistance tests indicate the friction coefficient to be around 0.5, while the friction between ballast particles is in the range of 0.9 to 1.4 [132] [133]. Meanwhile, other studies claim a friction coefficient between a concrete sleeper and ballast of roughly 0.1 [134] [135]. The lateral to vertical loading ratio which can be considered as the friction coefficient between sleeper base and ballast is found to be around 0.45 from lab tests in the University of Southampton [77]. The required lateral to vertical loading ratio tends to slightly reduce after the peak lateral resistance.

Therefore, the friction coefficient between the sleeper and ballast at zero and large vertical load can be estimated in proportion to the coefficient for sleepers. Table 4-18 shows the estimated friction coefficient for different sleeper-ballast contact conditions.

Table 4-18 Possible residual and friction coefficient values for simulation

	μ_r	μ_s
μ_1	0.01	0.45
μ_2	0.0083	0.3735
β (1/kN)	0.71	0.71

The coefficient is selected as 0.01 for residual deflection simulations, while a bigger friction coefficient of 0.45 will be used to determine sliding failure. In addition, the values of μ_1 and μ_2 should decrease with the number of load passes due to the ballast shear and wear under the cyclic sleeper movements. The percentage reduction in these constants is calculated to be 0.05% per pass or 5% for 100 passes.

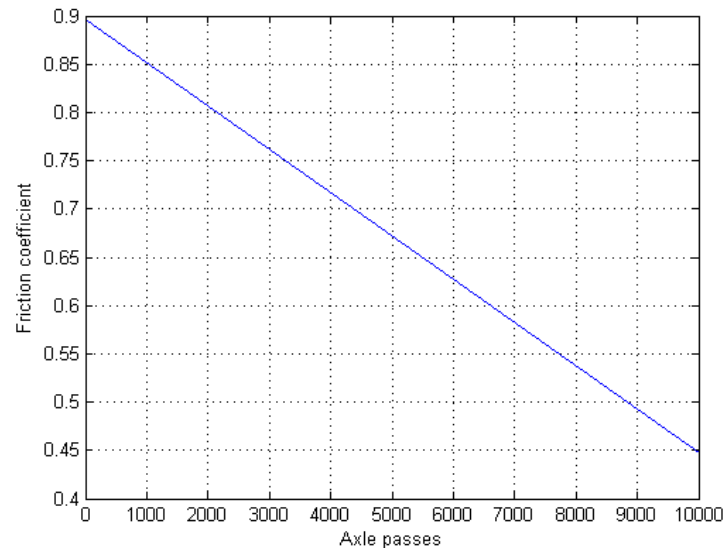


Figure 4-13 Friction coefficient reduction over loading passes

However, according to the traffic mix given in Chapter 4.4.2 there will be more than 10000 axle passes within a month and a large number of maintenance activities taking place on an operational railway line such as the WCML, and this linear reduction will not be valid. In order to include the friction reduction, and at the same time make it easier in the simulation, a 5% reduction of friction coefficient per 20000 axle passes is used to estimate the real situation.

4.2.7 Conclusion

It was found that the track component stiffness and damping are mainly measured and investigated in the vertical direction. The references for lateral track behaviour and parameters are limited due to its complicated interface and the highly nonlinear dynamic behaviour. It is straightforward to find the parameters for rails, rail fasteners, pads and sleepers, because enough information is available from industry suppliers. The stiffness and damping values of the sleeper-ballast interface is more difficult, due to lack of dynamic behaviour information of the track bed. Test results and measurements are required to study and compare the parameters of sleeper-ballast interface in detail. The additional sleeper-ballast interface parameters, including the lateral resistance characteristics and friction coefficient, are also studied in order to have a better understanding of the non-linear characteristic of this interface.

4.3 Track lateral shift model

A Finite Element (FE) model was selected to investigate the non-linear lateral behaviour of the track. Although it is widely used in engineering, the drawback is that it can be time consuming to model a complete track system due to the large number of elements and degrees of freedom required [76]. Track lateral settlement is caused by multiple passages of vehicles that would take an extremely long time to calculate using FE modelling.

In the single sleeper lateral shift analysis, the bending behaviour of the sleeper is simplified to have a linear relationship with the rail deflection. This can lead to an inaccurate analysis result, thus it is necessary to model the rail bending for a certain length of the track. In the track lateral shift analysis, the nonlinear factors are inevitable consequently an FE model is best suited to describe the behaviour of the rail, sleepers and track bed.

Unlike the lateral shift model for a single sleeper, the rail is not supported continuously but by each sleeper. Therefore, the nodes are defined above every sleeper on the rail as shown in Figure 4-14. The rails are divided by the length of the sleeper distance to create the discrete rail elements. When there are N nodes on the rail, there will be N sleepers and $N-1$ rail elements. For the lateral model only the track behaviour in the lateral direction is considered, so every rail node has 2 DOF which means that the total rail DOF is $2N$.

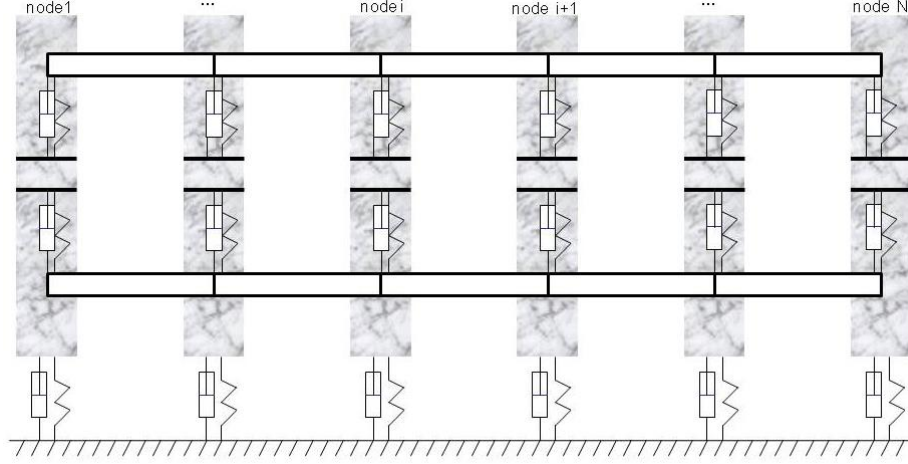


Figure 4-14 FE track model

The equations of motion of the track lateral shift model are defined in Equation 42 based on the principle of total potential energy of a dynamic system [136].

$$[M]\{\ddot{q}\} + [C]\{\dot{q}\} + [K]\{q\} = \{F(t)\} \quad \text{Equation 42}$$

The formulation of the model is made in two steps. After the FE rail model is built, the MBS model of the discrete sleeper and continuous track bed support will be added into the model.

4.3.1 FE rail model

Assuming on the i^{th} rail element, moment M_i , M_{i+1} and lateral forces F_i , F_{i+1} are applied respectively on node i and $i+1$, as shown in Figure 4-15. The rail element displacement vector is:

$$\{u_i\}^e = \begin{Bmatrix} \{u_1\}^e \\ \{u_2\}^e \end{Bmatrix} = \begin{Bmatrix} u_i \\ \theta_i \\ u_{i+1} \\ \theta_{i+1} \end{Bmatrix} \quad \text{Equation 43}$$

Where,

u_i , u_{i+1} ... the displacement of each node

θ_i , θ_{i+1} ... the roll angle of each node

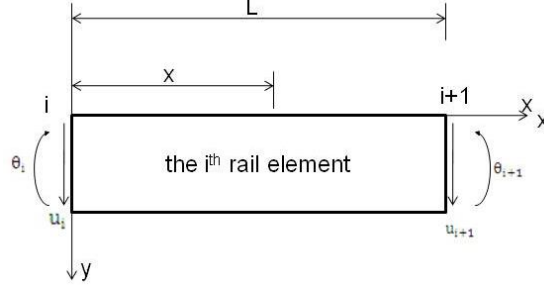


Figure 4-15 Rail element load and displacement condition

There are several different methods used to obtain the stiffness matrix of the rail element: Hermite interpolation[137], direct stiffness method and principle of virtual work [138]. The Hermite interpolation method is selected in this study due to its convenience in finding out the complete mass, damping and stiffness matrix. Therefore, the displacement of the rail element on any point is:

$$u_{ri}(x) = [N]\{u_i\}^e \quad \text{Equation 44}$$

In which,

$$[N] = [N_1, N_2, N_3, N_4] \quad \text{Equation 45}$$

Where,

$$\begin{cases} N_1 = 1 - 3\left(\frac{x}{L}\right)^2 + 2\left(\frac{x}{L}\right)^3 \\ N_2 = x\left[1 - 2\left(\frac{x}{L}\right) + 2\left(\frac{x}{L}\right)^2\right] \\ N_3 = \left(\frac{x}{L}\right)^2\left(3 - 2\frac{x}{L}\right) \\ N_4 = x\left[\left(\frac{x}{L}\right)^2 - \frac{x}{L}\right] \end{cases} \quad \text{Equation 46}$$

The vibration kinetic energy and bending strain energy of the rail element are respectively:

$$T_i = \frac{1}{2} \int_0^L m_r \dot{u}_i^2(x) dx = \frac{1}{2} \{\dot{u}_i\}^e T \left[\int_0^L m_r [N]^T [N] dx \right] \{\dot{u}_i\}^e \quad \text{Equation 47}$$

$$\begin{aligned} U_i &= \frac{1}{2} \int_0^L EI \left(\frac{d^2 u_i(x)}{dx^2} \right)^2 dx \\ &= \frac{1}{2} \{u_i\}^e T \left[\int_0^L EI \left(\frac{d^2 N}{dx^2} \right)^T \left(\frac{d^2 N}{dx^2} \right) dx \right] \{u_i\}^e \end{aligned} \quad \text{Equation 48}$$

Substituting Equation 46 into Equation 47 and integrating, the mass matrix of the rail element is established as:

$$[m] = \frac{m_r L}{420} \begin{bmatrix} 156 & 22L & 54L & -13L \\ 22L & 4L^2 & 13L & -3L^2 \\ 54L & 13L & 156 & -22L \\ -13L & -3L^2 & -22L & 4L^2 \end{bmatrix} \quad \text{Equation 49}$$

Substituting Equation 46 into Equation 48 and integrating, the stiffness matrix of the rail element is:

$$[k] = \frac{EI}{L^3} \begin{bmatrix} 12 & 6L & -12 & 6L \\ 6L & 4L^2 & -6L & 2L^2 \\ -12 & -6L & 12 & -6L \\ 6L & 2L^2 & -6L & 4L^2 \end{bmatrix} \quad \text{Equation 50}$$

Assuming there is a concentrated load $P(t)$ on $x=l$, then the virtual work done by the force is:

$$\delta W_i = P\delta u_i(l) = P\{\delta u_i\}^e T [N]_{x=l} \quad \text{Equation 51}$$

So, the force on the element is expressed as

$$\begin{aligned} \{F_i\}^e &= [F_i \quad M_i \quad F_{i+1} \quad M_{i+1}] = P[N]_x^T \\ &= [PN_1 \quad PN_2 \quad PN_3 \quad PN_4]_{x=l}^T \end{aligned} \quad \text{Equation 52}$$

4.3.2 Track lateral model development

According to the track lateral model shown in Figure 4-14, the unknown lateral displacement vector and the input force matrix of the two rails nodes and the sleepers are written as:

$$\{F\} = \begin{bmatrix} F_{11} \\ M_{11} \\ F_{12} \\ M_{12} \\ \vdots \\ F_{1N} \\ M_{1N} \\ F_{21} \\ M_{21} \\ F_{22} \\ M_{22} \\ \vdots \\ F_{2N} \\ M_{2N} \\ F_{s1} \\ F_{s2} \\ \vdots \\ F_{sN} \end{bmatrix} \quad \{u\} = \begin{bmatrix} u_{11} \\ \theta_{11} \\ u_{12} \\ \theta_{12} \\ \vdots \\ u_{1N} \\ \theta_{1N} \\ u_{21} \\ \theta_{21} \\ u_{22} \\ \theta_{22} \\ \vdots \\ u_{2N} \\ \theta_{2N} \\ u_{s1} \\ u_{s2} \\ \vdots \\ u_{sN} \end{bmatrix} \quad \text{Equation 53}$$

The same principle and method are used to build the complete track lateral shift model with N sleepers. The vibration kinetic energy, bending strain energy and the virtual work of the whole track system can be written as:

$$T = \frac{1}{2} \sum_{i=1}^{N-1} \{\dot{u}_{1i}\}^e T [m]^e \{\dot{u}_{1i}\}^e + \frac{1}{2} \sum_{i=1}^{N-1} \{\dot{u}_{2i}\}^e T [m]^e \{\dot{u}_{2i}\}^e$$

$$+ \frac{1}{2} \sum_{i=1}^N m_s \dot{u}_{si}^2$$
Equation 54

$$U = \frac{1}{2} \sum_{i=1}^{N-1} \{u_{1i}\}^e T [k]^e \{u_{1i}\}^e + \frac{1}{2} \sum_{i=1}^{N-1} \{u_{2i}\}^e T [k]^e \{u_{2i}\}^e$$

$$+ \frac{1}{2} k_r \sum_{i=1}^N (u_{1i} - u_{si})^2 + \frac{1}{2} k_r \sum_{i=1}^N (u_{2i} - u_{si})^2$$

$$+ \frac{1}{2} k_s \sum_{i=1}^N u_{si}^2$$
Equation 55

$$\delta W = c_r \sum_{i=1}^N (2\dot{u}_{si} - \dot{u}_{1i} - \dot{u}_{2i})(2\delta u_{si} - \delta u_{1i} - \delta u_{2i})$$

$$+ c_s \sum_{i=1}^N \dot{u}_{si} \delta u_{si} + F_1(t) \{\delta u_{1i}\} [N]_{x=1}$$
Equation 56

The mass and stiffness matrix of the whole track lateral system can be found from the first variation of Equation 54 and Equation 55, and the damping stiffness matrix can be found from Equation 56 (Appendix C.1). Subsequently, a numerical computer simulation model based on Equation 42 can be built using MATLAB. The Wilson- θ numerical integration is chosen to solve Equation 42. When $\theta > 1.37$, the Wilson- θ method will be unconditionally stable. In the simulation, θ is taken as 1.4 to ensure the accuracy of the numerical calculation. Taking each sleeper spacing on the rail as an element, there are 31 sleepers, which means 31 nodes on each of the rails and 155 DOF in total. The track irregularity profile from the ECML, therefore the 60E1 track fastening is used. The track properties are described in Table 4-19.

Table 4-19 Selected track parameters for linear simulation

	Symbol	Units	Value
Young modulus	E	N/m ²	2.108×10^{11}
Section mass of CEN60 rail	m_r	kg	60
G44 concrete sleeper mass	m_s	kg	308
Sleeper spacing	s	m	0.6
Section moment of area about vertical axis	I_{yy}	m ⁴	5.123×10^{-6}
Section moment of area about horizontal axis	I_{zz}	m ⁴	3.038×10^{-5}
Rail pad lateral stiffness	k_{ry}	N/m	3.98×10^7
Rail pad lateral damping	c_{ry}	N · s/m	3×10^4
Rail pad vertical stiffness	k_{rz}	N/m	6.3×10^7
Rail pad vertical damping	c_{rz}	N · s/m	4×10^4
Sleeper-ballast lateral stiffness	k_{sy}	N/m	4×10^7
Sleeper-ballast lateral damping	c_{sy}	N · s/m	2.5×10^4
Sleeper-ballast vertical stiffness	k_{sz}	N/m	9×10^7
Sleeper-ballast vertical damping	c_{sz}	N · s/m	8×10^4
Young modulus	E	N/m ²	2.108×10^{11}

When there are similar 30 kN loads on both rails, moving from the first node to the last at a speed of 33.35 m/s. The simulation gives a result of the centre rail node movement, shown in Figure 4-16.

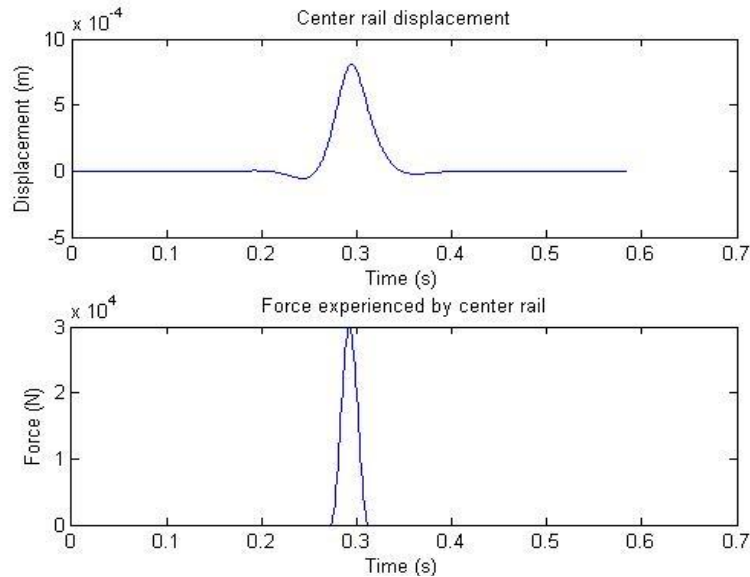


Figure 4-16 Centre rail node displacement and input vertical forces

The simulation results were found to be reasonable, and the shape of the rail deflection graph is quite similar to the BOEF static force output. However, the dynamic response can be different, and VAMPIRE is used to generate the dynamic lateral force input on the track. Figure 4-17 shows the centre rail node dynamic response when a four-axle vehicle runs along the track at 33.5m/s. The input force matrix is captured from the VAMPIRE simulation of a Class 365 EMU using measured ECML track data. The recorded site data has some small lateral irregularities, which cause the vibration of the vehicle-track system.

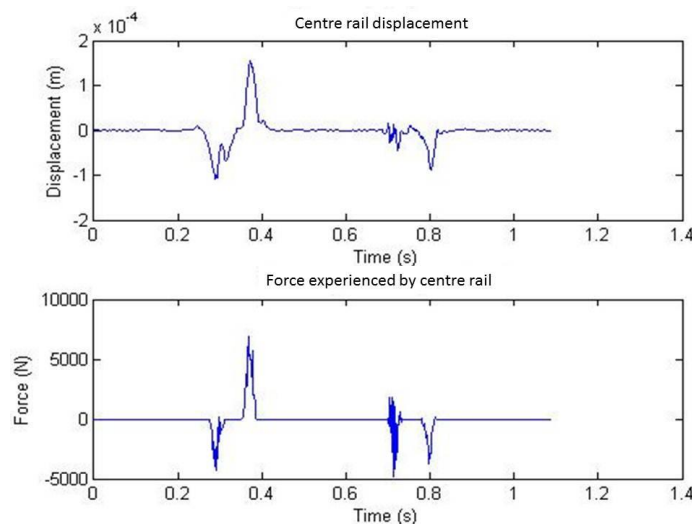


Figure 4-17 Dynamic response of the centre of rail and lateral force input from VAMPIRE

It is found that the dynamic lateral force is small, between 4 and 10 kN, thus it is difficult to reach the lateral to vertical load ratio failure point which is the triggering limit of the track lateral sliding according to the laboratory test results by the University of Southampton [77]. Normal track lateral irregularities do not excite the vehicle sufficiently to produce enough lateral force to move the sleeper laterally. Therefore, large irregularities of the track are required for ballast rearrangement and track lateral sliding.

The peak lateral displacements are important in determining if the failure point is reached. The previous simulation was conducted with only 2 nodes on each element, which means that only the sleeper and rail contact point is considered, and the rail bending is simplified. Therefore, the elements with 2 to 7 nodes are simulated, and the result is shown in Figure 4-18. It is clear that the more nodes that are considered, the more accurate the results. However, more nodes lead to longer calculation times. When the number of nodes on the element is more than 4, the peak displacements are quite similar.

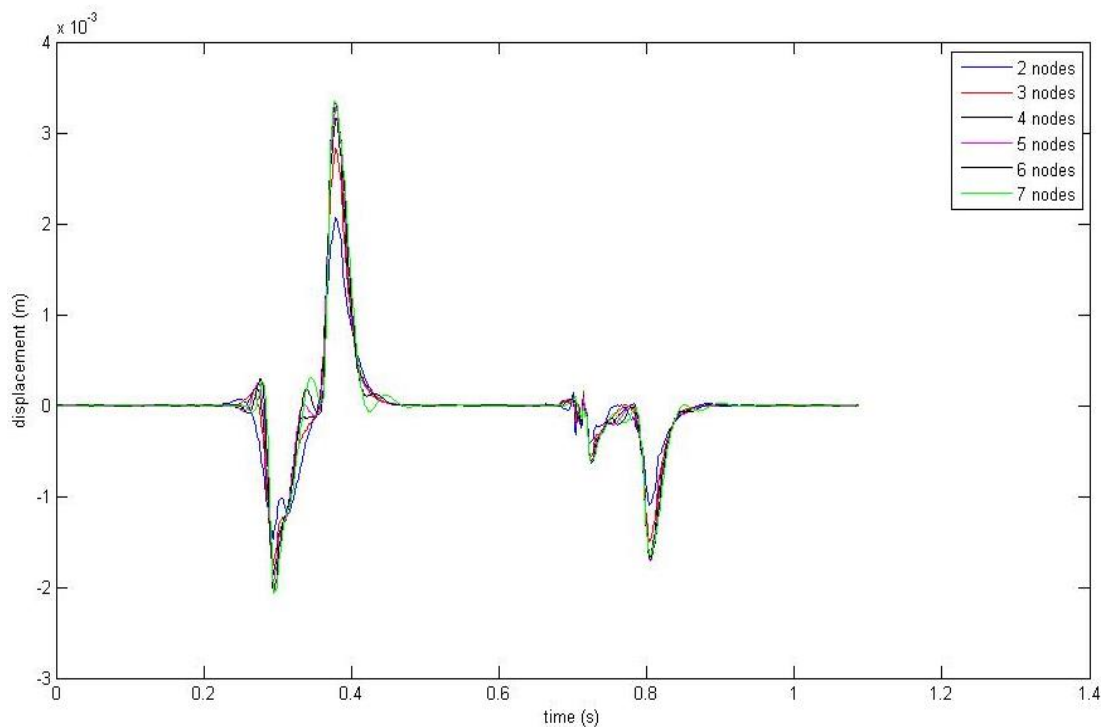


Figure 4-18 Simulation results with different number of nodes

However, more nodes lead to exponential increase in calculation time, as shown in Table 4-20. Considering the calculation speed, 4 nodes between adjacent sleepers are selected to give a good balance between accuracy and calculation time.

Table 4-20 Simulation time for a 30 m section of track

Num. of nodes between adjacent sleepers	2	3	4	5	6	7
Simulation time [min]	0.83	2.5	7.8	19.3	39.7	70.5

4.3.3 Define the non-linear load-deflection relationship

The lateral track model is a linear FE model which can only describe the track system vibration behaviour. However in reality, the track lateral position may not be restored after vehicle passages due to the residual and frictional characteristics of the sleeper-ballast interface, so the failure of this interface, which causes sliding is not detected. Kish et al. [93] claimed that both the theory and the test data indicate that the residual deflection has an exponential growth at first, and then tends to increase in an almost linear manner after some initial passes, furthermore, the growth of residual deflection w_r is also found to be related to lateral to vertical loading ratio L/V , as shown in Figure 4-19.

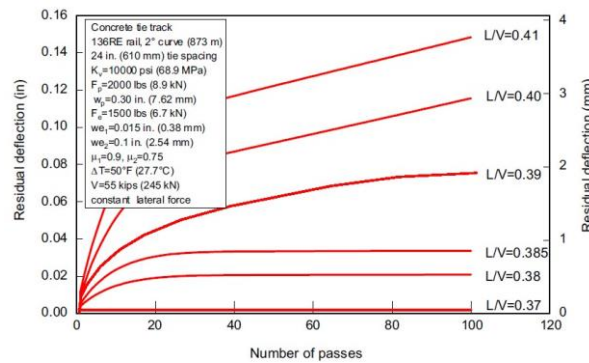


Figure 4-19 Residual deflection of sleepers versus number of passes

However, in reality the L/V ratio is not a constant value. It changes with different dynamic vertical and lateral loads, so in the vehicle-track dynamic simulation process the L/V ratio needs to be calculated at each time step in order to determine the residual or sliding deflection.

As over 30 years of research and tests have confirmed, lateral resistance is a load versus deflection nonlinear spring response as illustrated in Figure 4-20, which also includes a simplified analytic representation [139]. It can be found that the lateral displacement under peak resistance varies with different track conditions, and the non-linear characteristic is more force sensitive compared to the displacements. The softened lateral stiffness is also not a constant value, according to the figure it is a stiffness value close to the elastic lateral stiffness.

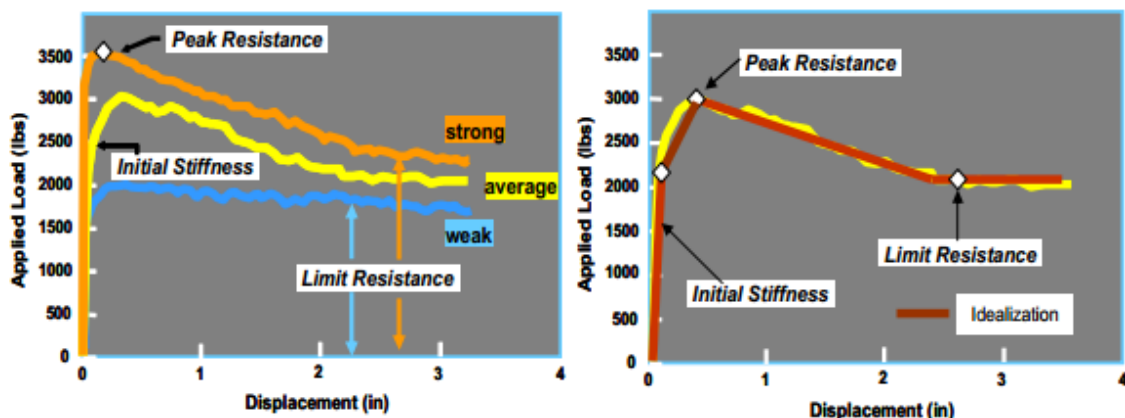
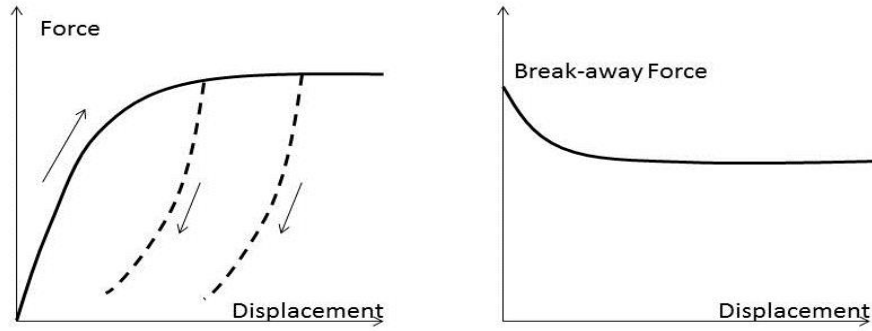


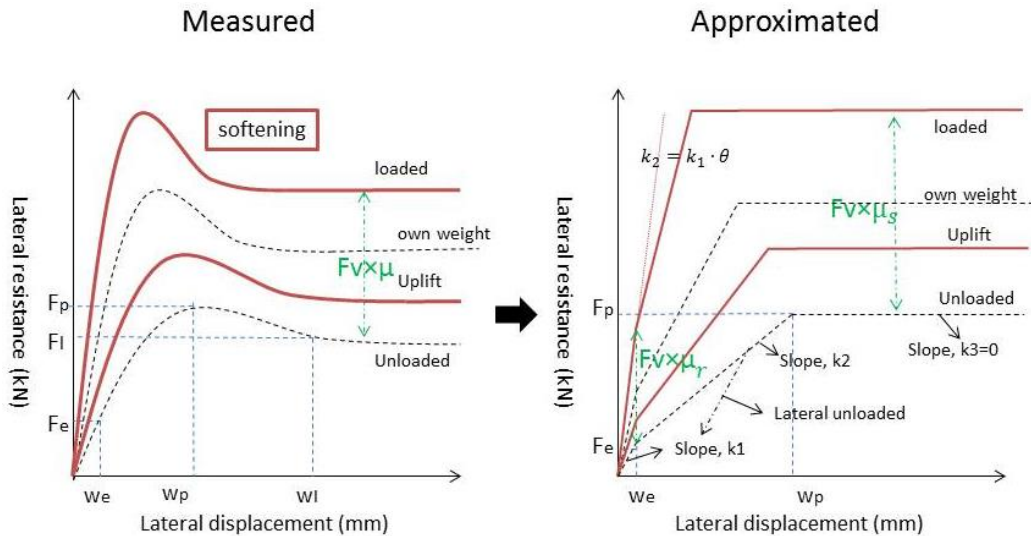
Figure 4-20 Lateral resistance load deflection characteristics

The sleeper stick-slip motion can be classified as an elastic displacement, residual deflection known as pre-sliding displacement and sliding which is a lateral resistance failure. Before sliding occurs, there is a linear and non-linear spring-like behaviour which is also known as hysteresis and the force as function of displacement is shown in Figure 4-21 a). The hysteresis was observed as the velocity varies, and the size of the loop increases with normal load, viscosity and frequency of the velocity variation. When the displacement is small and is almost recovered after loading, the behaviour can be seen as elastic.



a) Pre-sliding displacement [140] b) Break-away and sliding [141]
Figure 4-21 Force-displacement relationship in pre-sliding and sliding

A non-linear relationship exists between the lateral resistance and vertical loading, which influences the residual deflection, ballast softening and track lateral sliding. The non-linear lateral resistance characteristic is shown in Figure 4-22 (a), which was determined from experimental programmes by BR Research [125], DB [142], and TU Delft [143]. The simplified non-linear characteristic illustrated in Figure 4-22 (b) is employed in the actual track model in order to make the calculation process easier.



a) Track lateral resistance behaviour in reality b) Modified force-displacement function
Figure 4-22 Track lateral resistance characteristic

The softening part of the non-linear characteristic is simplified to sliding behaviour in the model as shown in the figure. In both figures, the dashed black line represents the lateral resistance without vertical loading on the track, while the dynamic case with vehicle loading on the track is shown as the red line. The influence factors are described below:

- F_e and w_e represent the elastic breaking force and displacement, these elastic limit values are only related to the sleeper-ballast interface without the influences from the rails. Thus the value of F_e and w_e are smaller and proved around 5% of the measured sleeper elastic limit forces and displacements during the model development and validation.
- F_p and w_p are respectively the break-away resistance and displacement, which are the force and displacement required to overcome the static friction and initiate motion [144]. They can be seen as the starting point when the sleeper slides laterally on the ballast bed, which is a serious failure mode. Whenever the forces exceed this limit, the model stops running and provides a warning.
- θ is the residual deflection stiffness softening factor, the softening factor has a 0.15% linear reduction for 20000 axle passages. It is found that 0.998 to 0.999 are reasonable softening factors in the model development process in the test simulations.
- F_v is the vertical force distributed from the rails onto the sleeper.
- Even small forces can cause residual deflections and it is not therefore sensible to use the actual coefficient between the sleeper and ballast in the residual deflection calculation. For example, the lateral forces are usually less than 5 kN on straight track, and using the actual friction coefficient which gives a dynamic elastic limit force of more than 10kN which will not capture any small accumulated residual deflection after a number of wheel passes. Therefore, a much smaller coefficient is defined and used in the model for residual deflection calculation. μ_r is the residual coefficient between the sleeper and ballast to determine the residual deflection, and μ_s is the actual friction coefficient between the sleeper and ballast, here μ_r is around 2-3% of μ_s . A 5% linear reduction of both residual and friction coefficient per 20000 axle passes is used in this simulation.

It is important to note that when a vehicle runs on the track, the lateral resistance will be weaker on the dynamic uplift sections as shown in Figure 4-23.

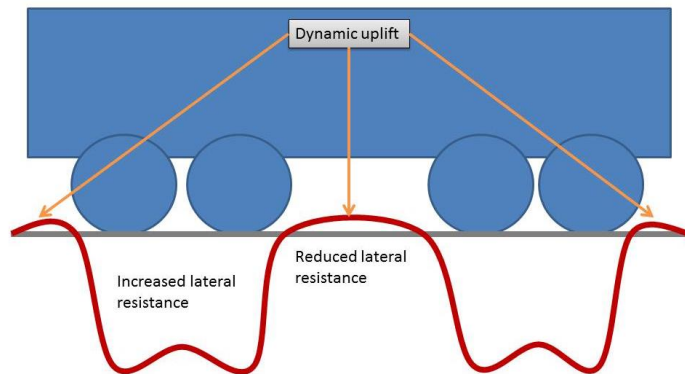


Figure 4-23 Dynamic lateral resistance influenced by vertical load

The lateral and vertical loads distributed onto each sleeper are used to determine the sleeper residual or sliding deflections. These distributed forces are the interaction forces between the rails and sleeper, which can be described in Equation 57.

$$F = (u_1 + u_2 - 2 \cdot u_s) \cdot k_r + (v_1 + v_2 - 2 \cdot v_s) \cdot c_r \quad \text{Equation 57}$$

Where,

u_1, u_2 and u_s ... rails and sleeper displacements

k_r ... stiffness between rails and sleeper

v_1, v_2 and v_s ... rails and sleeper velocities

c_r ... damping between rails and sleeper

After the vertical and lateral distributed loads are captured from the elastic track model, the sleeper residual and sliding deflection modes can be determined. The method for including pre-sliding and sliding characteristics into the model is discussed below.

4.3.3.1 Pre-sliding dynamics

All the sleeper displacements will be fully recovered when the lateral force and displacements are smaller than F_e and w_e as shown in Equation 58.

$$F_L \leq F_e + \mu_r \cdot F_v \quad \text{Equation 58}$$

When the sleeper-ballast interface behaves elastically, the lateral stiffness between the sleeper and ballast k_{s1} in Figure 4-24 can be calculated from Equation 59.

$$k_{s1} = \frac{F_e + \mu_r \cdot F_v}{w_e} \quad \text{Equation 59}$$

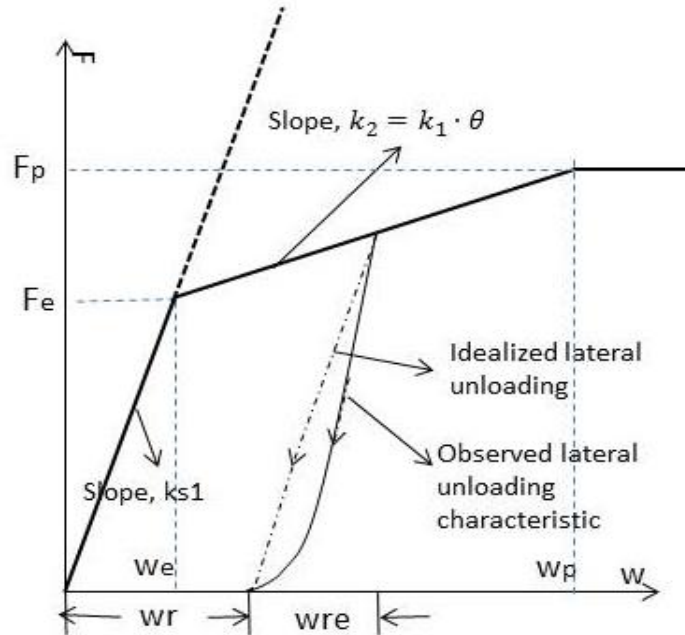


Figure 4-24 Definition of track lateral pre-sliding behaviour

When the lateral force is larger than the elastic limit force and smaller than the break-away force (Equation 60), there will be a permanent residual deflection which is represented by w_r in Figure 4-24. It is important to note that the forces here are the forces that only related to the stiffness term in the dynamic system. There are other parts of the total force related to damping and acceleration.

$$F_e + \mu_r \cdot F_v < F_L < F_p + \mu_s \cdot F_v \quad \text{Equation 60}$$

There will be an elastic recovery of the displacement represented by w_{re} , and the stiffness between sleeper and ballast will be smaller, and can be calculated from Equation 59.

$$k_{s2} = \theta \cdot k_{s1} \quad \text{Equation 61}$$

Where,
 θ ...softening factor

The idealized lateral unloading is parallel to the elastic slope, which indicates an elastic recovery the same as the elastic deflection under the same force. The permanent lateral residual deflection can be calculated using Equation 62.

$$w_r = w - w_{re} = w_{ks2} - w_{ks1} \quad \text{Equation 62}$$

It can be found that the slope of the residual deflection has a large influence on the overall residual deflection thereby having a big effect on track lateral residual deflection.

4.3.3.2 Sliding dynamics

When the lateral force is bigger than the dynamic break-away force, shown in Equation 63, the sleeper will slide on the ballast layer.

$$F_L \geq F_p + \mu_s \cdot F_v \quad \text{Equation 63}$$

The sliding behaviour can be modelled according to an Iwan friction element [145] as shown in Figure 4-25.

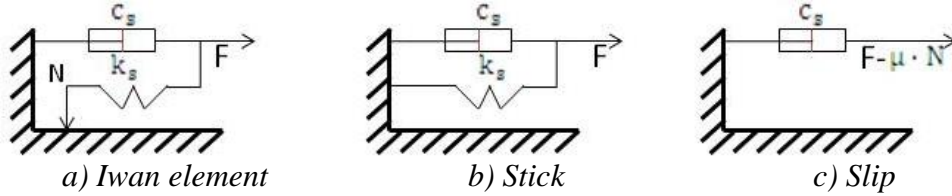


Figure 4-25 Iwan friction element

The spring-like behaviour does not exist in this failure motion, therefore the stiffness k_{s3} is considered as 0 without considering the track lateral softening. A large lateral to vertical loading ratio is required for sliding failure, which means a large defect of the track alignment. This defect may be caused by accumulated residual deflection from the dynamic interaction between the vehicle and track. Although the sliding failure is included in the model, this study mainly focus on the residual deflection component.

4.3.4 Track parameters determination

As described in section 4.3.2, there are 4 nodes on the rail between adjacent sleepers, which means that there are 3 rail elements between two sleepers. Therefore, the 60 m track section was modelled with 702 nodes, and at 4 DOF for each rail node and 2 DOF for each sleeper, there are 2605 DOF in total. All of the track parameters are shown in Table 4-21.

Table 4-21 Track parameters

	Symbol	Units	Value
Young modulus	E	N/m ²	2.108×10^{11}
Section mass of CEN60 rail	m_r	kg	60
G44 concrete sleeper mass	m_s	kg	308
Sleeper spacing	s	m	0.6
Section moment of area about vertical axis	I_{yy}	m ⁴	5.123×10^{-6}
Section moment of area about horizontal axis	I_{zz}	m ⁴	3.038×10^{-5}
Rail pad lateral stiffness	k_{ry}	N/m	3.98×10^7
Rail pad lateral damping	c_{ry}	N · s/m	3×10^4
Rail pad vertical stiffness	k_{rz}	N/m	6.3×10^7
Rail pad vertical damping	c_{rz}	N · s/m	4×10^4
Sleeper-ballast lateral stiffness	k_{sy}	N/m	4×10^7
Sleeper-ballast lateral damping	c_{sy}	N · s/m	2.5×10^4
Sleeper-ballast vertical stiffness	k_{sz}	N/m	9×10^7
Sleeper-ballast vertical damping	c_{sz}	N · s/m	8×10^4
Elastic breaking displacement for weak track	w_e	m	0.03×10^{-3}
Elastic breaking force for weak track	F_e	N	0.12×10^3
Peak resistance force	F_p	N	8×10^3
Residual deflection coefficient	μ_r	-	0.01
Friction coefficient	μ_s	-	0.4
Softening factor	θ	-	0.9986

Three sets of track sections are chosen from Table 3-17 in Chapter 3.3.3, to be used in the following track deterioration analysis and fractal analysis. In the track FE model, it takes at least 16 elements of the beam to get a result with relatively small impact factors [146], however 30 to 60 m long track is added into the model to get a stable result because the sleeper-ballast stiffness is not a constant number, but changes under different vertical load. The simulation time varies slightly depending on vehicle speed and calculation time step but it takes about 40 minutes for each vehicle to run along the track.

Figure 4-26 shows the results of a single sleeper during a simulation. The upper figure shows the distributed lateral forces and the dynamic elastic breaking force. Residual deflection will occur whenever the distributed lateral force exceeds the dynamic elastic breaking force. The lower figure is the resulting residual deflection created by each time step, represented by the blue line and the final accumulated residual deflection after one vehicle pass, represented by the black line. At the n th time step, if the resulting residual deflection is $w(n)$, the accumulated residual deflection of this sleeper is $\sum_{i=1}^n w(i)$.

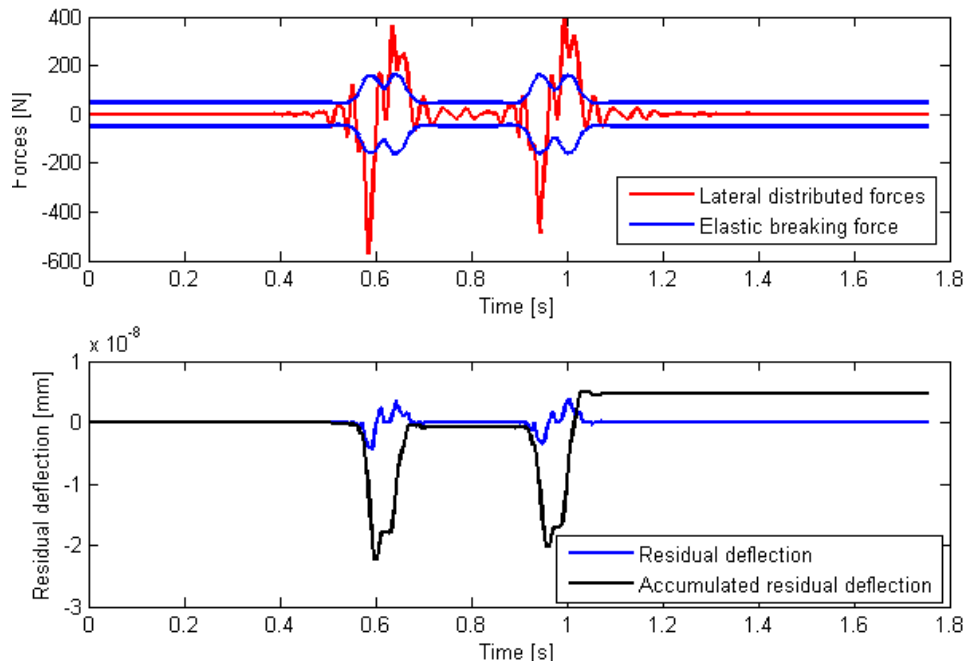


Figure 4-26 Single sleeper simulation result

4.3.5 Conclusion

The number of nodes between adjacent sleepers has a big impact on the rail dynamics. Therefore, the node number is selected as 4 in the following simulation so that the computation time is low. The rail-sleeper interface is expressed using linear stiffness and damping elements, whereas the sleeper-ballast interface contains a non-linear characteristic. This non-linear characteristic includes elastic lateral behaviour, pre-sliding behaviour and sliding failure.

4.4 Overall track lateral model and validation

VAMPIRE® and the track lateral FE model are coupled together to develop the final vehicle-track dynamic model. The scheme of the complete model is shown in Figure 4-27.

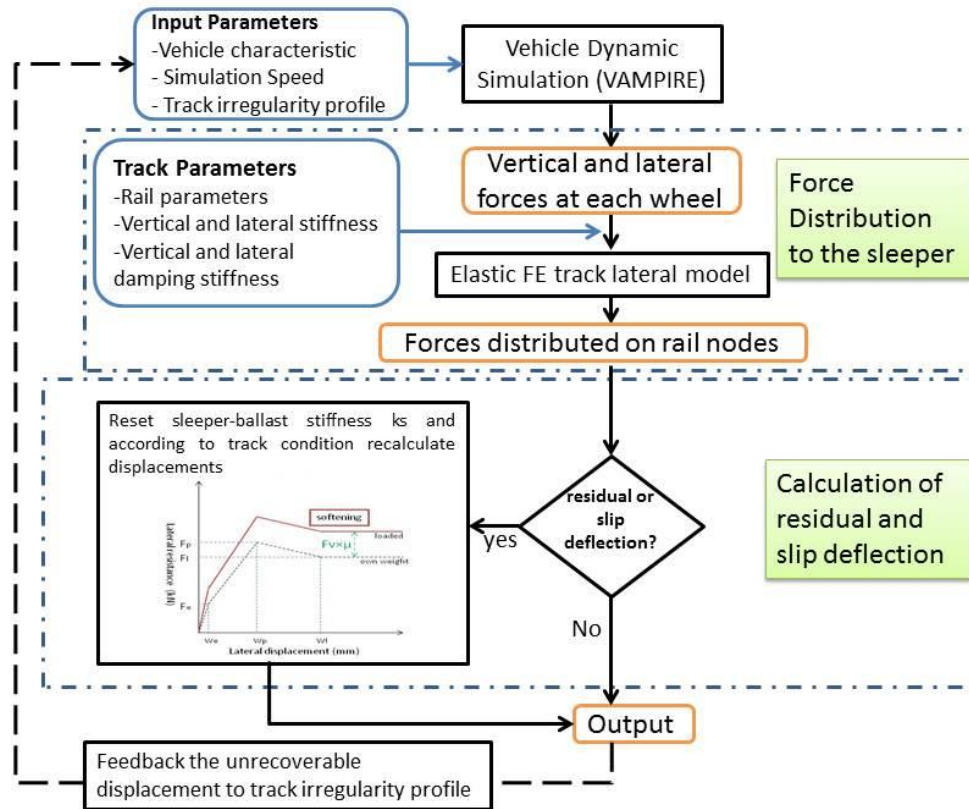


Figure 4-27 Scheme of vehicle-track dynamic model

The selected 120m track sections from the WCML in Table 3-17 are used for the simulation and model validation. The vehicle dynamics and track lateral deterioration will be simulated according to the actual condition of those track sections as much as possible.

4.4.1 Assumptions

Some assumptions have been made for the vehicle-track dynamic model:

- The ground under the ballast layer is assumed rigid.
- The track bed stiffness is assumed to be constant, although it is usually uneven in reality.
- The sleeper points of the measured data and the track are assumed synchronised with the track model.
- The traffic on the track section is assumed to be uniformly distributed over a 13×4 week period in a year.
- The influence of temperature of this section of track is ignored, as are the longitudinal traction and breaking forces.
- The residual deflection accumulated is assumed to grow linearly within a maximum of one month of traffic.
- The vehicles which make up a small proportion of the total traffic mix are neglected.

- The track irregularity file is not absolute, but filtered at 70m for both vertical and lateral irregularity data.
- The residual and slipping deflections from each sleeper are interpolated using splines and distributed on to the rails with all the high frequency changes filtered out.
- Only tamping and stone blowing maintenance activities are considered and are evenly distributed over a 13 × 4 week period in a year.

4.4.2 Traffic mix

The detailed traffic data of this section of the WCML is shown in Appendix D.1 during a 13 × 4 week period in a year, and it is summarised to Table 4-22.

Table 4-22 Summarise of traffic information

Total wheelsets passages 135990		
Type of vehicle	Traffic percentage [%]	Total wheelsets pass
390 Motor	53.88	73272
390 Trailer	26.94	36636
221 Motor	6.02	8180
FEAB	3.14	4264
FSAO	3.11	4232
MKIII	1.09	1480
FTAI	0.77	1048
IPAV	0.75	1016
KFAF	0.64	876
MKII	0.38	520
Class 66 Locomotive	0.37	504

Assuming that the traffic is evenly distributed against time, the wheelset passages can be easily found for each type of vehicle between every measured track dataset, as shown in Table 4-23.

Table 4-23 Traffic scenario between measured track datasets

	Duration as a percentage in a period	390 Motor	390 Trailer	221 Motor	FEAB	FSAO	MKIII	FTAI	IPAV	KFAF	MKII	Class 66 Locomotive
14/04/2010		Wheelsets passages between two measured data sets										
09/06/2010	0.1538	11273	5636	1258	656	651	228	161	156	135	80	78
14/07/2010	0.0962	7045	3523	787	410	407	142	101	98	84	50	48
11/08/2010	0.0769	5636	2818	629	328	326	114	81	78	67	40	39
13/10/2010	0.1731	12682	6341	1416	738	732	256	181	176	152	90	87
08/12/2010	0.1538	11273	5636	1258	656	651	228	161	156	135	80	78
19/01/2011	0.1154	8454	4227	944	492	488	171	121	117	101	60	58
16/03/2011	0.1538	11273	5636	1258	656	651	228	161	156	135	80	78
18/05/2011	0.1731	12682	6341	1416	738	732	256	181	176	152	90	87
15/06/2011	0.0769	5636	2818	629	328	326	114	81	78	67	40	39
20/07/2011	0.0962	7045	3523	787	410	407	142	101	98	84	50	48
17/08/2011	0.0769	5636	2818	629	328	326	114	81	78	67	40	39
14/09/2011	0.0769	5636	2818	629	328	326	114	81	78	67	40	39

16/11/2011	0.1731	12682	6341	1416	738	732	256	181	176	152	90	87
18/01/2012	0.1731	12682	6341	1416	738	732	256	181	176	152	90	87
15/02/2012	0.0769	5636	2818	629	328	326	114	81	78	67	40	39
18/04/2012	0.1731	12682	6341	1416	738	732	256	181	176	152	90	87
18/07/2012	0.25	18318	9159	2045	1066	1058	370	262	254	219	130	126

It is important to be aware of the loading condition of the freight wagons in the simulation, which can lead to quite different results. The blue line in Figure 4-28 shows the distribution of the freight vehicle loading condition. As the freight traffic only makes up a small percentage of the overall traffic, the percentage of tare and laden vehicles can be approximated from this figure. Any axle load less than 13kN is considered as a tare wagon, while axle loads of more than 13kN are considered as laden wagons. Therefore, almost 41% of the traffic is tare and 59% of the traffic is laden.

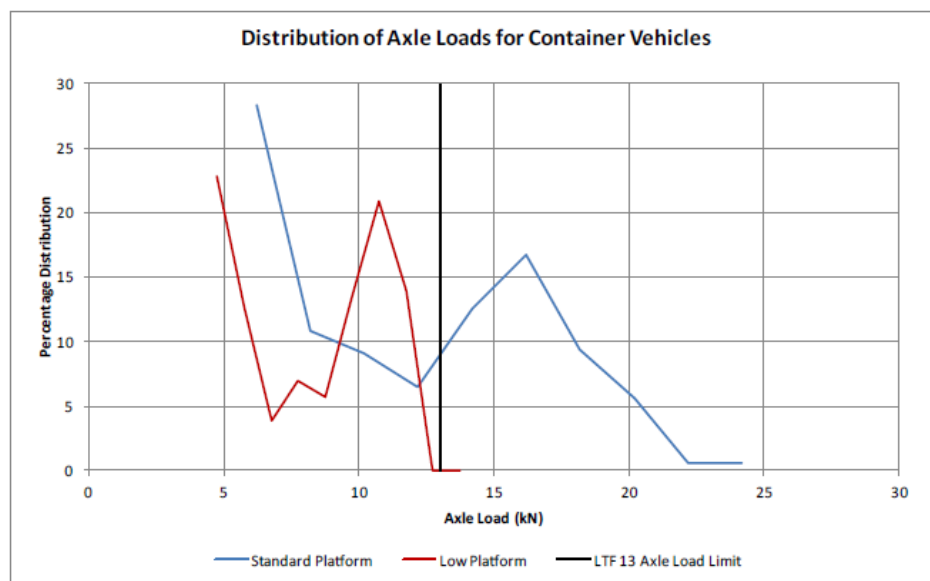


Figure 4-28 Distribution of freight vehicle loading condition [147]

According to Section 4.1.3, there will be 7 VAMPIRE® vehicle models to represent the majority of vehicles. The vehicle models and the corresponding wheelset passages are shown in Table 4-24.

Table 4-24 Traffic scenario for later simulation

		Class390	Class221	MKII & KIII	FEAB, FSAO, FTAI, KFAF laden	FEAB, FSAO, FTAI, KFAF tare	IPAV laden	IPAV tare
		Veh.1	Veh.2	Veh.3	Veh.4	Veh.5	Veh.6	Veh.7
D1	14/04/2010	Wheelsets passages between two measured data sets						
D2	09/06/2010	16909	1258	308	946	657	46	32
D3	14/07/2010	10568	787	192	591	411	29	20
D4	11/08/2010	8454	629	154	473	329	23	16
D5	13/10/2010	19023	1416	346	1064	739	52	36
D6	08/12/2010	16909	1258	308	946	657	46	32
D7	19/01/2011	12682	944	231	709	493	35	24

D8	16/03/2011	16909	1258	308	946	657	46	32
D9	18/05/2011	19023	1416	346	1064	739	52	36
D10	15/06/2011	8454	629	154	473	329	23	16
D11	20/07/2011	10568	787	192	591	411	29	20
D12	17/08/2011	8454	629	154	473	329	23	16
D13	14/09/2011	8454	629	154	473	329	23	16
D14	16/11/2011	19023	1416	346	1064	739	52	36
D15	18/01/2012	19023	1416	346	1064	739	52	36
D16	15/02/2012	8454	629	154	473	329	23	16
D17	18/04/2012	19023	1416	346	1064	739	52	36
D18	18/07/2012	27477	2045	500	1537	1068	75	52

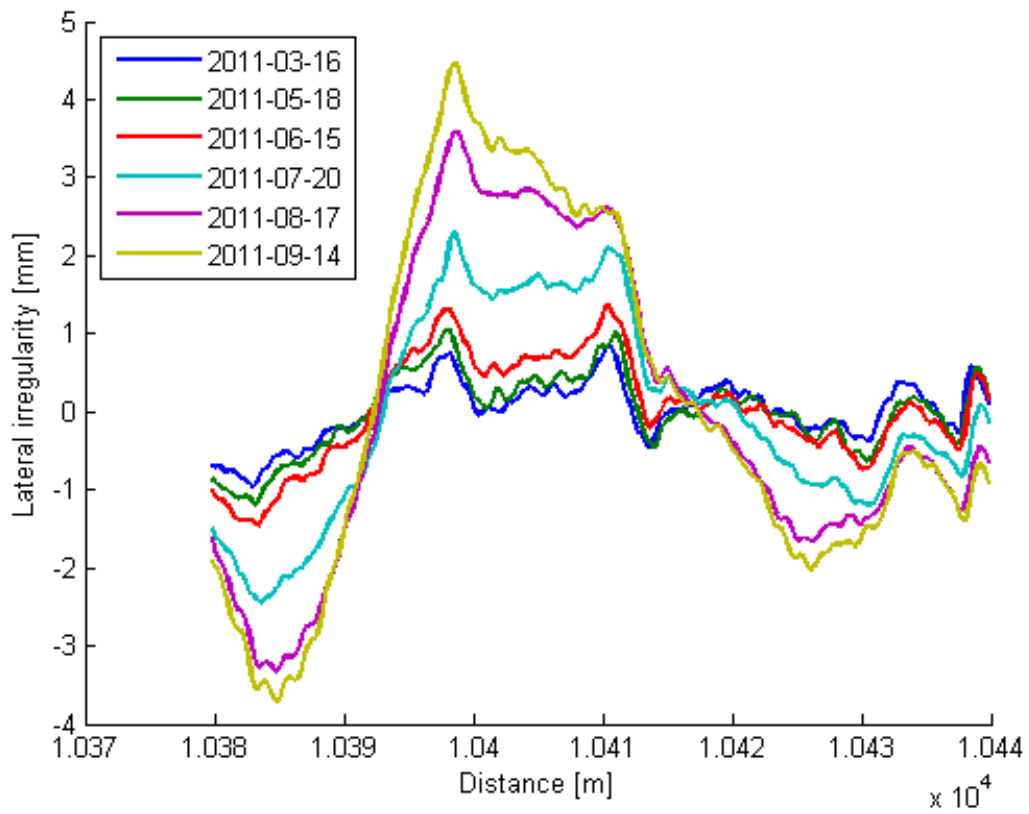
4.5 Model validation

Four 60 m sections of track are used in the validations which are S10, S15, S16 and S17 from Table 3-10. The measured and predicted track lateral irregularities were compared, as well as the measured and calculated track lateral deterioration.

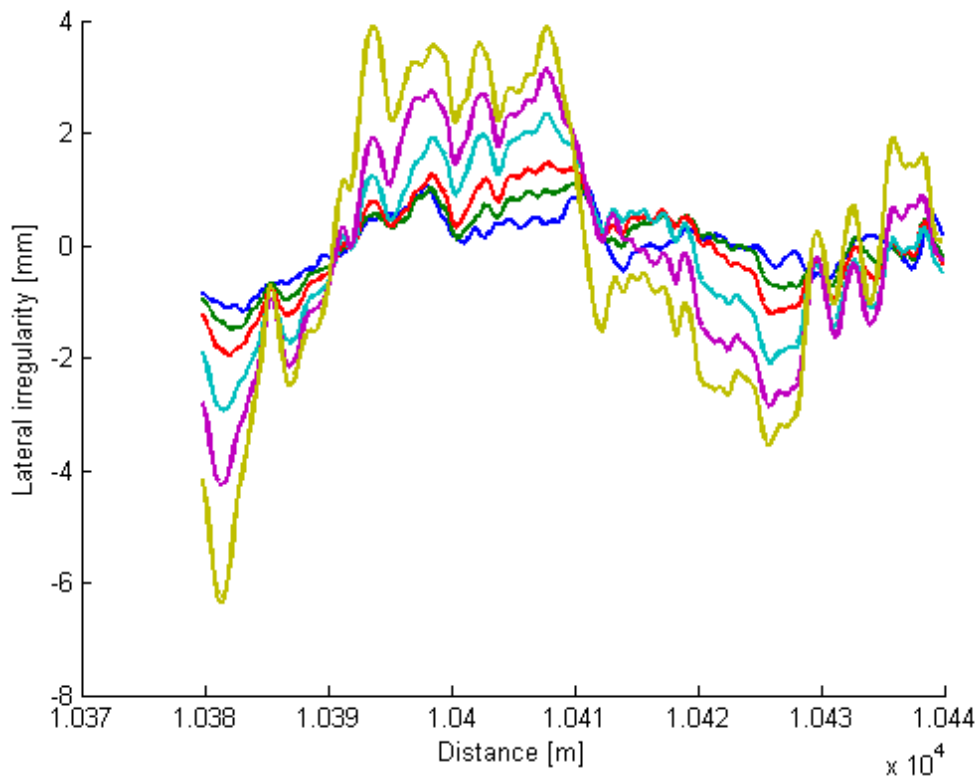
- S15 results

Figure 4-29 a) and b) are respectively the measured and predicted track lateral irregularities. The result indicates a good match between actual measurements and prediction of track deterioration.

Figure 4-30 a) shows the comparison between measured and predicted lateral deterioration, which is the difference between two measured track lateral irregularities. Figure 4-30 b) illustrates the SD value of this section of track, as well as the RMS and correlation coefficient values of the measured and predicted lateral deterioration. The RMS value indicates the magnitude of the difference between measured and predicted lateral deterioration, therefore, the larger the RMS value is the less accurate the prediction. The correlation coefficient measures the linear correlation between the measured and predicted deterioration.

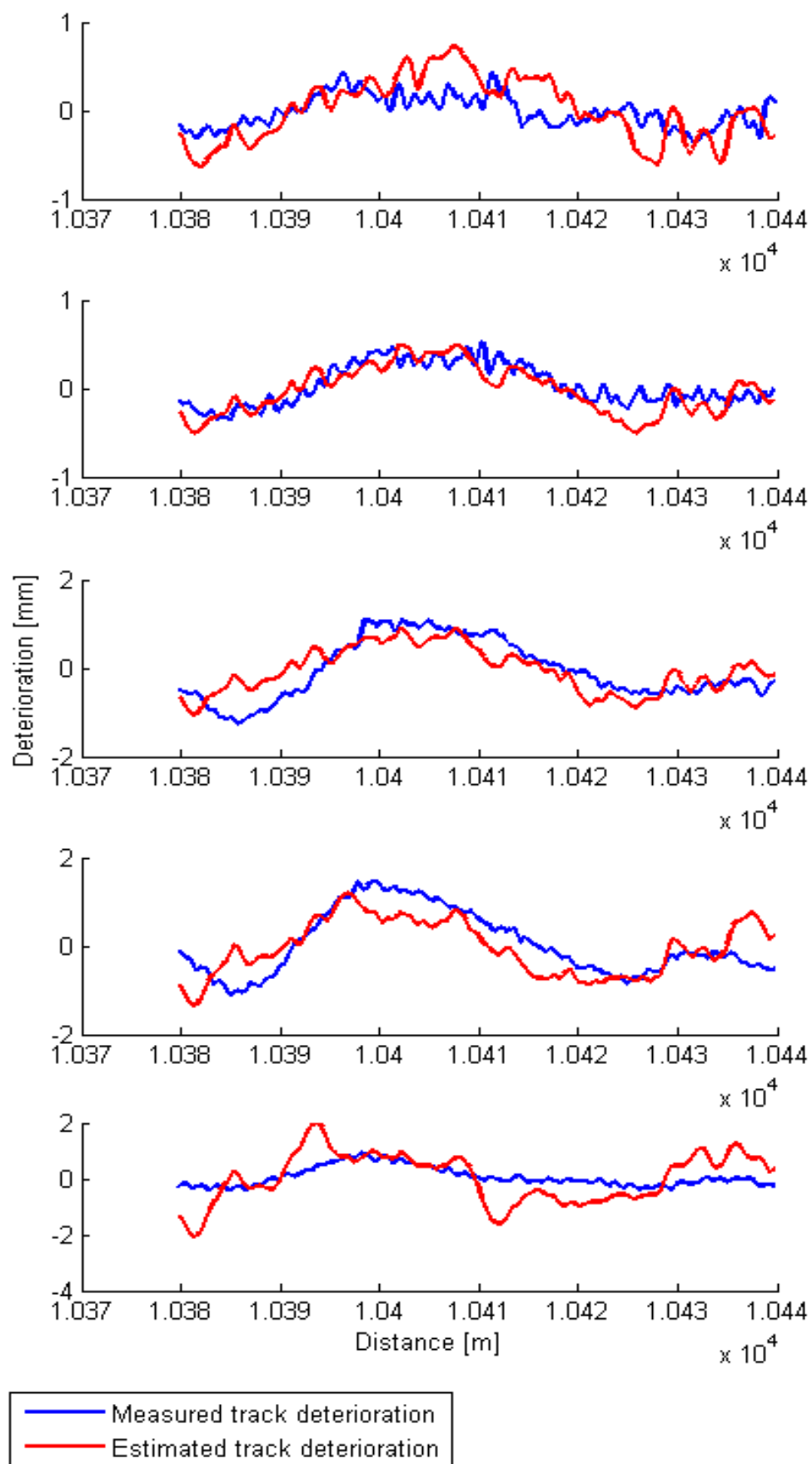


a) Measured lateral irregularity

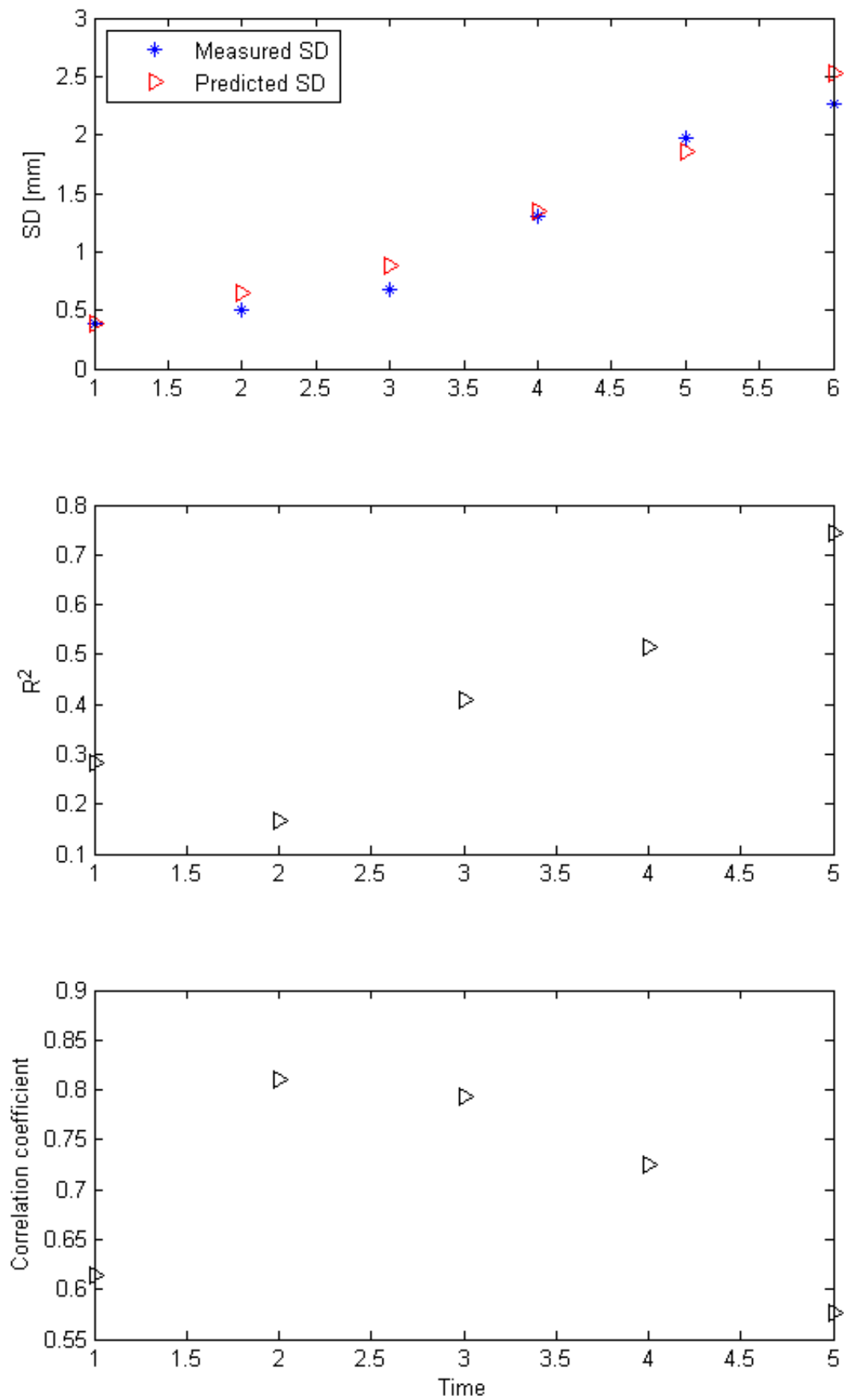


b) Predicted lateral irregularity

Figure 4-29 Measured and predicted track irregularity comparison



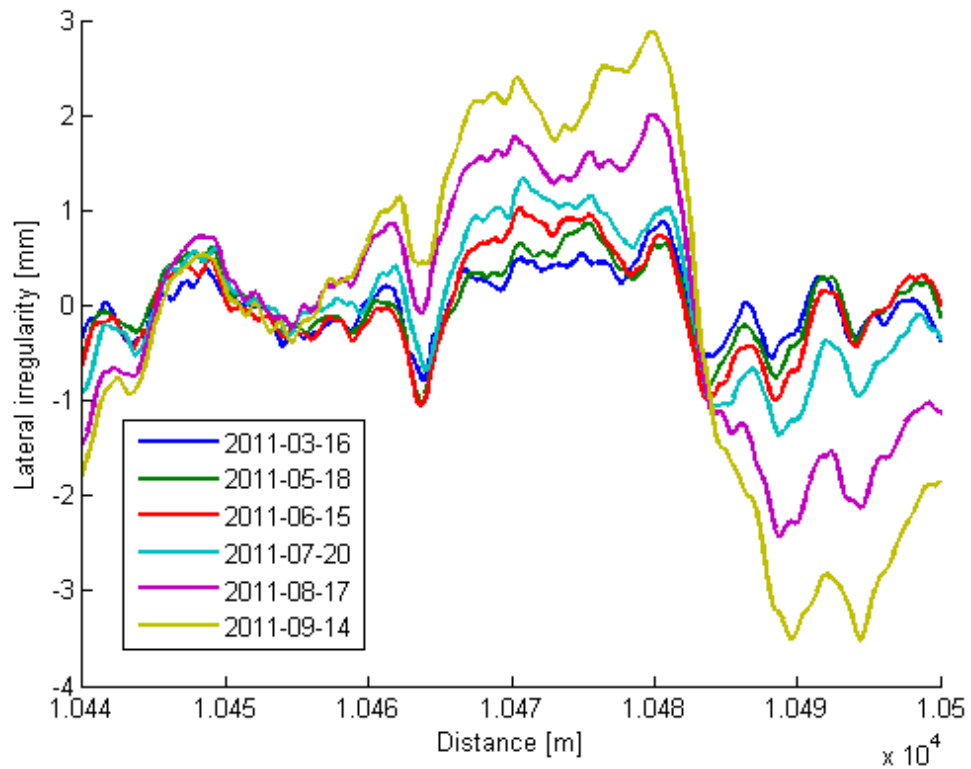
a) Measured and predicted lateral deterioration



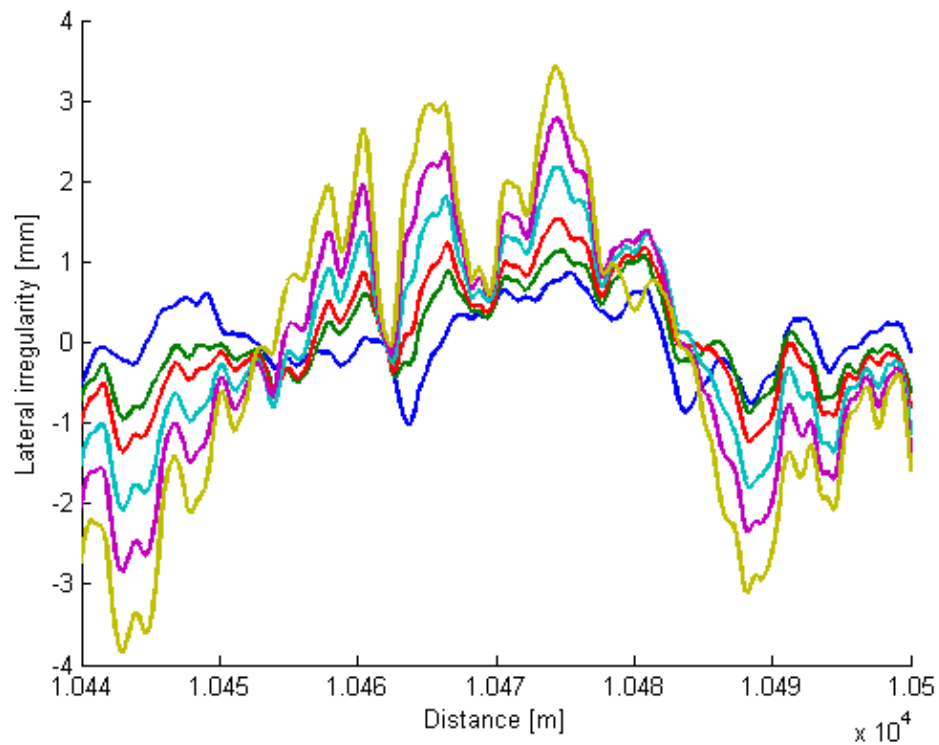
b) Precision measures

Figure 4-30 Deterioration comparison and precision measurement

- S16 results

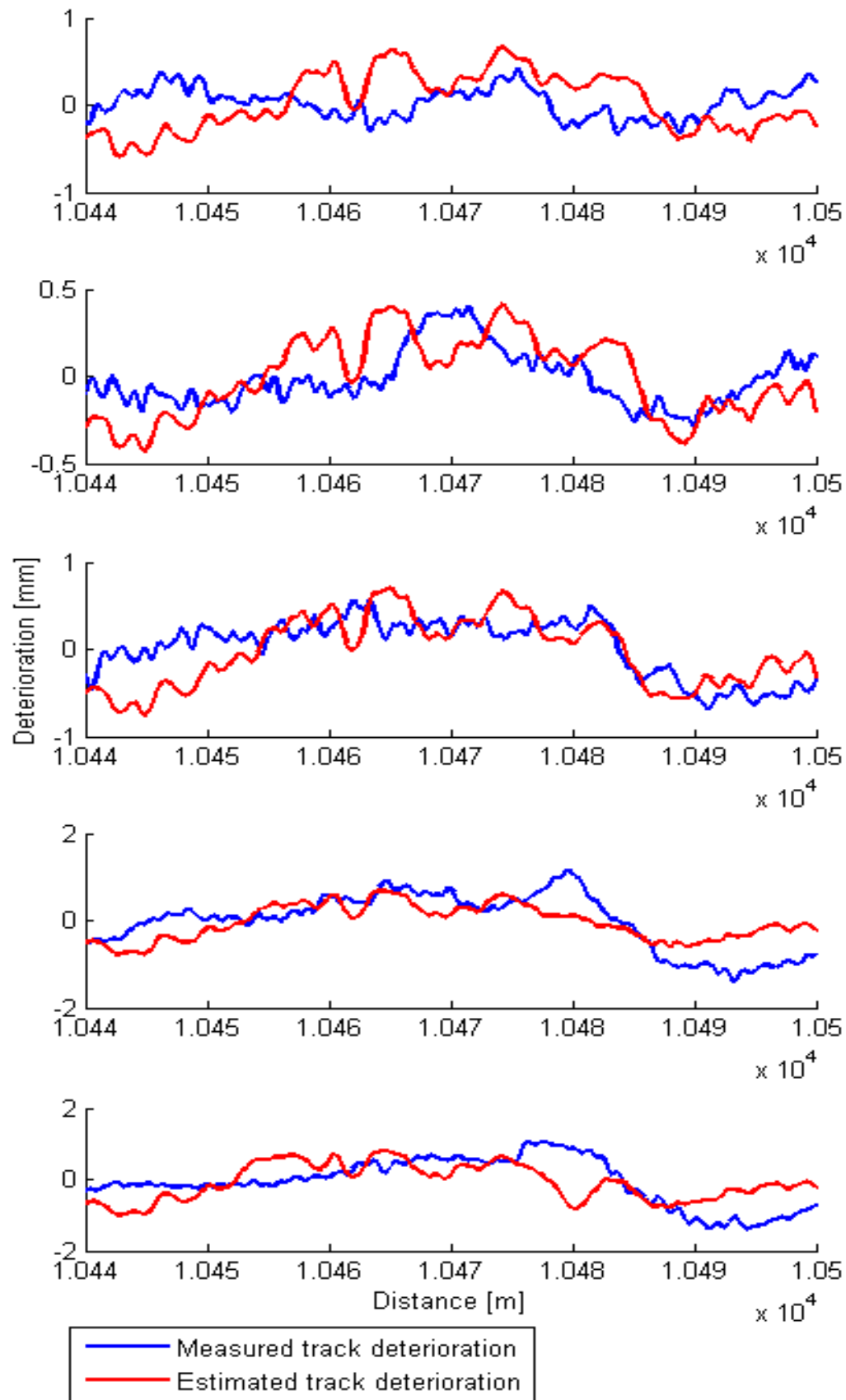


a) Measured lateral irregularity

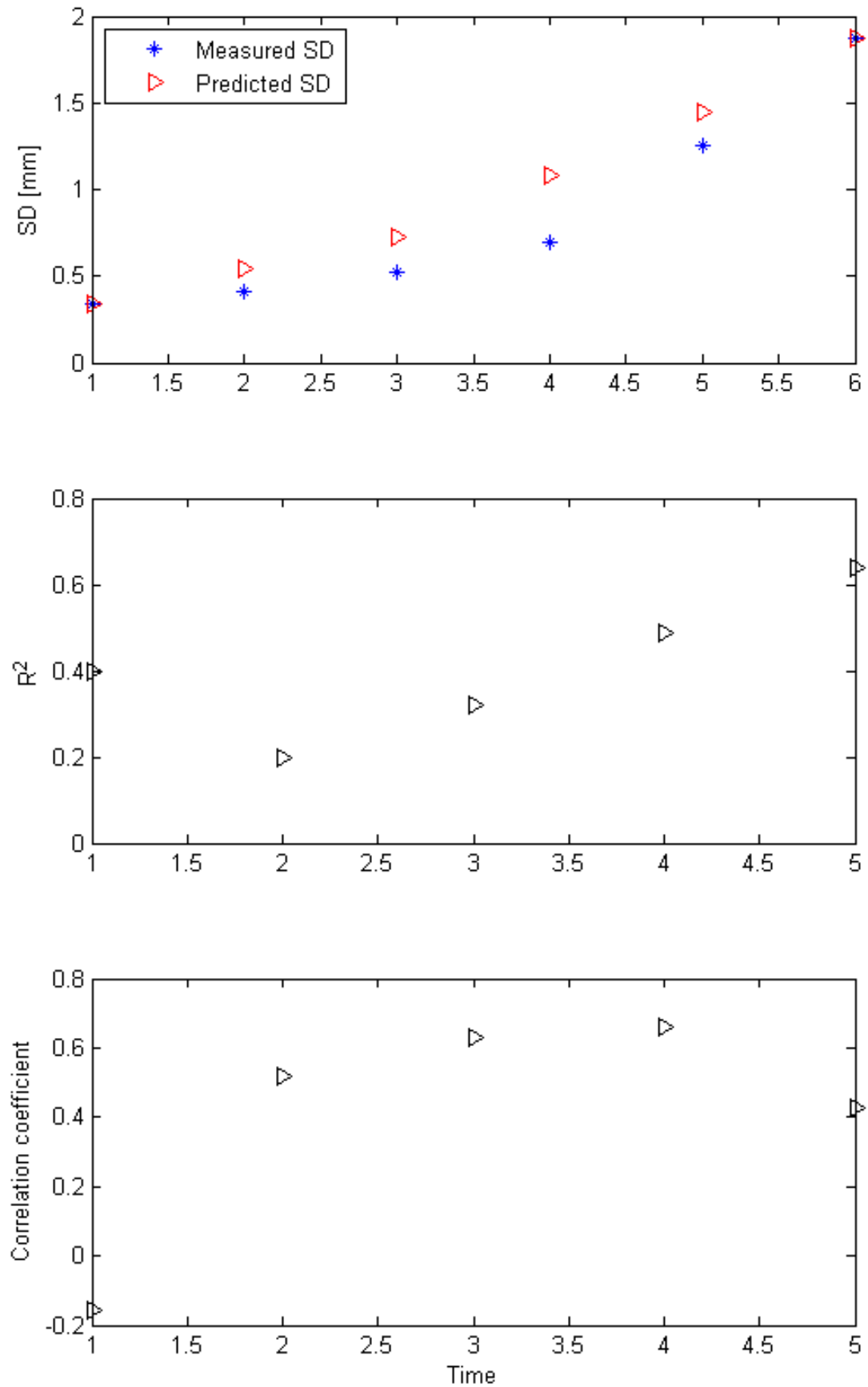


b) Predicted lateral irregularity

Figure 4-31 Measured and predicted track irregularity comparison



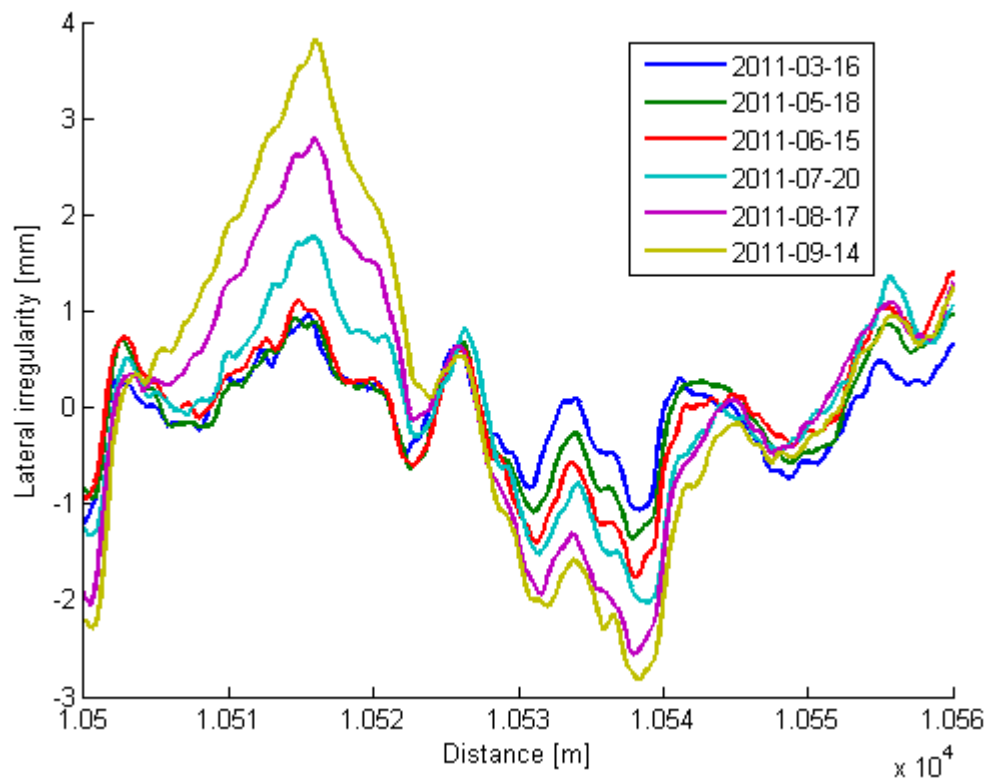
a) Measured and predicted lateral deterioration



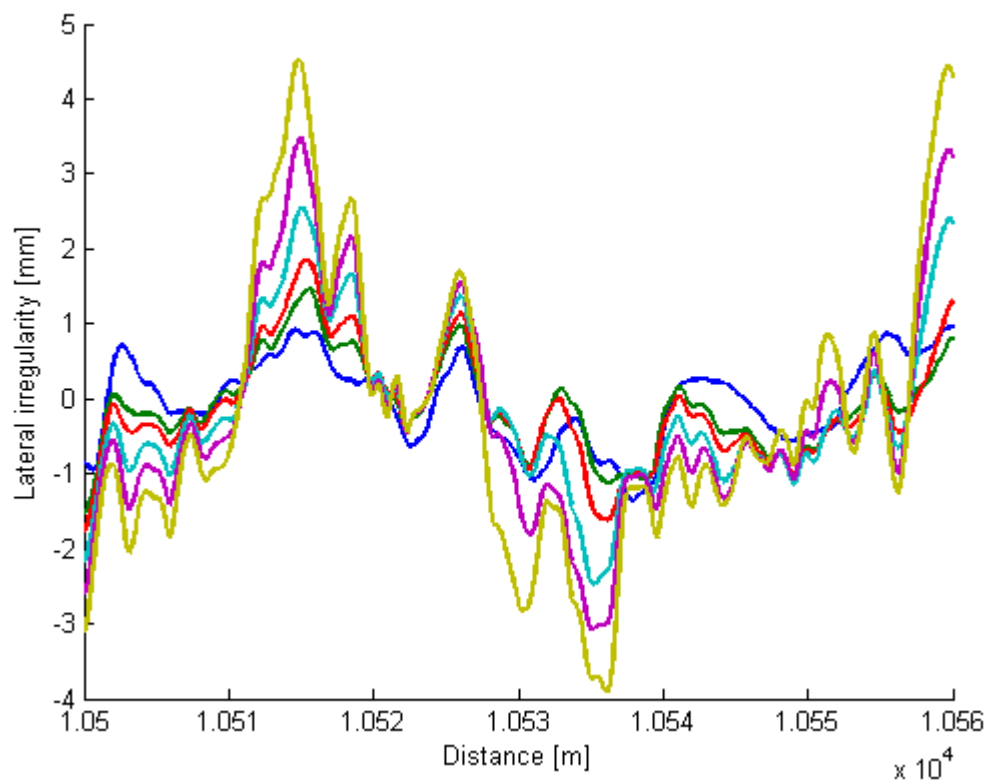
b) Precision measures

Figure 4-32 Deterioration comparison and precision measurement

- S17 results

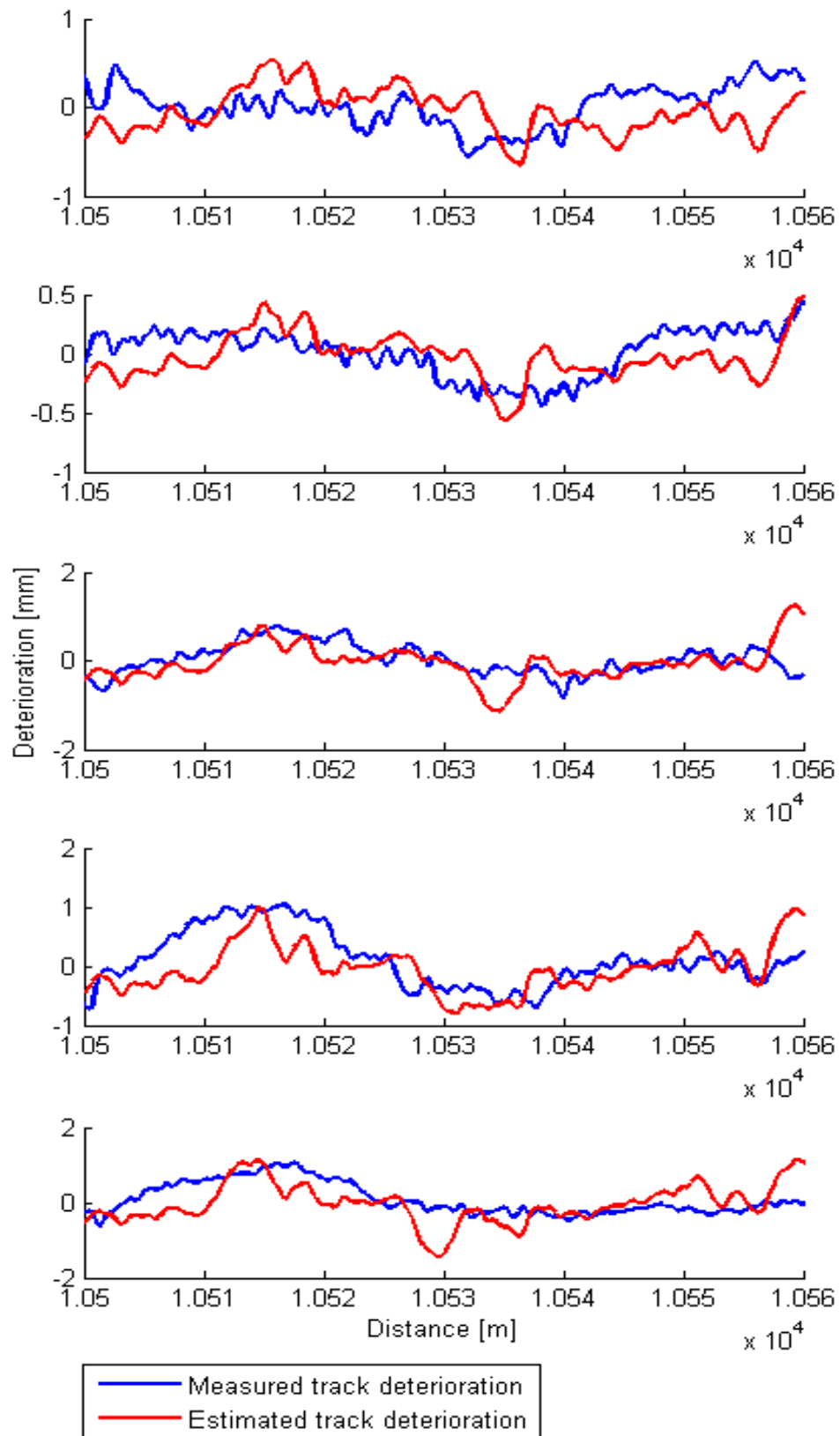


a) Measured lateral irregularity

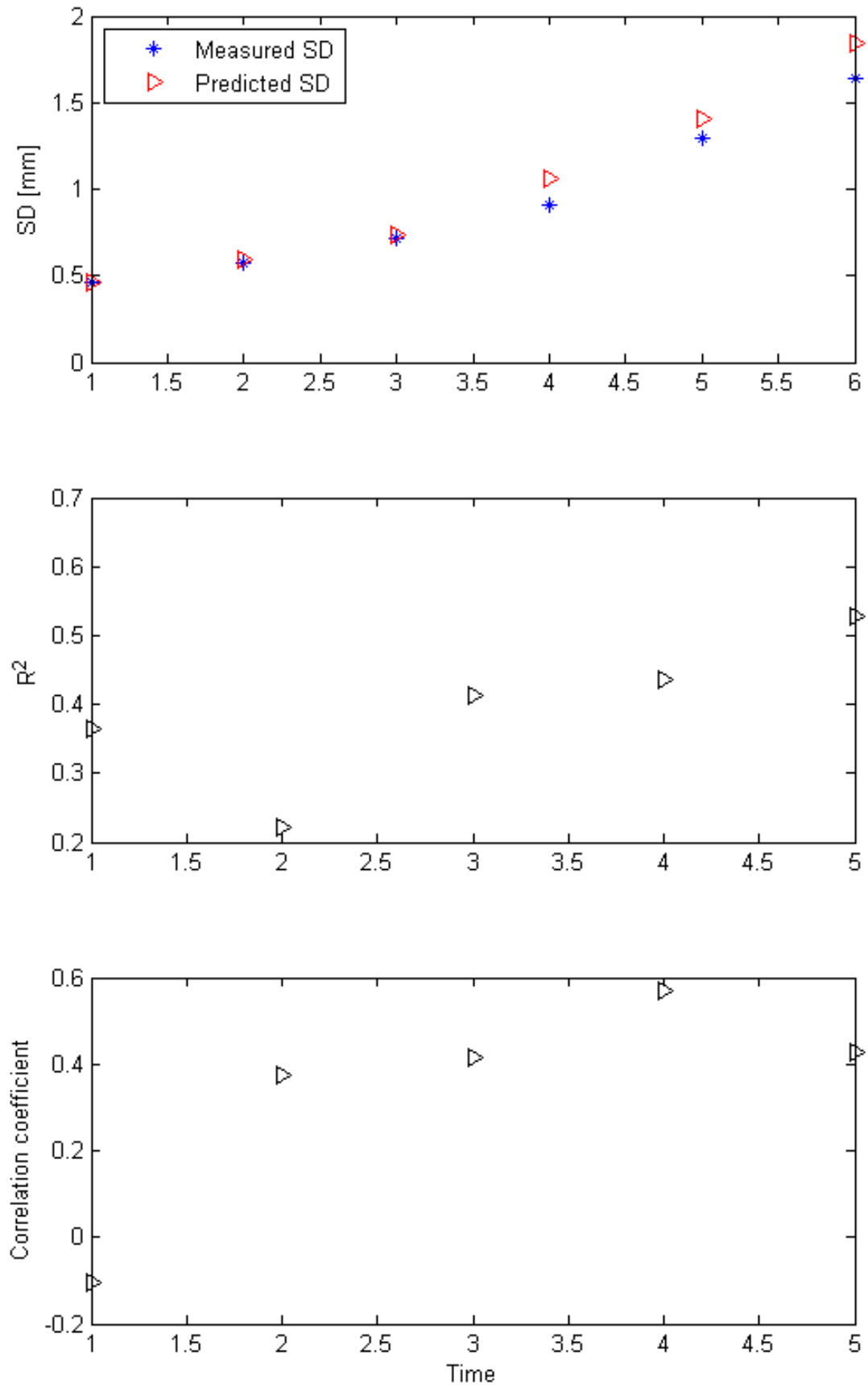


b) Predicted lateral irregularity

Figure 4-33 Measured and predicted track irregularity comparison



a) Measured and predicted lateral deterioration

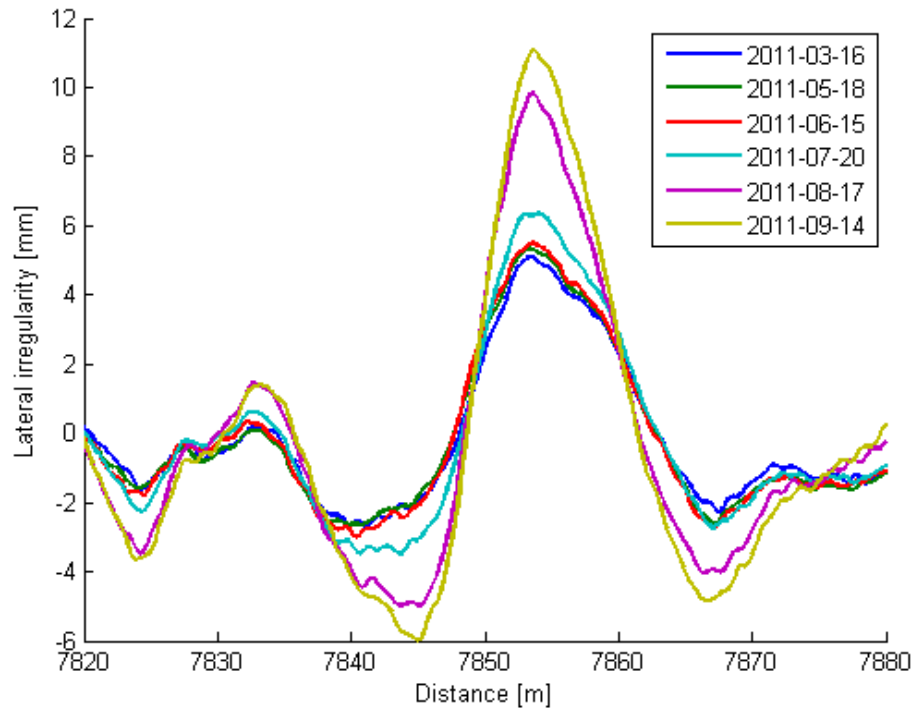


b) Precision measures

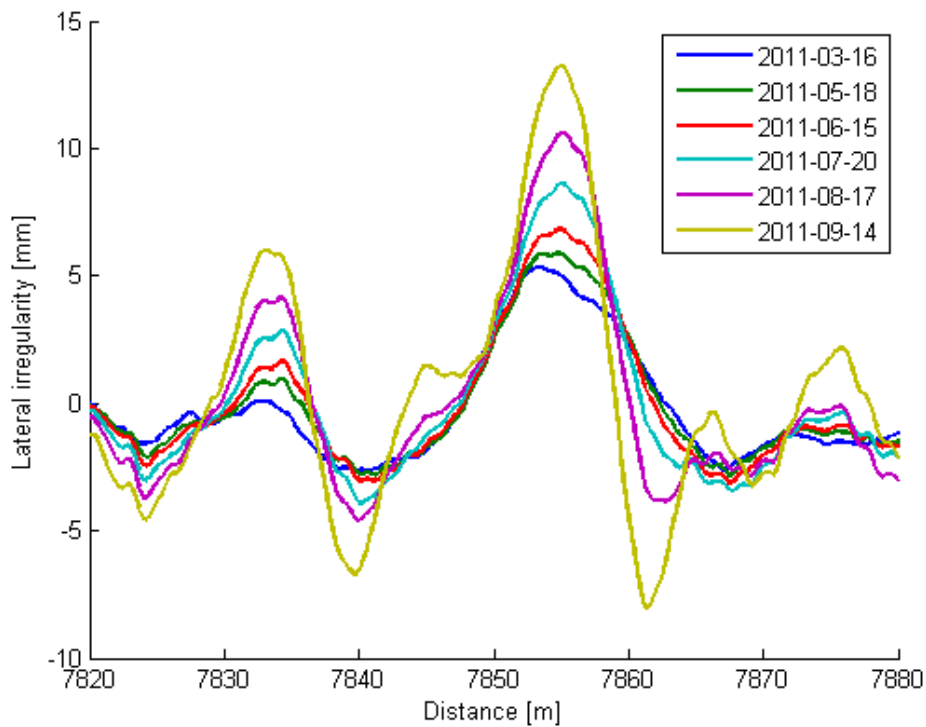
Figure 4-34 Deterioration comparison and precision measurement

- S10 results

There is limited data for worn rail profile on curves available and only curve C5 has data for worn profiles of both high and low rails available. Lateral irregularities on curves reach a maximum of 12 mm, which is much larger than the lateral irregularities on tangent lines.

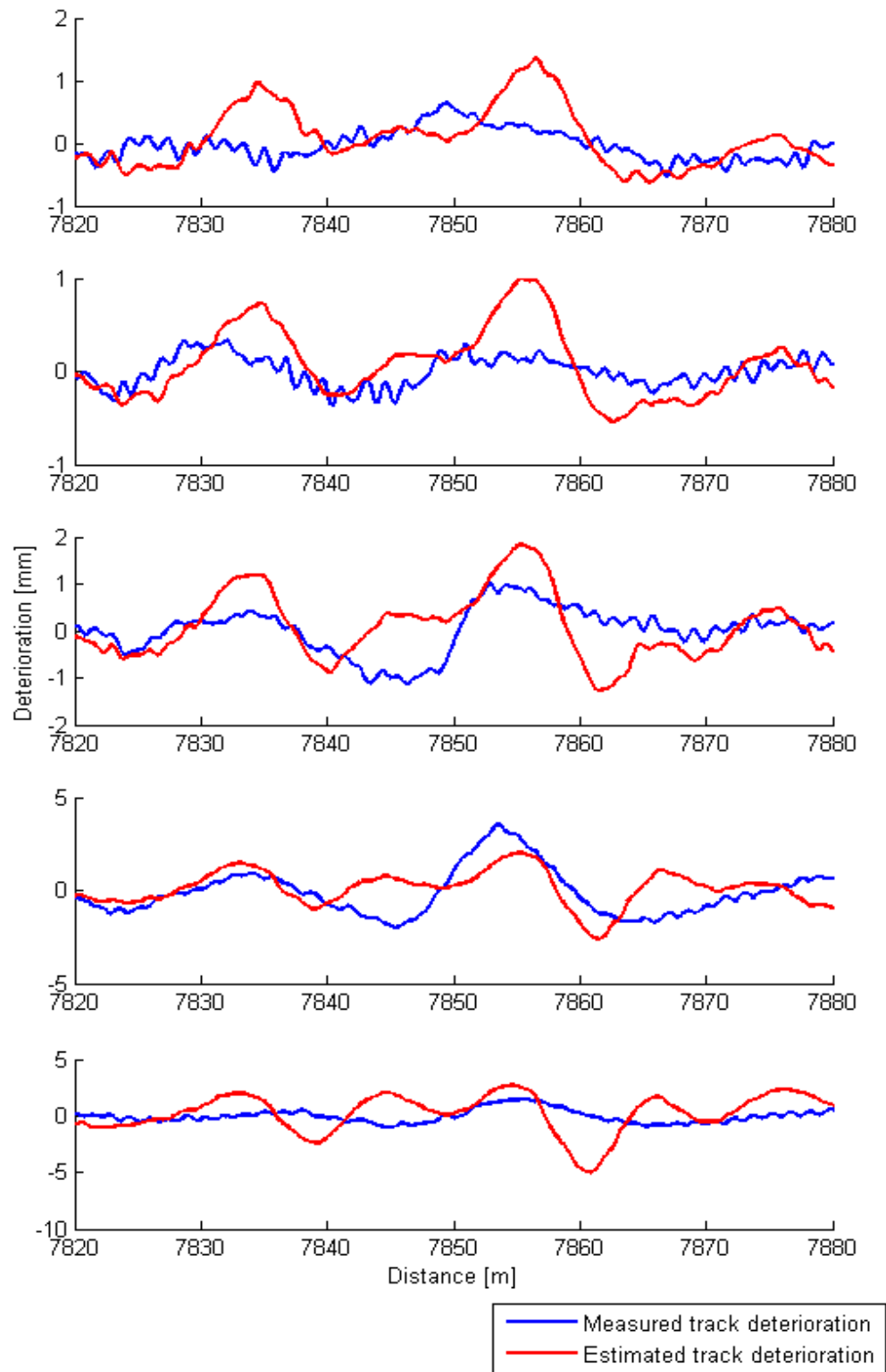


a) Measured lateral irregularity

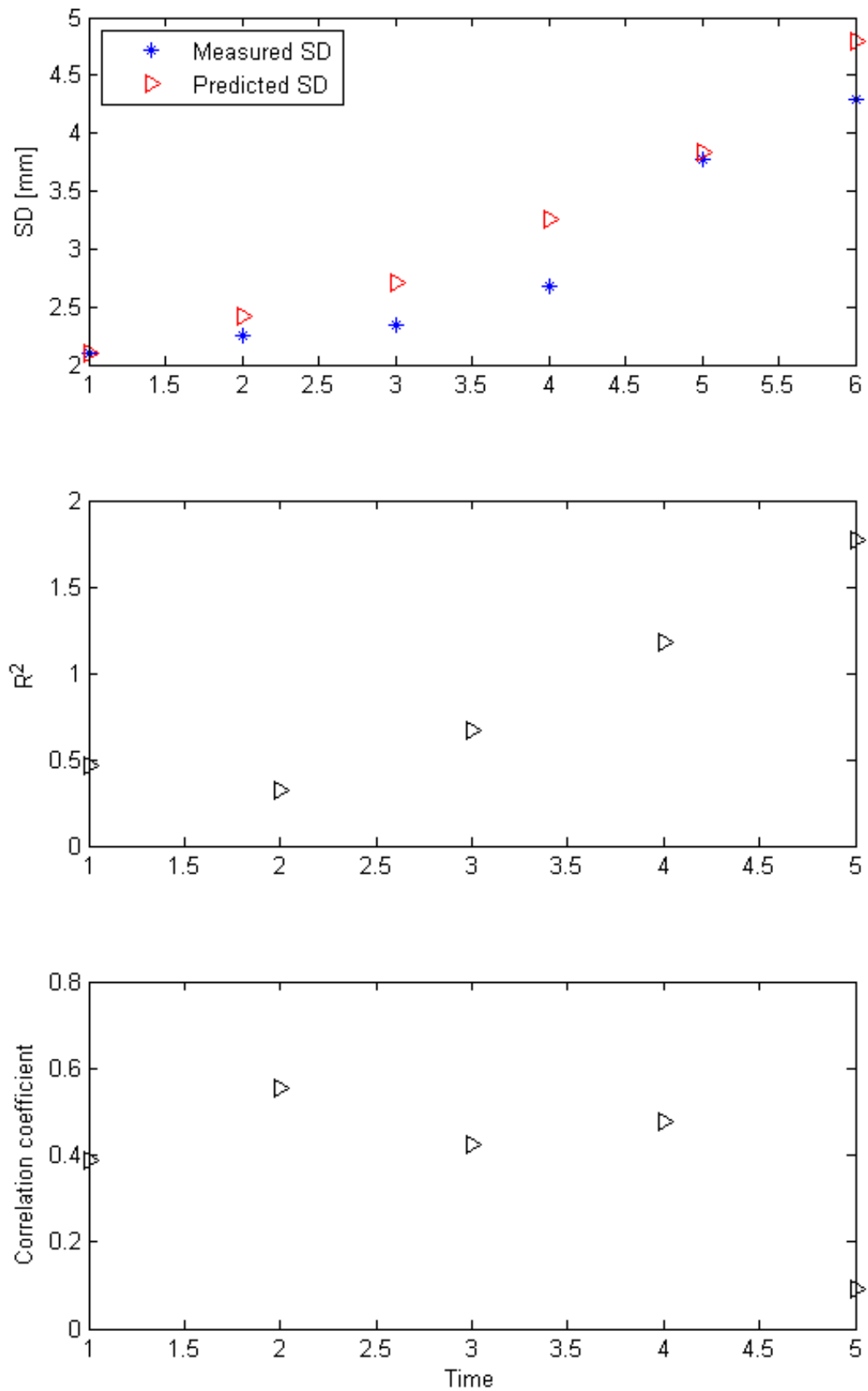


b) Predicted lateral irregularity

Figure 4-35 Measured and predicted track irregularity comparison



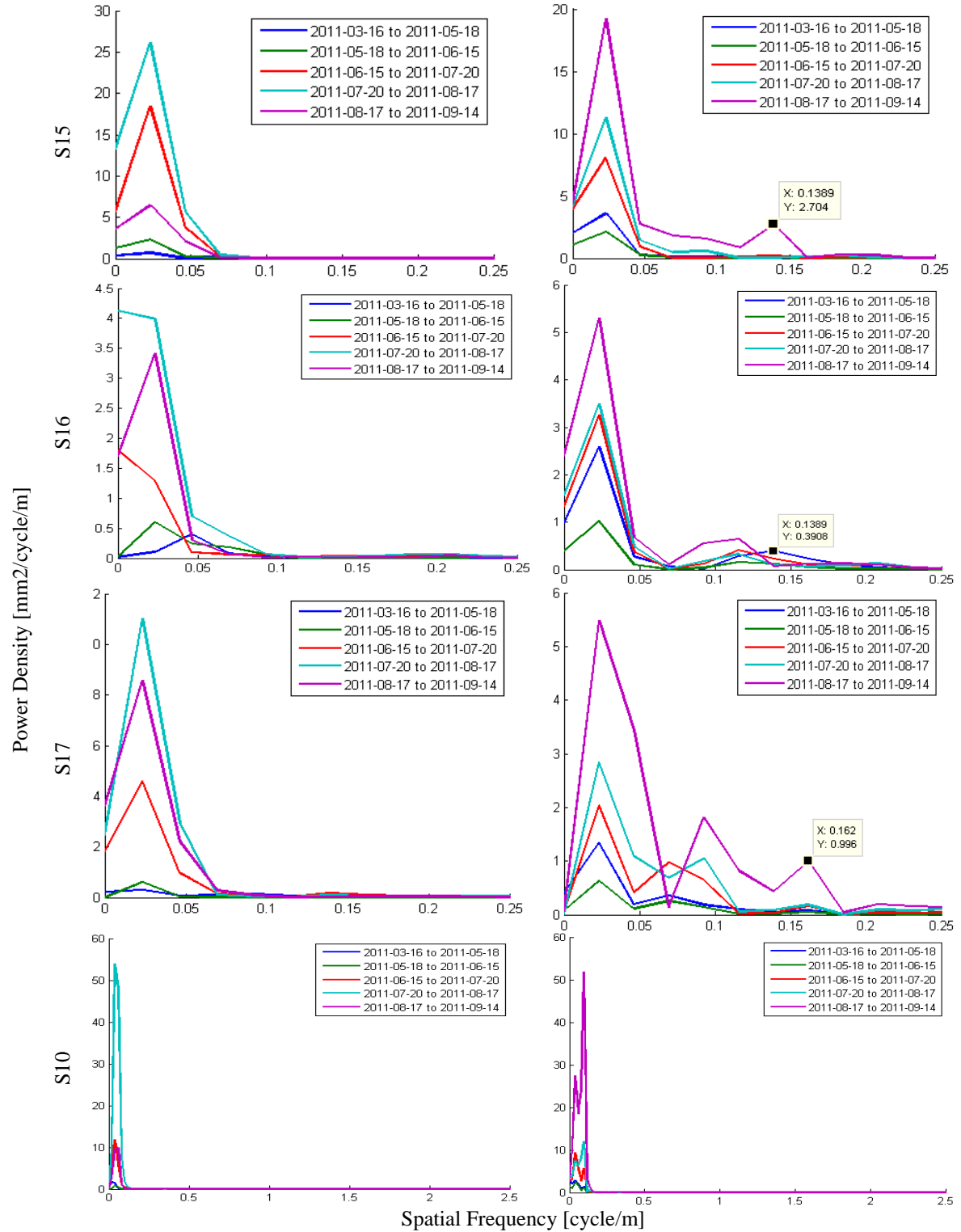
a) Measured and predicted lateral deterioration



b) Precision measures

Figure 4-36 Deterioration comparison and precision measurement

It can be found from these four sets of results that the RMS and correlation values of the prediction are reasonably accurate for the first 4 to 5 months, and become less accurate with increasing time. From the actual measured and predicted track lateral irregularities comparison it can be found that there is an additional small wavelength irregularity in the prediction results that does not appear in the measured data. The PSD of both the measured and predicted lateral deterioration are produced for these four sections of track.



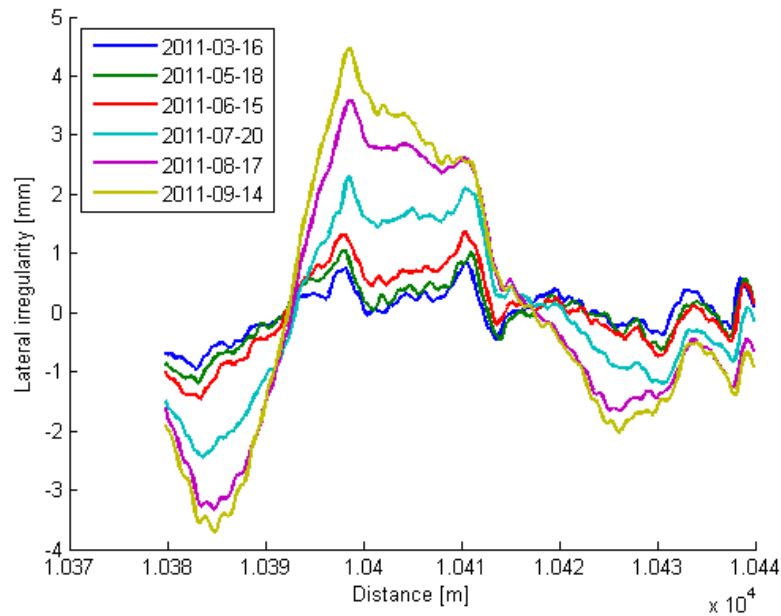
a) Measured lateral deterioration

b) Predicted lateral deterioration

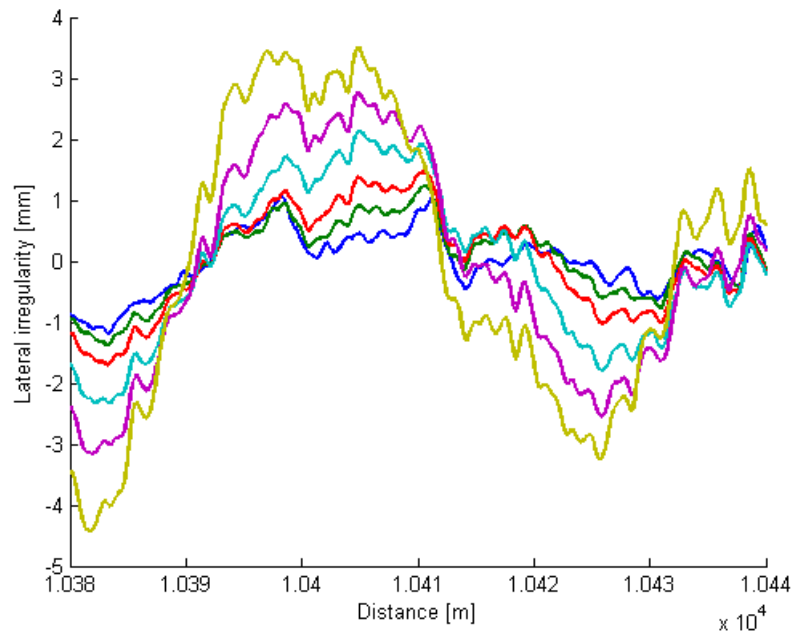
Figure 4-37 Comparison between measured and predicted lateral deterioration PSD

In addition to this major frequency, the predicted deterioration developed a higher frequency change in the track deterioration between 0.09259 and 0.1389 cycle/m (6.17 to 10.800 m). For the curved element (S10), the additional short wavelength irregularities are not obvious due to the large magnitude of the long wavelength irregularities. As the vehicle dynamic forces are the input into the track lateral model, this may be caused by different vehicle dynamic modes that are excited by different factors. If the 3 to 10.8 m wavelengths are filtered out from the results, the resulting lateral deterioration is shown below.

- S15 m filtered results

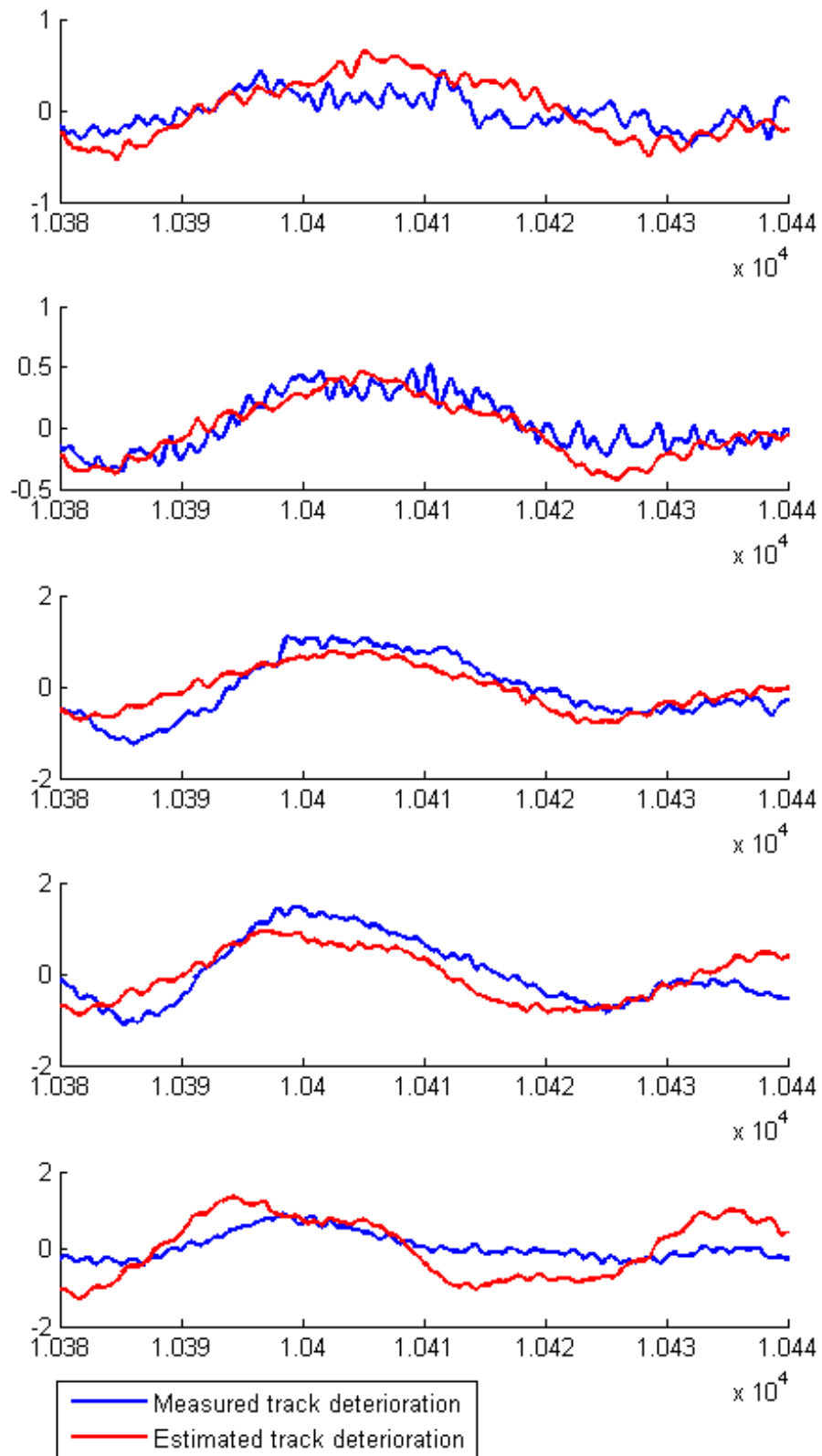


a) Measured lateral irregularity

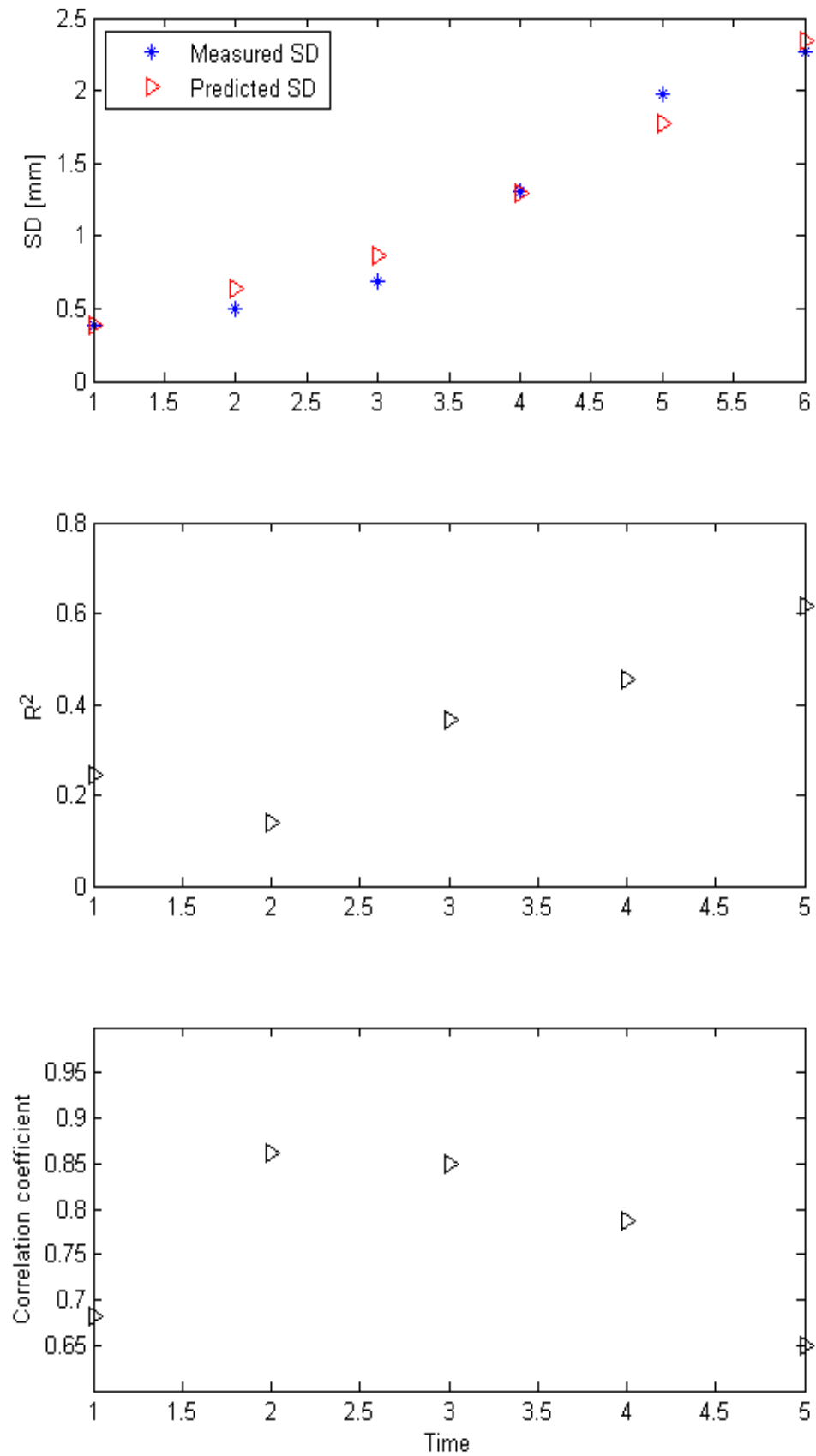


b) Filtered predicted lateral irregularity

Figure 4-38 Measured and filtered predicted track irregularity comparison



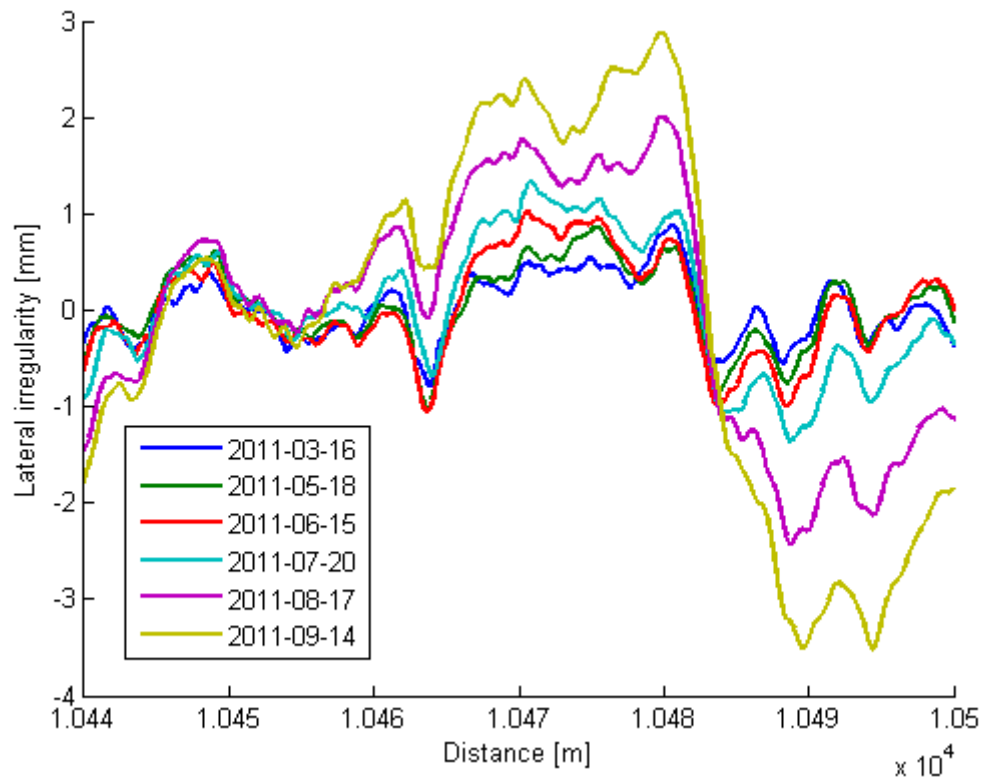
a) Measured and filtered predicted lateral deterioration



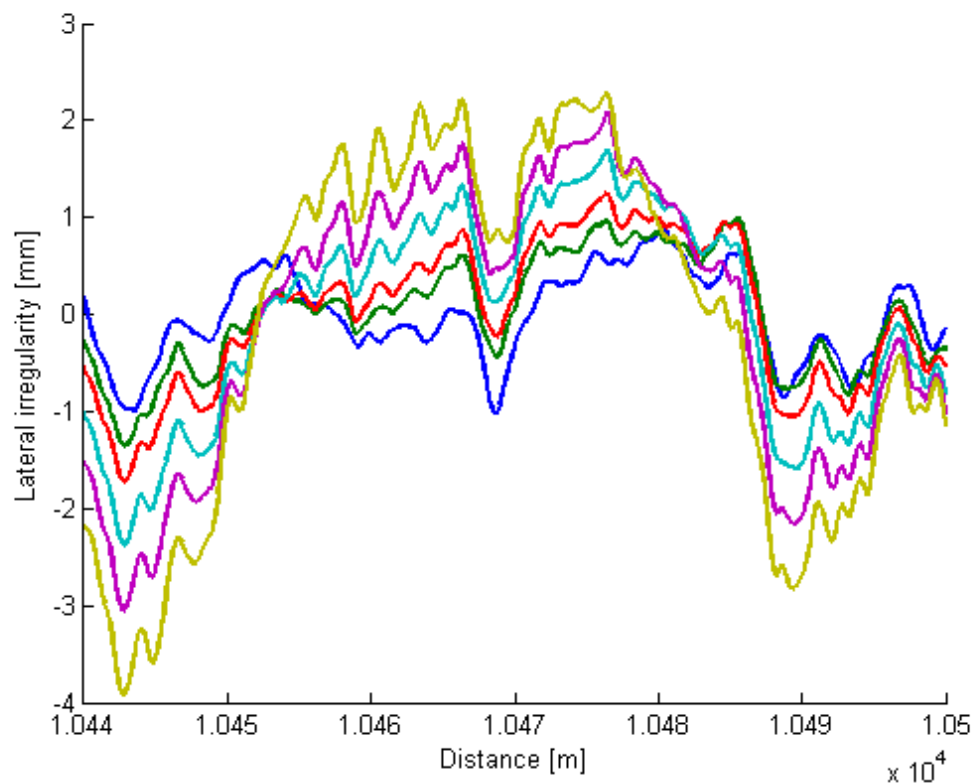
b) Precision measures

Figure 4-39 Deterioration comparison and filtered precision measurement

- S16 m filtered results

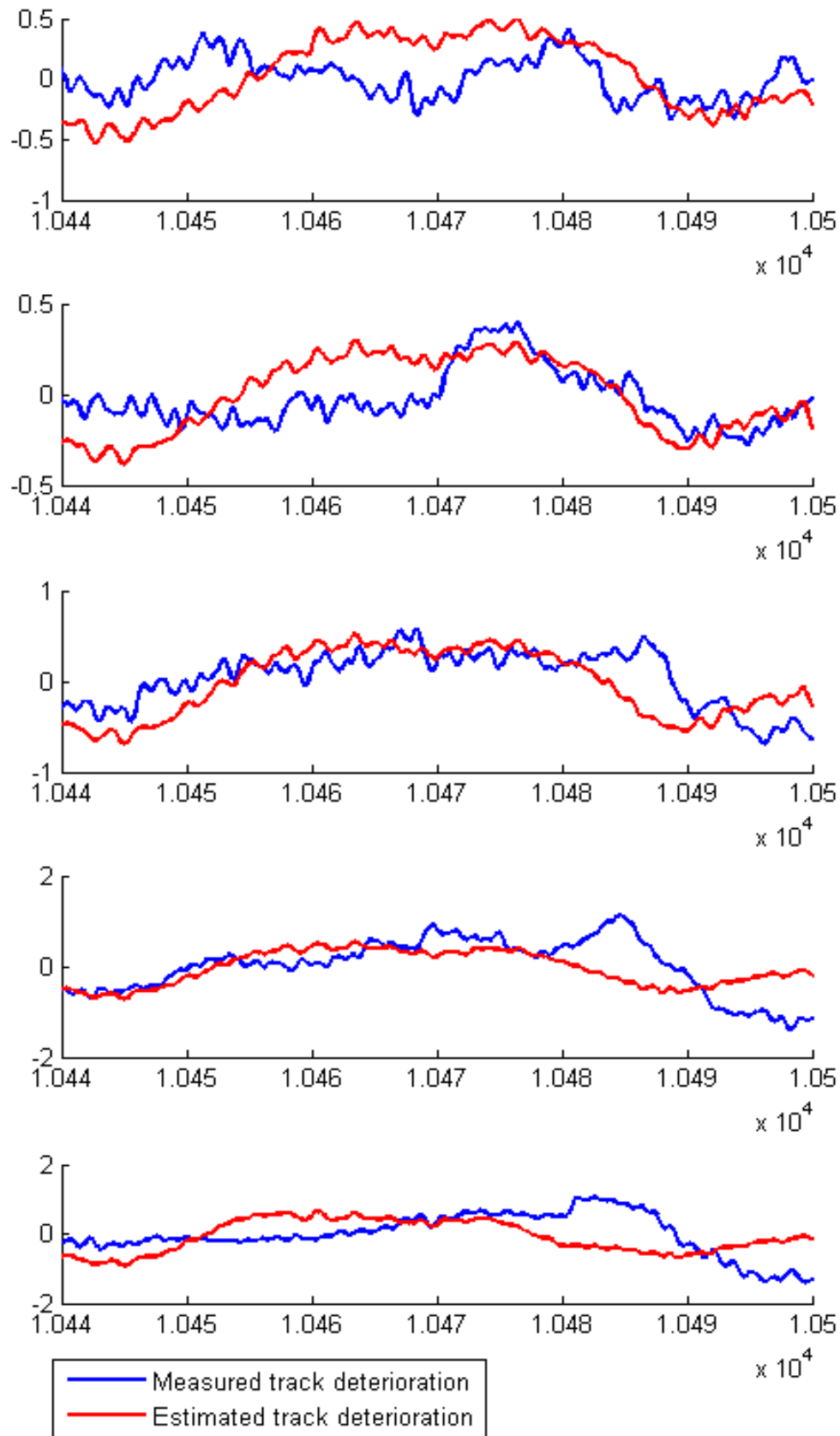


a) Measured lateral irregularity

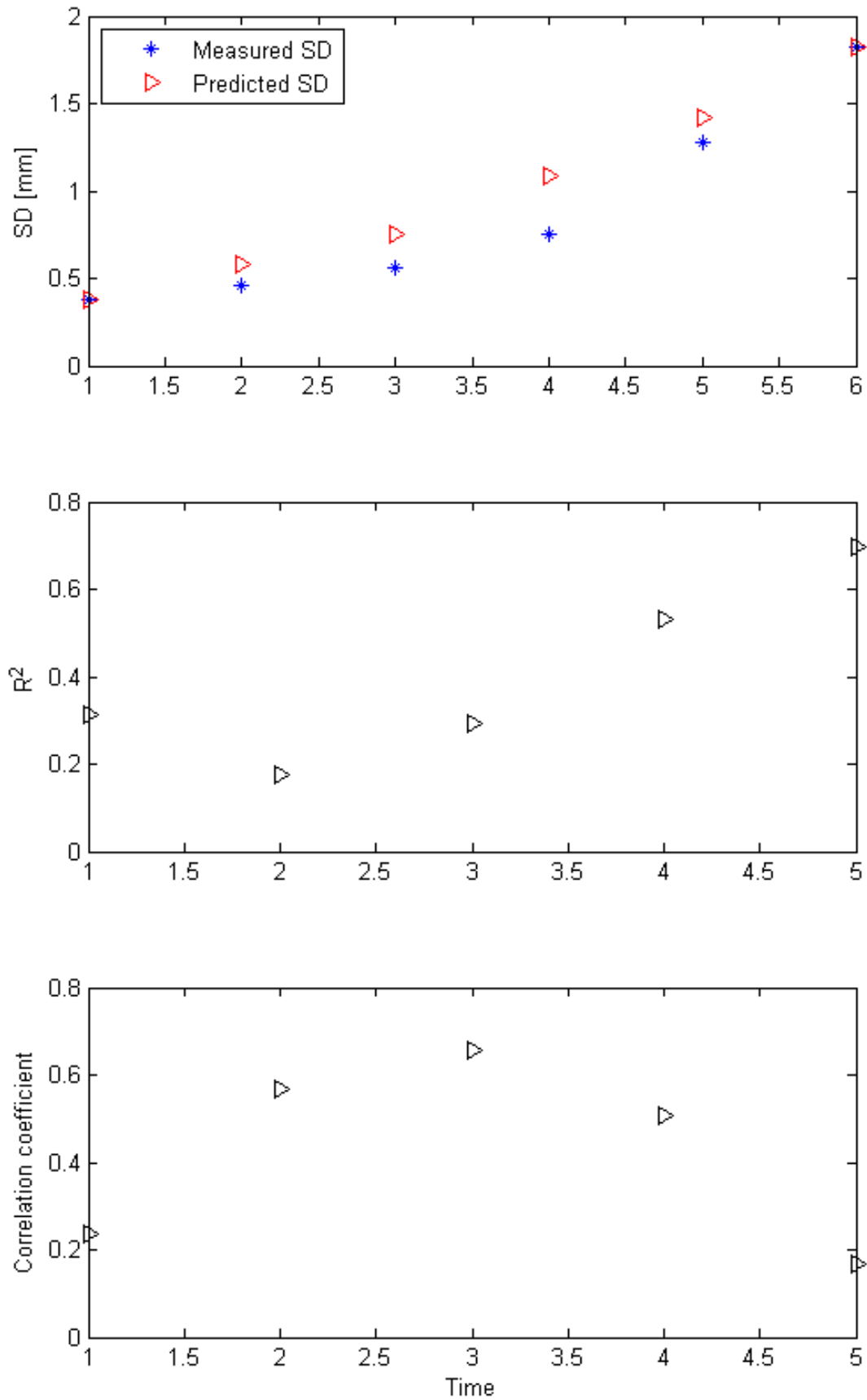


b) Filtered predicted lateral irregularity

Figure 4-40 Measured and filtered predicted track irregularity comparison



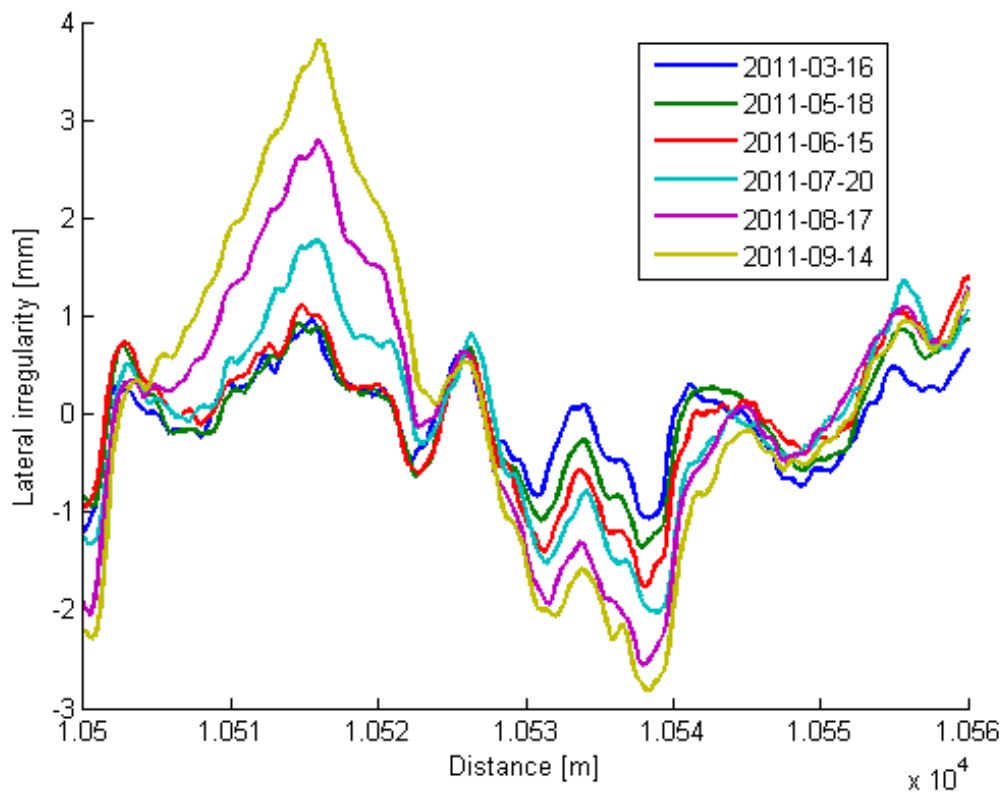
a) Measured and filtered predicted lateral deterioration



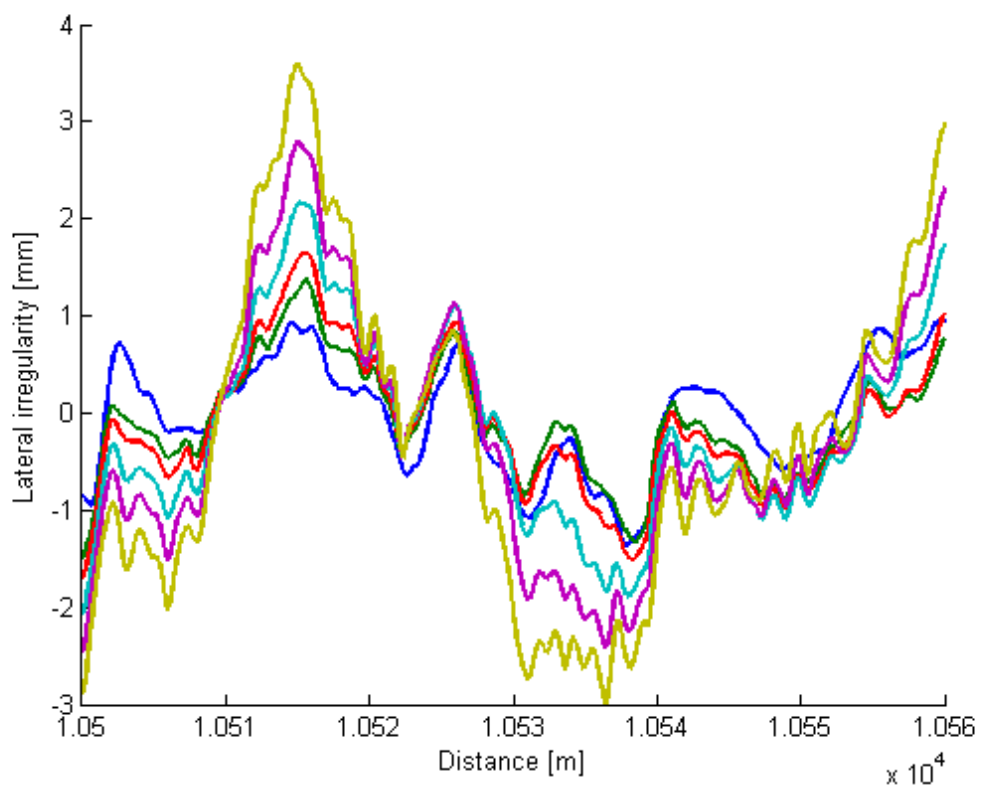
b) Precision measures

Figure 4-41 Deterioration comparison and filtered precision measurement

- S17 filtered results

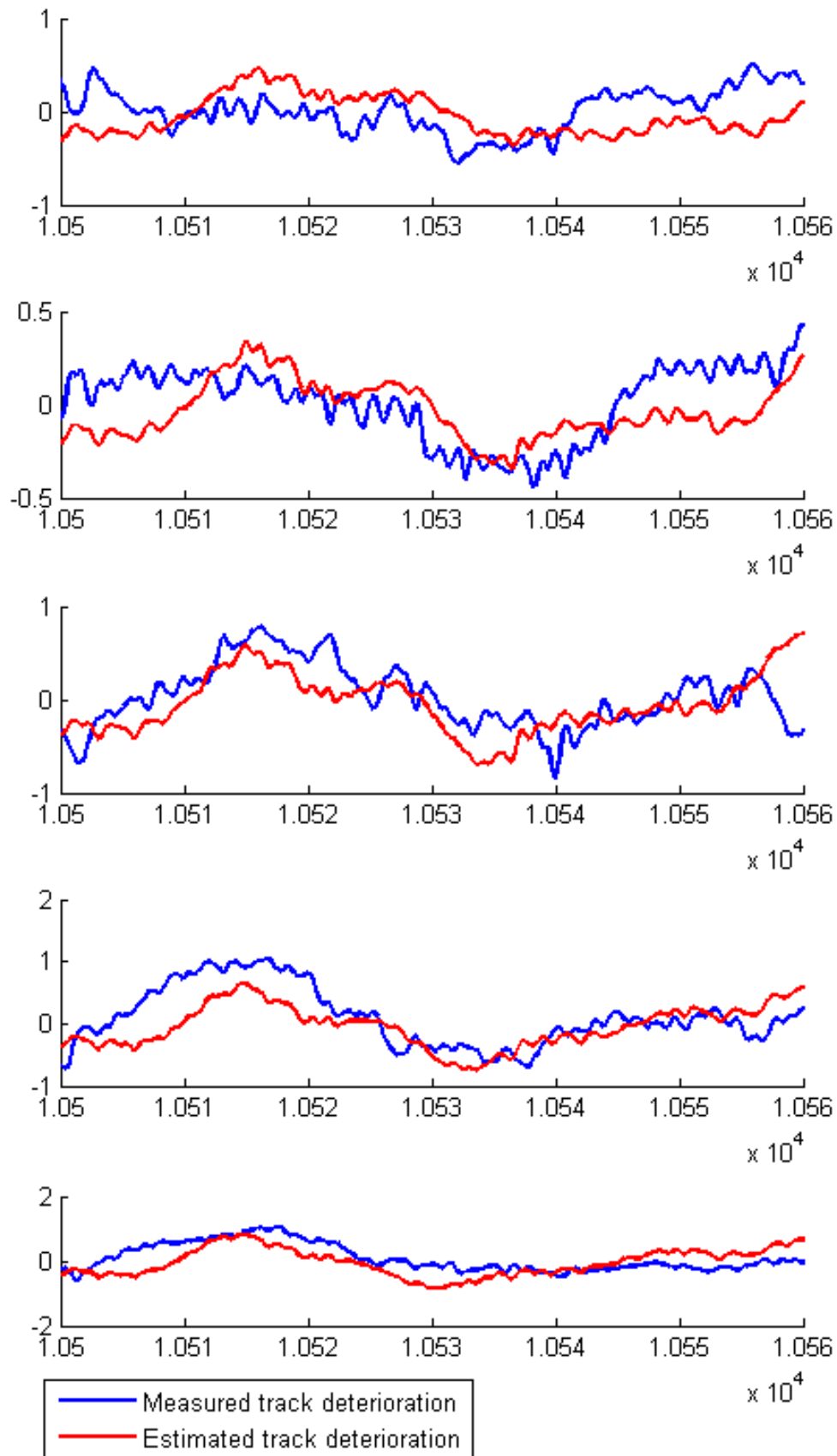


a) Measured lateral irregularity

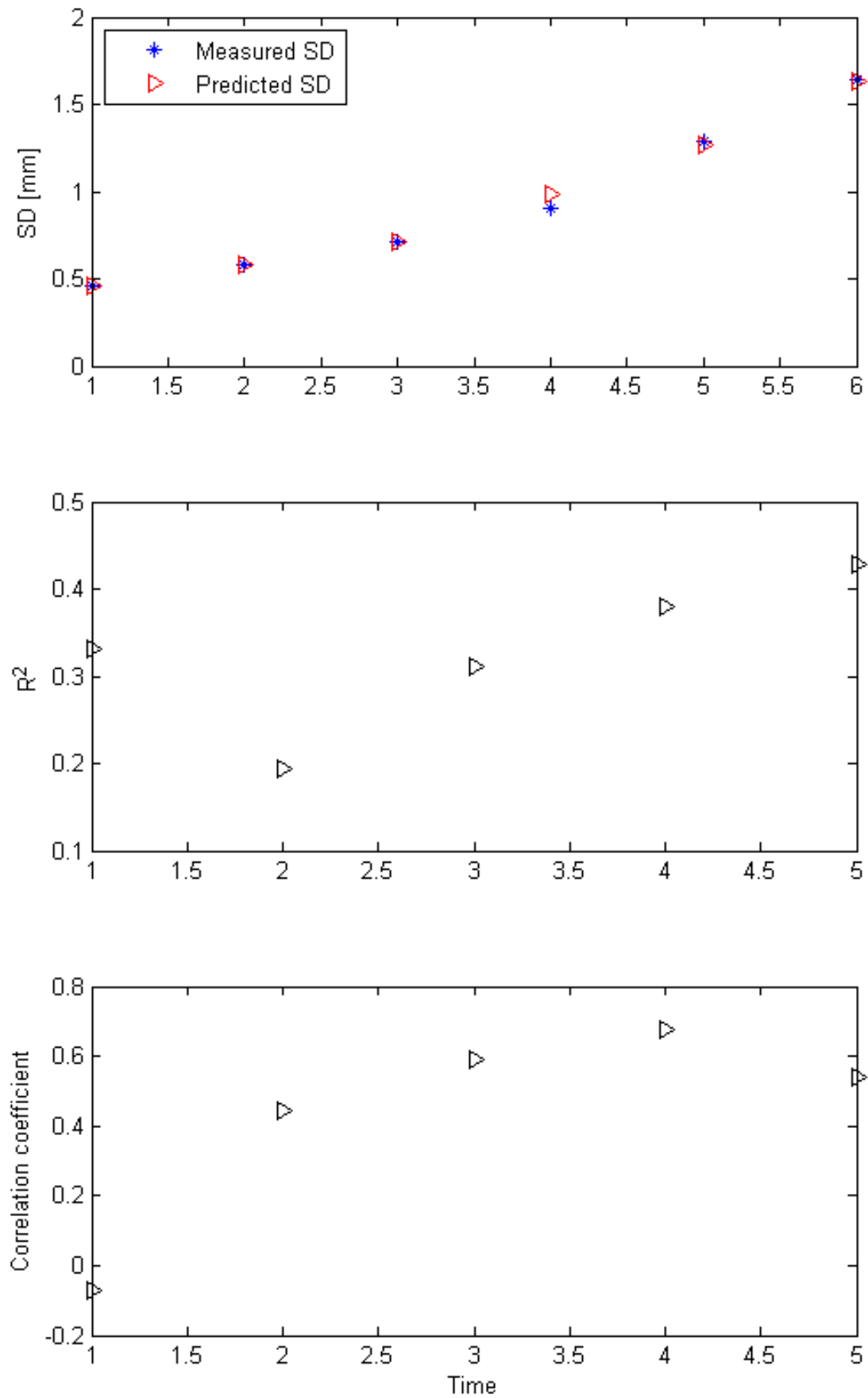


b) Filtered predicted lateral irregularity

Figure 4-42 Measured and filtered predicted track irregularity comparison



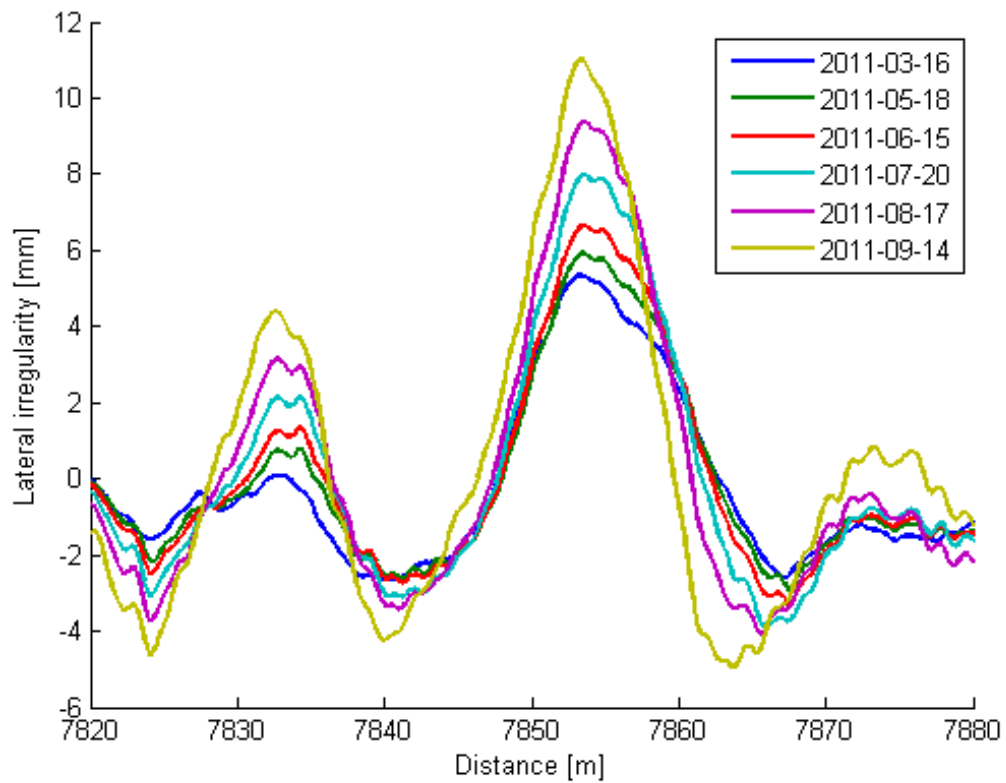
a) Measured and filtered predicted lateral deterioration



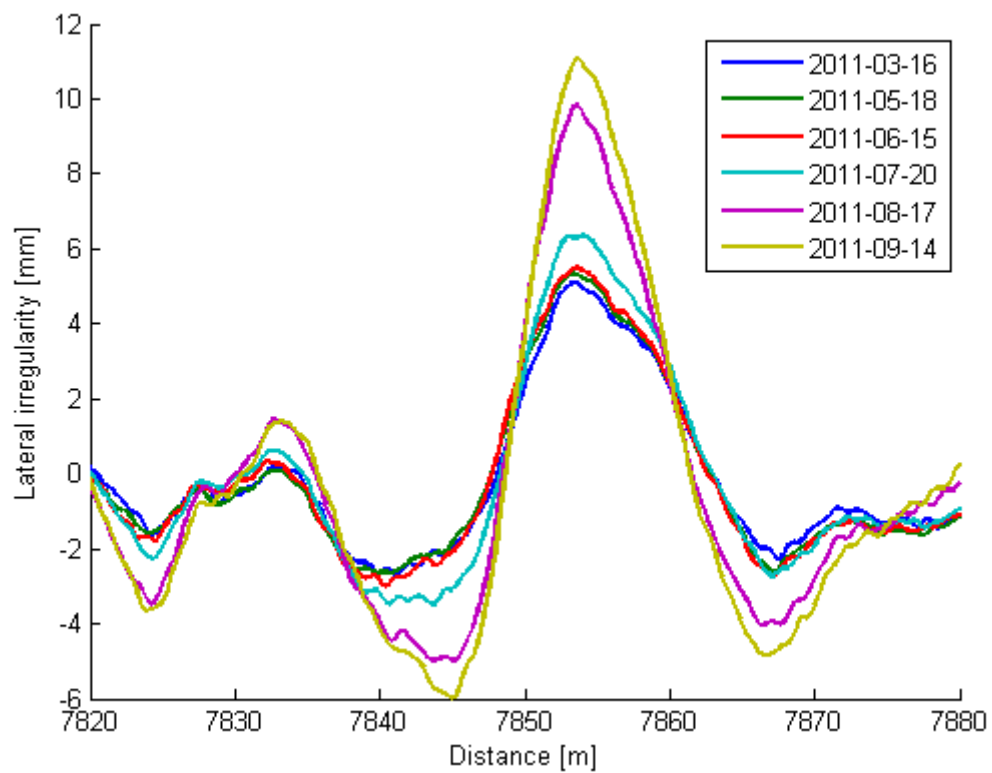
b) Precision measures

Figure 4-43 Deterioration comparison and filtered precision measurement

- S10 filtered results

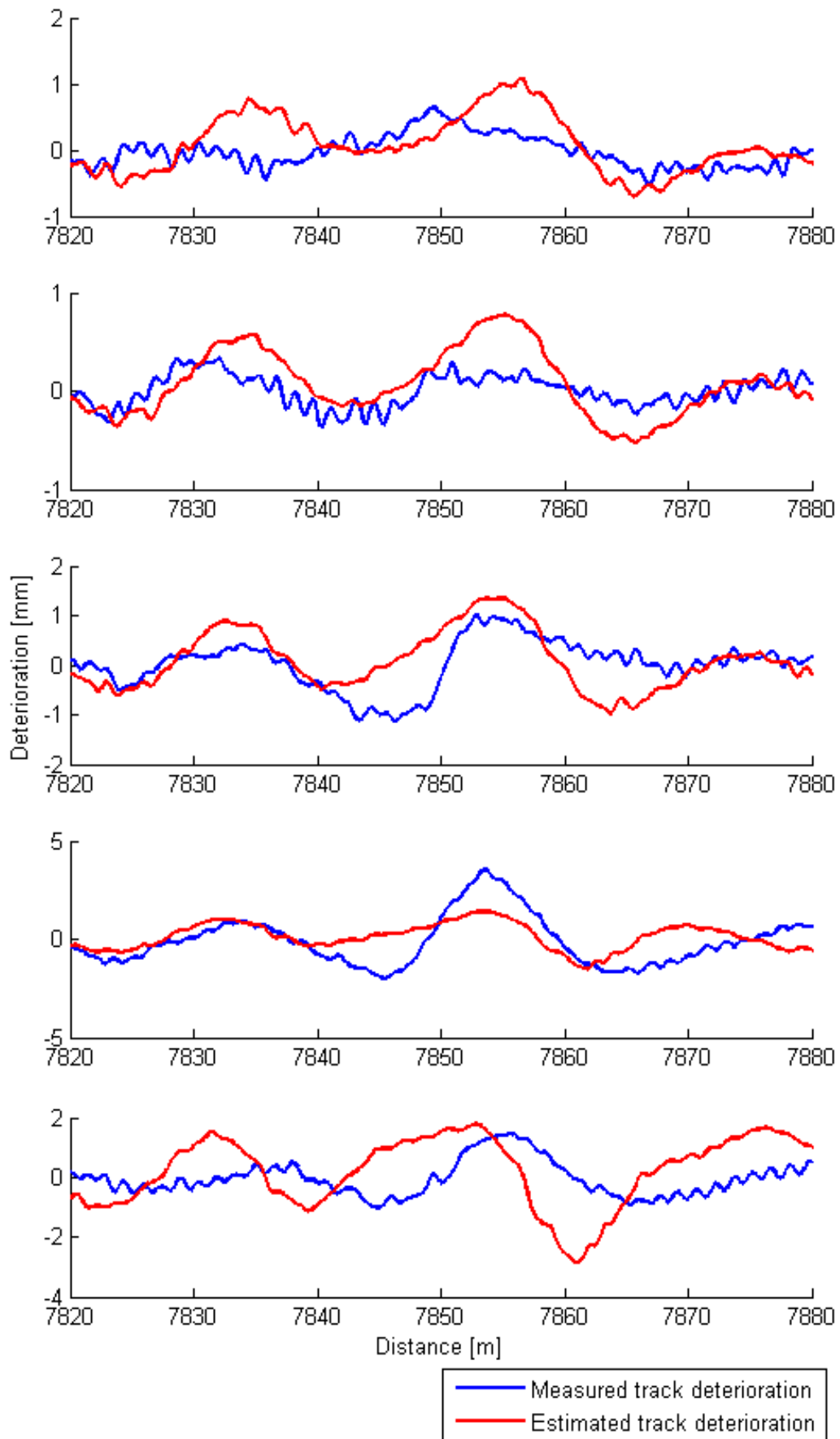


a) Measured lateral irregularity

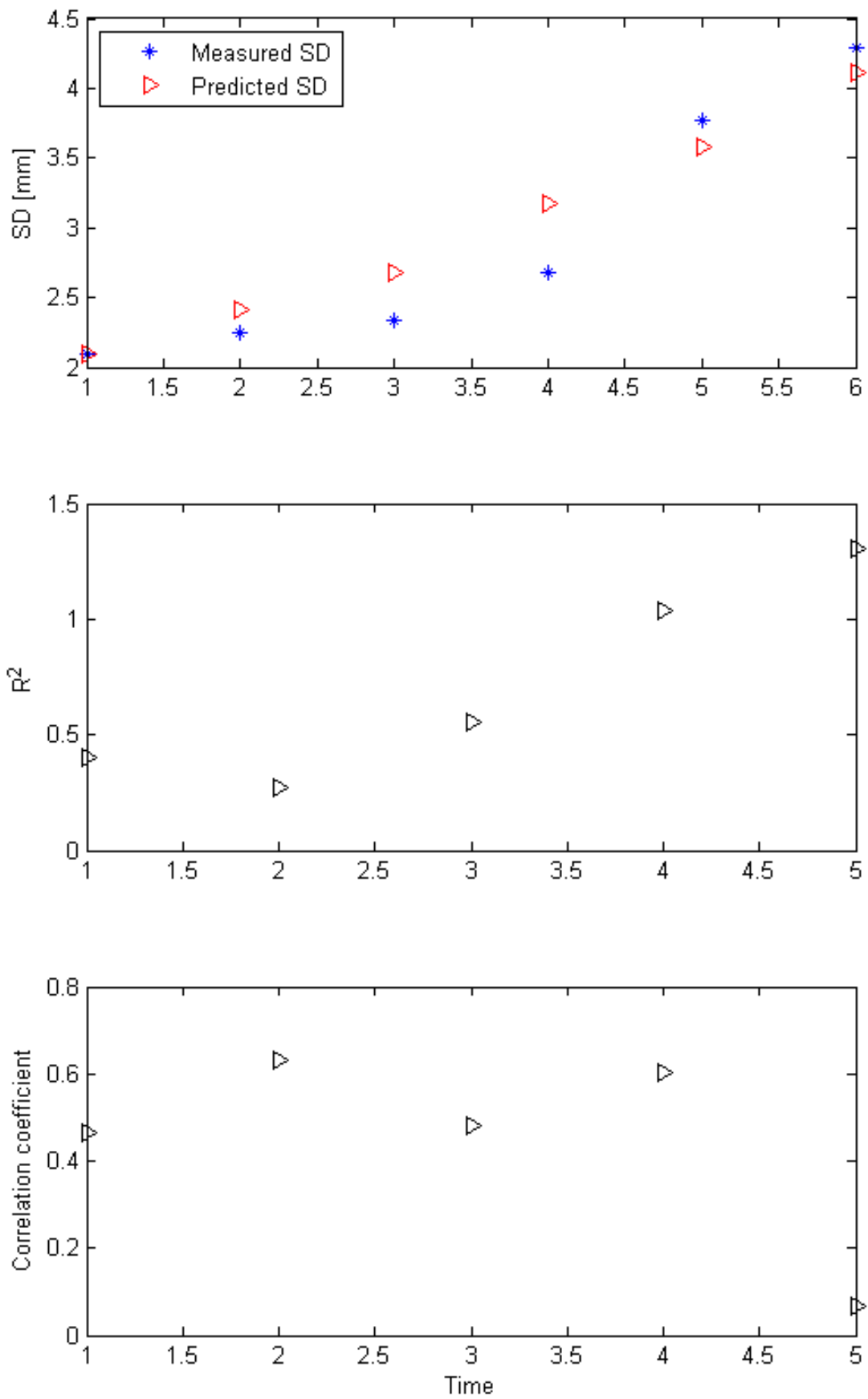


b) Filtered predicted lateral irregularity

Figure 4-44 Measured and filtered predicted track irregularity comparison



a) Measured and filtered predicted lateral deterioration



b) Precision measures

Figure 4-45 Deterioration comparison and filtered precision measurement

The SD values are much better matched, meanwhile, the RMS and correlation coefficient values indicate much more accurate prediction results with the filtered data. Therefore, it will be quite important to establish why this certain range of short wavelength deterioration does not exist in the actual track.

In conclusion, a novel vehicle-track lateral dynamic interaction model has been created to simulate the link between dynamic behaviour of railway vehicles and track lateral alignment deterioration, and this model has been validated against recorded track data. It has been found that the model gives a reasonably accurate prediction of the development of track irregularities, however it tends to additionally predict a short wavelength deterioration that is not seen in the actual track deterioration.

4.6 Chapter conclusion

The vehicle-track lateral deterioration model consists of two major sub-models, which are the vehicle-track dynamic model using VAMPIRE® and the track lateral deterioration model built in MATLAB. The input factors of both models are studied in detail, so that the models are set up to match track sections on the WCML as much as possible for model validation. The model gives a reasonably accurate prediction of the development of track irregularities, although it tends to additionally predict a short wavelength deterioration that is not seen in the actual track deterioration.

5 SENSITIVITY ANALYSIS

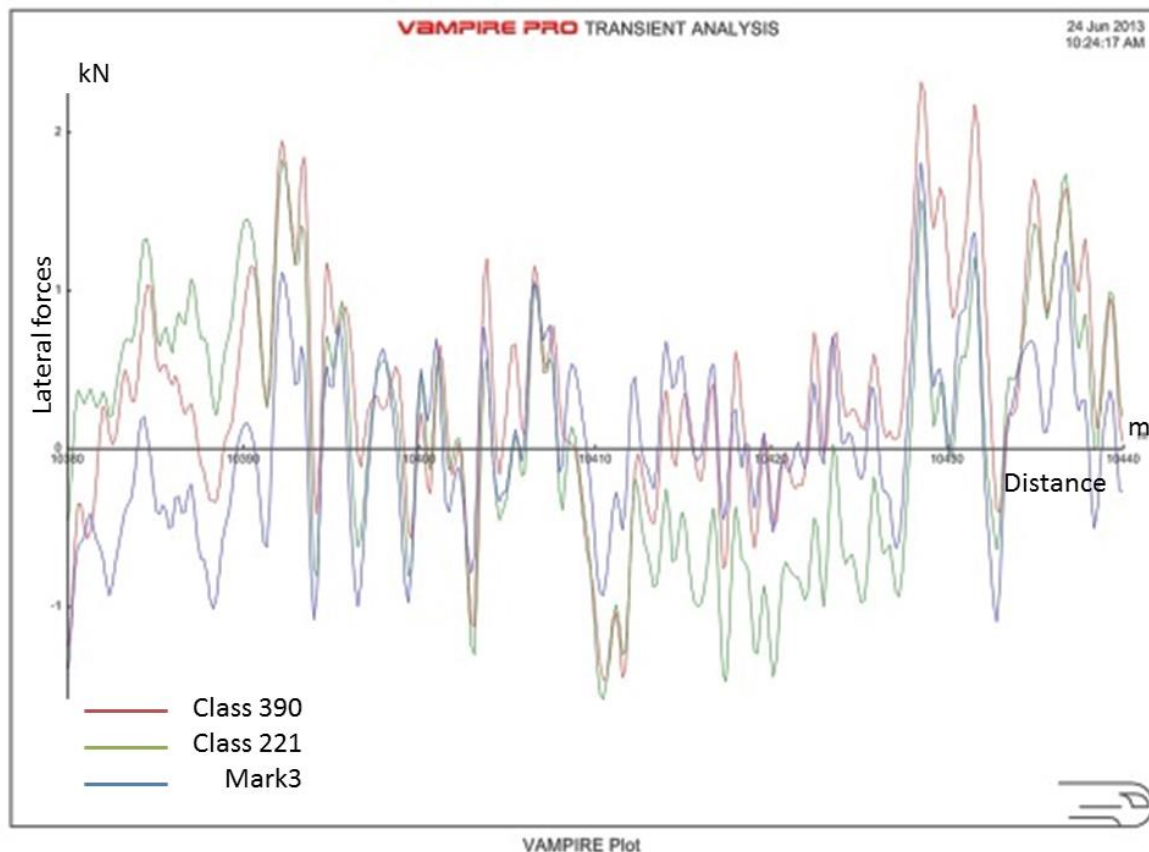
Different sub-systems of the vehicle-track dynamic system are studied separately and the influences of them on the track lateral deterioration are discussed. As a result, the triggering limits in regard to the influences by vehicles, wheel-rail contact conditions and the track system itself can be identified. For quantities varying both positively and negatively like track deterioration, RMS is a good measure of the amplitude. Therefore, the RMS values are used to measure and represent the overall amplitude and amplitude change of the irregularities.

5.1 Effect of vehicles

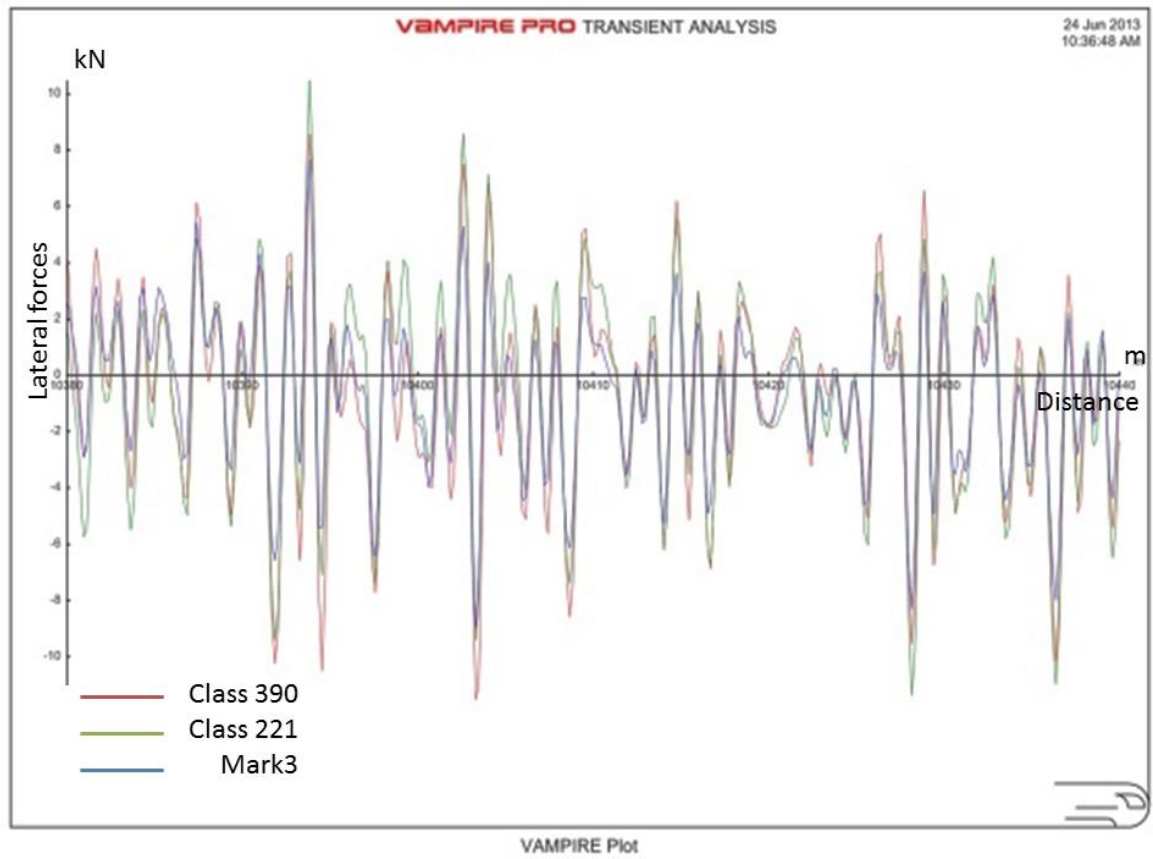
The vehicle dynamic impact on track lateral deterioration is discussed in this section. All parameters used in Chapter 5.1 are those used in the validation for measured data S15 in dataset D8 referred to in Chapter 4. The influences of different types of vehicles, running speed of the vehicles and different wheel rail contacts will be discussed.

5.1.1 Effect of different types of vehicles

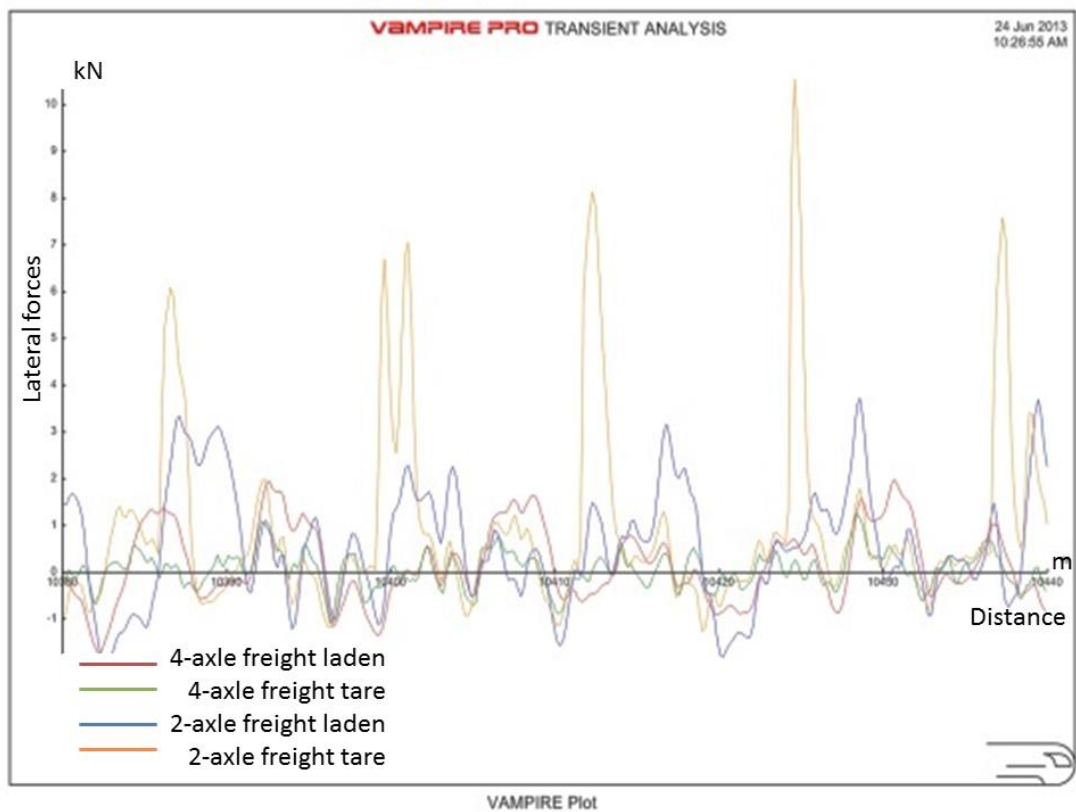
The simulation results for all the vehicle models Veh.1 to Veh.7 will be discussed in this section. As different vehicles have different suspension designs, weight and wheel profiles, the dynamic wheel-rail forces will be quite different. Figure 5-1 a, b, c and d shows the VAMPIRE® simulation results of the vertical and lateral dynamic wheel-rail forces of the leading axle left wheel for both passenger (Veh.1-3) and freight vehicles (Veh.4-7). The vertical dynamic force does not include the static vertical load.



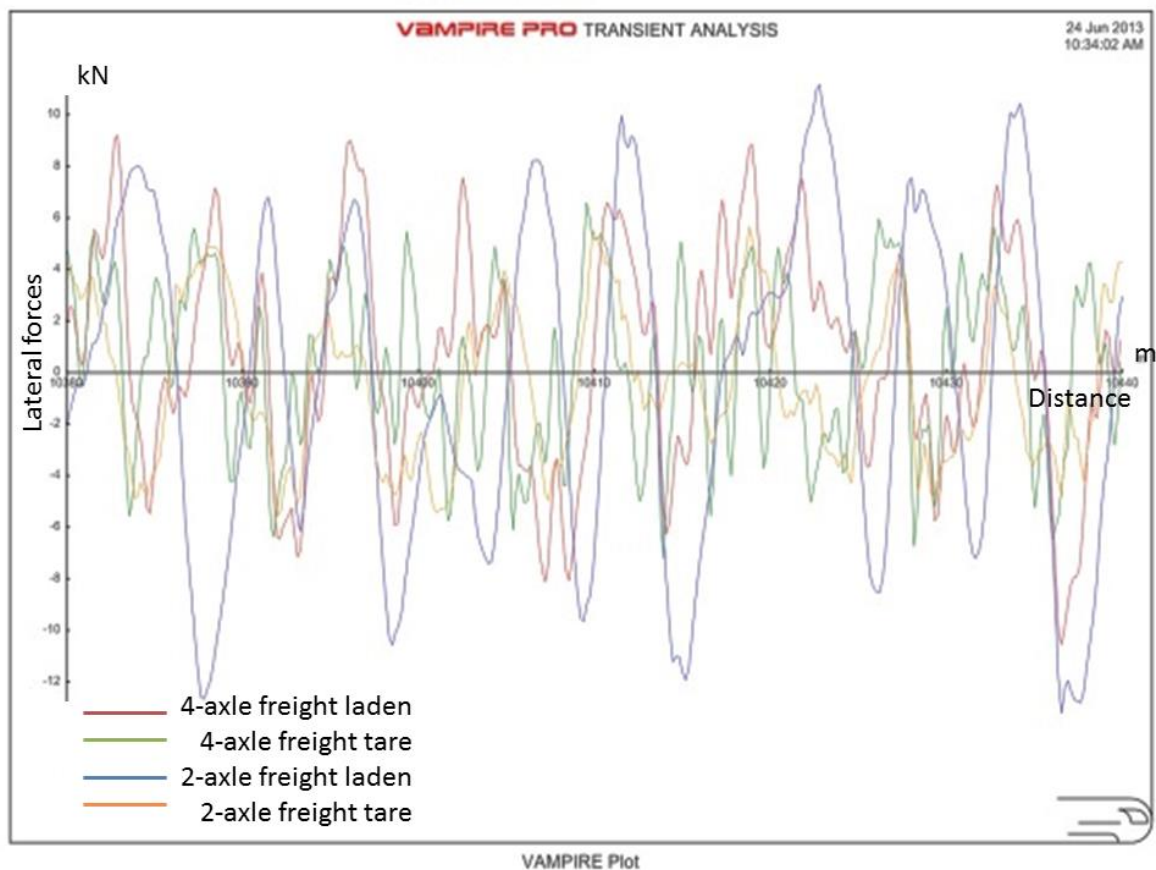
a) Passenger vehicle lateral forces



b) Passenger vehicle vertical forces



c) Freight vehicle lateral forces

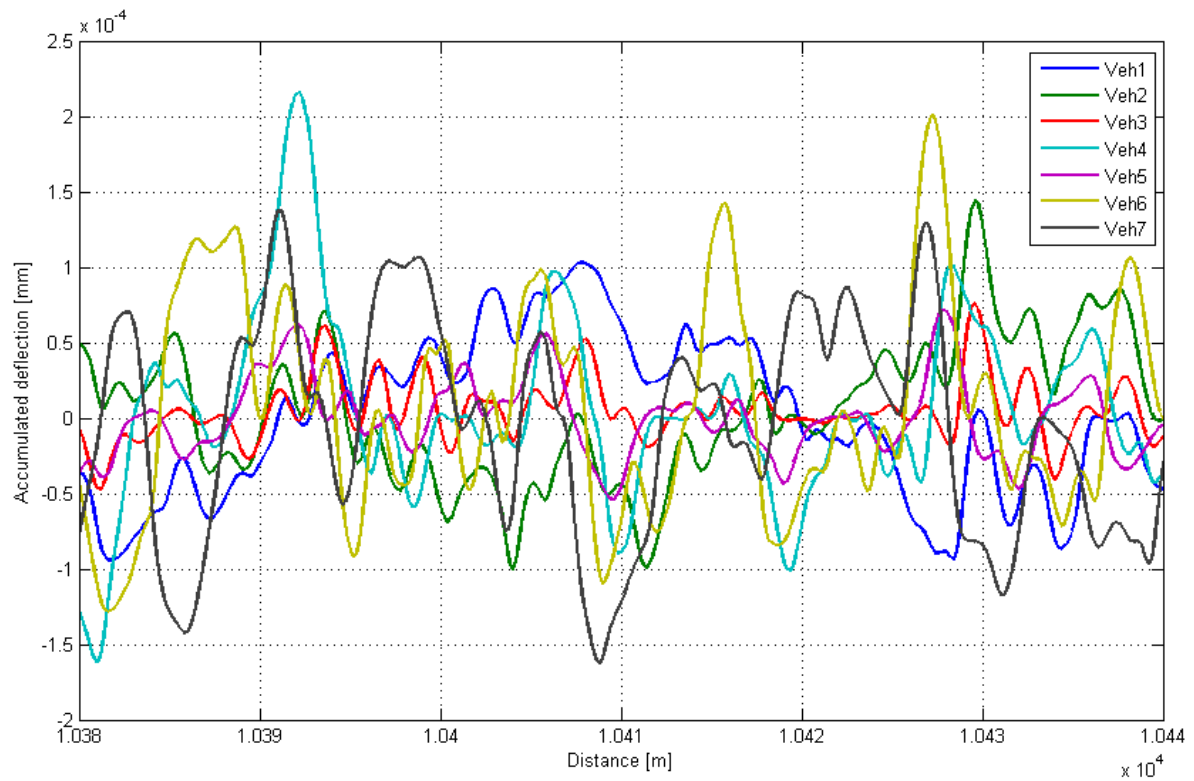


d) Freight vehicle vertical forces

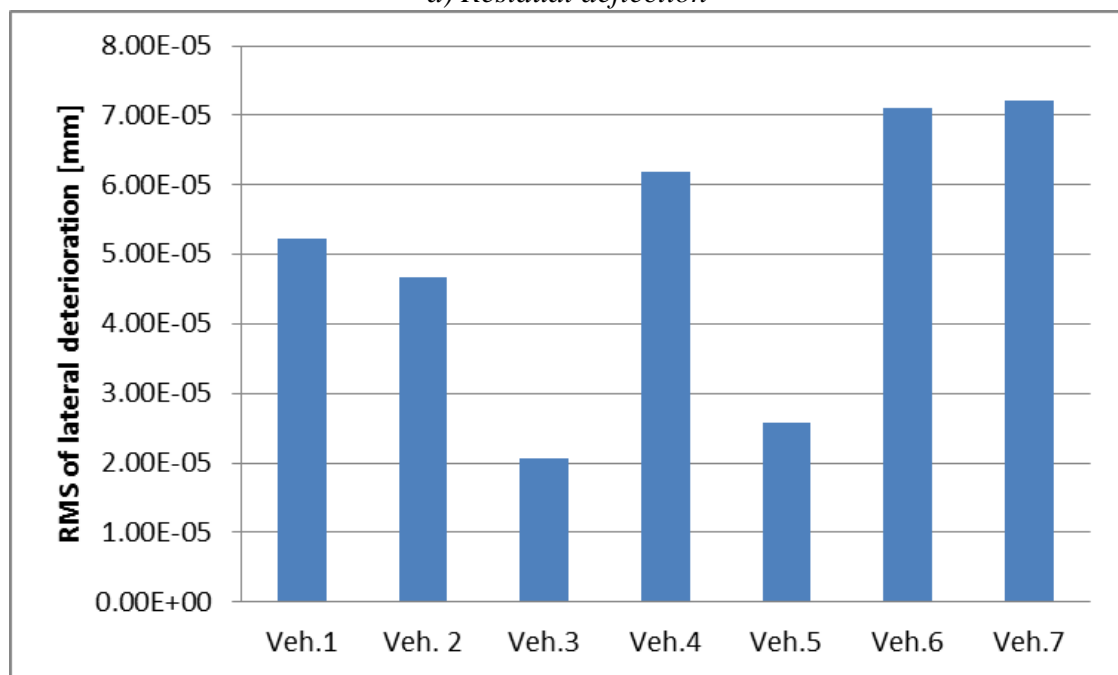
Figure 5-1 Leading left wheel lateral and vertical wheel-rail dynamic forces of passenger and freight vehicles

It can be found that due to the more effective suspension design, the lateral wheel-rail forces of 4-axle vehicles have a peak amplitude of less than 2 kN, and are much smaller than the 2-axle freight vehicles with a peak amplitude of roughly 10 kN. It can also be found that the freight vehicles produce a higher frequency large force while the passenger vehicles create a lower frequency small force. This may be caused by the combination of the difference between the suspension design, the wheel-rail profiles combination and the running speeds.

According to Equation 60 to Equation 62 in Section 4.3.3, the distributed dynamic lateral forces have to exceed a certain dynamic lateral resistance to create a residual deflection or a sliding failure. These lateral resistance limits are all a linear function of the vertical load on the sleeper and the sleeper-ballast friction coefficient. Therefore, an increase of the lateral forces will not necessarily lead to an increase of lateral deterioration. The simulation result of the track deflection caused by different vehicles for one vehicle pass on the tangent track is shown in Figure 5-2.



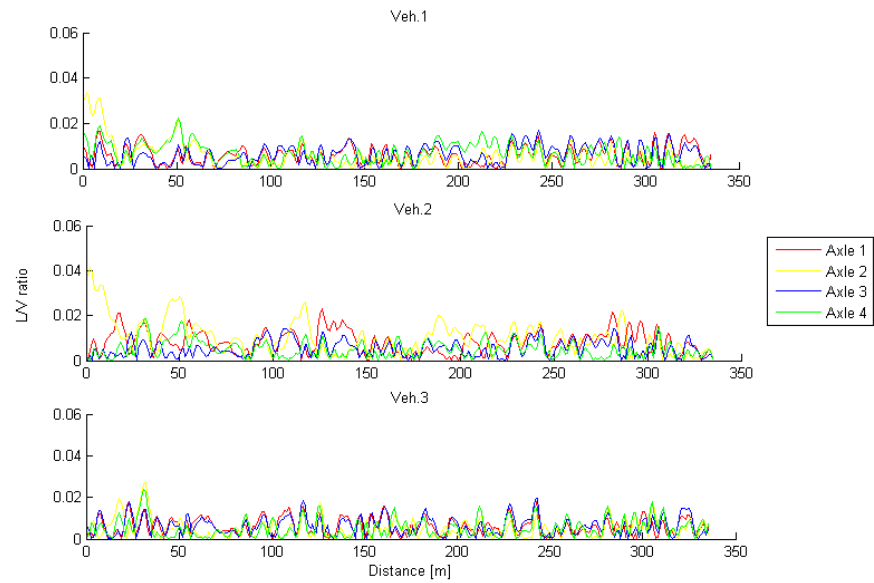
a) Residual deflection



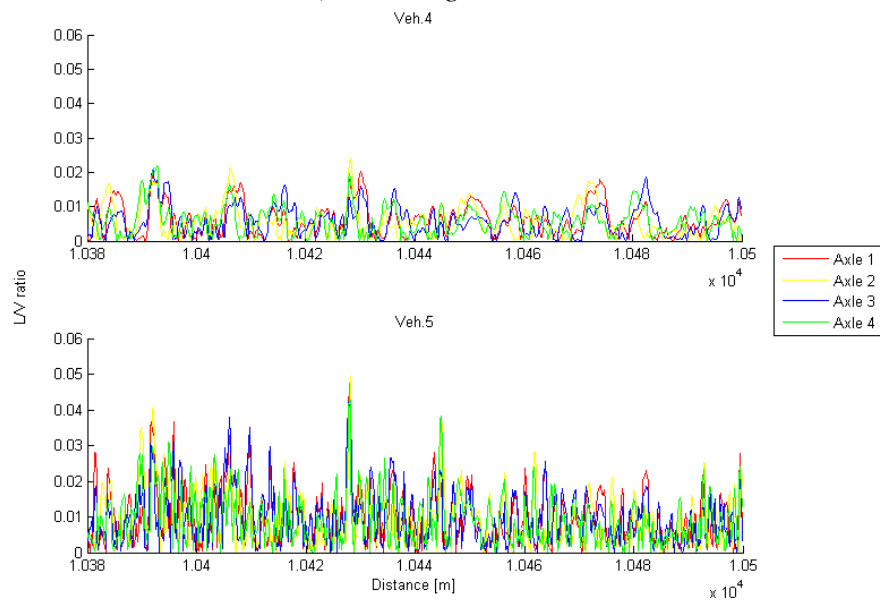
b) RMS of residual deflection

Figure 5-2 Track residual deflection caused by one pass of different vehicles

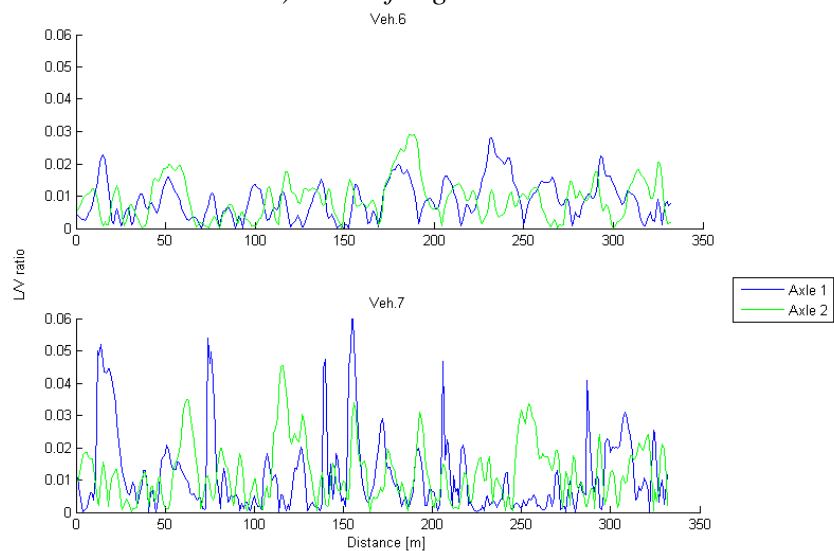
It can be seen that generally the freight vehicles Veh.6 and Veh.7 have the biggest impact. Since the L/V ratio is considered the biggest impact factor on the residual deflection, the dynamic lateral to vertical loading ratios for all vehicles are calculated, and shown in Figure 5-3.



a) Passenger vehicles



b) 4-axle freight vehicles



c) 2-axle freight vehicles

Figure 5-3 Lateral to vertical loading ratio delivered from vehicles to rail

Figure 5-4 is the summary of the average RMS of lateral forces and L/V ratio from different vehicles. For the passenger vehicles Veh.1 to Veh.3, Veh.1 has the largest lateral forces and L/V ratio while Veh.3 has the smallest. Therefore, the resulting residual deflection caused by Veh.1 is the largest, as shown in Figure 5-2 b). On the other hand, the laden freight vehicles have much smaller L/V ratios than tare, but create larger residual deflections. The reason is that the laden vehicles have higher lateral forces. Therefore, it can be deduced that the residual deflection depends on both the magnitude of the lateral forces and the L/V loading ratio.

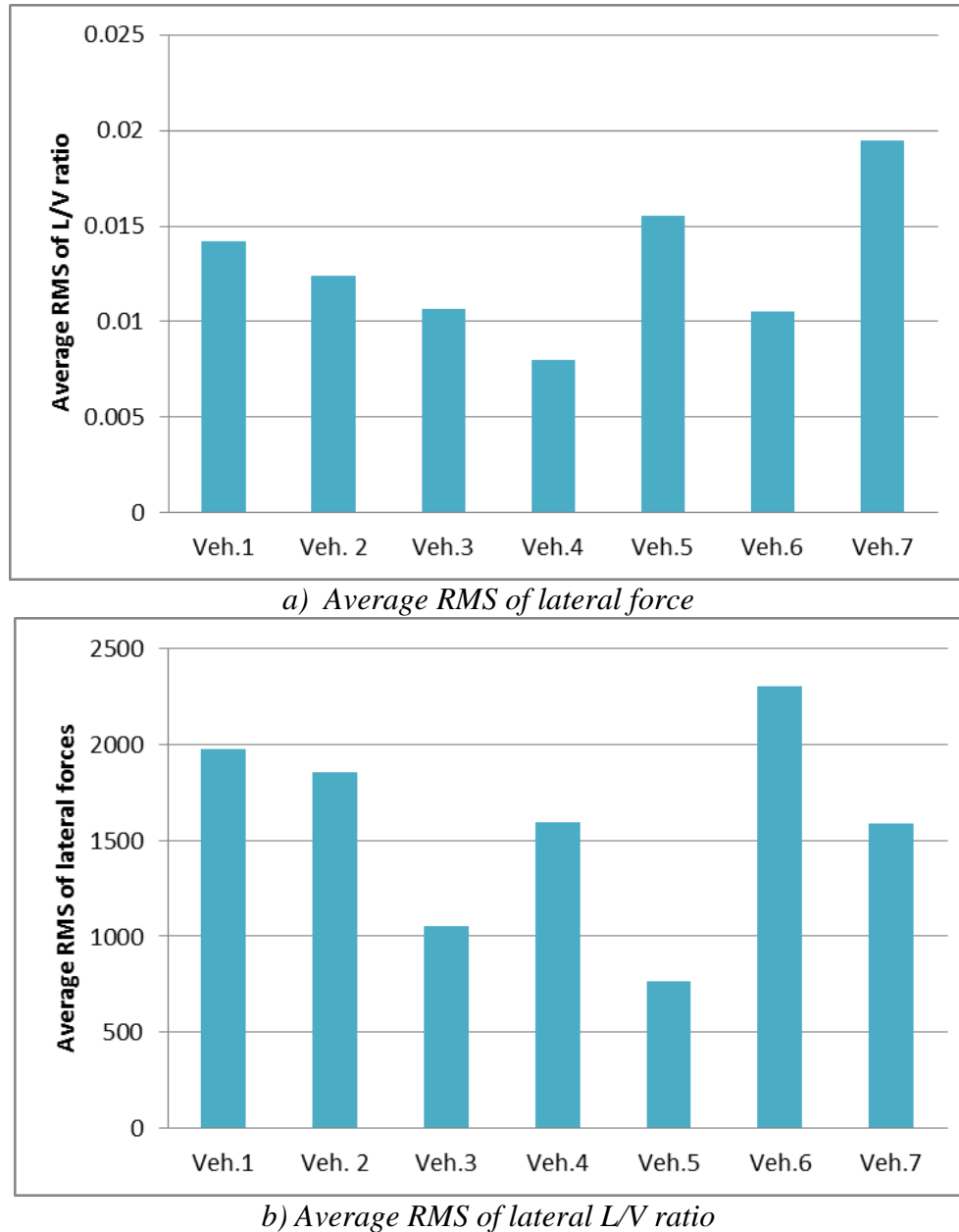


Figure 5-4 Summary of average lateral forces and L/V ratio of different vehicles

Considering the dynamic forces experienced by each sleeper, the influence factors can be determined. According to Chapter 4.3.3, the residual deflection under certain lateral and vertical forces can be calculated as described in Figure 5-5. Therefore, the lateral residual deflection can be calculated using Equation 64.

$$w_r = w_{re} - w = \left(\frac{F_L - c_r \cdot w_{re}' - b}{k_2} \right) - \left(\frac{F_L - c_r \cdot w'}{k_1} \right) \quad \text{Equation 64}$$

Substitute the values in Figure 5-5 into Equation 64 and rearranging gives:

$$w_r = \frac{w_e}{\theta} \cdot \left(\frac{F_{Lstiff1} - \theta \cdot F_{Lstiff2}}{\mu_r \cdot F_V + F_e} - (1 - \theta) \right) \quad \text{Equation 65}$$

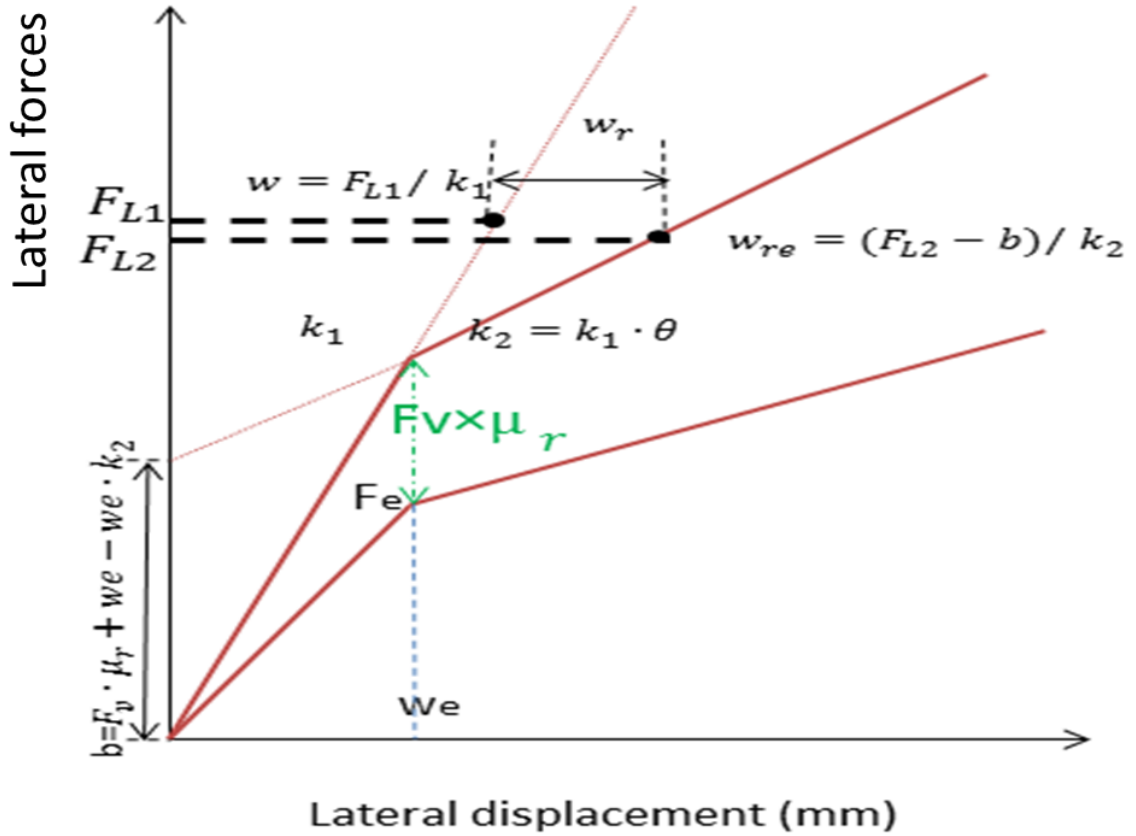


Figure 5-5 Residual deflection calculation

With the complicated vehicle-track dynamic interactions, it is difficult to solve the equation and establish a simple equation for the force influence factor of the lateral residual deflection. If the damping is not considered, the only influence factors are the L/V loading ratio (F_L/F_V) and distributed lateral forces on the sleeper (F_L).

$$w_r = w_e \cdot \left(\frac{1}{\theta} - 1 \right) \left(\frac{1}{\frac{\mu_r}{F_{Lstiff}/F_V} + \frac{F_e}{F_{Lstiff}}} - 1 \right) \quad \text{Equation 66}$$

For vehicles with similar lateral forces, the larger the L/V ratio becomes the larger the residual deflection is. Meanwhile, vehicles with a similar L/V ratio, but larger lateral forces result in a larger lateral residual deflection. For vehicles with different L/V ratios and lateral forces, it is better to use the vehicle-track model to simulate the influences. For the WCML data, the 2-axle vehicles give the largest residual deflection for each vehicle pass, even though the speed limit for these vehicles is lower.

5.1.2 Effect of different running speed

The running speed of the vehicle has a significant influence on the vehicle-track dynamics, and different types of vehicles have different speed limits. Veh.1 is chosen to investigate how the running speed of the vehicle can influence the lateral residual deflection. The speeds that will be considered are shown in Table 5-1. All the simulations are under 1000 vehicle passes.

Table 5-1 Different vehicle running speed

	mph	m/s
-20%	80	35.763
-15%	85	37.998
-10%	90	40.234
-5%	95	42.469
Original	100.00	44.704
+5%	105	46.939
+10%	110	49.174
+15%	115	51.410
+20%	120	53.645

Figure 5-6 shows the resulting residual deflection for the different speeds mentioned above. There is no obvious relationship that can be determined from these results.

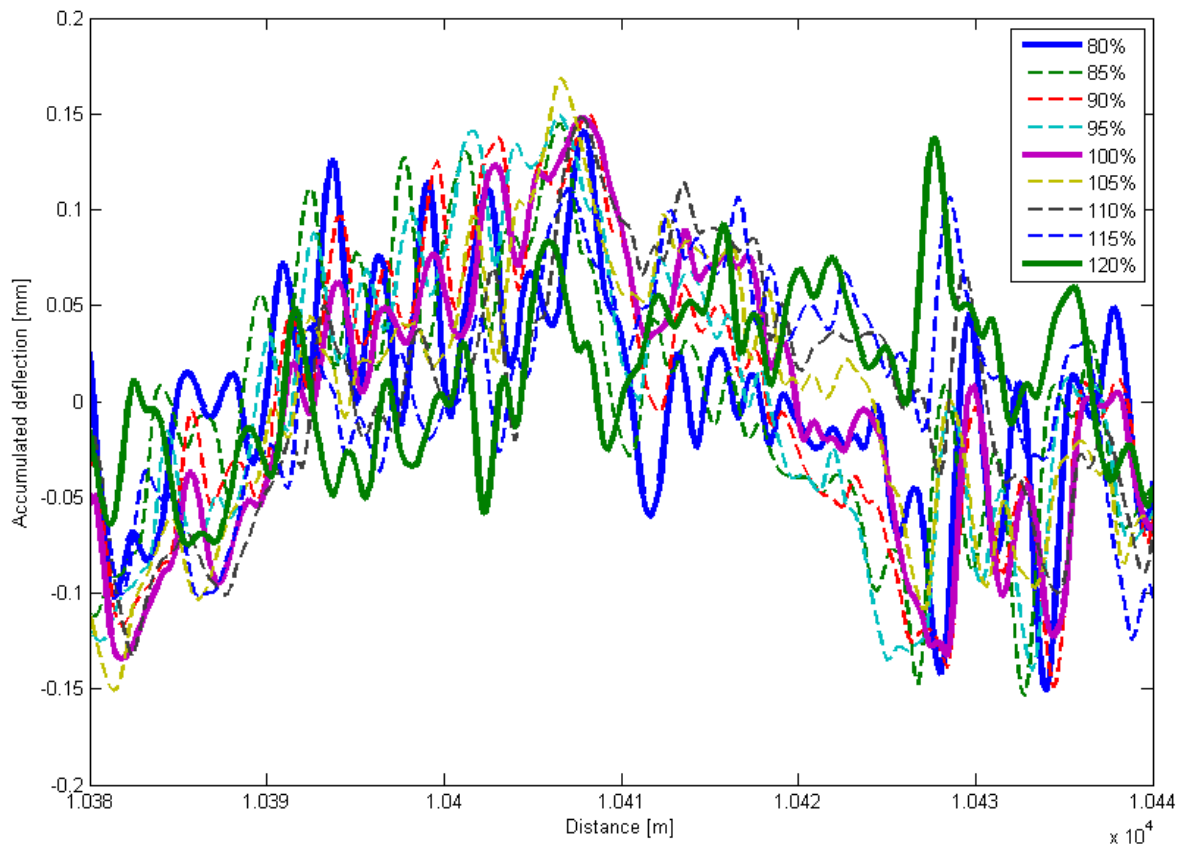
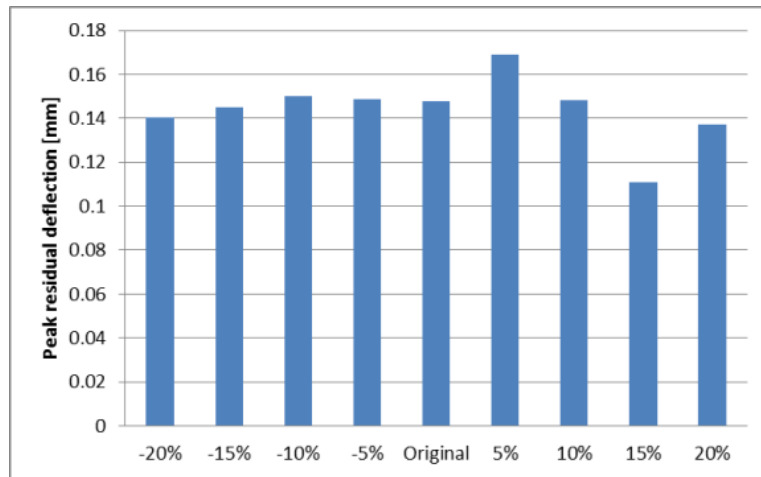
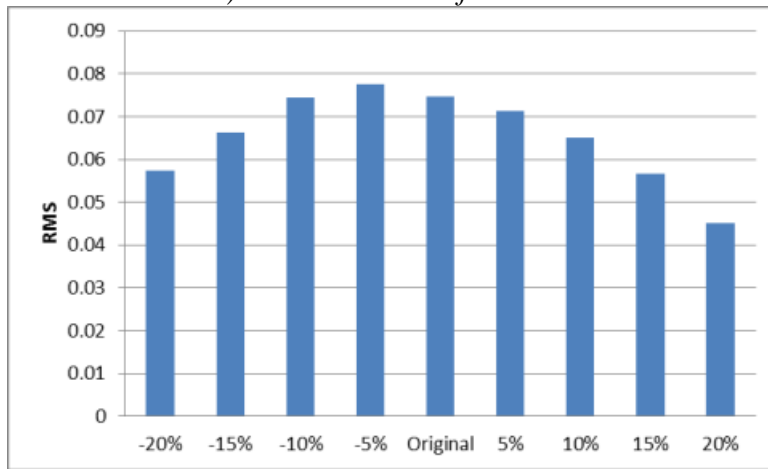


Figure 5-6 Residual deflection at different speed

Figure 5-7 illustrates the peak residual deflections obtained from running the vehicle at different speeds. No clear trend can be found for the peak residual deflection although the maximum RMS of the residual deflection is the largest at 95 mph.



a) Peak residual deflections



b) RMS of residual deflections

Figure 5-7 Peak and average residual deflection at different speed

It is informative to examine the impact of speed on the residual deflection in the spatial domain. Figure 5-8 and Table 5-2 summarise the lateral force PSD peak changes in spatial domain.

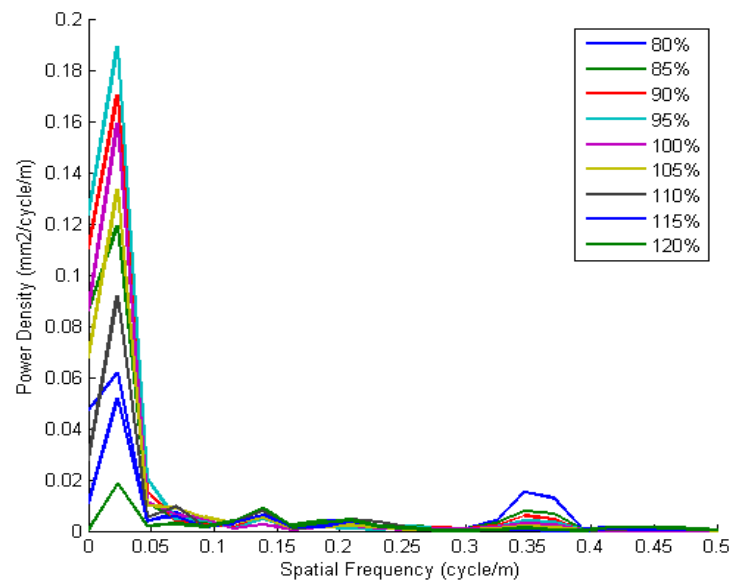
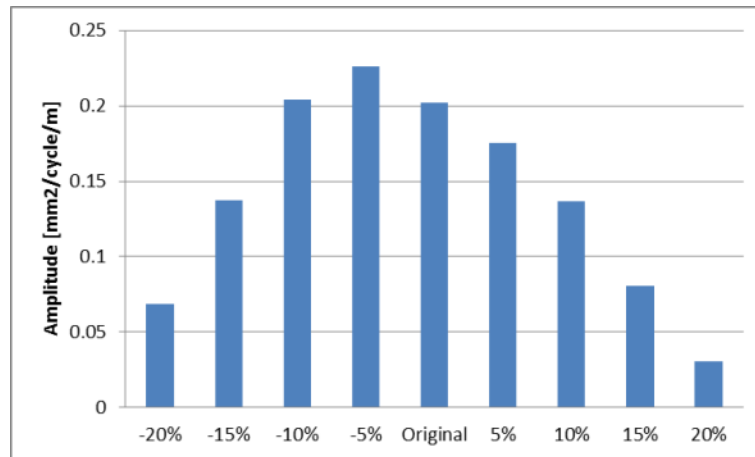


Figure 5-8 PSD of residual deflections resulted by different speeds

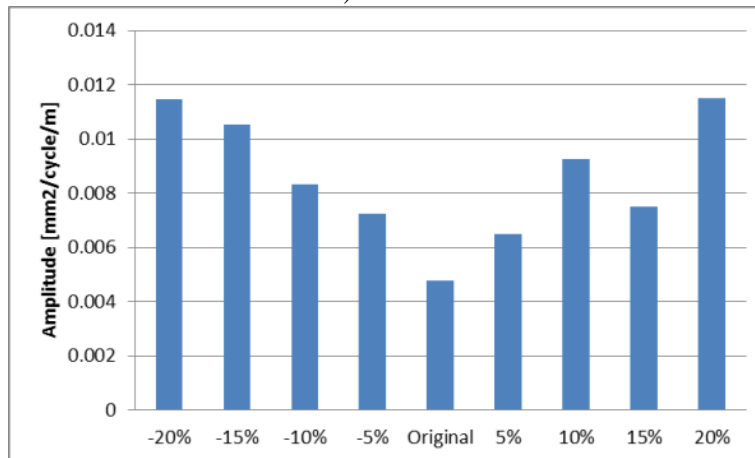
Table 5-2 Summary of two peaks in PSD of residual deflections

	Peak 1			Peak2		
	Frequency [cycle/m]	Wavelength [m]	Amplitude [mm ² /cycle/m]	Frequency [cycle/m]	Wavelength [m]	Amplitude
-20%	0.01953	51.2033	0.0687	0.1367	7.3153	0.01148
-15%	0.01953	51.2033	0.1376	0.1367	7.3153	0.01052
-10%	0.01953	51.2033	0.2040	0.1367	7.3153	0.00832
-5%	0.01953	51.2033	0.2263	0.1367	7.3153	0.00724
Original	0.01953	51.2033	0.2020	0.1367	7.3153	0.00479
+5%	0.01953	51.2033	0.1755	0.1367	7.3153	0.00651
+10%	0.01953	51.2033	0.1364	0.1367	7.3153	0.00926
+15%	0.01953	51.2033	0.0809	0.1367	7.3153	0.00752
+20%	0.01953	51.2033	0.0306	0.1367	7.3153	0.01149

It is found that the wavelengths of the first two peaks do not change, while the power density of the residual deflection at these peaks does change. The 1st peak PSD change agrees with the result of the average residual deflection change, while the 2nd peak PSD has the opposite trend. As the peak PSD of the 1st peak is much bigger than the 2nd, the influence of the 1st peak is much larger on the residual deflection.



a) Peak 1



b) Peak 2

Figure 5-9 Two peak power densities change

The change of the vehicle speed does not necessarily bring about a wavelength change in the residual deflection, however, it creates small amplitude change to the track deterioration. There will be a critical speed that creates the peak residual deflection and reducing or increasing the vehicle speed, within permitted operational speed, can reduce the residual deflection.

5.1.3 Effect of axle passages

The effect of the different vehicles on the residual deflection taking into account the actual traffic mix by factoring the obtained residual deflection for one pass with the number of axle passes is shown in Figure 5-10. It shows that Veh.1 has the major influence on the lateral track irregularity growth compared to other vehicles. This is due to the fact that this vehicle makes up more than 95% of the traffic on this section of the WCML, as shown in in Table 5-3.

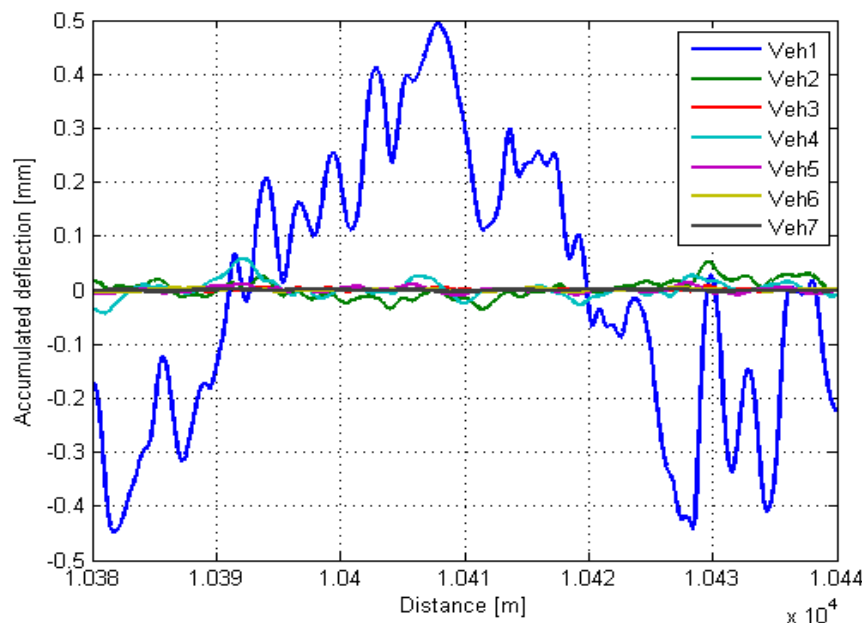


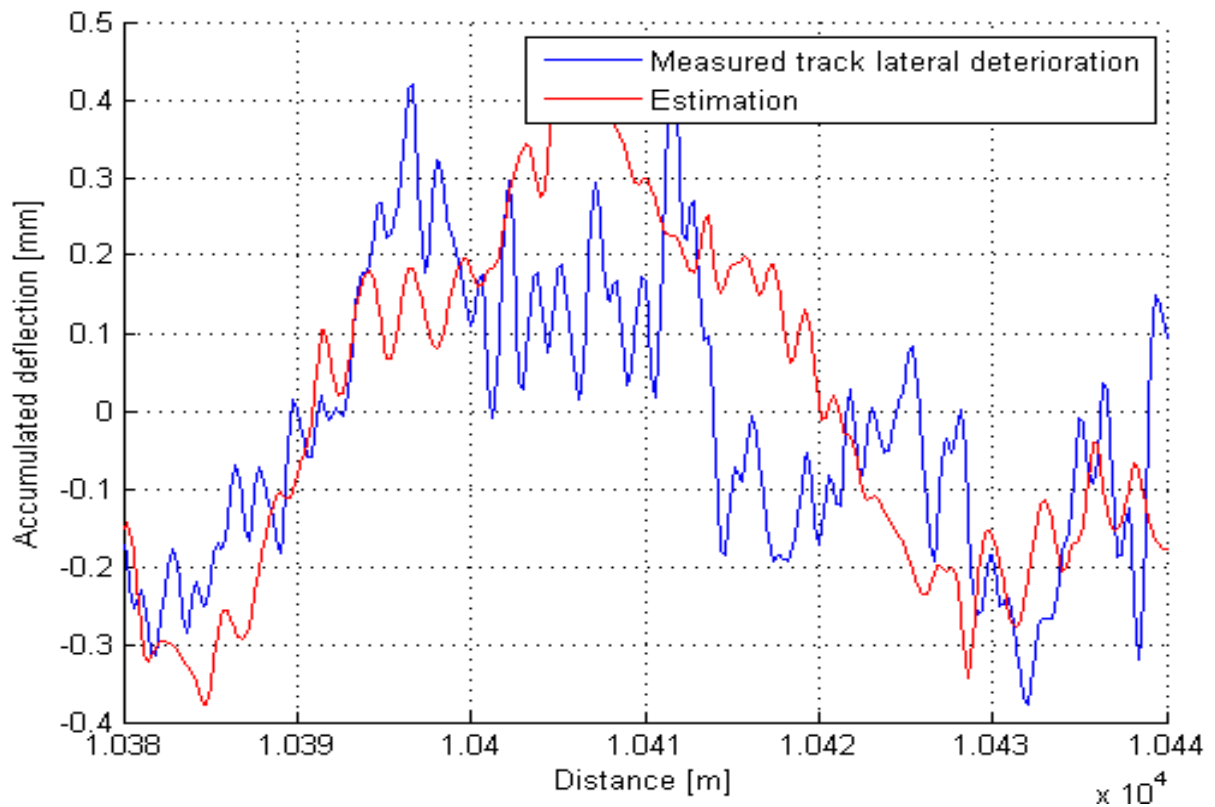
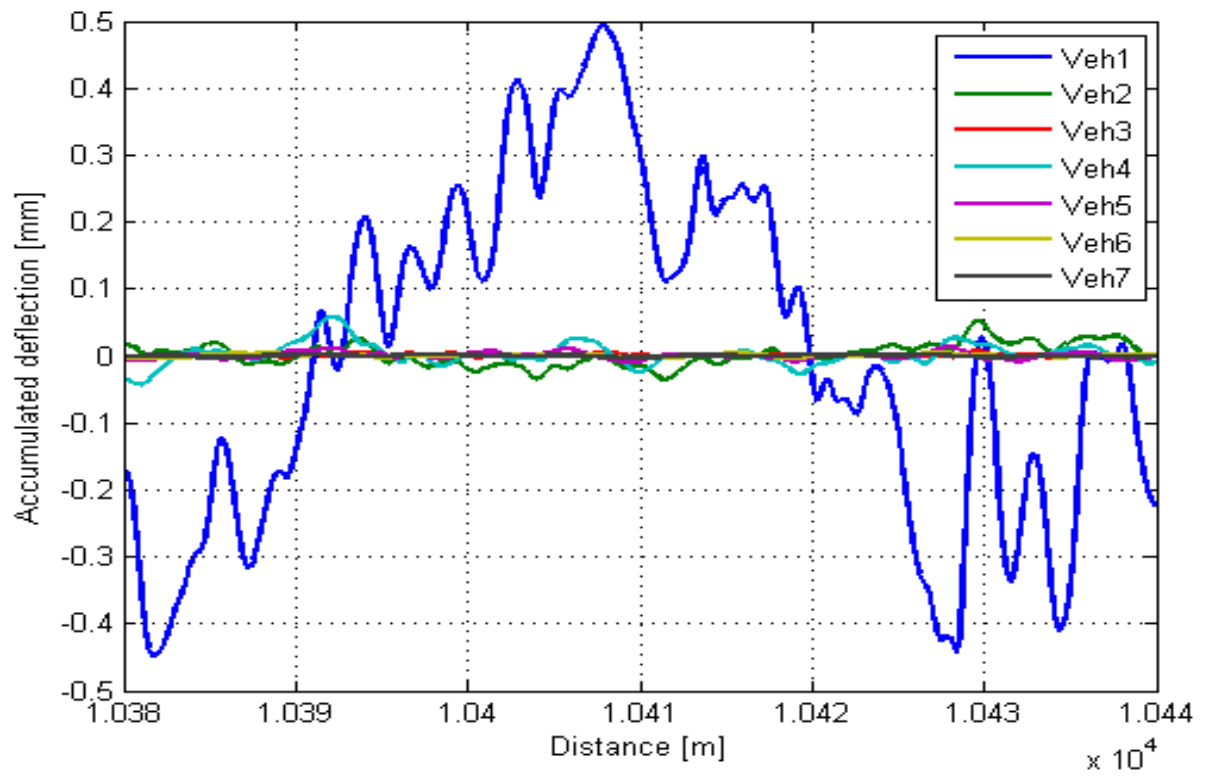
Figure 5-10 Residual deflection caused by different vehicles

Different vehicles have different dynamic behaviour thereby creating different lateral damage to the track. From the results shown in Figure 5-2 a), Veh.2 appears to create a lateral deterioration with a negative correlation to the deterioration created by Veh.1. Interestingly, a different traffic mix can help to reduce the lateral deterioration created by different vehicles. To illustrate this, the traffic pattern has been altered between Veh.1 and Veh.2; the resulting changed D8 – D9 traffic is shown in the table below.

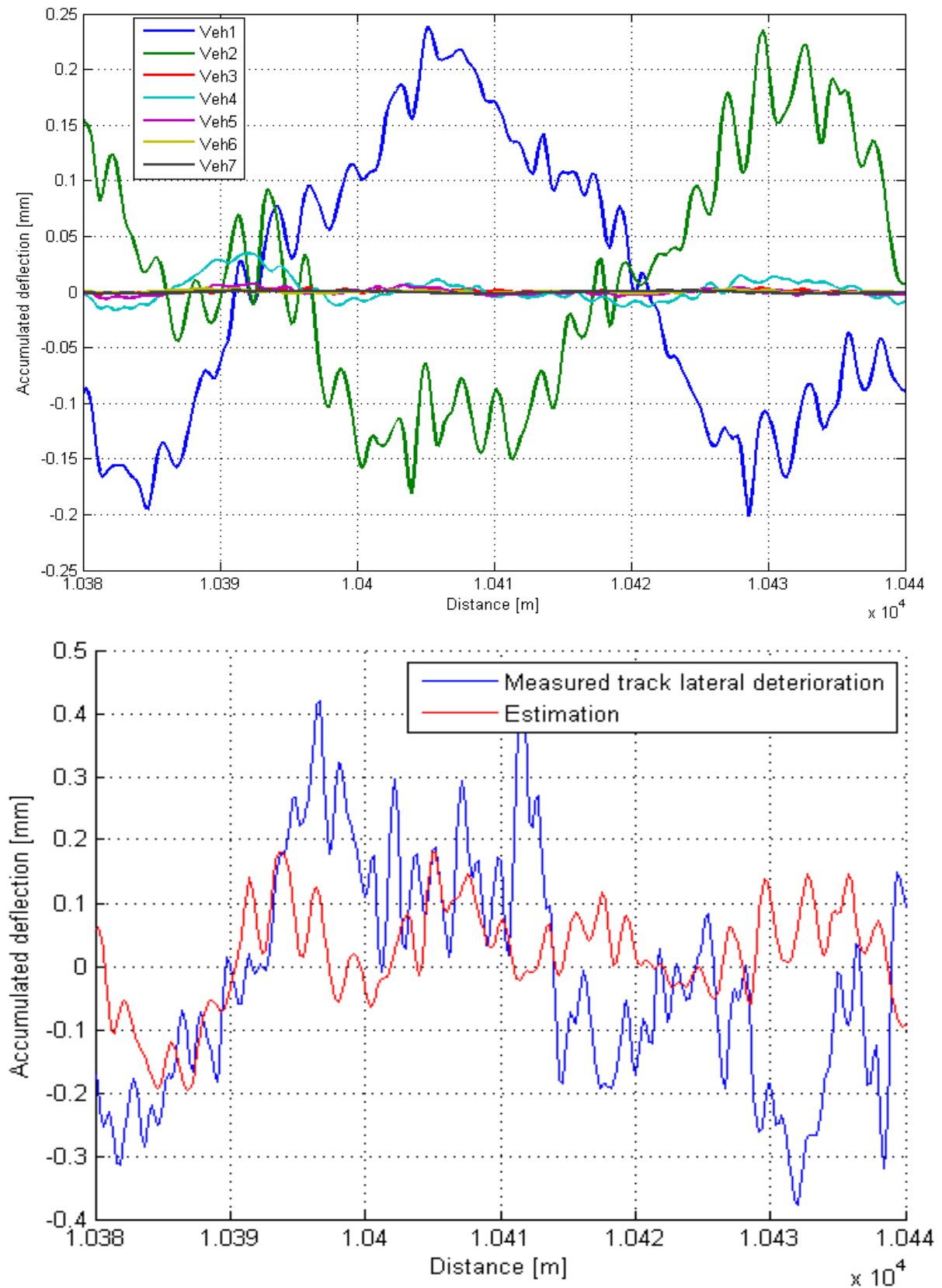
Table 5-3 Axle passages for each vehicle

	Veh.1	Veh.2	Veh.3	Veh.4	Veh.5	Veh.6	Veh.7
D8 – D9	19023	1416	346	1064	739	52	36
Changed D8 – D9	10219	10219	346	1064	739	52	36

Figure 5-11 shows the results of the track lateral deterioration under the actual and optimised traffic scenario. It can be seen that the lateral deterioration created by Veh.1 is almost opposite to the deterioration created by Veh.2, so more axle passages of Veh.2 can effectively reduce the deterioration created by Veh.1. The SD of the track section drops to 0.4283 from 0.5476 by changing the traffic mix.



a) Actual traffic scenario (D8-D9)



b) Designed traffic scenario (Changed D8-D9)

Figure 5-11 Track deterioration under actual traffic and designed traffic scenario

5.1.4 Conclusion

The lateral damage to the track caused by the vehicle depends on both the L/V ratio and the lateral loads but is a complicated dynamic process that cannot be easily expressed through a simple function. It is therefore more sensible to establish the damage to the track from each vehicle by carrying out a dynamic simulation. Two-axle freight vehicles are found to produce the most lateral track damage due to their high axle load, simple suspension design and resulting dynamic behaviour. The change of vehicle speed does not necessarily result in a wavelength change of the residual deflection but does create amplitude changes of the track deterioration. Within a certain speed range, there will be a critical speed that creates a peak in the residual deflection and changing the vehicle speed can reduce the residual deflection. The traffic mix can be optimised according to different vehicle dynamics in order to reduce the lateral deterioration.

5.2 Effect of different wheel-rail contact conditions

Over time, wear processes affect the profile shape of the rails and wheels. In order to examine the effects of worn rail and worn wheel profiles on the vehicle-track dynamics some comparisons are made by running the vehicle-track lateral simulation with different combinations of wheel and rail profiles. The first section discusses the impact of worn rail profiles by using actual profiles measured on different sections of track in rail-wheel contact combination set 1. The second section examines the effect of worn wheel profiles by using actual profiles measured on different vehicles in rail-wheel contact combination set 2. The third section analyses the impact of wheel profiles suffering from different amounts of wear as measured on a particular Class390 train in rail-wheel contact combination set 3. The Class 390 vehicle model previously described and the measured track data S15 in dataset D8 are used in the simulations in this section.

5.2.1 Effect of worn rails measured in different track sections

The rails used in these simulations are actual measured rail profiles taken from the WCML at different locations on the Up Fast Line, around 70 miles, from London. The wheel-rail contact profiles discussed in this section are listed in Table 5-4. All of the rail profiles are in what is considered to be a slightly worn condition.

Table 5-4 Rail-wheel profile combination 1

	Num.	Rail profile	Wheel profile
Rail-wheel contact set 1	C1_1	New CEN60-20 rail	New br-p8 wheel
	C1_2	Measured worn CEN 60-20 rail 1	
	C1_3	Measured worn CEN 60-20 rail 2	
	C1_4	Measured worn CEN 60-20 rail 3	

Figure 5-12 is simulated lateral track deterioration using the different measured rails.

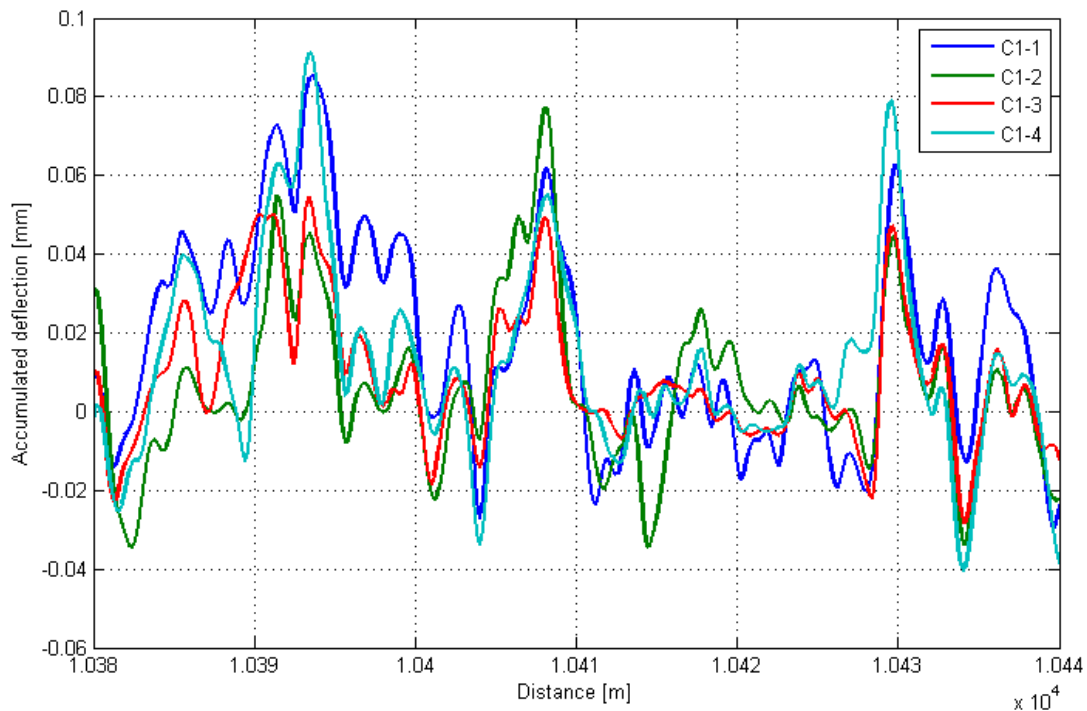
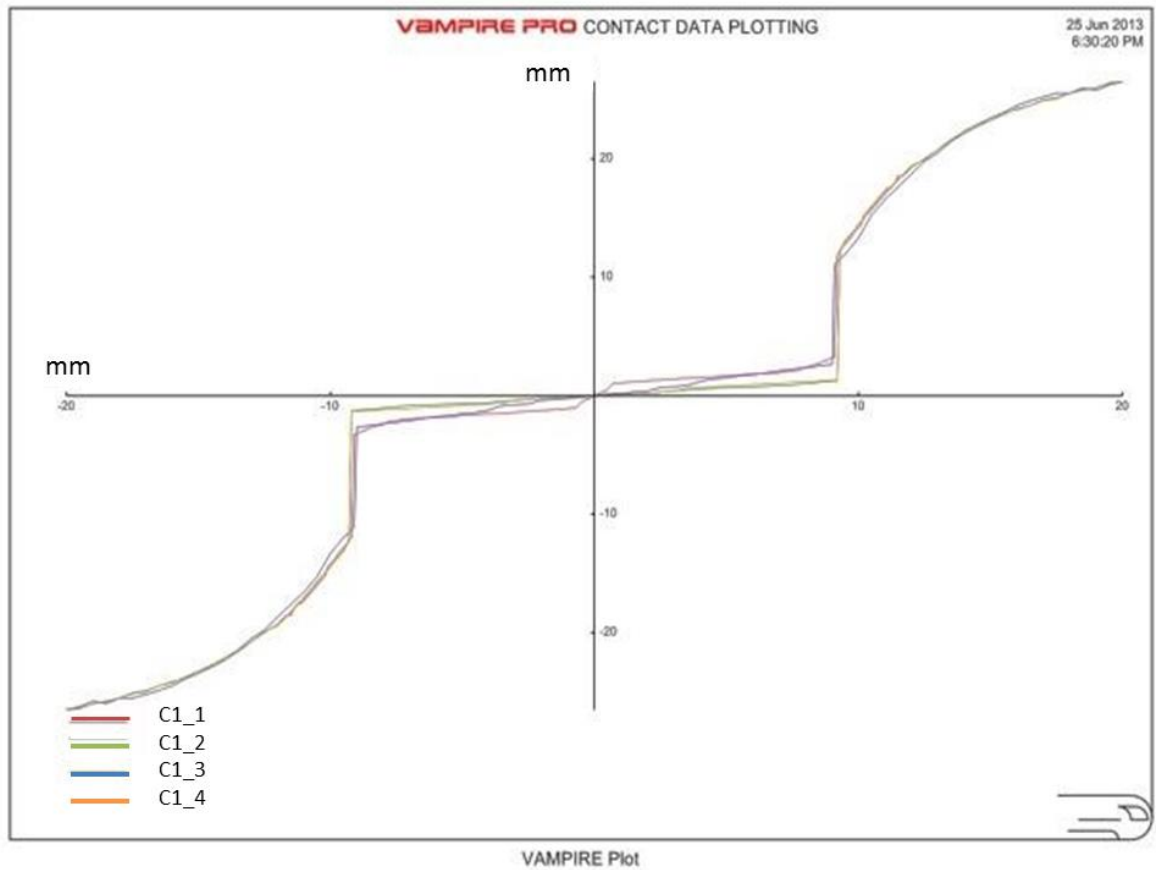
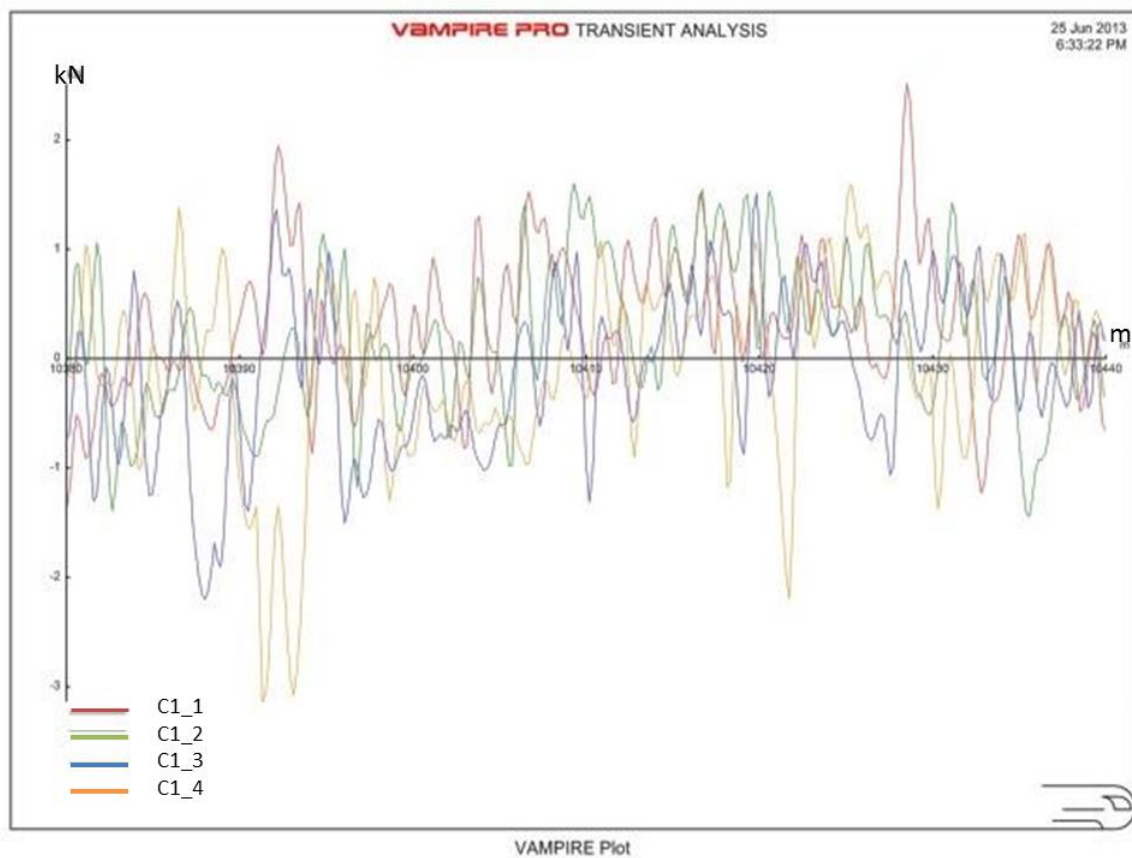


Figure 5-12 Track lateral deterioration with different worn rails

The graph shows that while similar deterioration occurs at similar locations, the amplitude of the deflection varies with different worn rail profiles. Small differences of rolling radius difference due to rails in different wear condition can lead to very different dynamic lateral forces, as shown in Figure 5-13.



a) Rolling radius difference all contact files



b) Leading left wheel lateral forces

Figure 5-13 Leading left wheel lateral forces with different rail profiles

Figure 5-14 and Table 5-5 give the PSD results of the lateral track deterioration with different worn wheel profiles. They show that the dominant wavelength of the lateral track deterioration changes due to different vehicle lateral dynamics. The changes of the lateral deterioration are mainly in the short wavelengths which are less than 18 m in these results. The condition of the worn rail has a strong influence on the track lateral deterioration.

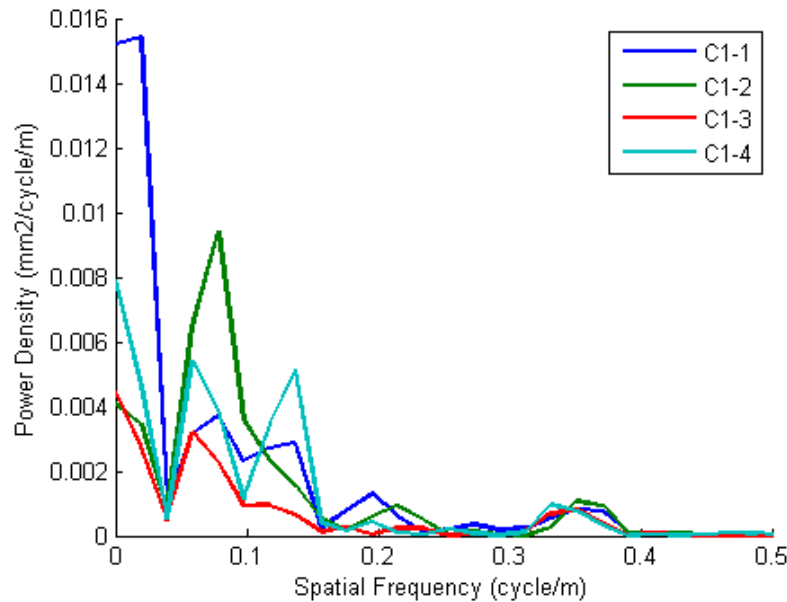


Figure 5-14 PSD of track lateral deterioration with different rail profiles

Table 5-5 Peak PSD of track lateral deterioration with different rail profiles

	Peak 1		Peak 2	
	Frequency (Hz)	Wavelength (m)	Frequency (Hz)	Wavelength (m)
New CEN60-20 rail	0.0781	12.7992	0.1367	7.3153
Measured worn CEN 60-20 rail 1	0.0781	12.7992	0.2148	4.6655
Measured worn CEN 60-20 rail 2	0.0586	17.0678	0.1172	8.5624
Measured worn CEN 60-20 rail 3	0.0586	17.0678	0.1367	7.1529

5.2.2 Effect of worn wheels measured on different vehicles

The average worn wheel profiles of different vehicles running on ECML are obtained from the software VTISM [148].

Table 5-6 Rail-wheel profile combination 2

Rail-wheel contact set 2	Num.	Rail profile	Wheel profile
	C2_1	New CEN60-20 rail	New br-p8 wheel
	C2_2		Class373 worn br-p8 wheel
	C2_3		Mark4 worn br-p8 wheel
	C2_4		Class 43 worn br-p8 wheel

Figure 5-15 shows the simulated lateral deterioration with different measured worn wheels.

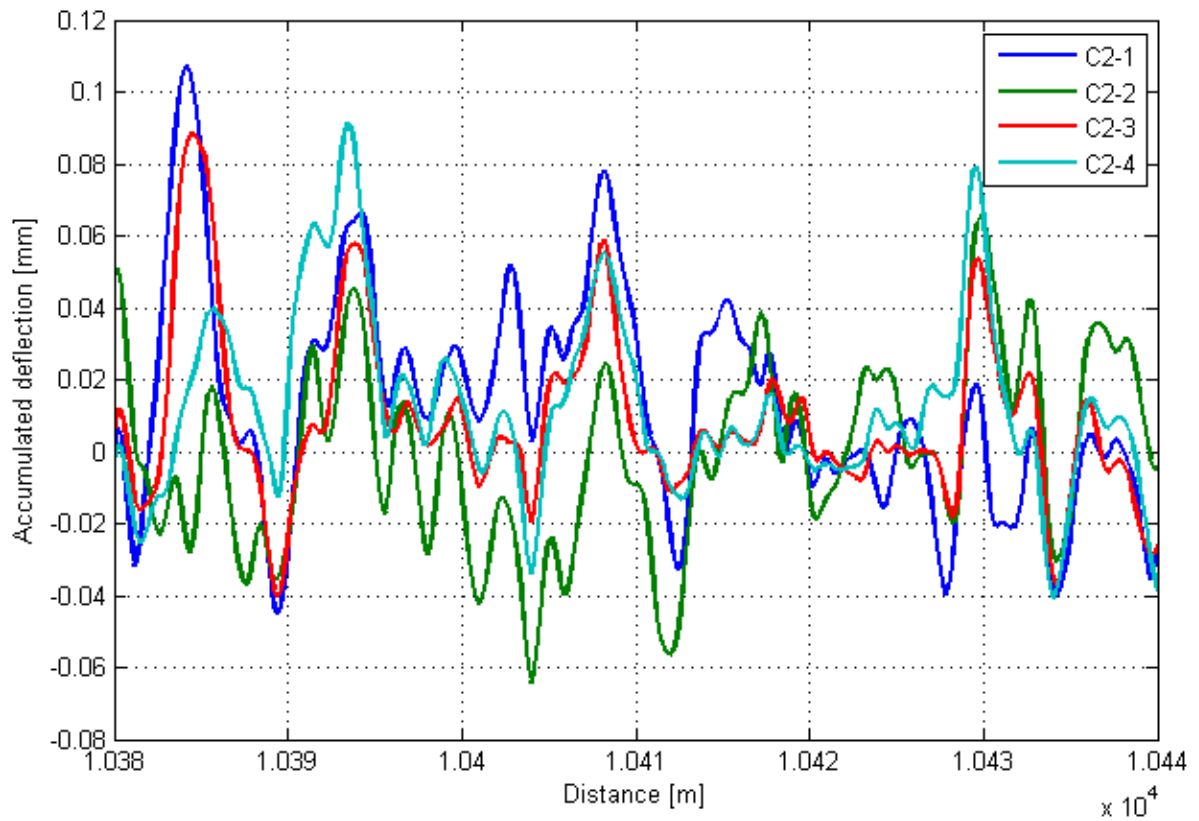
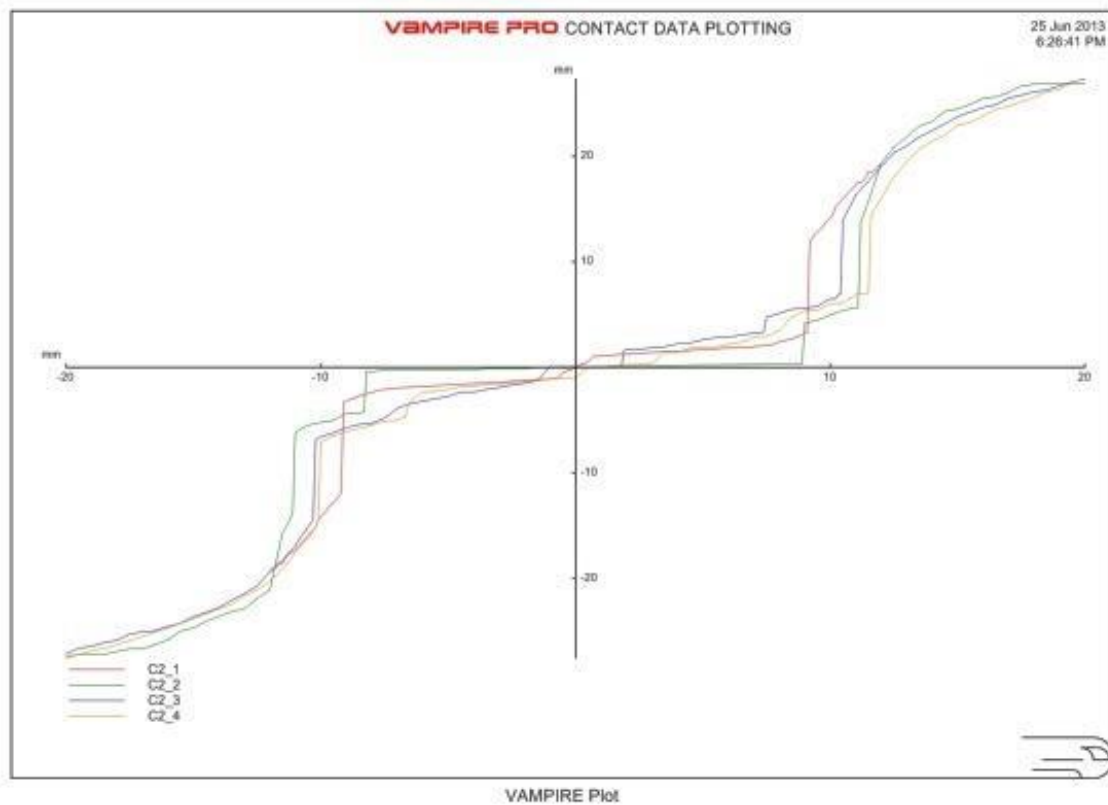
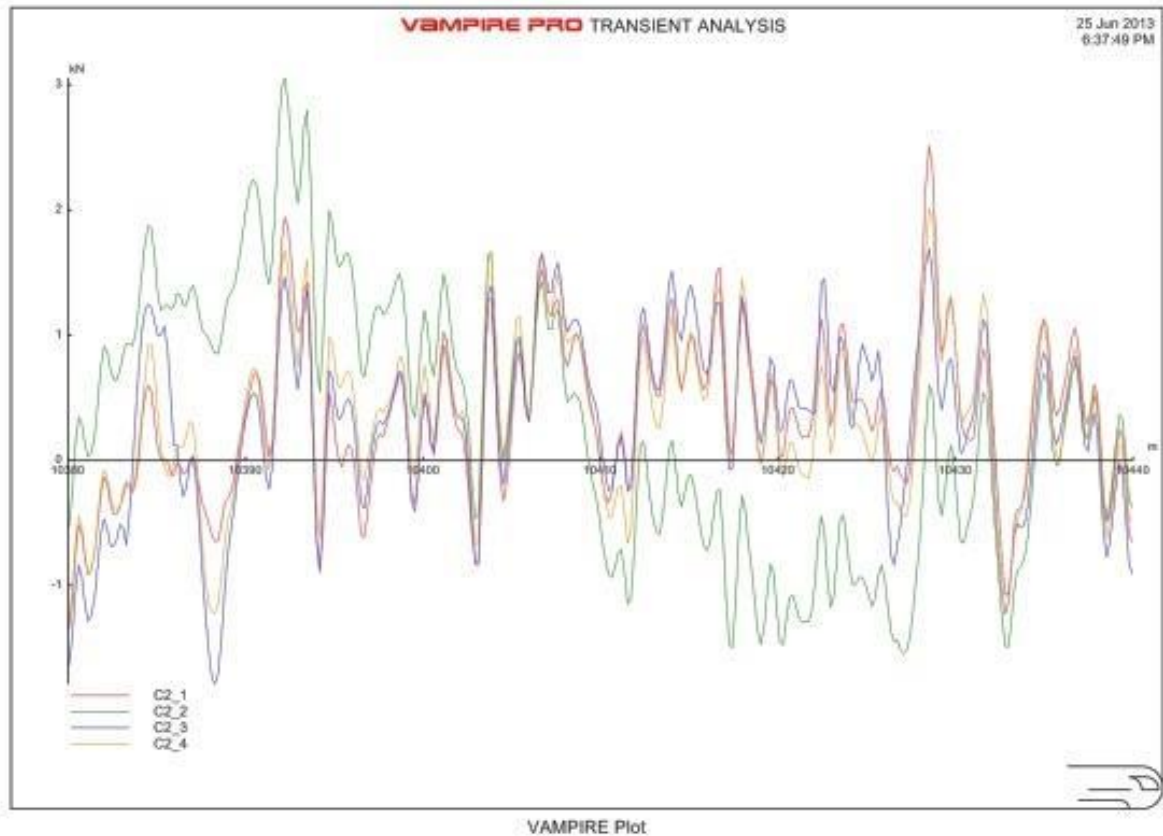


Figure 5-15 Track lateral deterioration with different worn wheels

The results are different from each other mainly due to the vehicle lateral dynamic behaviour changing with the different contact conditions, as shown in Figure 5-16.



a) Rolling radius difference for all contact files



b) Leading left wheel lateral forces

Figure 5-16 Leading left wheel lateral forces with different wheel profiles

Figure 5-17 and Table 5-7 are the PSD results of the track lateral deterioration with different worn wheel profiles. It can be found that the track lateral deterioration changes over a large wavelength range due to the different lateral dynamic behaviour of the vehicles.

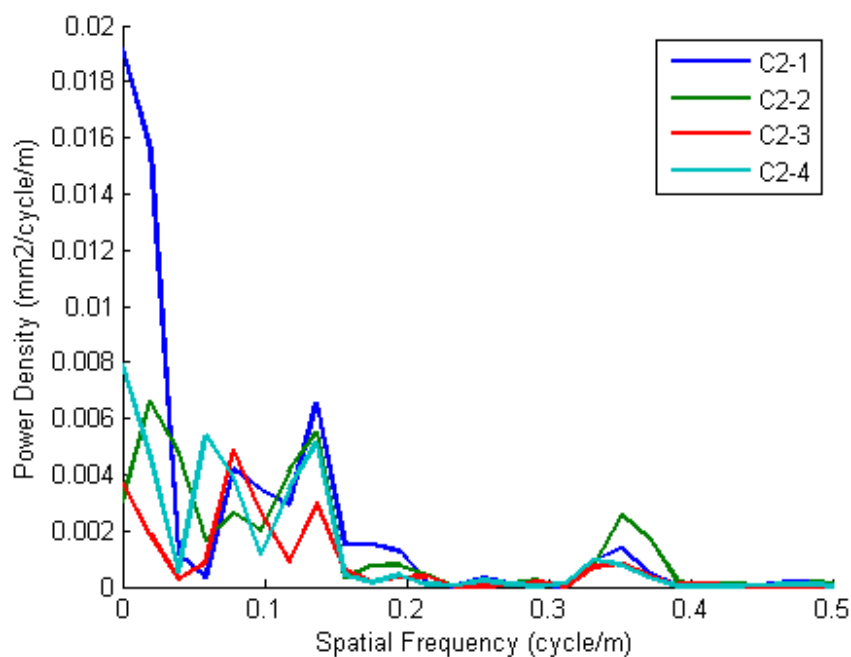


Figure 5-17 PSD of track lateral deterioration with different wheel profiles

Table 5-7 Peak PSD of track lateral deterioration with different wheel profiles

	Peak 1		Peak 2	
	Frequency (Hz)	Wavelength (m)	Frequency (Hz)	Wavelength (m)
New BR-P8 wheel	0.0781	12.7992	0.1367	7.3153
Class373 worn BR-P8 wheel	0.0195	51.2033	0.1367	7.3153
Mark4 worn BR-P8 wheel	0.0781	12.7992	0.1367	7.3153
Class43 worn BR-P8 wheel	0.0586	17.0678	0.1367	7.3153

5.2.3 Effect of different level of worn wheels

A conclusion can be drawn from section 5.2.1 and section 5.2.2 that the wheel-rail contact condition makes a significant difference to the vehicle lateral dynamics, and hence the lateral track deterioration. In reality, wheels tend to wear differently, and there may be different amounts of wear occurring on the different wheels of a train. Therefore, it is necessary to examine how different levels of wear affect the lateral deterioration. The worn wheel profiles used in this section were measured on one Class390 train.

Table 5-8 Rail-wheel profile combination 3

	Num.	Rail profile	Wheel profile
Rail-wheel contact set 3	C3_1	Measured worn CEN 60-20 rail 1	Class390 worn br-p8 wheel 1
	C3_2		Class390 worn br-p8 wheel 2
	C3_3		Class390 worn br-p8 wheel 3
	C3_4		Class390 worn br-p8 wheel 4
	C3_5		Class390 worn br-p8 wheel 5
	* 1 to 5 indicates increasing wear		

Figure 5-18 is the simulated lateral track deterioration for different levels of wheel wear. It is clear that different worn profiles have a large impact on lateral track deterioration.

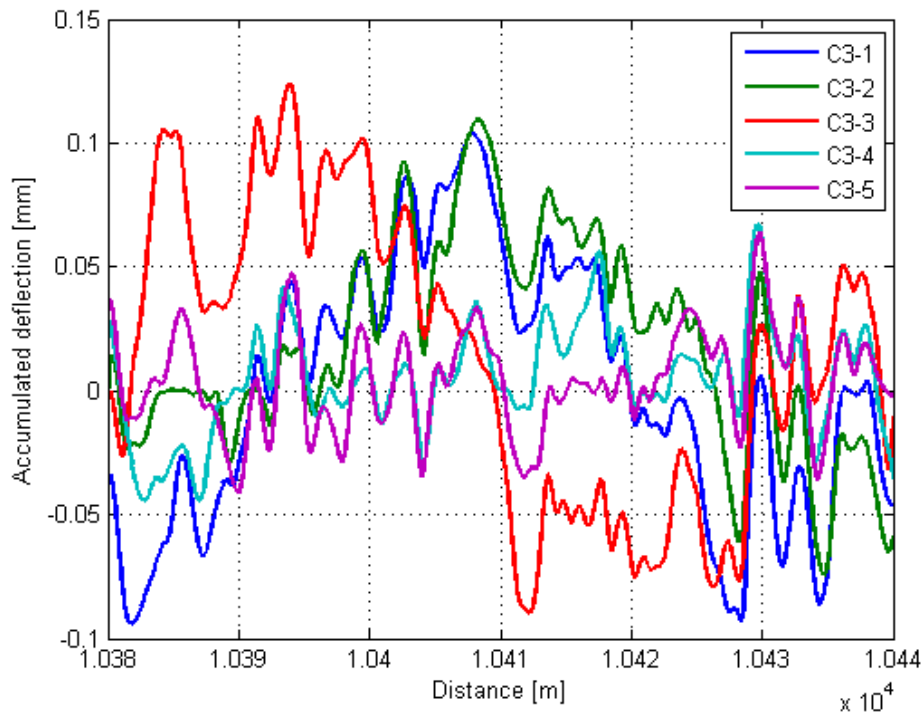
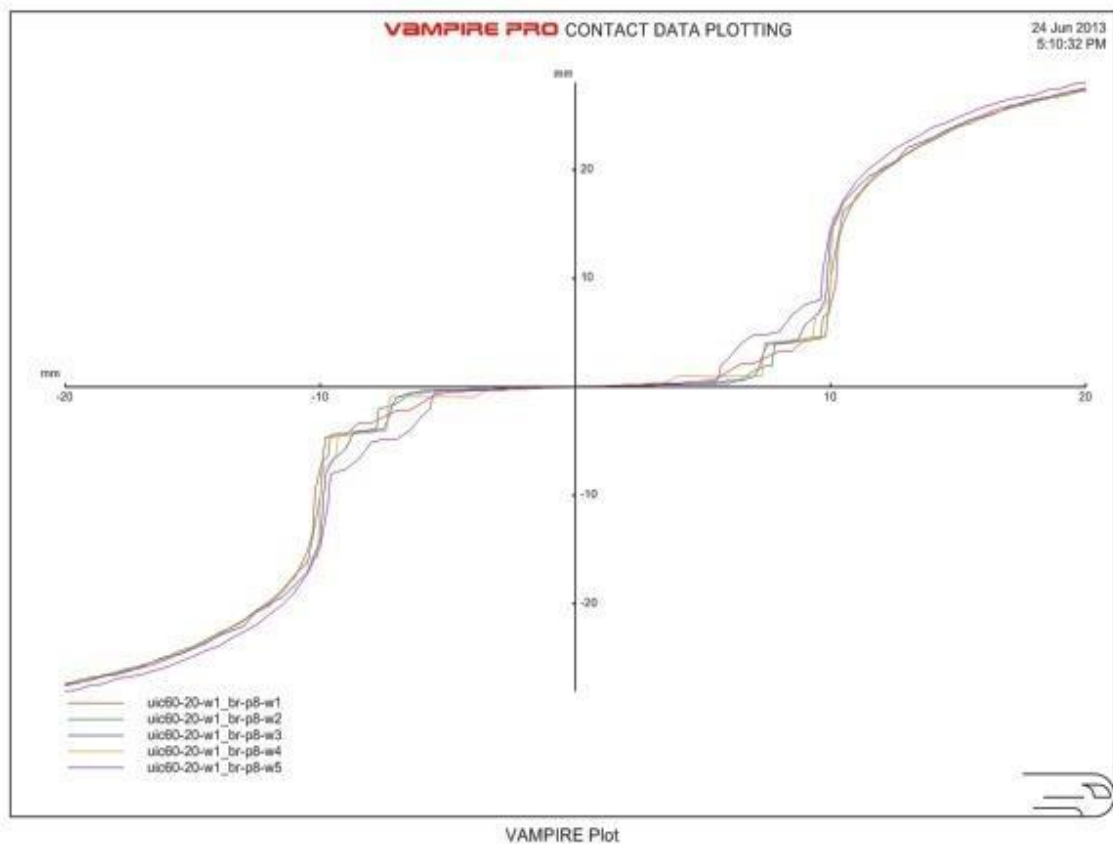
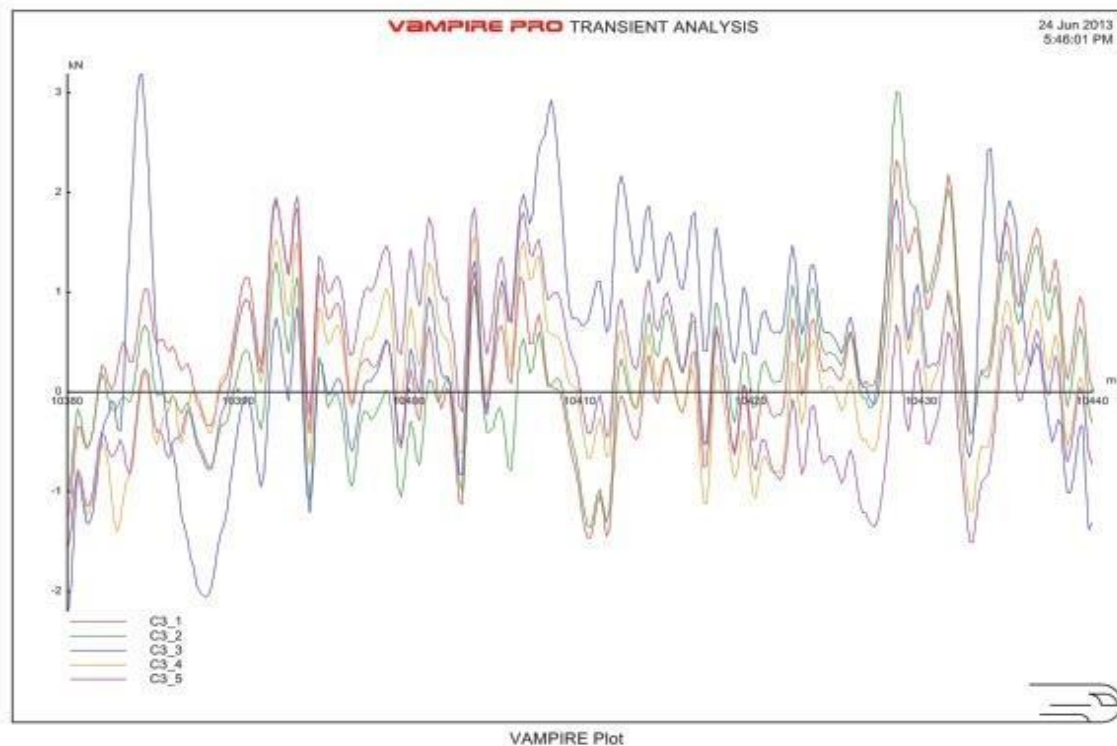


Figure 5-18 Track lateral deterioration with different level of worn wheels

Figure 5-19 is the rolling radius difference and the dynamic lateral forces of the leading left wheel for all of the wheel-rail contact profiles. Vehicles have very different lateral behaviours under different wear conditions.



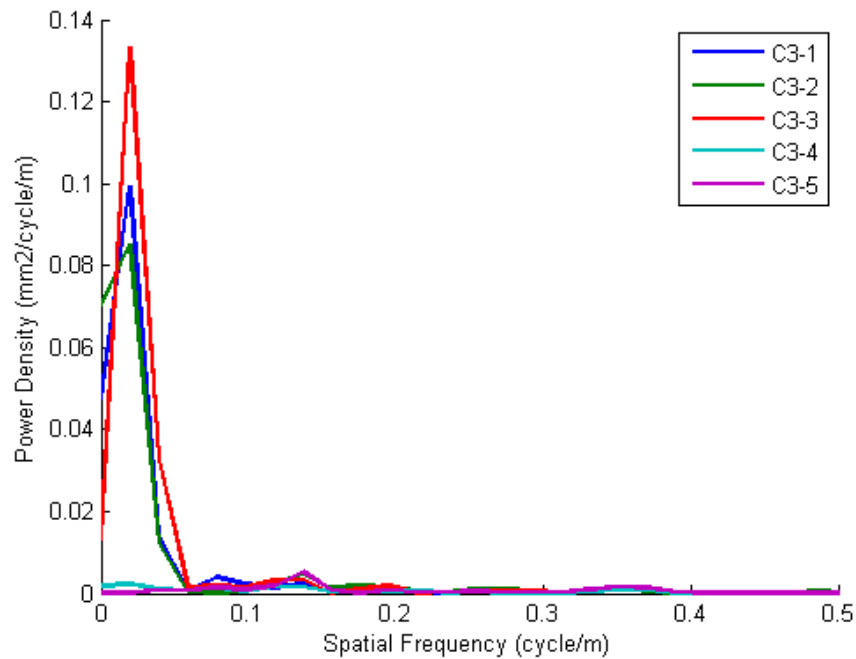
a) Rolling radius difference of five contact files



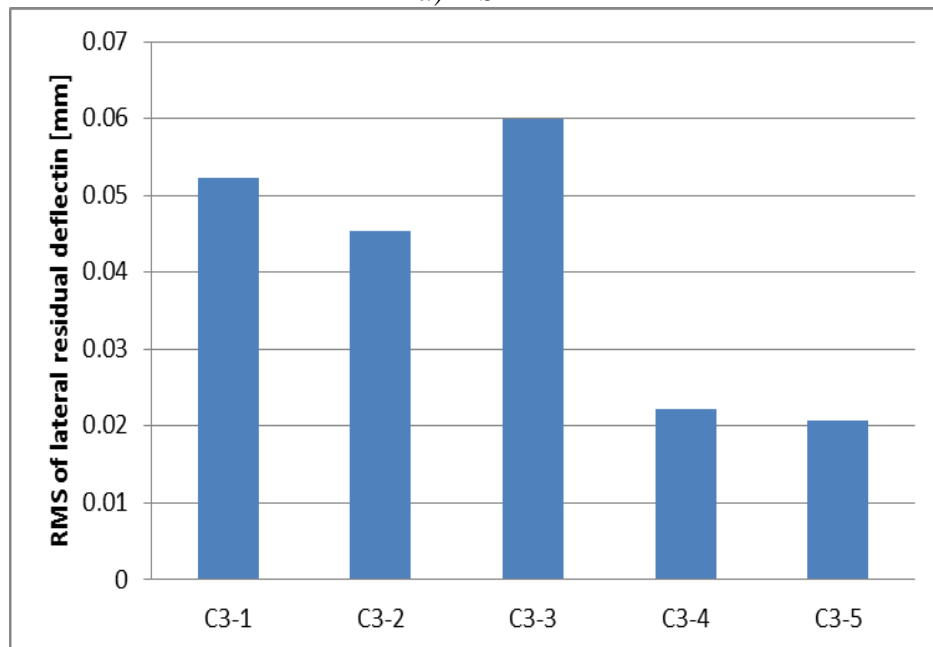
b) Leading left wheel lateral forces

Figure 5-19 Rolling radius difference of five contact files

Figure 5-20 and Table 5-9 are the PSD results of the lateral track deterioration with different worn wheel profiles. It shows that if the wheel is seriously worn, the conicity between the wheel and rail reduces. This leads to a decrease in the long wavelength lateral deterioration at around 50 m. When the wheel is worn into different shapes as for example C2-2 and C3-3, the vehicle lateral dynamics can change significantly. It is noted that with the most worn wheel profiles, as in C3-4 and C3-5, there is a noticeable drop in the lateral track deterioration.



a) PSD



b) RMS

Figure 5-20 PSD and RMS of track lateral deterioration with different level of worn wheel profiles

Table 5-9 Peak PSD of track lateral deterioration with different level of worn wheel profiles

	Peak 1		Peak 2	
	Frequency (Hz)	Wavelength (m)	Frequency (Hz)	Wavelength (m)
C3_1	0.0195	51.2033	0.0781	12.7992
C3_2	0.0195	51.2033	0.1367	7.3153
C3_3	0.0195	51.2033	0.1367	7.3153
C3_4	0.0195	51.2033	0.1367	7.3153
C3_5	0.1367	7.3153	0.1953	5.1203

In general, as the wheels wear, there is a general trend for the conicity to reduce leading to lower lateral forces and reduced track damage. This result on a curve maybe different as the reduced steering can also lead to large dynamic forces due to flange contact. However, the life of railway wheels is usually limited by wear, and the wear between rail and wheel can lead to problems in stability, increased life cycle cost and passenger discomfort. This results in a conflict between the optimum worn rail and wheel profile for lateral track deterioration and for other aspects.

5.2.4 Conclusion

It was found that the wheel and rail profiles play a very important role in the track lateral deterioration by influencing the vehicle-track lateral dynamics. Different worn rail and wheel profiles lead to significantly different lateral dynamic forces for the vehicle. For a fixed worn rail and variations in wheel wear on a particular type of vehicle, the increase in wheel wear tends to reduce the lateral track deflection due to a reduction in both conicity and lateral forces. Therefore, it is important to select correct wheel and rail profiles, and find representative wheel-rail contact data for the track section that needs to be analysed. A better understanding of rail-wheel wear can lead to a more accurate prediction.

5.3 Effects of different track parameters

The influence of track parameters on lateral track deterioration is investigated in this section. The Class390 model Veh.1, is chosen to run over track section 1 in Section 4.5 as it is the predominant vehicle operating on this section. Due to the small effect one vehicle pass will have on the lateral track alignment, 1000 passes of the vehicle will be simulated. The method is to change one of the track parameters and then run simulations in order to assess the sensitivity of the lateral track deterioration to this parameter. The original parameters used in the analysis are shown in Table 5-10.

Table 5-10 Original parameters

k_{ry}	N/m	3.98×10^7
c_{ry}	N · s/m	3×10^4
k_{rz}	N/m	6.3×10^7
c_{rz}	N.s/m	4×10^4
c_{sy}	N.s/m	2.5×10^4
k_{sz}	N/m	9×10^7
c_{sz}	N.s/m	8×10^4
m_r	kg	60
m_s	kg	308
w_e	mm	0.03
F_e	kN	0.12

F_p	kN	8.9
θ	-	0.9986
μ_r	-	0.01
μ_s	-	0.045

Due to the highly non-linear characteristics of the model, the change of the parameters may introduce dynamic impacts into the results. Therefore, clear regular patterns can be found in the results with some small exceptions.

5.3.1 Effects of track stiffness

Track stiffness has a big influence on the forces that are distributed from the rails to the sleeper. Additionally, the stiffness values have an impact on sleeper-ballast pre-sliding behaviour. Table 5-11 shows the stiffness values that are used in the following study. Each stiffness value is varied from 80% to 120% of the original value one at a time. As the sleeper-ballast lateral stiffness changes dynamically depending on the vertical load, the variation of this value is achieved by altering the elastic breaking displacement, as shown in the table.

Table 5-11 Stiffness variation

	k_{rz}	k_{ry}	k_{sz}	$k_{sy} = \frac{F_e + \mu \cdot F_v}{x \times w_e}$
	Rail-sleeper vertical stiffness	Rail-sleeper lateral stiffness	Sleeper-ballast vertical stiffness	Sleeper-ballast lateral stiffness
	kN/mm			w_e [mm]
-20%	50.40	31.84	72.00	$\frac{1}{0.8} \times w_e = 0.625$
-15%	53.55	33.83	76.50	$\frac{1}{0.85} \times w_e = 0.588$
-10%	56.70	35.82	81.00	$\frac{1}{0.9} \times w_e = 0.556$
-5%	59.85	37.81	85.50	$\frac{1}{0.95} \times w_e = 0.526$
Original	63.00	39.80	90.00	$1 \times w_e = 0.500$
+5%	66.15	41.79	94.50	$\frac{1}{1.05} \times w_e = 0.476$
+10%	69.30	43.78	99.00	$\frac{1}{1.1} \times w_e = 0.454$
+15%	72.45	45.77	103.50	$\frac{1}{1.15} \times w_e = 0.434$
+20%	75.60	47.76	108.00	$\frac{1}{1.2} \times w_e = 0.417$

The resulting accumulated track lateral deterioration is shown in Figure 5-21. It is found that the shape of the residual deflection does not change and the amplitude changes by a small amount.

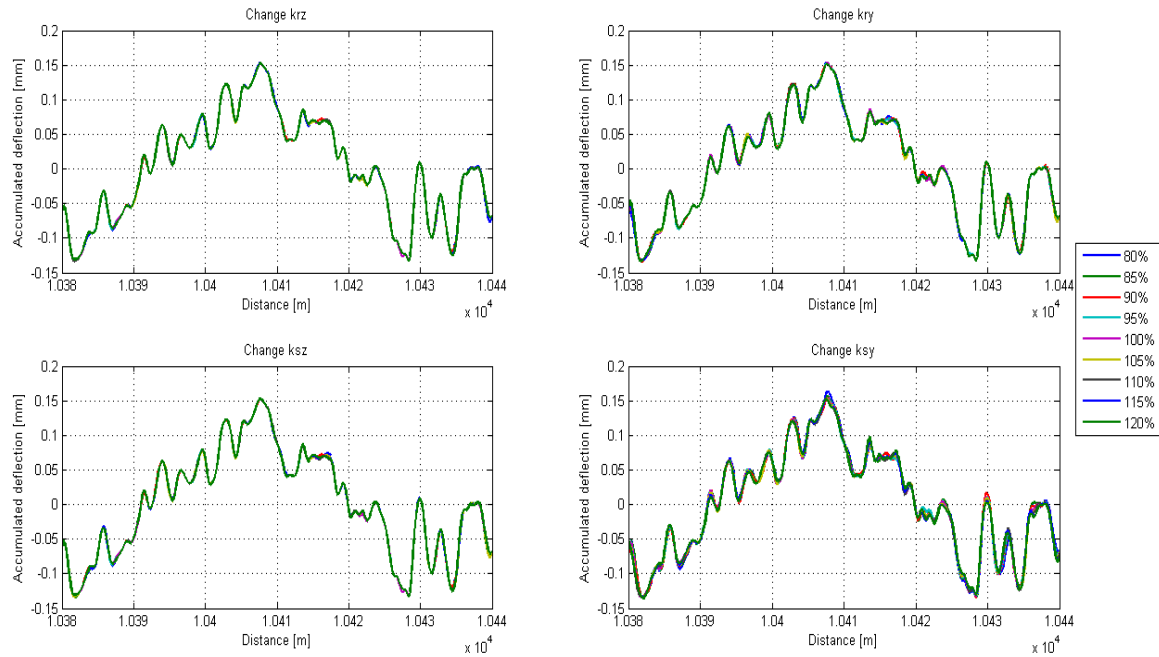


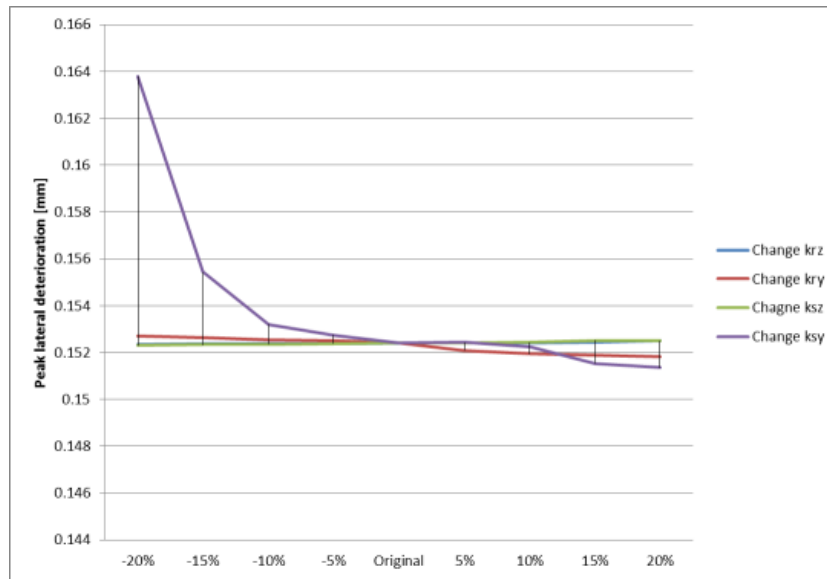
Figure 5-21 Track lateral deflection with different rail-sleeper vertical stiffness values

The peak and RMS of the accumulated lateral deflection values with respect to all stiffness changes are summarised in Table 5-12. Although the dynamic lateral sleeper-ballast stiffness changes with the vertical distributed load, the dynamic stiffness varies around 18 kN/mm. This 18 kN/mm value is mainly defined by the static vertical forces due to vehicle weight, and the variations are dependent on the dynamic vertical force variations which are much smaller. It is therefore sensible to approximate the average change of the deterioration per unit change of lateral sleeper-ballast stiffness according to this 18 kN/mm value.

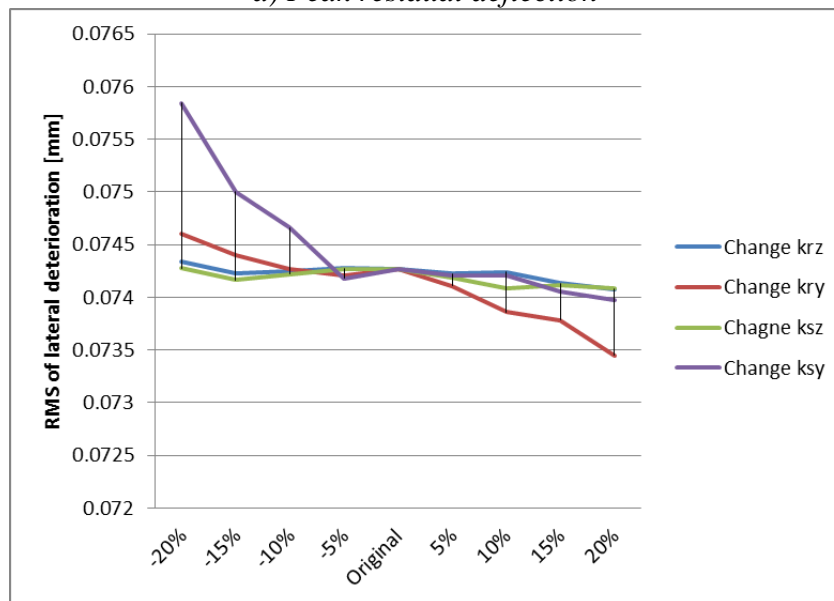
Table 5-12 Peak residual deflection under different rail-sleeper vertical stiffness

	Peak deflection				RMS of deflection			
	k_{rz}	k_{ry}	k_{sz}	k_{sy}	k_{rz}	k_{ry}	k_{sz}	k_{sy}
	Unit [mm]							
-20%	0.15234	0.15272	0.15230	0.16379	0.07433	0.07461	0.07427	0.07584
-15%	0.15236	0.15263	0.15233	0.15544	0.07422	0.07440	0.07416	0.07500
-10%	0.15238	0.15255	0.15236	0.15320	0.07425	0.07426	0.07422	0.07466
-5%	0.15239	0.15251	0.15238	0.15274	0.07428	0.07421	0.07427	0.07418
Original	0.15240	0.15240	0.15240	0.15240	0.07427	0.07427	0.07427	0.07427
+5%	0.15241	0.15210	0.15242	0.15243	0.07423	0.07411	0.07419	0.07421
+10%	0.15242	0.15194	0.15244	0.15225	0.07424	0.07386	0.07409	0.07421
+15%	0.15243	0.15188	0.15251	0.15153	0.07413	0.07378	0.07412	0.07406
+20%	0.15250	0.15182	0.15251	0.15136	0.07408	0.07345	0.07408	0.07398
Average Δ ($\times 10^{-5}$)	1.93	-11.2	2.53	-156	-3.21	-14.46	-2.39	-23.31
Δ per unit mm/kN/mm ($\times 10^{-5}$)	0.61	-5.63	0.56	-173	-1.02	-7.27	-0.53	-25.90
In %	0.0127	-0.0735	0.0166	-1.0202	-0.0432	-0.1948	-0.0322	-0.3139
* 'Average Δ ' – the average change of the residual deflection for each 5% change of the stiffness * ' Δ per unit' – the average Δ per 1 kN/mm change of the stiffness. * 'In %' – the proportion average Δ takes of the original residual deflection value								

Among all stiffness parameters, the sleeper-ballast lateral stiffness has the greatest impact on the track lateral deterioration as shown in Figure 5-22.



a) Peak residual deflection



b) RMS of residual deflection

Figure 5-22 Residual deflection change of every 5% increase of stiffness values

The average change in peak deflection by increasing the stiffness values by 1 kN/mm are shown in Figure 5-23. Generally, the residual deflections decrease with an increase of the all stiffness values. The increase of every unit of sleeper-ballast lateral stiffness k_{sy} has the largest impact on lateral deterioration.

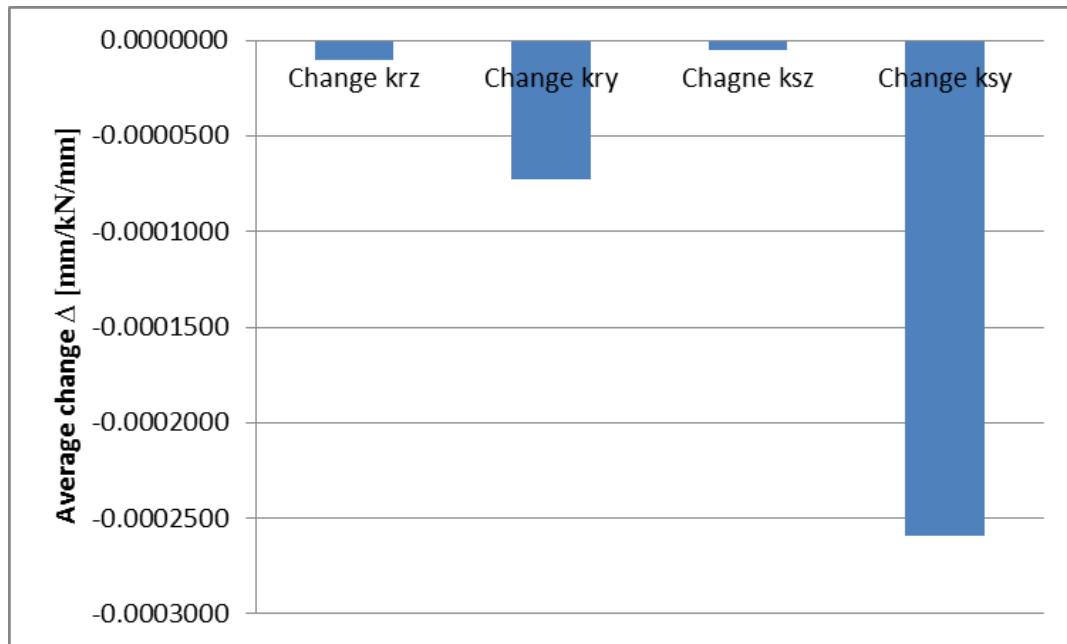


Figure 5-23 Average change per unit increase of stiffness value

5.3.2 Effects of track damping

Table 5-13 shows the rail-sleeper and sleeper-ballast damping values that are used in the following simulations. Each damping value is varied between 80% and 120% of the original value.

Table 5-13 Damping variation [kN.s/m]

	c_{rz}	c_{ry}	c_{sz}	c_{sy}
	Rail-sleeper vertical damping	Rail-sleeper lateral damping	Sleeper-ballast vertical damping	Sleeper-ballast lateral damping
-20%	32.0	24.0	64.0	24.0
-15%	34.0	25.5	68.0	25.5
-10%	36.0	27.0	72.0	27.0
-5%	38.0	28.5	76.0	28.5
Original	40.0	30.0	80.0	30.0
+5%	42.0	31.5	84.0	31.5
+10%	44.0	33.0	88.0	33.0
+15%	46.0	34.5	92.0	34.5
+20%	48.0	36.0	96.0	36.0

The lateral track deterioration results are shown in Figure 5-24. The differences between all of the results are small when changing damping values.

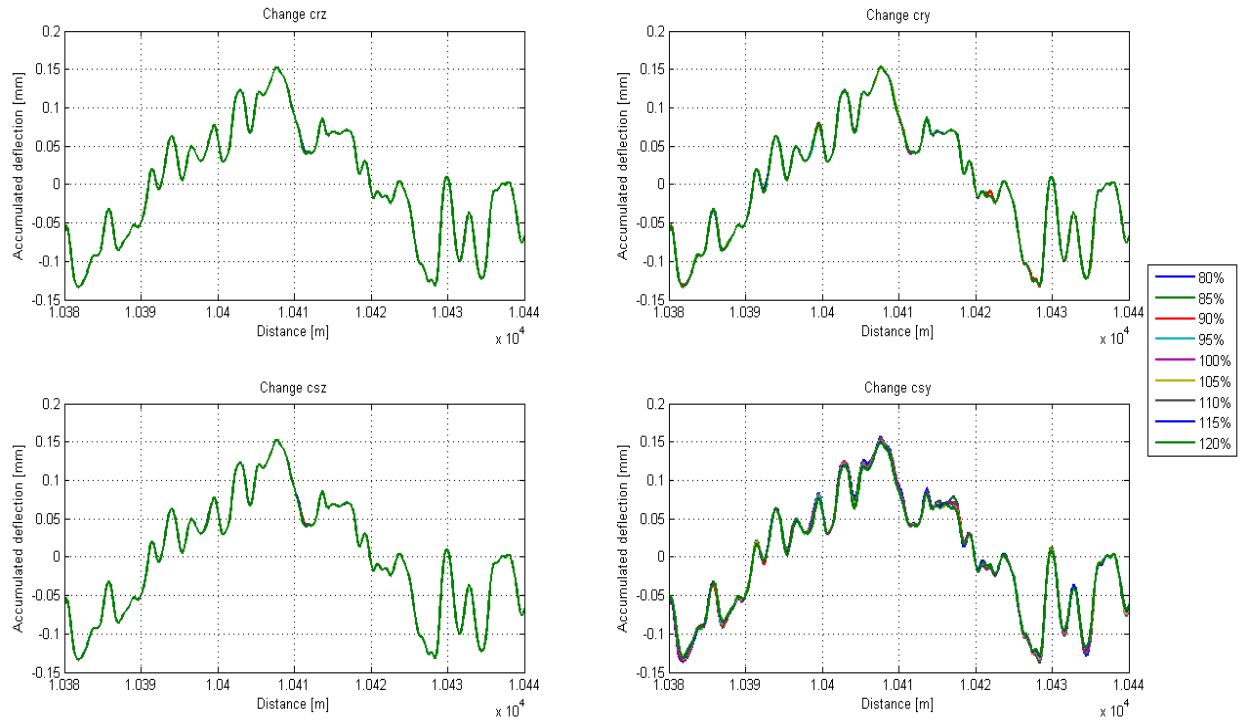


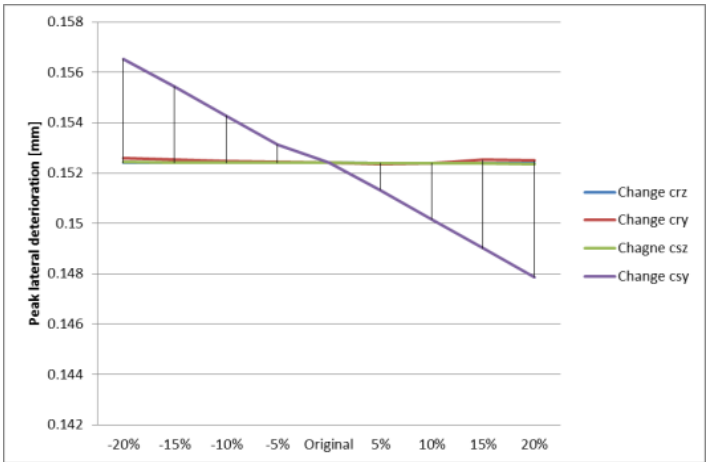
Figure 5-24 Track lateral deflection with different rail-sleeper vertical damping values

The peak and RMS of the accumulated lateral deflection values are summarised in Table 5-14. Generally, it can be found that the residual deflection decreases with an increase of all damping values.

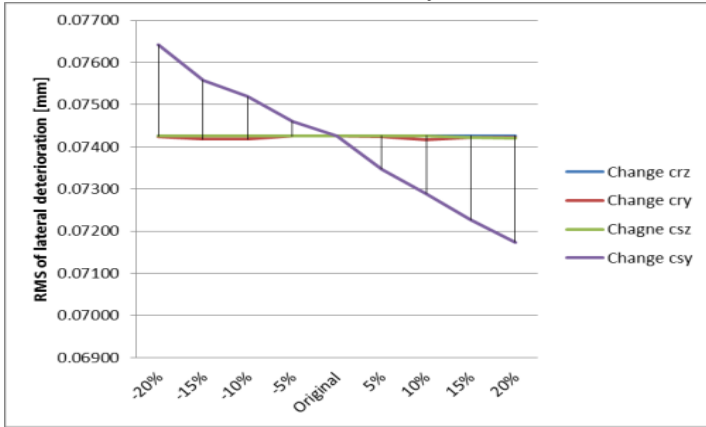
Table 5-14 Peak residual deflection under different damping values

	Peak deflection				RMS of deflection			
	c_{rz}	c_{ry}	c_{ry}	c_{sy}	c_{rz}	c_{ry}	c_{ry}	c_{sy}
	Unit [mm]							
-20%	0.15241	0.15260	0.15243	0.15654	0.07426	0.07425	0.07426	0.07642
-15%	0.15241	0.15253	0.15242	0.15544	0.07426	0.07418	0.07427	0.07558
-10%	0.15240	0.15248	0.15242	0.15428	0.07426	0.07418	0.07426	0.07520
-5%	0.15240	0.15244	0.15241	0.15313	0.07426	0.07426	0.07426	0.07460
Original	0.15240	0.15240	0.15240	0.15240	0.07427	0.07427	0.07427	0.07427
+5%	0.15240	0.15236	0.15239	0.15133	0.07427	0.07424	0.07427	0.07347
+10%	0.15240	0.15238	0.15239	0.15016	0.07427	0.07418	0.07427	0.07289
+15%	0.15240	0.15253	0.15238	0.14900	0.07427	0.07423	0.07423	0.07227
+20%	0.15239	0.15249	0.15237	0.14787	0.07427	0.07422	0.07420	0.07173
Average $\Delta(\times 10^{-5})$	-0.19	-1.35	-0.78	-108.37	0.01	-0.32	-0.76	-58.56
In Δ mm/kN.s/ mm ($\times 10^{-5}$)	-0.09	-0.90	-0.20	-72.25	0.01	-0.22	-0.19	-39.04
In %	-0.0012	-0.0089	-0.0051	-0.7111	0.0002	-0.0044	-0.0102	-0.7886

Among all of the damping parameters, the sleeper-ballast lateral damping has the greatest impact on lateral track deterioration.



a) Peak residual deflection



b) RMS of residual deflection

Figure 5-25 Residual deflection change for every 5% increase of damping values

In general, the lateral residual deflection tends to reduce with the growth of all damping values. The change in sleeper-ballast damping value c_{sy} , has the largest impact on lateral deterioration. Other damping values have negligible effect.

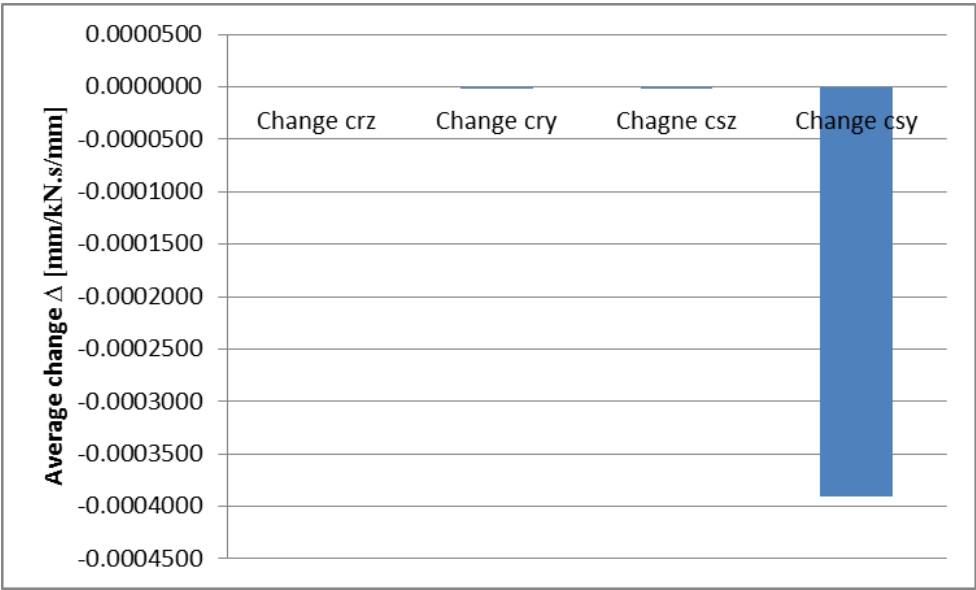


Figure 5-26 Average change per unit increase of damping value

5.3.3 Effect of rail and sleeper mass

Rail and sleeper mass have a direct influence on the unloading condition shown in Figure 4-23. The unloading of the track creates a low resistance to lateral deterioration. Table 5-15 shows the rail and sleeper masses that are used in the following study. Each mass is varied from 80% to 120% of the original mass values.

Table 5-15 Rail and sleeper masses variation [kg]

	m_r	m_s
-20%	48	246.4
-15%	51	261.8
-10%	54	277.2
-5%	57	292.6
Original	60	308
+5%	63	323.4
+10%	66	338.8
+15%	69	354.2
+20%	72	369.6

The resulting lateral track deterioration is shown in Figure 5-27.

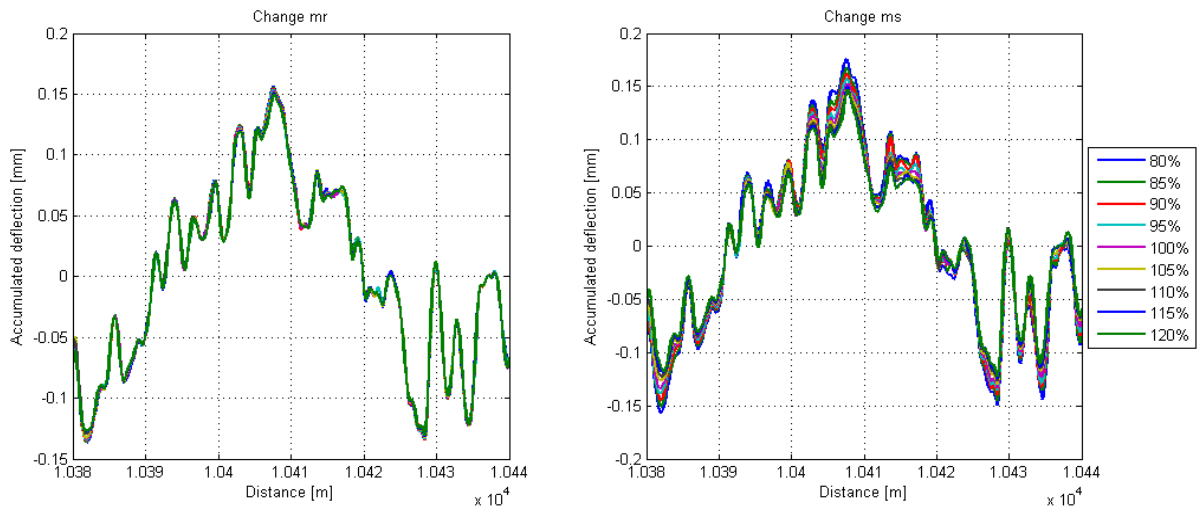


Figure 5-27 Track lateral deflection with different rail and sleeper masses

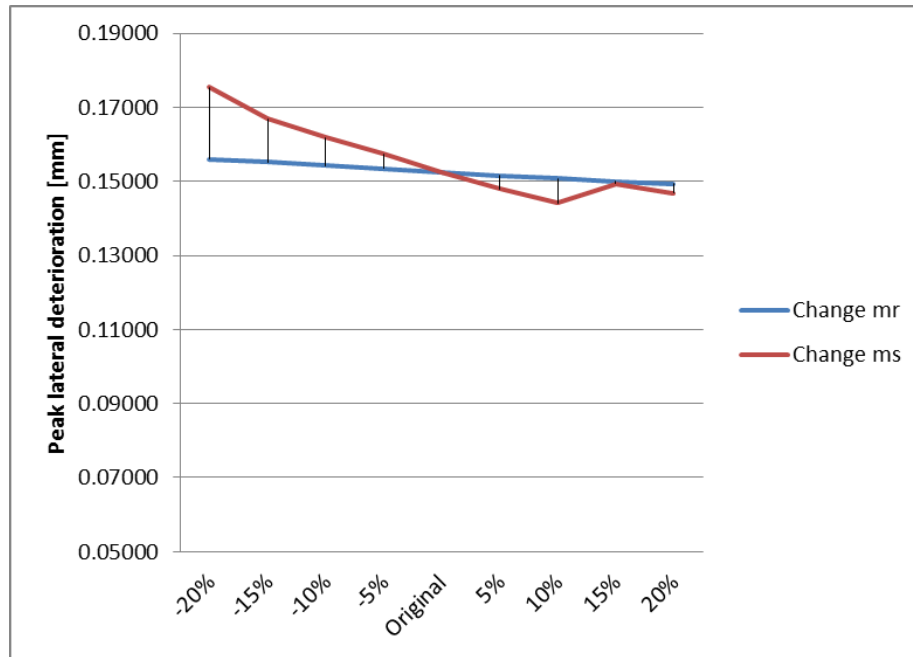
The peak and RMS of the accumulated lateral deflection values with respect to rail and sleeper mass changes are summarised in Table 5-14.

Table 5-16 Peak residual deflection under different rail and sleeper masses [mm]

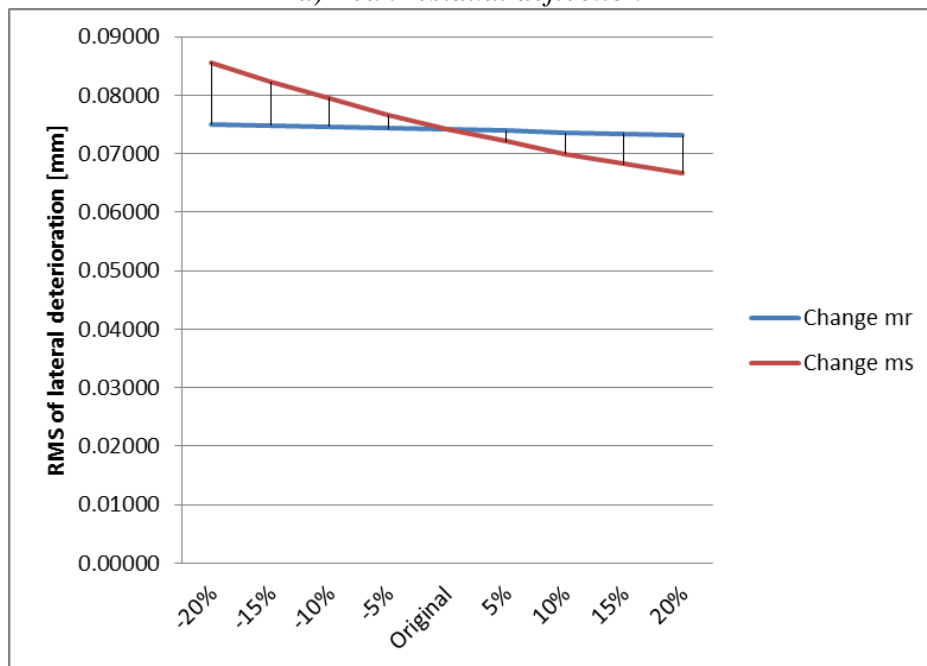
	Peak deflection		RMS of deflection	
	m_r	m_s	m_r	m_s
	Unit [mm]			
-20%	0.15603	0.17542	0.07510	0.08558
-15%	0.15517	0.16686	0.07485	0.08223
-10%	0.15432	0.16187	0.07467	0.07951
-5%	0.15350	0.15744	0.07436	0.07659
Original	0.15240	0.15240	0.07427	0.07427
+5%	0.15161	0.14802	0.07390	0.07209
+10%	0.15075	0.14423	0.07357	0.07001

+15%	0.15005	0.14935	0.07342	0.06823
+20%	0.14937	0.14691	0.07314	0.06668
Average Δ ($\times 10^{-5}$)	-83.32	-356.44	-24.52	-236.29
In Δ mm/kg ($\times 10^{-5}$)	-27.77	-23.15	-8.17	-15.34
In %	-0.5467	-2.3388	-0.3301	-3.1816

It is found that the residual deflection decreases with every 5% increase of both rail and sleeper masses. The sleeper mass has the largest effect.



a) Peak residual deflection



b) RMS of residual deflection

Figure 5-28 Residual deflection amplitude change of every 5% increase of masses

Figure 5-29 shows that for every kilogram that the sleeper mass m_s increase leads to a further decrease of the lateral track deterioration.

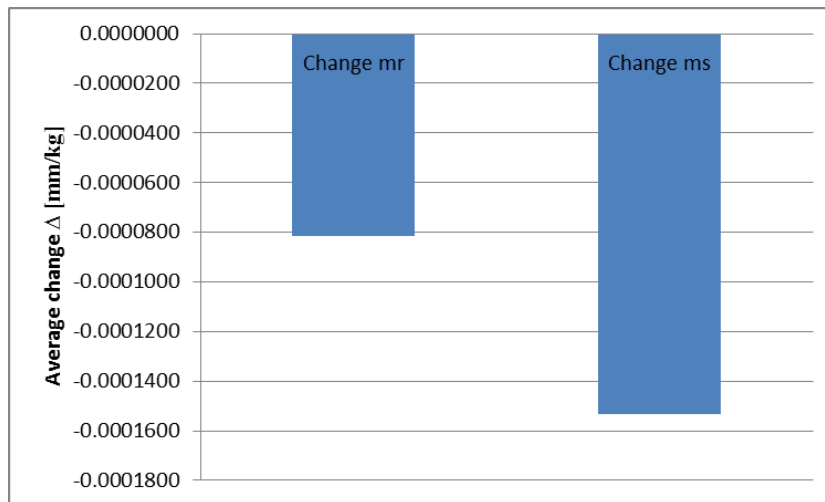


Figure 5-29 Average change per unit increase of rail and sleeper masses

5.3.4 Effect of softening factor

The softening factor depends on the condition of the sleeper-ballast interface, and track in good condition has a softening factor close to 1. A variation in θ alters the hysteresis characteristic and indicates a more gentle stiffness for residual deflection calculation. As a result, a reduction in θ leads to an increase in residual deflection as shown in Figure 5-30.

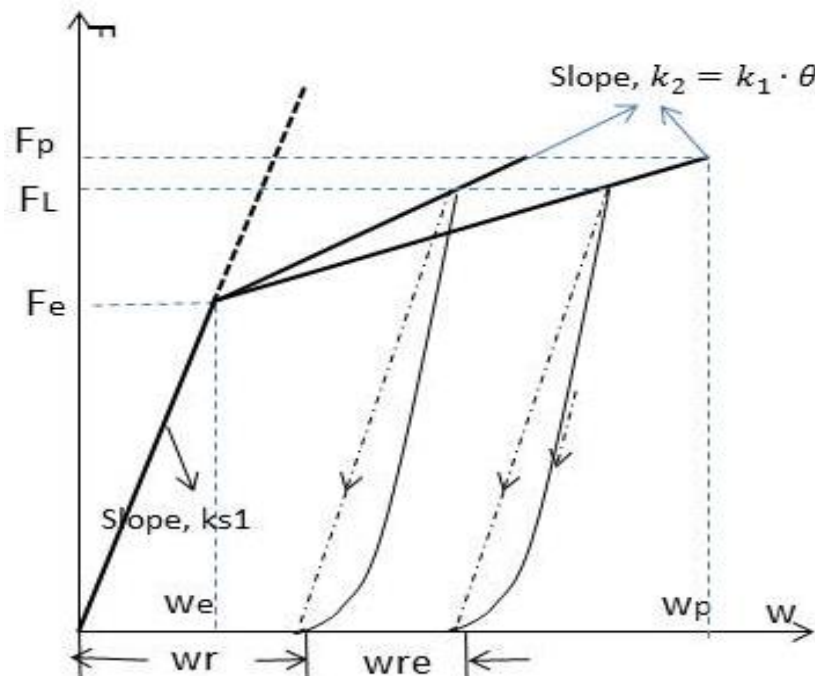


Figure 5-30 Change of softening factor

The stiffness for residual deflection must be less than the elastic stiffness, therefore the softening factor value needs to be smaller than 1. Table 5-17 is the softening factor that is used in this section.

Table 5-17 Softening factor variation

	θ
-2.0%	0.9604
-1.5%	0.9653
-1.0%	0.9702
-0.5%	0.9751
Original	0.9800
+0.5%	0.9849
+1.0%	0.9898
+1.5%	0.9947
+2.0%	0.9996

The simulated lateral track deterioration using different softening factors is shown in Figure 5-30.

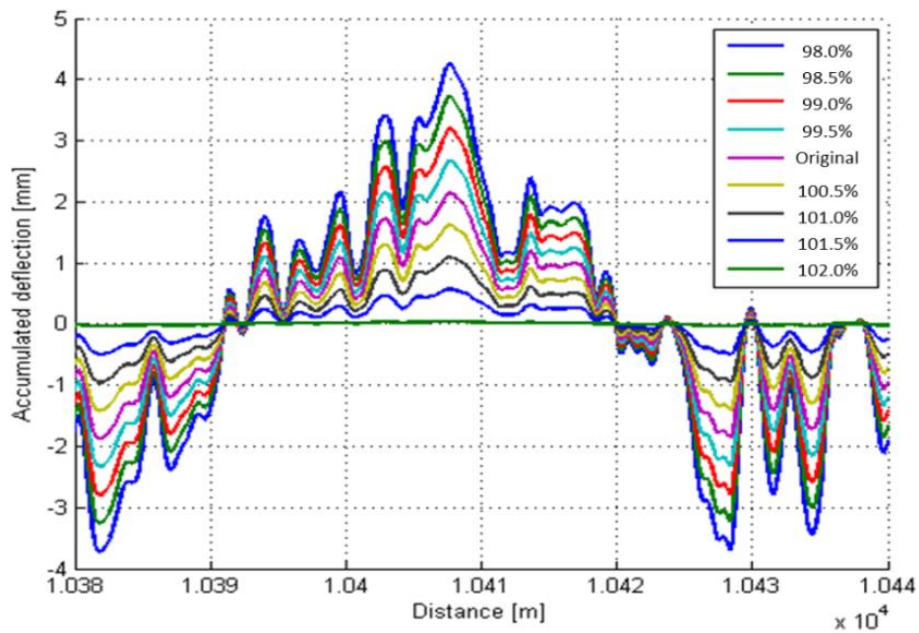


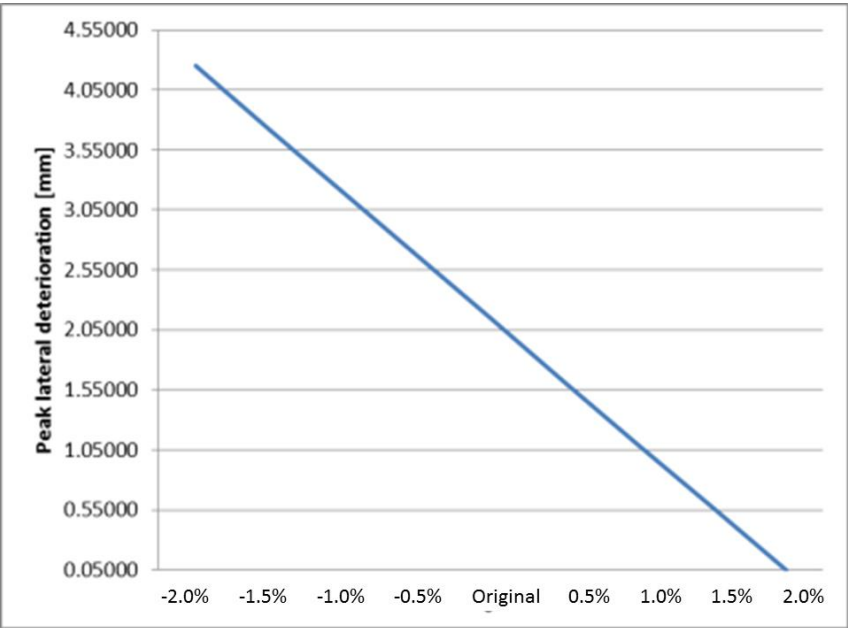
Figure 5-31 Track lateral deflection with softening factors

The peak and RMS of the accumulated lateral deflection values with respect to different softening factors are summarised in Table 5-18.

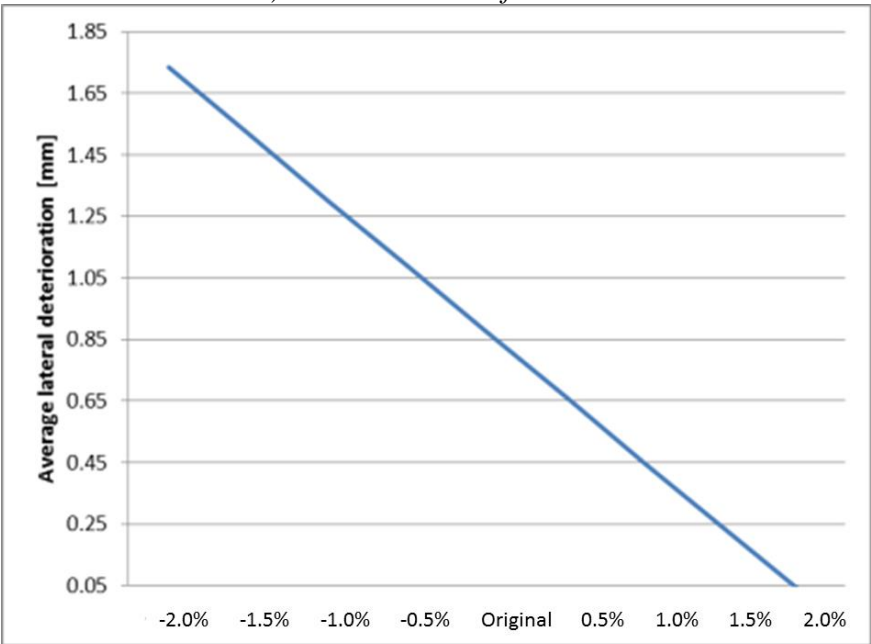
Table 5-18 Peak residual deflection under different softening factors [mm]

	Peak deflection	RMS of deflection
	Unit [mm]	
-2.0%	4.25319	1.73421
-1.5%	3.72427	1.51853
-1.0%	3.19609	1.30315
-0.5%	2.66867	1.08809
Original	2.14199	0.87334
+0.5%	1.61606	0.65890
+1.0%	1.09087	0.44476
+1.5%	0.56643	0.23094
+2.0%	0.04272	0.01742
Average Δ	-0.52631	-0.21460
In %	-24.5710	-24.5722

The change of softening factor only brings an amplitude change to the residual deflection. The impact of this parameter on the residual deflection is linear, and for every 0.5% increase of this value causes a 24.5% reduction in the lateral residual deflection.



a) Peak residual deflection



b) RMS of residual deflection

Figure 5-32 Residual deflection change of every 0.5% increase in softening factor

5.3.5 Effect of elastic breaking force and displacement and residual coefficient

The elastic breaking force, displacement and residual coefficient all depend on the condition of the sleeper-ballast interface. Track in good condition has a larger elastic breaking limit, which means larger F_e , w_e and μ_r values. The variation of elastic breaking force F_e and elastic breaking displacement w_e values change the static elastic breaking limit, while the changing residual coefficient μ_r value brings a difference to the dynamic elastic breaking limit. These values are mainly influenced by the size, shape and weight of the sleeper. The variations of these values have a direct impact on the sleeper-ballast non-linear characteristic, as shown in Figure 5-33 a). Considering the dynamics of an individual sleeper, a change in elastic breaking force and displacement values will increase or decrease the dynamic elastic envelope, and varying the residual coefficient value will change the peak amplitude of the dynamic elastic envelope as shown in Figure 5-33 b).

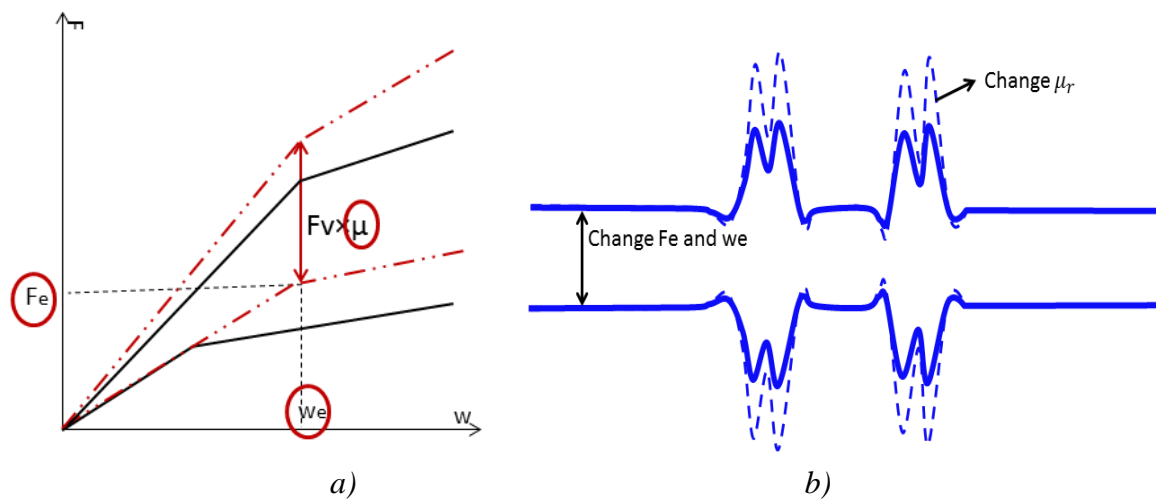


Figure 5-33 Dynamic elastic breaking limit

Table 5-19 illustrates the elastic breaking limit variation that will be used for the simulations in this section.

Table 5-19 Elastic breaking limit variation

	w_e [mm]	F_e [kN]	μ_r -
-20%	0.024	0.096	0.008
-15%	0.0255	0.102	0.0085
-10%	0.027	0.108	0.009
-5%	0.0285	0.114	0.0095
Original	0.03	0.12	0.01
+5%	0.0315	0.126	0.0105
+10%	0.033	0.132	0.011
+15%	0.0345	0.138	0.0115
+20%	0.036	0.144	0.012

Figure 5-34 gives the results of the simulation, showing the effects of changing the elastic breaking displacement, force, and residual coefficient.

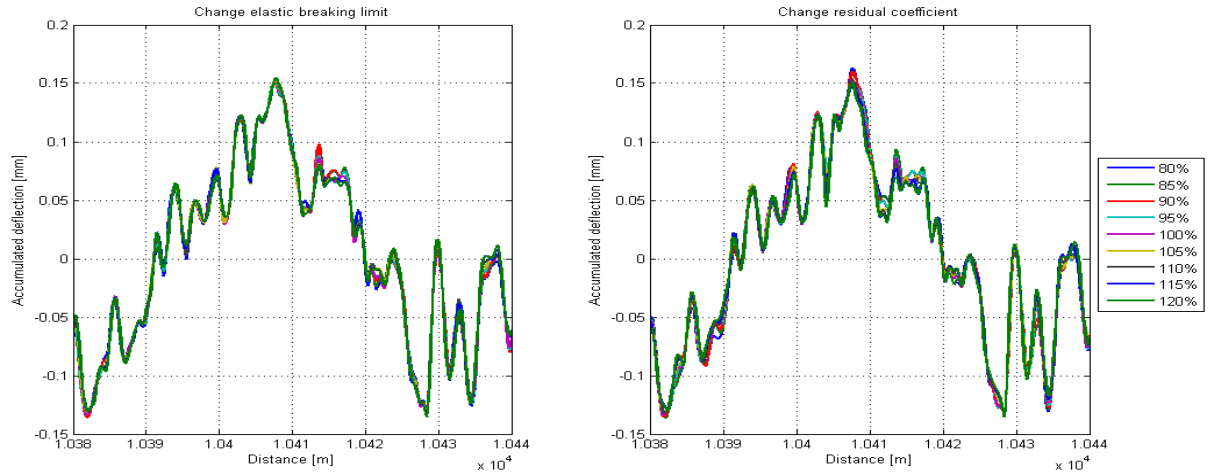


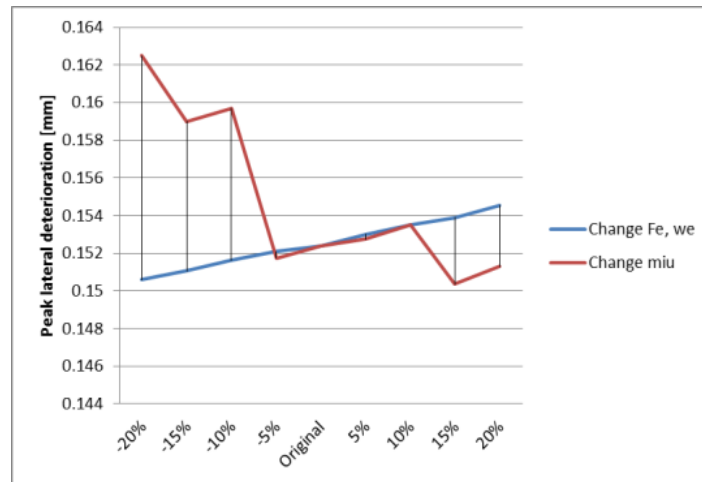
Figure 5-34 Track lateral deflection with different elastic breaking limits

Table 5-20 summarises the peak and RMS values of the residual deflection with different elastic breaking limits.

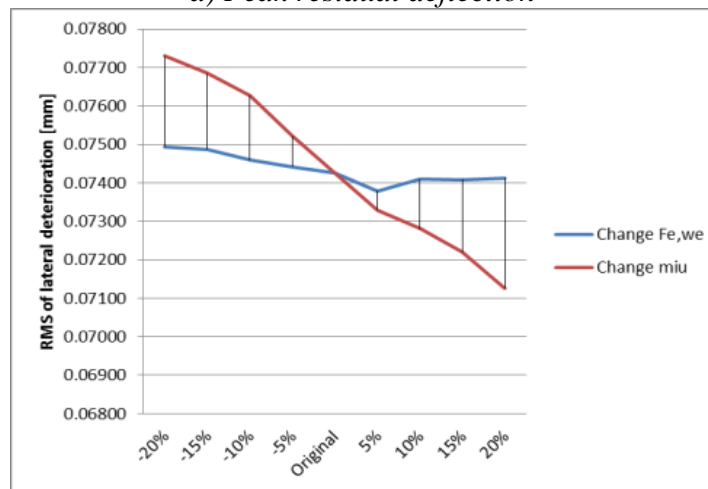
Table 5-20 Average residual deflection under different elastic breaking limits

	Peak deflection		RMS of deflection	
	Unit [mm]			
	w_e and F_e	μ_r	w_e and F_e	μ_r
-20%	0.15060	0.16250	0.07494	0.07730
-15%	0.15106	0.15900	0.07487	0.07684
-10%	0.15162	0.15970	0.07459	0.07628
-5%	0.15210	0.15175	0.07442	0.07523
Original	0.15240	0.15240	0.07427	0.07427
+5%	0.15300	0.15274	0.07379	0.07329
+10%	0.15351	0.15352	0.07410	0.07280
+15%	0.15389	0.15036	0.07408	0.07220
+20%	0.15455	0.15130	0.07413	0.07127
Average Δ ($\times 10^{-5}$)	49.37	-140.10	-10.16	-75.41
In %	0.3239	-0.9193	-0.1368	-1.0153

The change of the elastic breaking limit has a strong dynamic impact on the lateral track deterioration. There is an increasing trend of the peak deflection with different static elastic breaking limits, w_e and F_e , and a clear negative slope of peak deflection change with varying μ_r value. The increase of the elastic breaking limit leads to a reduction in the overall residual track deflection according to the RMS results.



a) Peak residual deflection



b) RMS of residual deflection

Figure 5-35 Residual deflection change by elastic breaking limits

5.3.6 Effect of sleeper spacing

Changing the sleeper spacing changes the supporting condition of the rails, so it can influence the track lateral dynamics. The sleeper spacing values simulated in this section are shown in Table 5-21.

Table 5-21 Sleeper spacing variation [m]

	Sleeper spacing
-20%	0.48
-15%	0.51
-10%	0.54
-5%	0.57
Original	0.6
+5%	0.63
+10%	0.66
+15%	0.69
+20%	0.72

The resulting lateral track deteriorations with different sleeper spacing values are shown in Figure 5-36.

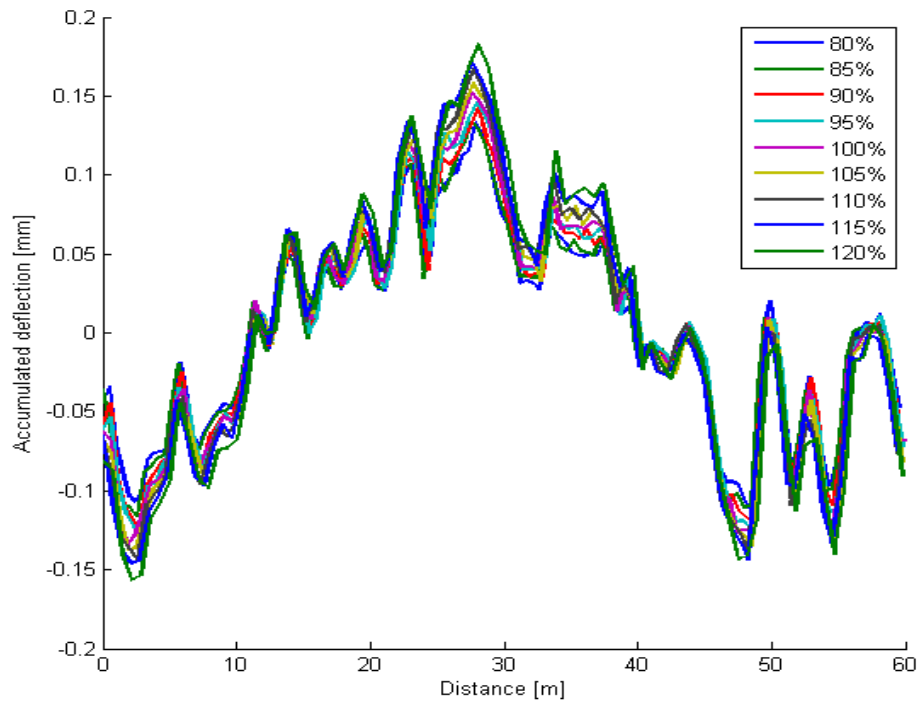


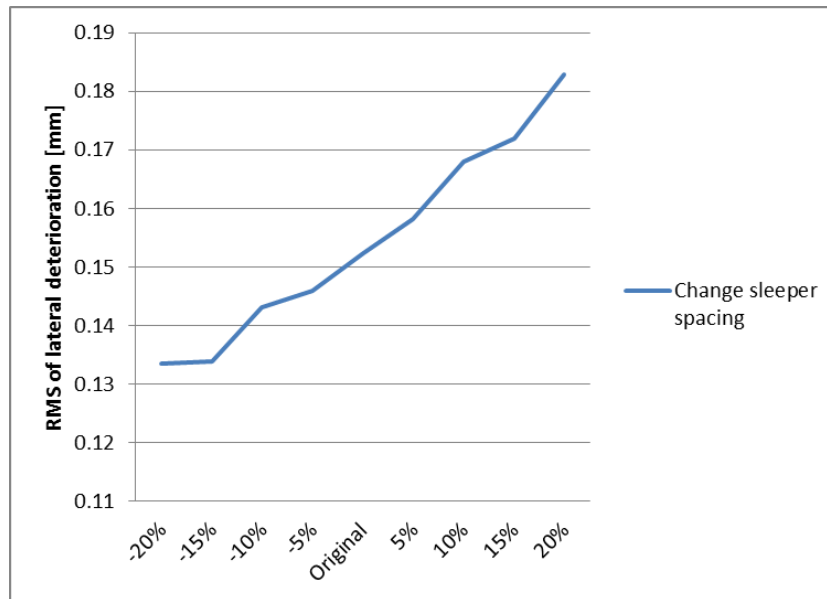
Figure 5-36 Track lateral deflection with different sleeper spacing

The peak and RMS of the accumulated lateral deflection values with respect to different sleeper spacing values are summarised in Table 5-22.

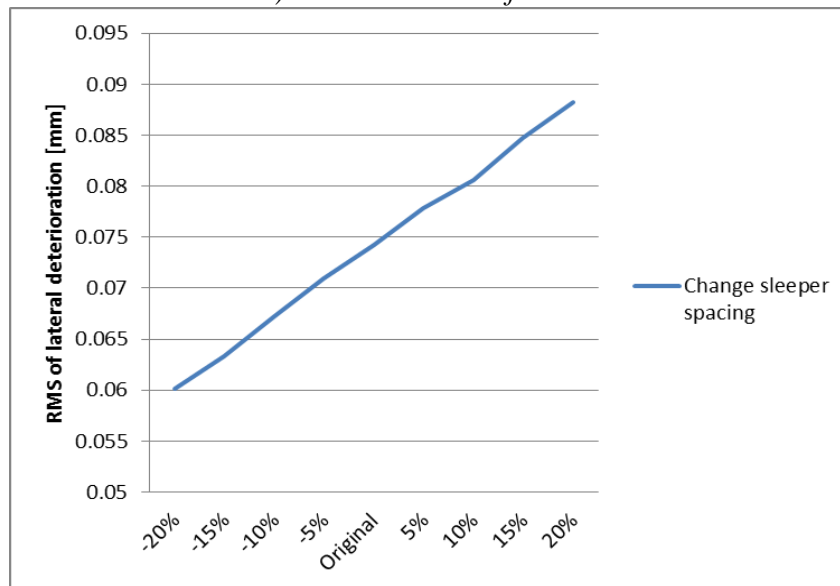
Table 5-22 Peak residual deflection under different sleeper spacing [mm]

	Peak deflection	RMS of deflection
	Unit [mm]	
-20%	0.13341	0.06017
-15%	0.13380	0.06336
-10%	0.14300	0.06728
-5%	0.14598	0.07094
Original	0.15240	0.07427
+5%	0.15814	0.07783
+10%	0.16796	0.08064
+15%	0.17197	0.08474
+20%	0.18289	0.08820
Average Δ ($\times 10^{-3}$)	6.1858	3.5035
In Δ mm/m	0.2062	0.1168
In %	4.06	4.72

The increase of sleeper spacing brings a nearly linear rise in the residual deflection. Every 5% increases of this value causes around 4.5% average growth on the lateral residual deflection.



a) Peak residual deflection



b) RMS of residual deflection

Figure 5-37 Residual deflection change of every 5% increase of sleeper spacing

5.3.7 Conclusion

Changing the track parameters does not have strong impact on the shape of the track lateral deterioration compared to changes in the vehicle and wheel-rail contact conditions. At a specific location on the track, for example where the peak deflection occurs, the influences of all track parameters are not quite linear due to the resulting dynamic effects. Nonetheless, the RMS of the residual deflection changes appear relatively linear with respect to the track parameter variation.

The residual deflections decrease with an increase of all stiffness values, and the sleeper-ballast lateral stiffness has the biggest impact on the lateral track deterioration. The lateral stiffness values generally have a bigger impact on the lateral track deterioration than the vertical stiffness values.

Track deterioration decreases as damping values increase, and the sleeper-ballast damping in the lateral direction is found to have the biggest influence.

The increase in mass of both rails and sleepers leads to a reduction of the lateral track deflection, and changes of sleeper mass have a greater effect than changes in the mass of the rails.

Increasing of the softening factor in the ballast-sleeper interface model creates amplitude reduction in the lateral track deterioration. The relationship between the softening factor and track deterioration is linear.

The impact of the elastic breaking limits, which are determined by the elastic breaking force, displacement and residual coefficient, is discussed. An increase in the elastic breaking limit, which means a stronger lateral sleeper-ballast interface, leads to an amplitude reduction in the overall track residual deflection.

An increase in sleeper spacing weakens the track support condition to some degree, thereby leading to a potential growth in track lateral deterioration.

As expected, the sleeper-ballast interface has the biggest impact on the lateral track deterioration since the parameters related to this interface all appear to have the greatest impact on lateral deterioration.

5.4 Chapter conclusion

This chapter presented the influences of different aspects on the lateral track deterioration in terms of the vehicles, wheel-rail contact conditions and track parameters.

The lateral damage caused by the vehicle depends on both the L/V ratio and the lateral load but it is a complicated dynamic process that cannot easily be expressed through a simple function. It is therefore sensible to establish the damage from different types of vehicle by carrying out vehicle-track dynamic simulations. Two-axle freight vehicles were found to produce most lateral track damage due to their high axle load, simple suspension design and resulting dynamic behaviour. The change of vehicle speed does not necessarily bring a wavelength change of the residual deflection but does cause a change to the amplitude of the track deterioration. Within a certain speed range, there will be a critical speed that creates a peak in the residual deflection, and reducing or increasing the vehicle speed can help reduce the residual deflection.

It is found that the wheel and rail profiles play a very important role in the development of lateral track deterioration by influencing the lateral dynamics of the vehicle. Different worn rail and wheel profiles result in very different lateral dynamic forces. For a fixed worn rail and worn wheel on a particular type of vehicle, the increase in wheel wear can make the residual track deflection lower due to reduced conicity and lateral forces. It is important to choose the correct wheel and rail profiles, and find representative wheel-rail contact conditions for the track section that is being analysed. A better understanding of rail-wheel wear can lead to a more accurate prediction.

The sleeper-ballast interface is found to have the biggest impact on the lateral track deterioration since the parameters related to this interface all have the strongest impact on the lateral deterioration. The change of track parameters does not have a large impact on the shape of the lateral track deterioration compared to the vehicle and wheel-rail contact changes. At the specific location on the track where the peak deflection occurs, the influences by all different track parameters are not quite linear due to the resulting dynamic effects. Nevertheless, the RMS of the residual deflection changes appear relatively linear with respect to the track parameter variation. The changes in track lateral deterioration with respect to various changing parameters are listed below:

- The residual deflections decrease with an increase of all stiffness and damping values, and the sleeper-ballast lateral stiffness and damping have the largest impact on lateral track deterioration.
- An increase of rail and sleeper mass gives a reduction in the lateral track residual deflection, and for every kilogram increase in sleeper mass, a reduction in the residual deflection is seen that is greater than that for a similar change in the mass of the rails.
- Increasing the softening factor gives a linear amplitude reduction of the lateral track deterioration.
- An increase of the elastic breaking limit in the model leads to an amplitude reduction of the residual track deflection.
- If the sleeper spacing increases, the lateral track deterioration will also increase.

6 FURTHER WORK AND RECOMMENDATIONS

The mechanism of railway track lateral deterioration has been studied through statistical analysis and modelling processes. Scenarios that have not been attempted are discussed here as potential further research subjects. Points for further development of the vehicle-track lateral deterioration model are given in order to improve the accuracy, speed and applicability of the model.

6.1 Further work

6.1.1 Extension of statistical analysis

It was shown that the track lateral and vertical irregularities are correlated to some extent in both the distance domain and spatial domain. On average the lateral quality is slightly better than the vertical, however there are cases where it can be significantly worse. Due to the limitation of the recorded track data, the lateral track deterioration against the curvature and time are studied separately, so the parameters for these empirical functions are only valid on specific networks. The growth in the standard deviation of the lateral track irregularity against track curvature has only been validated using the DynoTrain track data, and the growth of the track lateral irregularity SD against time is only validated using a particular section of WCML track data. Further work will be useful to create a more comprehensive equation by combining the curvature and time (or loading cycles) factors, and in addition, the factors that have not been included in this study, such as temperature, ground condition, and traffic etc. To achieve this, additional analysis using measured track data that includes all of the information mentioned above will be required.

6.1.2 Extension of parameters study

The track parameters in the lateral direction are not well understood, and previous research in this area is quite limited. This is probably due to the difficulty of measuring these parameters and the highly non-linear characteristics of lateral track behaviour. More laboratory or field tests should be carried out to examine the track lateral stiffness and damping values thereby making future research more accurate.

The sleeper-ballast interface failure has been studied in detail by Le Pen [72, 77]. However, the lateral pre-sliding characteristics of the sleeper-ballast interface is not well understood, in terms of the hysteresis features or the force-displacement characteristics. An in-depth study of the pre-sliding characteristics would provide a better understanding and more accurate parameters for future research.

6.1.3 Extension of model capabilities

The development of the model, presented in Chapter 4, potentially forms the basis for further work to be carried out on each sub-system in the model. The validation results predict a short wavelength deterioration that is not seen in the actual track deterioration. It will be useful to understand the reason for the existence of this additional prediction, and under what conditions it can be filtered out. The discussion below may explain the reason for this behaviour.

For the vehicle dynamic model using VAMPIRE® software, efforts can be made to improve the vehicle models to describe the actual vehicle suspension system better such as the tilting mechanism of Class390, and be more representative of the exact vehicle type running on a specific track section

The track model can be improved and modified in two different ways. One is to develop a more comprehensive and complex model including additional key parameters, and the other is to simplify certain aspects of the model and thus create a faster model that describes the basic concept of lateral track deterioration. Both are discussed in more detail below:

1. More complex model including additional key parameters

There are a few factors that were not considered in the model and including these factors can make the model better at describing the complex dynamic behaviour of the actual track system. However, this leads to a more complicated and time consuming model. The potential factors that can be included in further development, as well as their advantages and drawbacks, are listed below:

- Add longitudinal dynamics to the model, so for each rail node there will be 6 DOF instead of 4, and for sleeper nodes there will be 3 DOF instead of 2. In this way, the influences of the longitudinal forces from the wheels to the track system will be included as presented in Figure 2-8. This may increase the calculation time significantly.
- The track data used in this research was collected between March and September for which the temperature change does not cover all variation expected over one year time. When the temperature changes through a significant range, it creates thermal expansion and contraction of the rails. It can be worthwhile to include the temperature influence on lateral track deterioration at some locations.
- The track bed, including ballast, sub-ballast and capping layers are considered as one track bed layer sitting on a rigid surface. This track bed layer can be modelled in detail in terms of ballast layer, sub-ballast layer, geotextile layer and subgrade. The change brought about by adding these layers on the lateral deterioration results are unknown and may be worth investigating, although there may be a chance that there will be no influence resulting from these changes.
- The sleeper-ballast elastic and hysteresis characteristics are simplified into two sections of linear force-displacement relationships. This non-linear characteristic can be improved to a curve that is closer to the condition in reality. The numerical calculation of this calculation can be solved using many different methods, such as: Newton-Raphson method, displacement control method, the constant work method and the minimum residual displacement method.

- Uneven stiffness and damping exists on most railway lines especially those in poor condition, and variations in track stiffness and damping can be included in the model. This may lead to a large influence on lateral deterioration. Again, it may lead to increasing complexity and simulation time in the model.
- As the wheel-rail contact condition is a critical interface between the vehicle and track, and has an enormous influence on the vehicle track dynamic interactions. The wear conditions of rails are different on different section of track, and the wheels within a fleet can have different amounts of wear. Therefore, it will be useful to include a larger range of representative contact profiles and simulating each independently, thereby combining their cumulative effects.

2. Simplify the model

In actual engineering work, it is not necessary to have a comprehensive and accurate simulation tool. Therefore, simplifying the model without sacrificing too much on the accuracy is another way of improving the model. A simple model tends to have a much faster simulation speed and is easier for users to understand. Some potential ideas for simplifying the existing model, as well as their benefits and drawbacks, are listed below:

- As the static vertical loads of the vehicles are much larger than the dynamic vertical forces, the distributed vertical loads from the rails to the sleepers are similar on each sleeper. It is possible to calculate the uniform vertical distributed load shape function relating to only the vehicle weight instead of carrying out the whole vertical dynamic simulation.
- Instead of using VAMPIRE®, it is possible to calculate the quasi-static vertical and lateral forces from the track layout (curve radius and cant deficiency) and superimpose a coefficient for the dynamic part of the force from the track quality. For a specific track section, these can be representative of different vehicle speed, track layout and quality of the track. On one hand, the net forces of different vehicles can be viewed as a constant force travelling along a section of track. On the other hand, the FE track model can also be modified to a single sleeper model representing the track support condition, and the deterioration model will be possible to be tuned into a function of quasi-static forces, dynamic force component and track parameters.

6.2 Recommendations

Potential ideas for improving the understanding and prediction of lateral track deterioration are summarised below.

- Collect track data with comprehensive information, regarding measuring time intervals, curvature ranges, loading tonnage, traffic, temperature, ground condition etc. and establish a more representative empirical equation for lateral track deterioration.

- Conduct an in-depth study into the interface between sleeper and ballast in terms of stiffness and damping values: force-displacement behaviour including hysteresis characteristic.
- Improve and optimise the VAMPIRE® vehicle models, such improving modelling the tilting mechanism of Class 390 fleets.
- Take into account additional factors in the lateral track deterioration model, such as the influence of longitudinal forces from the wheels to the rails, different weather and temperatures, more representative layers of the track bed, uneven stiffness and larger range of wheel-rail contact conditions, etc.
- Simplify the lateral track deterioration model by using a distributed vertical load shape function, or by replacing dynamic lateral and vertical forces with representative net vertical and lateral loads.

7 CONCLUSIONS

The study of vehicle-track lateral dynamic interaction has previously been based on a statistical analysis of track geometry data and vehicle-track dynamic modelling. The work undertaken in this thesis attempts to build a better understanding of track lateral quality characteristics and its deterioration under railway vehicle traffic. This chapter summarises the achievements made during the research and discusses the validity of the results and the impact this work may have in this area.

The aim of the research to develop a novel method for analysing and predicting railway track lateral deterioration caused by traffic has been met. Unlike most track lateral models, this model includes the nonlinear characteristics of the sleeper-ballast interface, and it also describes the dynamic process of the track lateral deterioration. The triggering limits in terms of vehicle, wheel-rail contact conditions and the track system are analysed using this model.

The track system, the measurements of the track geometry and the definition of the track quality are explained in detail in Chapter 1. This background study forms fundamental knowledge for the vehicle-track lateral dynamic interaction study.

A review of the current research in the field of vertical and lateral railway track deterioration was presented in Chapter 2 in order to establish a better understanding of track deterioration mechanisms, highlighting the weakness and limitations in these studies. There are a large number of vertical deterioration models which are mainly empirical settlement models. Different simulation models that describe the track system behaviour using simple BOEF analytical results or multi-body and FE methods are illustrated. The track lateral behaviour is not widely studied, and most of the track lateral studies are focused on sliding or buckling failure modes. The lateral resistance limits used nowadays in many countries are based on the modified Prud'homme limit defined many years ago primarily for use with wooden sleepers and relatively light rail sections. It is evident from the literature review that the development of railway track irregularities in the lateral direction is not well understood. Improving the understanding of the lateral deterioration is essential to prevent failures in the future and find technical solutions to help infrastructure managers maintain their track system at reasonable cost.

Based on the background review in this field, a statistical analysis, model development and sensitivity analysis are carried out in order to investigate the relationship between vehicle-track lateral dynamic interactions and lateral track deterioration. The achievements and discussions of these studies are summarised below.

7.1.1 Statistical analysis of track quality

Statistical analysis has been carried out in Chapter 3 in order to analyse the relationship between the vertical and lateral irregularities, the relationship between lateral irregularities and curvature, and the lateral track deterioration. From the statistical analysis results presented in Chapter 3, some understanding of the lateral track deterioration has been established and summarised below:

- The relationship between vertical and lateral track irregularities is obvious in both the distance domain and spatial domain. The track quality in the vertical direction is generally worse than in the lateral direction, but a number of track sections have lateral quality significantly worse than the vertical one.

- Lateral deterioration of track geometry is generally greater on curves, and there is an exponential growth of lateral irregularity against a decrease in curve radius. This growth is described by a power function based on track data for a large range of railway networks.
- Lateral track deterioration is normally corrected before it reaches an intolerable level due to frequent maintenance activities on railway lines in operation.
- Unlike vertical settlement, track lateral irregularities grow exponentially and this growth can be described using a power function.
- Track irregularities grow in both size and length according to both Power Spectral Density (PSD) and fractal analysis results.
- Long wavelength irregularities tend to be more stable, yet the small percentage of growing irregularities have a major impact on lateral irregularity development.
- Short wavelength irregularities have little impact on the development of irregularities overall, nevertheless, they can possibly grow into medium or long wavelength irregularities that cannot be neglected.

These findings give an overview of the characteristics of lateral track irregularities and track deterioration. A power function appears to give a good description of lateral deterioration growth against both curvature and time. As mentioned in the section on further work, to form a better empirical function requires a large amount of track data that includes more comprehensive information.

7.1.2 Model development

A non-linear vehicle-track lateral dynamic interaction model has been developed to simulate the link between the dynamic behaviour of railway vehicles and track lateral alignment growth. The model development process was described in Chapter 4. The model was validated against the recorded track data on the UK West Coast Main Line (WCML). It has been found that the model gives a reasonably accurate prediction of the development of track irregularities. Existing track lateral models mostly focus on lateral failures such as buckling and lateral sliding. The development of track lateral irregularities is mostly studied with representative net lateral forces and Lateral to Vertical (L/V) loading ratios. Unlike the other track lateral deterioration models, this model focuses on the detailed impact of lateral dynamic interactions between the vehicles and track system on the development of lateral irregularities. Consequently, this model makes it possible to describe the dynamic process of the lateral track deterioration in detail.

7.1.3 Sensitivity analysis

Based on the vehicle-track lateral dynamic interaction model, some sensitivity studies were carried out in Chapter 5 in order to develop a good understanding of the influencing factors and the triggering limits for the lateral track deterioration. The analysis consisted of three parts, which were the influence of the vehicles, wheel-rail contact conditions and track conditions. The analysis results are summarised below.

Good suspension design and appropriate running speed selection of the vehicle are the key factors in minimising the lateral track damage from the vehicles. Freight vehicles are found to produce the most lateral track damage due to their high axle load, simple suspension design and resulting dynamic behaviour. Within a certain speed range, there will be a critical speed that creates a peak in the residual deflection and reducing or increasing the vehicle speed can help reduce the residual deflection. It may be possible to vary the traffic mix in order to reduce the lateral deterioration and mitigate the effect of particularly damaging vehicles.

The wheel and rail profiles are critical in the track lateral deterioration due to their influence on the vehicle-track lateral dynamics. An increase in wheel wear makes the track lateral residual deflection smaller due to reduced lateral forces. Therefore, it is important to select the right measurement of the wheel and rail profiles, and find representative wheel-rail contact data for the track section that needs to be analysed. A better understanding of rail and wheel wear can lead to a more accurate prediction.

The sleeper-ballast interface is found to be the most important in lateral track deterioration. The strengthening of this interface can largely reduce lateral track deterioration, and this strengthening can be achieved by changing the parameters of this interface, such as:

- Increasing stiffness and damping values.
- Increasing the sleeper mass.
- Optimising the hysteresis characteristic of the sleeper-ballast interface.
- Enlarging the elastic breaking limit, which means increasing the elastic breaking displacement, force and friction coefficient between the sleeper and ballast.
- Decreasing sleeper spacing.

With this understanding of the lateral deterioration mechanisms, simulations can be carried out on different railway networks and for different traffic scenarios. It may be possible to quantify and plan in detail a strategy to prevent lateral track deterioration.

8 References

8.1 Documents

- [1] I. Makoto, "Track Technology Measurements of TRack Settlement and Its Prediction with Track Dynamic Model," *RTRI (Rail Technical Research Institute)*, vol. 16, pp. 41-46, 2002.
- [2] A. Kish, G. Samavedam, and D. Wormely, "Fundamentals for Track Lateral Shift for High Speed Rail Applications," *Bureau of Transportation Statistics*, 2004.
- [3] A. M. Remennikov and S. Kaewunruen, "A review of loading conditions for railway track structures due to train and track vertical interaction," *Structural Control and Health Monitoring*, vol. 15, p. 207, 2008.
- [4] F. C. Norman, I. Monticello, and E. K. Max, "Method of Welding Continuous Rail," in *United States Patent Office*, ed USA: Railway Automation Maintenance Specialties Company, 1963.
- [5] S.-Y. Lee and Y.-C. Cheng, "Hunting stability analysis of high-speed railway vehicle trucks on tangent tracks," *Journal of Sound and Vibration*, vol. 282, p. 881, 2005.
- [6] H. M. Tournay and J. M. Mulder, "The transition from the wear to the stress regime," *Wear*, vol. 191, p. 107, 1996.
- [7] I. Y. Shevtsov, V. L. Markine, and C. Esvelde, "Optimal design of wheel profile for railway vehicles," *Wear*, vol. 258, p. 1022, 2005.
- [8] P. Remington and J. Webb, "Estimation of wheel/rail interaction forces in the contact area due to roughness," *Journal of Sound and Vibration*, vol. 193, p. 83, 1996.
- [9] J. J. Kalker, *Three-Dimensional Elastic Bodies in Rolling Contact*. Netherlands: Kluwer Academic Publishers, 1990.
- [10] E. Magel, M. Roney, J. Kalousek, and P. Sroba, "The blending of theory and practice in modern rail grinding," *Fatigue & Fracture of Engineering Materials & Structures*, vol. 26, p. 921, 2003.
- [11] S. Kaewunruen, *New Research on Acoustics*. New York: Nova Science Publishers, 2008.
- [12] G. G. Leeves, "Standards for Track Components," in *Cost-Effective Maintenance of Railway Track*. vol. Chapter 2, ed Great Britain: Redwood Press, 1992, pp. 33-34.
- [13] J. S. Mundery, *Railway Track Engineering*. India: Tata McGraw-Hill Publishing, 2000.
- [14] H. Jahed, B. Farshi, M. A. Eshraghi, and A. Nasr, "A numerical optimization technique for design of wheel profiles," *Wear*, vol. 264, p. 1, 2008.
- [15] S. Kaewunruen, "Experimental And Numerical Studies for Evaluating Dynamic Behaviour of Prestressed Concrete Sleepers Subject to Severe Impact Loading," Doctor of Philosophy, Mining & Environmental Engineering - Faculty of Engineering, University of Wollongong, Wollongong, 2007.
- [16] A. M. Remennikov and S. Kaewunruen, "Investigation of Vibration Characteristics of Prestressed Concrete Sleepers in Free-free and In-situ Conditions," *Research Online*, 2005.
- [17] W. W. Hay, "Chapter 2 Ballast," in *Railroad Engineering*, ed US: John Wiley & Sons, 1982.
- [18] FIP Commission on Prefabrication, *Concrete Railway Sleepers*. London: Thomas Telford, 1987.

- [19] J. Lackenby, "Triaxial Behaviour of Ballast and The Role of Confining Pressure under Cyclic Loading," PhD, School of Civil Mining and Environmental Engineering, University of Wollongong, 2006.
- [20] J. P. Love, H. J. Burd, G. W. E. Milligan, and G. T. Houlsby, "Analytical and Model Studies of Reinforcement of A Layer of Granular Fill on A Soft Clay Subgrade," *Geotech*, vol. 24, 1987.
- [21] K. B. Ullman and W. B. O'Sullivan, "The Effect of Track Geometry on Ride Quality," *Industry and General Applications, IEEE Transactions on*, vol. IGA-7, p. 755, 1971.
- [22] P. Xu, Q. Sun, R. Liu, and F. Wang, "A short-Range Prediction Model for Track Quality Index," *Rail and Rapid Transit*, vol. 225, 2010.
- [23] M. Bocciolone, A. Caprioli, A. Cigada, and A. Collina, "A measurement system for quick rail inspection and effective track maintenance strategy," *Mechanical Systems and Signal Processing*, vol. 21, p. 1242, 2007.
- [24] E. Yazawa and K. Takeshita, "Development of Measurement Device of Track Irregularity using Inertial Mid-chord Offset Method," *Quarterly Report of RTRI*, vol. 43, pp. 125-130, 2002.
- [25] H. Tanaka, Y. Saruki, A. Shimizu, and M. Fukuyama. Detection Method for Rail Corrugation on Railway Track by Using On-board Measured Data [Online]. Available: www.poly.ac.mw/cesar/Full%20Papers/198.pdf
- [26] M. Molodova, Z. Li, and R. Dollevoet, "Axle box acceleration: Measurement and simulation for detection of short track defects," *Wear*, vol. In Press, Corrected Proof, 2010.
- [27] R. B. Lewis, "Track-recording techniques used on British Rail," *IEE Proc.*, vol. 131, pp. 73-81, 1984.
- [28] E. G. Berggren, "Efficient track maintenance: methodology for combined analysis of condition data," *Proceedings of the Institution of Mechanical Engineers, Part F: Journal of Rail and Rapid Transit*, vol. 224, p. 353, 2009.
- [29] RSSB, "Railway Group Standard," vol. GC/RT5021, ed: Railway Safety and Standards Board, 2003.
- [30] R. N. Iyengar and O. R. Jaiswal, "Random Field Modelling of Railway Track Irregularities," *Transportation Engineering*, vol. 121, pp. 303-308, 1995.
- [31] Y. H. Liu, F. Li, and Y. H. Huang, "Numerical Simulation Method of Railway Track Irregularity," *Journal of Traffic and Transportation Engineering*, vol. 6, pp. 29-33, 2006.
- [32] J. F. Huang, S. L. Lian, D. M. Zong, and W. Q. Hu, "Analysis of Cohercnce Between Track Random Irregularity and Vehicle Dynamic Response," *Journal of Tongji University*, vol. 31, pp. 16-20, 2003.
- [33] H. B. Jiang, S. H. Luo, and Z. M. Dong, "Numerical Simulation of Track Irregularities Based on Blackman-Tukey," *China Measurement Technology*, vol. 32, pp. 97-100, 2006.
- [34] P. F. Weston, S. C. Ling, and C. Roberts, "Monitoring Vertical Track Irregularity from In-service Railway Vehicles," *Rail and Rapid Transit*, vol. 221, 2006.
- [35] A. Massel, "Power Spectrum Analysis-Modern Tool in The Study of Rail Surface Corrugation," *NDT&E International*, vol. 32, pp. 429-436, 1999.
- [36] V. K. Garg and R. V. Dukkipati, *Dynamics of Railway Vehicle Systems*. New York: Academic Press, 1984.
- [37] D. Lyon, "Forces in The Track Due to Dipped Joints And Wheel flats," *Second ORE Colloquium Technical Computer Programs*, 1972.

- [38] K. L. Knothe and S. L. Grassie, "Modelling of Railway Track and Vehicle/Track Interaction at High Frequencies," *Vehicle System Dynamics*, vol. 22, pp. 209-262, 1993.
- [39] T. Dahlberg, *Hand book of Railway Vehicle Dynamics* vol. Track Issues. Boca Raton: CRC Press, 2006.
- [40] K. Werner, "Diskrete Riffelabsta und die Suche nach Den Ursachen der Schienenriffeln," *ZEV Classers Annalen*, vol. 10, pp. 353-359, 1986.
- [41] F. Fastenrath, "Die Eisenbahnschiene," *Verlag von Wilhelm Ernst&Sohn*, 1977.
- [42] B. Lichtberger, *Track Compendium*. Berlin: Eurail Press, 2005.
- [43] S. L. Grassie and J. Kalousek, "Rail Corrugation: Characteristics, Gauges and Treatments," *Rail and Rapid Transit*, pp. 57-58, 1993.
- [44] Y. Sato, A. Matsumoto, and K. Knothe, "Review on rail corrugation studies," *Wear*, vol. 253, p. 130, 2002.
- [45] X. Jin, Z. Wen, and K. Y. Wang, "Effect of Track Irregularities on Initiation and Evolution of Rail Corrugation," *Journal of Sound and Vibration*, vol. 285, pp. 121-148, 2004.
- [46] S. L. Grassie, "Short Wavelength Rail Corrugation: Field Trails and Measuring Technology," *Wear*, vol. 191, pp. 149-160, 1996.
- [47] S. Alfi and S. Bruni, "Estimation of long wavelength track irregularities from on board measurement," in *Railway Condition Monitoring, 2008 4th IET International Conference on*, 2008, pp. 1-6.
- [48] G. Wolf, "Preventing track buckles," *The Journal of Wheel/Rail Interaction*, 2005.
- [49] U. Espling, 2003.
- [50] C. O. Frederick, "The Effect of Rail Straightness on Track Maintenance," presented at the Advanced Techniques in Permanent Way Design, Construction and Maintenance, Madrid, 1981.
- [51] T. Dahlberg, "Some railroad settlement models—a critical review," *Proceedings of the Institution of Mechanical Engineers, Part F: Journal of Rail and Rapid Transit*, vol. 215, p. 289, 2001.
- [52] M. J. Shenton, "Ballast Deformation and Track Deterioration, Track Technology of the Next Decade," in *proceedings of a conference organised by the Institution of Civil Engineers and held at the University of Nottingham in 1984*, London, 1995, pp. 253-265.
- [53] Y. Sato, "Japanese Studies on Deterioration of Ballasted Track," *Vehicle System Dynamics*, vol. 24, pp. 197-208, 1995.
- [54] R. D. Frohling, "Deterioration of Railway Track due to Dynamic Vehicle Loading and Spatially Varing Track Stiffness," PhD, Faculty of Engineering, University of Pretoria, Pretoria, 1998.
- [55] J. E. Alva-Hurtado and E. T. Selig, "Permanent Strain Behavior of Railroad Ballast," in *10th International Conference on Soil Mechanics and Foundation Engineering*, Stockholm, Sweden, 1981, pp. 543-546.
- [56] A. Hecke, "Effects of Future Mixed Traffic on Track Deterioration, Report TRITA-FKT," *Railway Technology*, 1998.
- [57] D. Lonescu, B. Indraratna, and H. D. Christie, "Deformation of Railway Ballast under Dynamic Load," presented at the Core 98 Conference on Railway Engineering 7, 1998.
- [58] R. Ford, "Differential Ballast Settlement & Consequent Undulations in Track, Caused by Vehicle Track Interaction," *Vehicle System Dynamics*, vol. 24(Supplement), pp. 222-233, 1995.

- [59] A. Al Shaer, D. Duhamel, K. Sab, G. Foret, and L. Schmitt, "Experimental settlement and dynamic behavior of a portion of ballasted railway track under high speed trains," *Journal of Sound and Vibration*, vol. 316, p. 211, 2008.
- [60] J. Gao and W. M. Zhai, "Application of Vehicle-track Dynamics to Study on Settlement of Railway Tracks," *Journal of Southwest Jiaotong University*, vol. 4, 2007.
- [61] S. Wood, "Eurobalt--Revised & Validated Vertical Track Geometry Deterioration Model," British Rail Research RR-TCE-048, 1995.
- [62] Y. Q. Sun and M. Dhanasekar, "A dynamic model for the vertical interaction of the rail track and wagon system," *International Journal of Solids and Structures*, vol. 39, p. 1337, 2002.
- [63] S. Timoshenko, "Model of Analysis of Statical and Dynamical Stress in Rail," in *Congress for Appl. Mech*, Zurich, 1926, pp. 407-418.
- [64] B.-Z. Guo, "Riesz Basis Property and Exponential Stability of Controlled Euler--Bernoulli Beam Equations with Variable Coefficients," *SIAM Journal on Control and Optimization*, vol. 40, p. 1905, 2002.
- [65] L. Xueyi and W. Ping, *Dynamic Behaviour of Vehicle-track-foundation System (in Chinese)*. Chengdu: Southwest Jiaotong University Publish, 2010.
- [66] S. L. Grassie, R. W. Gregory, D. Harrison, and K. L. Johnson, "The dynamic response of railway track to high frequency vertical excitation," *ARCHIVE: Journal of Mechanical Engineering Science 1959-1982 (vols 1-23)*, vol. 24, p. 77, 1982.
- [67] Z. Cai and G. P. Raymond, "Modelling The Dynamic Response of Railway Track to Wheel/rail Impact Loading," *Structural Engineering and Mechanics*, vol. 2, pp. 95-112, 1994.
- [68] S. S. Radampola, "Evaluation and Modelling Preformance of Capping Layer in Rail Track Substructure," Doctor of Philosophy, Centre for Railway Engineering, Central Queensland University, Rockhampton, 2006.
- [69] S. C. Chang, E. T. Selig, and C. W. Adegoke, "GEOTRACK Model for Railroad Truck Performance," *Journal of the Geotechnical Engineering Division*, vol. 106, pp. 1201-1218, 1980.
- [70] T. X. Wu and D. J. Thompson, "Analysis of Lateral Vibration Behaviour of Railwa Track at High Frequencies Using a Continuously Supported Multiple Beam Model," vol. 106, pp. 1369-1376, 1999.
- [71] S. F. Brown and J. W. Pappin, "Analysis of Pavements With Granular Bases," *Transportation Research Record*, vol. 810, pp. 17-23, 1981.
- [72] L. Le Pen, "The Importance of The Sleeper to Ballast Interface," Doctor of Philosophy, Faculty of Engineering, Science and Mathematics, University of Southampton, Southampton, 2008.
- [73] M. Burstow, J. Ammore, J. Paragreen, P. Richards, B. Eickhoff, S. Mills, *et al.*, "Priorities and Actions from Track-Ex Next Steps Meeting," 2010.
- [74] A. Prud'homme, "Resistance of The Track to Lateral Loads Exerted by Rolling Stock," *Trvue Generale des Chemins de Fer*, 1967.
- [75] F. Amans and R. Sauvage, "Railway Track Stability in Relation to Transverse Stresses Exerted by Rolling Stock. ATheoretical Study of Track Behaviour," 1969.
- [76] E. Kabo, "A Numerical Study of The Lateral Ballast Resistance in Railway Tracks," *Rail and Rapid Transit*, vol. 220, 2006.
- [77] L. M. Le Pen and W. Powrie, "Contribution of base, crib, and shoulder ballast to the lateral sliding resistance of railway track: a geotechnical perspective," *Proceedings of the Institution of Mechanical Engineers, Part F: Journal of Rail and Rapid Transit*, vol. 225, p. 113, 2010.

- [78] R. Butterfield and G. Gottardi, "A Complete Three-dimensional Failure Envelope for Shallow Footings on Sand," *Geotechnique*, vol. 44, pp. 181-184, 1994.
- [79] G. G. Meyerhof, "Some recent research on the bearing capacity of foundations," *Canadian Geotechnical Journal*, vol. 1, pp. 16-26, 1963.
- [80] C. Esveld, "Improved Knowledge of Forces in CWR Track," European Rail Research Institute, Committee D202, Utrecht 2, 1995.
- [81] ORE, "A Study of The Factor Influencing The Resistance to Transverse Displacement of Unloaded Track,," Office for Research and Experiments of The International Union of Railways, Committe D117 8, 1976.
- [82] OMNISIM, "Program and User's Guide," U. D. F. Software, Ed., ed, 1998.
- [83] A. Kish and G. Samavedam, "Risk Analysis Based CWR Track Buckling Safety Evaluations," 2001.
- [84] N. H. Lim and I. H. Sung, "Thermal Buckling Behavior of Continuous Welded Rail Track," *Steel Structures*, vol. 4, pp. 111-119, 2004.
- [85] B. Lichtberger, "The lateral resistance of the track," *European Railway Review*, vol. 13, pp. 68-71, 2007.
- [86] EN14363, "Railway Applications. Testing for The Acceptance of Running Characteristics of Railway Vehicles. Testing of Running Behaviour and Stationary Tests.,," ed, 2005.
- [87] HS-RST, "Technical Specification for Interoperability," ed, 2008.
- [88] ChineseTB/T2360, "Accreditation Method and Evaluation Standard in The Dynamic Performance for Railway Locomotives," ed.
- [89] ALS07, "Russia Gost R51625, Gost 7174, NB ZhT CT 03-98," 2006.
- [90] SIE05, "Austria "Anforderungskatalog an triebfahrzeuge fur die Zulassung im Netz der OBB",," vol. 1.2.3, ed. Austria, 2010.
- [91] SIE11, "Swizerland Ausfuhrungsbestimmungen zur Eisenbahnverordnung AB-EBV",," vol. AB31, ed.
- [92] G. Cervi, "High Speed Rail Track Structure Design and Maintenance," in *Transportation Research Board, Annual Congress*, 1997.
- [93] A. Kish, G. Samavedam, and D. Wormley, "New Track Shift Safety Limits For High-speed Rail Application," in *World Congress on Railway Research*, Germany, 2001.
- [94] N. Thom, "Factors Affecting Trackbed Maintenance Requirements: A Theoretical Study," *Railway Engineering*, 2007.
- [95] N. Rail, "Inspection and maintenance of permanent way - geometry and gauge clearance," in *Nr/12/trk/001/c01*, ed, 2009.
- [96] P. Weston, C. Ling, C. Goodman, C. Roberts, P. Li, and R. Goodall, "Monitoring lateral track irregularity from in-service railway vehicles," *Proceedings of the Institution of Mechanical Engineers, Part F: Journal of Rail and Rapid Transit*, vol. 221, p. 89, 2007.
- [97] E. T. Selig and J. M. Waters, *Track Geometry and Substructure Management*. London: Thomas Telford, 1994.
- [98] R. Taylor, "Interpretation of the correlation coefficient: a basic review," *Journal of diagnostic medical sonography*, vol. 6, pp. 35-39, 1990.
- [99] X. M. Chen, F. C. Yang, W. Q. Wu, and X. S. Chai, "The PSD Analyse of Qin-Shen Track Irregularity " *Railway Engineering*, pp. 94-97, 2006.
- [100] D. Avnir, O. Biham, D. Lidar, and O. Malcai, "Is the Geometry of Nature Fractal?," *Science*, vol. 279, pp. 39-40, 1998.
- [101] B. Mandelbrot, "How Long Is the Coast of Britain? Statistical Self-Similarity and Fractional Dimension," *Science*, vol. 156, pp. 636-638, 1967.

- [102] C. O. Tan, M. A. Cohen, D. L. Eckberg, and J. A. Taylor, "Fractal properties of human heart period variability: physiological and methodological implications," *The Journal of Physiology*, vol. 587, pp. 3929-3941, 2009.
- [103] A. Karperien, H. F. Jelinek, J. J. Leandro, J. V. Soares, R. M. Cesar, and A. Lukie, "Automated detection of proliferative retinopathy in clinical practice," *Clin Ophthalmol*, vol. 2, 2008.
- [104] S. Hu, Q. Cheng, L. Wang, and S. Xie, "Multifractal characterization of urban residential land price in space and time," *Applied Geography*, vol. 34, pp. 161-170, 5// 2012.
- [105] J. Hyslip, "Fractal Analysis of Track Geometry Data," *Transportation Research Record: Journal of the Transportation Research Board*, vol. 1785, pp. 50-57, 01/01/ 2002.
- [106] S. Jaggi, D. A. Quattrochi, and L. Nina Siu-Ngan, "Implementation and operation of three fractal measurement algorithms for analysis of remote-sensing data," *Computers & Geosciences*, vol. 19, pp. 745-767, 7// 1993.
- [107] M. Ishida, M. Takikawa, and Y. Jin. Gauge Face Wear Caused with Vehicle/Track Interaction.
- [108] W. Zhai and X. Sun, "A detailed model for investigating vertical interaction between railway vehicle and track," *Vehicle System Dynamics*, vol. 23, pp. 603-615, 1994.
- [109] DeltaRail, "VAMPIRE PRO V5.42," in *Introductory Training Course*, ed. UK: DeltaRail, 2011.
- [110] Network Rail, "Working Timetables and Books of Rules and Regulations," N. Rail, Ed., Private and not for publication ed, 2012.
- [111] C. Esveld, *Modern railway track*. Duisburg, West Germany: MRT Productions], 1989.
- [112] T. R. Sussmann, W. Ebersöhn, and E. Selig, T., "Fundamental Nonlinear Track Load-Deflection Behaviour for Condition Evaluation," presented at the Transortation Research Record 1742, 2001.
- [113] R. D. Frohling, "Deterioration of Railway Track Due to Dynamic Vehicle Loading and Spatially Varing Track Stiffness," Philosophiae Doctor (Engineering), Civil Engineering, University of Pretoria, 1997.
- [114] E. Burggren, "Railway Track Stiffness," Doctoral, Aeronautical and vehicle engineering, Royal Institute of Technology (KTH), Stockholm, 2009.
- [115] D. Thompson, C. Jones, T. Waters, and D. Farrington, "A tuned damping device for reducing noise from railway track," *Applied acoustics= Acoustique applique = Angewandte Akustik*, vol. 68, pp. 43-57, 2007.
- [116] E. Berggren and G. Saussine, "Innotrack guideline," Innotrack2006.
- [117] X. Liu and P. Wang, *Dynamic Behaviour of Vehicle-track-foundation System (in Chinese)*. Chengdu: Southwest Jiaotong University Publish, 2010.
- [118] Corus, *Rail Products: Technical Handbook*: Corus, 2005.
- [119] Railtrack Line Specification, "Track Construction Standards," vol. RT/CE/S/006, ed, 2002.
- [120] D. J. Thompson and J. W. Verheij, "The Dynamic Behaviour of Rail Fasteners at High Frequencies," *Elsevier*, vol. 52, pp. 1-17, 1997.
- [121] E. Laurence and P. E. Daniels, "Direct Fixation Track Design," 2004.
- [122] H. L. Wong, "Analysis of Vibrations and Infrastructure Deterioration Caused by High-Speed Rail Transit," University of Southern California Los Angeles2005.
- [123] C. Gong, "Analysis of the Behaviour of a Selection of Different Rail Fastenings," Master, University of Birmingham, 2010.

- [124] Y. Bezin, "An Integrated Flexible Track System Model for Railway Vehicle Dynamics," PhD, Department of Engineering & Technology, Manchester Metropolitan University, Manchester, 2008.
- [125] G. A. Hunt and Z. M. Yu, "Measurement of Lateral Resistance Characteristics for Ballasted Track BR Research Report BR-TCE-81," 1997.
- [126] D. M. Clark, M. McCann, and M. C. Forde, "Infrared Thermographic Investigation of Railway Track Ballast," *NDT&E international*, vol. 35, pp. 83-94, 2002.
- [127] G. A. Hunt, "EUROBALT: Vertical Dynamic Model for Track Damage Studies," British Rail Research Report 2008.
- [128] V. Markine and C. Esvelde, "ANALYSIS OF LONGITUDINAL AND LATERAL BEHAVIOUR OF A CWR TRACK USING A COMPUTER SYSTEM LONGIN," *TU Delft University, Railway department*.
- [129] N.-H. Lim, N.-H. Park, and Y.-J. Kang, "Stability of continuous welded rail track," *Computers & Structures*, vol. 81, pp. 2219-2236, 9// 2003.
- [130] T. X. Wu and D. J. Thompson, "Wheel/Rail Non-linear Interactions With Coupling Between Vertical and Lateral Directions," *Vehicle System Dynamics*, vol. 41, pp. 27-49, 2004/01/01 2004.
- [131] T. R. Sussmann, A. Kish, and M. J. Trosino, *Investigation of the influence of track maintenance on the lateral resistance of concrete tie track*: John A. Volpe National Transportation Systems Center, 2007.
- [132] J. A. Zakeri, "Lateral Resistance of Railway Track," in *Reliability and Safety in Railway*, X. Perpinya, Ed., ed, 2012.
- [133] G. Q. Jing, S. Lin, and S. Shao, "Micro-Analysis of Railway Ballast Bond Effect by DEM (in Chinese)," *Chinese Science Journal*, 2010.
- [134] J. A. Zakeri, "Frictional Concrete Sleeper and its Influence on the Lateral Resistance of Track," Iran University of Science and Technology, Tehran 2011.
- [135] A. Bakhitriy, "Investigation of Parameters Affecting on the Lateral Resistance of Ballasted Railway Track," ed. Tehran, Iran: Iran University of Science and Technology, 2011.
- [136] P. Lou and Q. Y. Zeng, "On Three Approaches to Formulation of the Equations of Motion of A Dynamic System," *Journal of Structural Engineering*, vol. 29, pp. 119-123, 2002.
- [137] L. Ping and Z. Qingyuan, "Finite Element Analysis of Slab Track Subjected to Moving Load," *Journal of Traffic and Transportation Engineering*, vol. 4, 2004.
- [138] L. Renxian, *Finite-element Fundamental Theory (In Chinese)*. Beijing: Guo Fang Gong Ye 2009.
- [139] A. Kish, "On the Fundamentals of Track Lateral Resistance," presented at the AREMA, MA, USA, 2011.
- [140] J. S. Courtney-Pratt and E. Eisner, "The effect of a tangential force on the contact of metallic bodies," *Proceedings of the Royal Society of London. Series A. Mathematical and Physical Sciences*, vol. 238, pp. 529-550, 1957.
- [141] E. Rabinowicz, "The nature of the static and kinetic coefficients of friction," *Journal of applied physics*, vol. 22, pp. 1373-1379, 1951.
- [142] Reinicke, Herrmann, and Parmentier, "Lateral Resistance Tests," DB1997.
- [143] J. van't Zand and J. Moraal, "Ballast Resistance under Three Dimensional Loading," TU Delft 1996.
- [144] H. Olsson, K. J. Åström, C. Canudas de Wit, M. Gäfvert, and P. Lischinsky, "Friction models and friction compensation," *European journal of control*, vol. 4, pp. 176-195, 1998.

- [145] D. V. Deshmukh, E. J. Berger, M. R. Begley, and U. Komaragiri, "Correlation of a discrete friction (Iwan) element and continuum approaches to predict interface sliding behaviour," *European Journal of Mechanics*, pp. 212-224, 2006.
- [146] J. R. Rieker, Y.-H. Lin, and M. W. Trethewey, "Discretization considerations in moving load finite element beam models," *Finite elements in analysis and design*, vol. 21, pp. 129-144, 1996.
- [147] P. Shackleton and J. Stow, "Controlling rail vertical contact stresses," presented at the Vehicle Track Interaction, UK, 2011.
- [148] M. Burstow and M. Ryan, "VTISM: Integration of RCF modelling with T-SPA," DeltaRail, Derby2007.

8.2 Websites

- Website Reference 1** <http://www.websters-dictionary-online.com/definitions/fishplate?cx=partner-pub-0939450753529744:v0qd01-tdlq&cof=FORID:9&ie=UTF-8&q=fishplate&sa=Search#906> – for figure of rail joint with fishplate (Accessed 23 Feb 11)
- Website Reference 2** http://images.quickblogcast.com/101200-93910/railroad_spike.jpg - for figure of rail spike (Accessed 29 Jul 10)
- Website Reference 3** <http://www.pandrol.com/images/products/ediag.jpg> - for figure of Pandrol E-clip (Accessed 1 Aug 10)
- Website Reference 4** <http://www.pandrol.com/images/fastclip/intro/FASTCLIP%20working%20position.jpg> – for figure of Pandrol Fastclip (1 Aug 10)
- Website Reference 5** <http://www.VAMPIRE®-dynamics.com/> – for VAMPIRE® simulation tool published by DeltaRail (Accessed 7 Mar 11)\
- Website Reference 6** http://en.wikipedia.org/wiki/File:Virgin_Pendolino_390009_at_Carlisle_2005-10-08_01.jpg – for Virgin Pendolino (Accessed 08 Jan 13)
- Website Reference 7** http://en.wikipedia.org/wiki/File:Virgin_SuperVoyager_@Crewe.jpg – for Virgin SuperVoyager (Accessed 08 Jan 13)
- Website Reference 8** <http://www.garethbayer.co.uk/wotw/great-britain/f-coded/fea-bogie-flat/#> - for FEAB wagon (Accessed 08 Jan 13)
- Website Reference 9** <http://www.garethbayer.co.uk/wotw/great-britain/f-coded/fsa-container-flat/#> - for FSAO wagon (Accessed 08 Jan 13)

9 Appendices

Appendix A statistical analysis

- A.1 Least-squares regression
- A.2 MSC results between track lateral and vertical irregularities
- A.3 Box-plot of track irregularities against track curvature
- A.4 Fractal analysis results

Appendix B governing equations for boef track model

Appendix C mass, stiffness and damping matrix creation for track model

- C.1 Mass, stiffness and damping matrix of FE track lateral model

Appendix D track model parameter selection

- D.1 Traffic information on WCML
- D.2 Lateral resistance parameters

Appendix A STATISTICAL ANALYSIS

A.1 Least-squares regression

Assume the fitted straight line to be

$$y = a_0 + a_1 x \quad \text{Equation 67}$$

Then the error in y between the data point (x_i, y_i) is

$$e_i = y_i - (a_0 + a_1 x_i) \quad \text{Equation 68}$$

Therefore, the total error of the data can be

$$S_r = \sum_{i=1}^n e_i \quad \text{Equation 69}$$

The value of a_0 and a_1 can be found as below

$$\begin{cases} a_1 = \frac{n \sum x_i y_i - \sum x_i \sum y_i}{n \sum x_i^2 - (\sum x_i)^2} \\ a_0 = \frac{\sum y_i}{n} - a_1 \frac{\sum x_i}{n} \end{cases} \quad \text{Equation 70}$$

The correlation coefficient r can be defined as

$$r = \frac{n \sum x_i y_i - \sum x_i \sum y_i}{\sqrt{n \sum x_i^2 - (\sum x_i)^2} \sqrt{n \sum y_i^2 - (\sum y_i)^2}} \quad \text{Equation 71}$$

The data is perfectly linear if $r=1$, while the data is totally not linear if $r=0$.

A.1.1 Tangent track results

Figure 9-1 to Figure 9-10 shows both the vertical and lateral irregularity SD values of each 200 m, 600 m and 1000 m section on tangent track in all types of Networks and the linear relationship between them. The pink dashed line represents the condition when the lateral irregularity SD equals vertical irregularity SD.

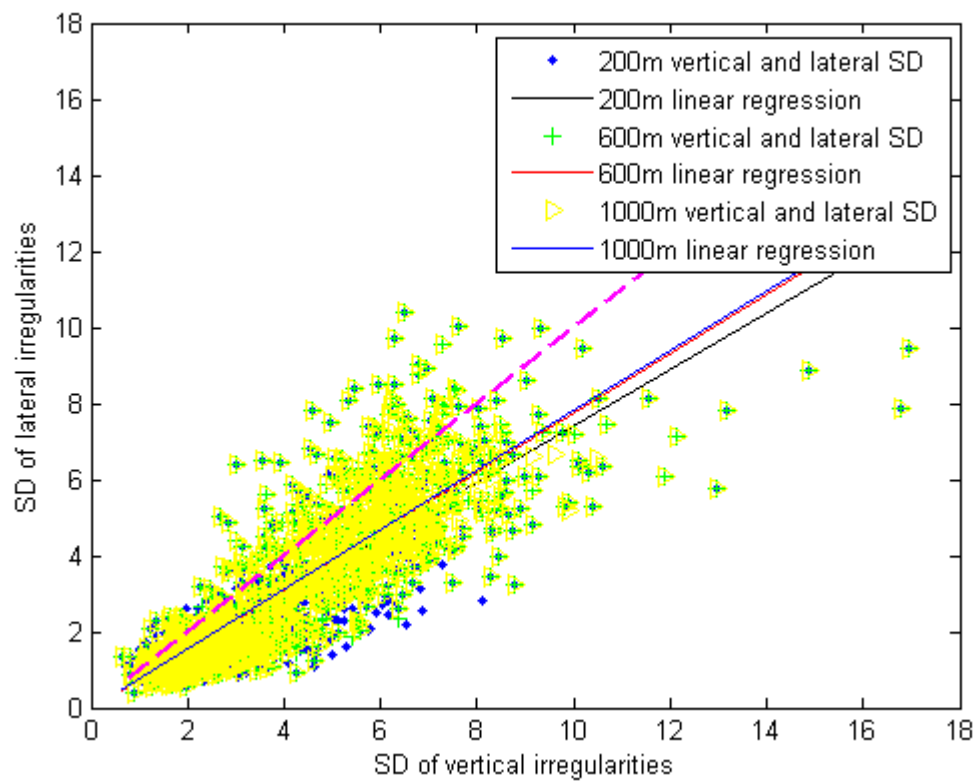


Figure 9-1 Vertical and lateral SD values in freight lines of Network A

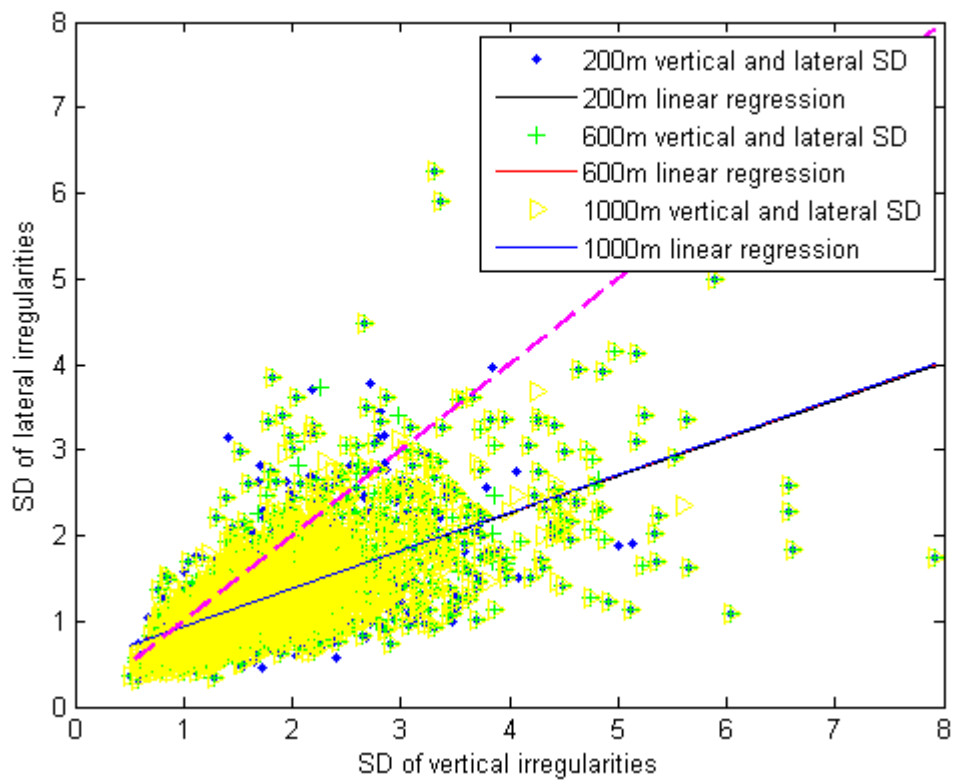


Figure 9-2 Vertical and lateral SD values in regional lines of Network A

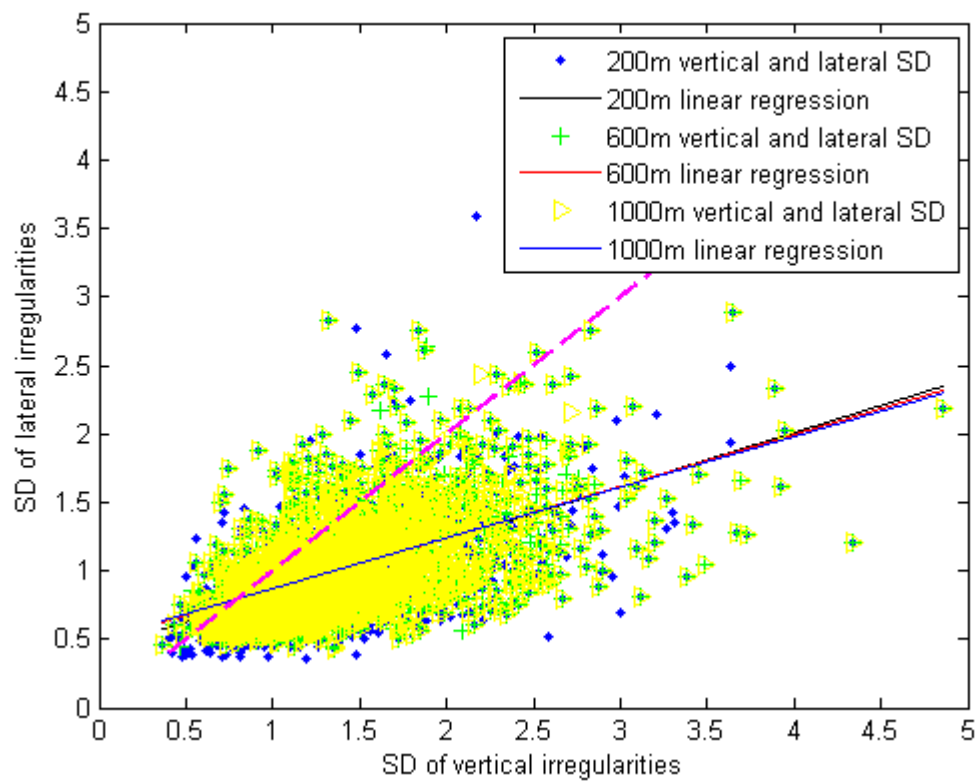


Figure 9-3 Vertical and lateral SD values in upgraded lines of Network A

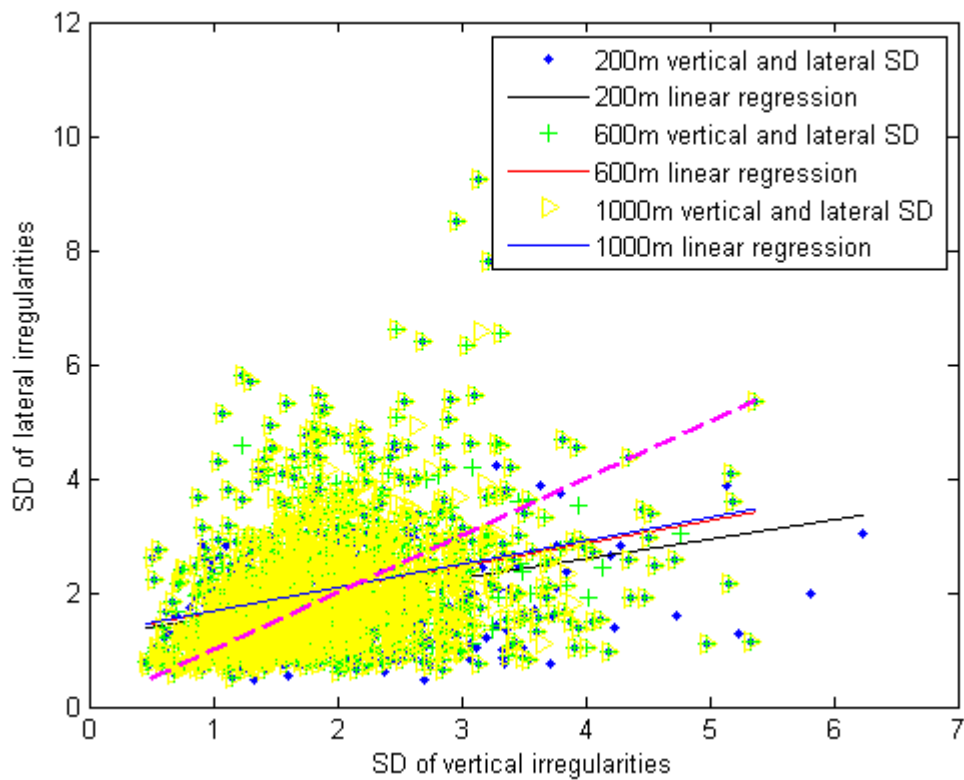


Figure 9-4 Vertical and lateral SD values in high speed lines of Network A

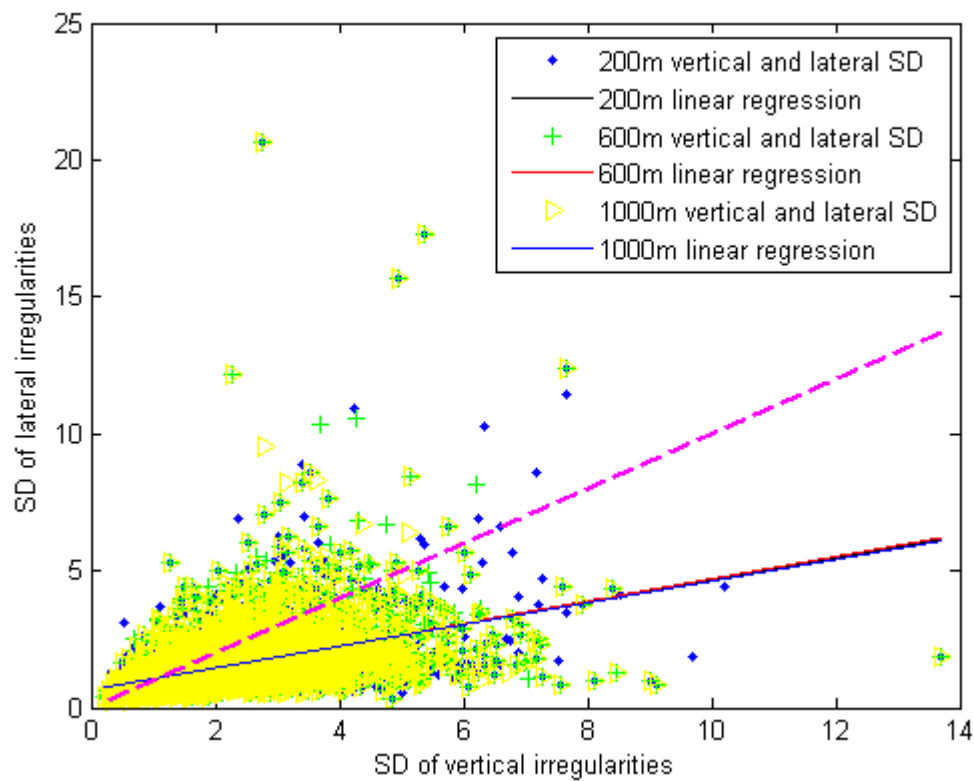


Figure 9-5 Vertical and lateral SD values in regional lines of Network B

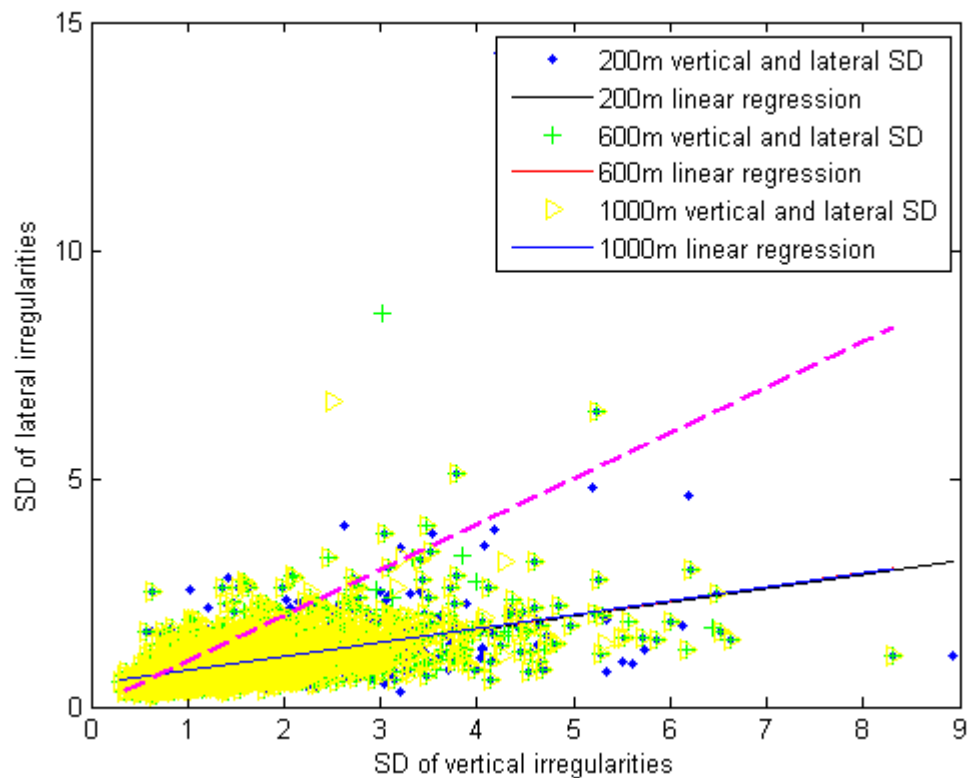


Figure 9-6 Vertical and lateral SD values in upgraded lines of Network B

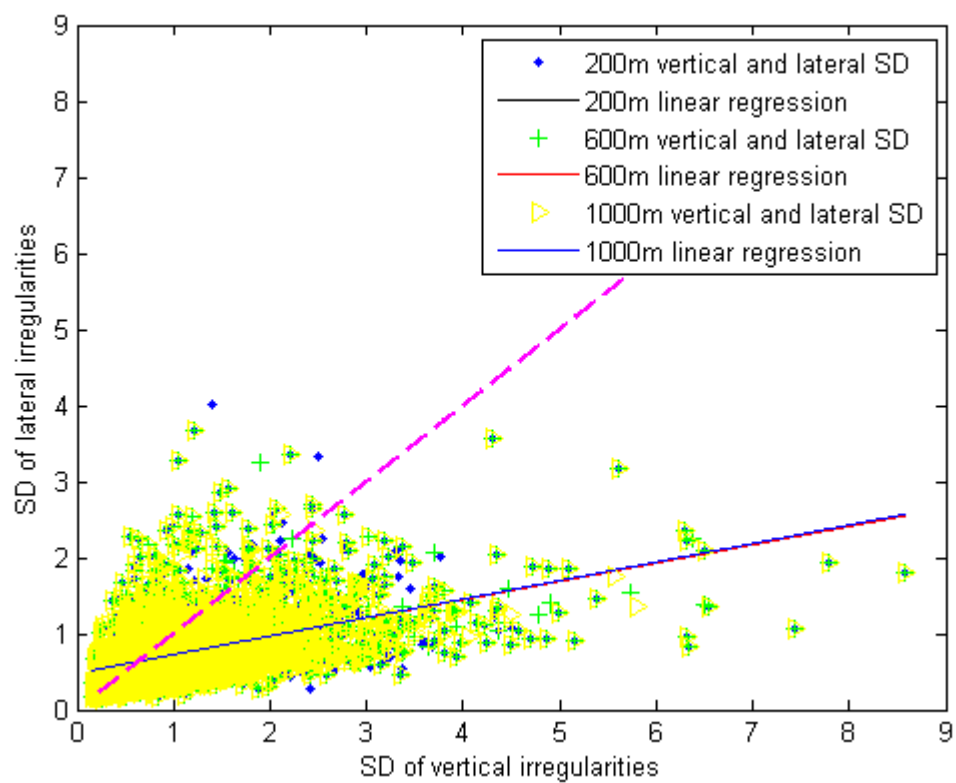


Figure 9-7 Vertical and lateral SD values in high speed lines of Network B

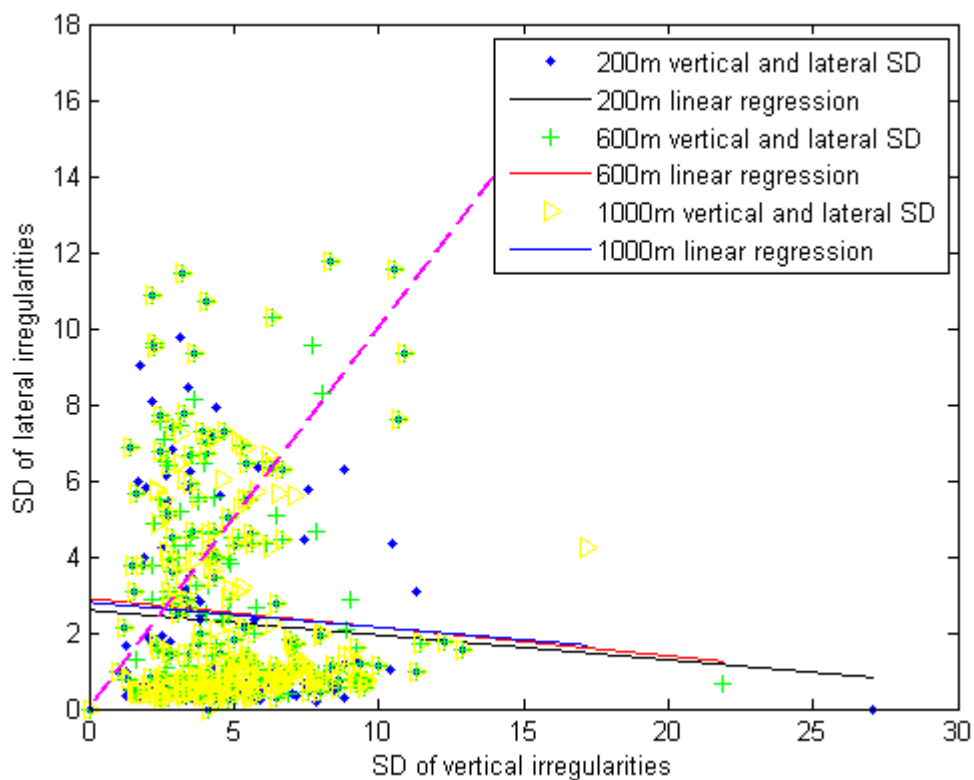


Figure 9-8 Vertical and lateral SD values in freight lines of Network C

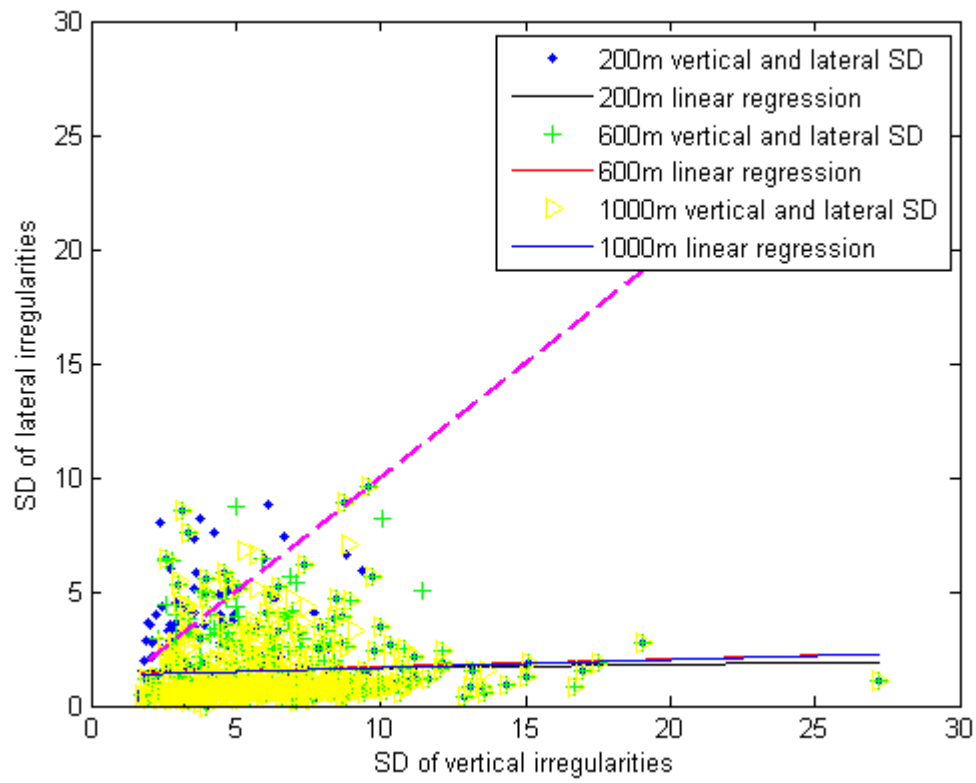


Figure 9-9 Vertical and lateral SD values in regional lines of Network C

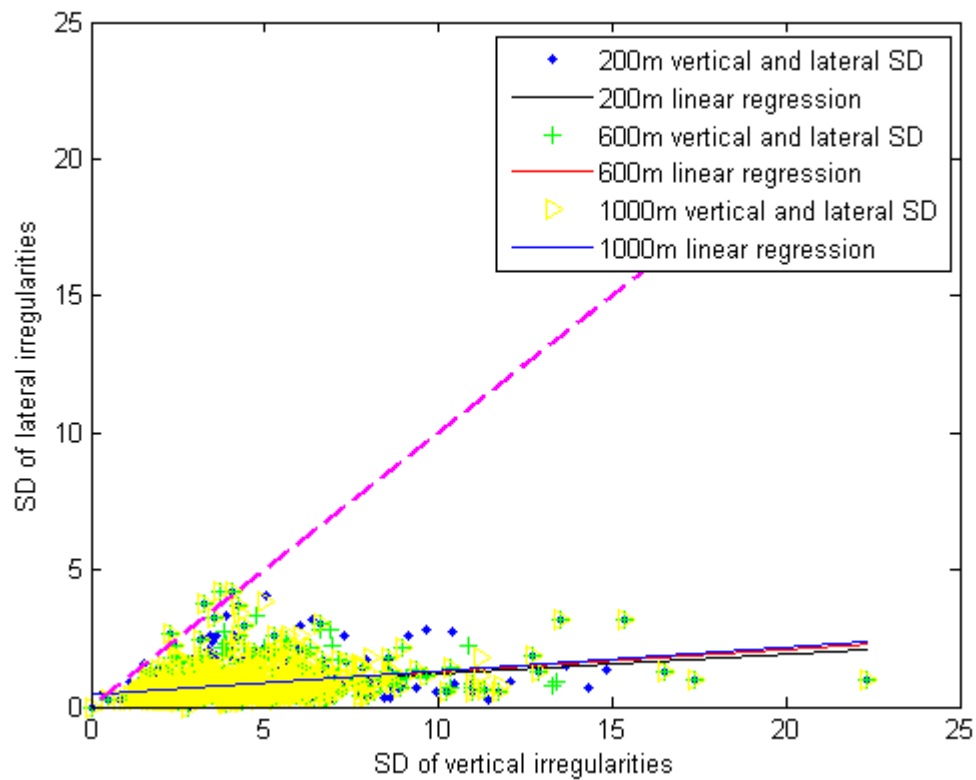


Figure 9-10 Vertical and lateral SD values in upgraded lines of Network C

A.1.2 Curved track results

Figure 9-11 to Figure 9-20 shows both the vertical and lateral irregularity SD values of each 200 m, 600 m and 1000 m section on curves in all types of Networks and the linear relationship between them. The pink dashed line represents the condition when the lateral irregularity SD equals vertical irregularity SD.

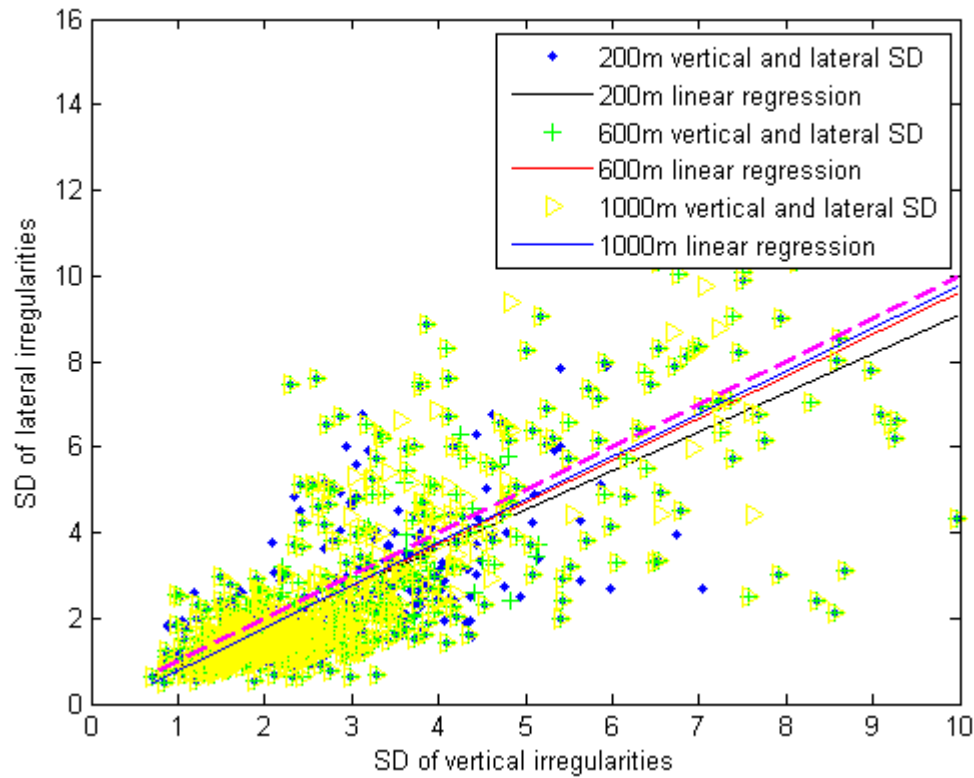


Figure 9-11 Vertical and lateral SD values in freight lines of Network A

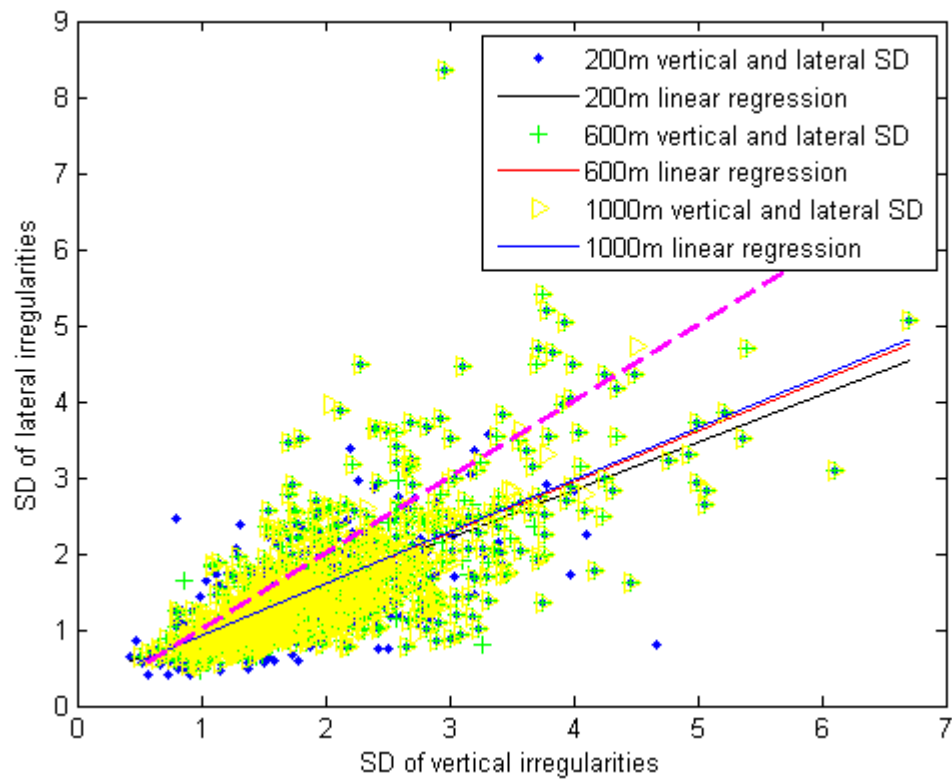


Figure 9-12 Vertical and lateral SD values in regional lines of Network A

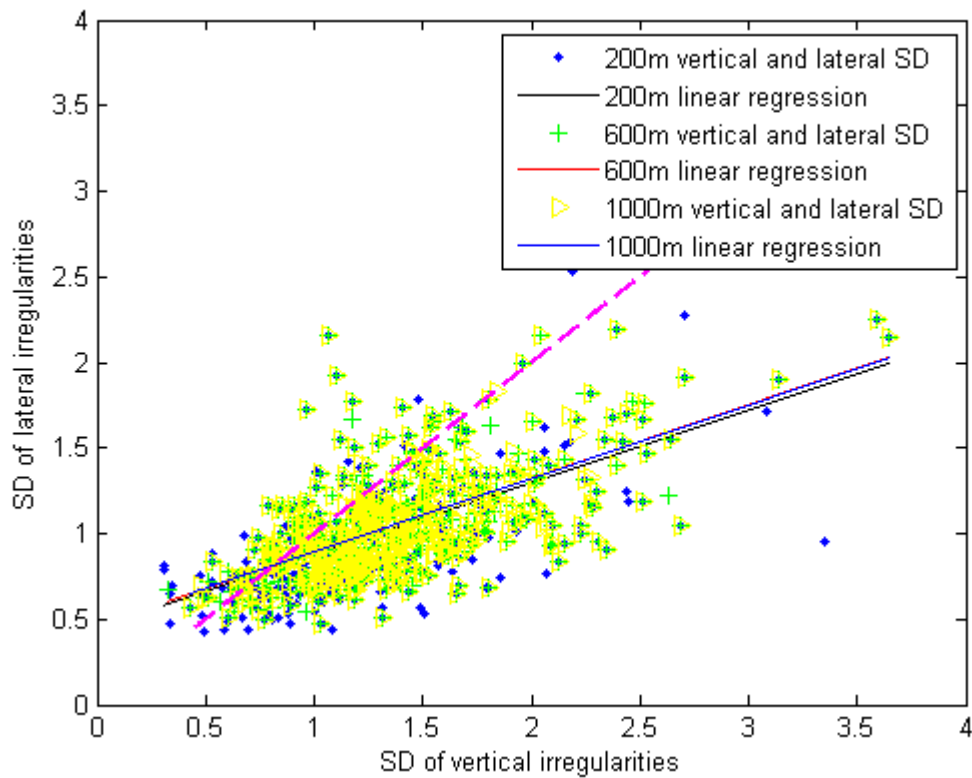


Figure 9-13 Vertical and lateral SD values in upgraded lines of Network A

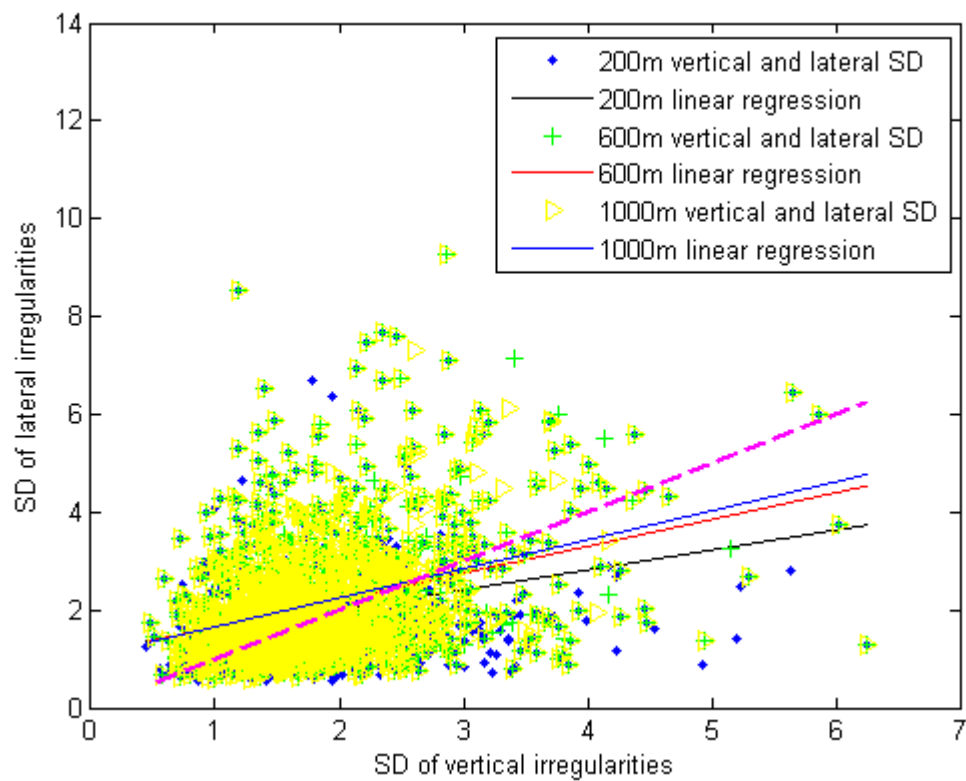


Figure 9-14 Vertical and lateral SD values in high speed lines of Network A

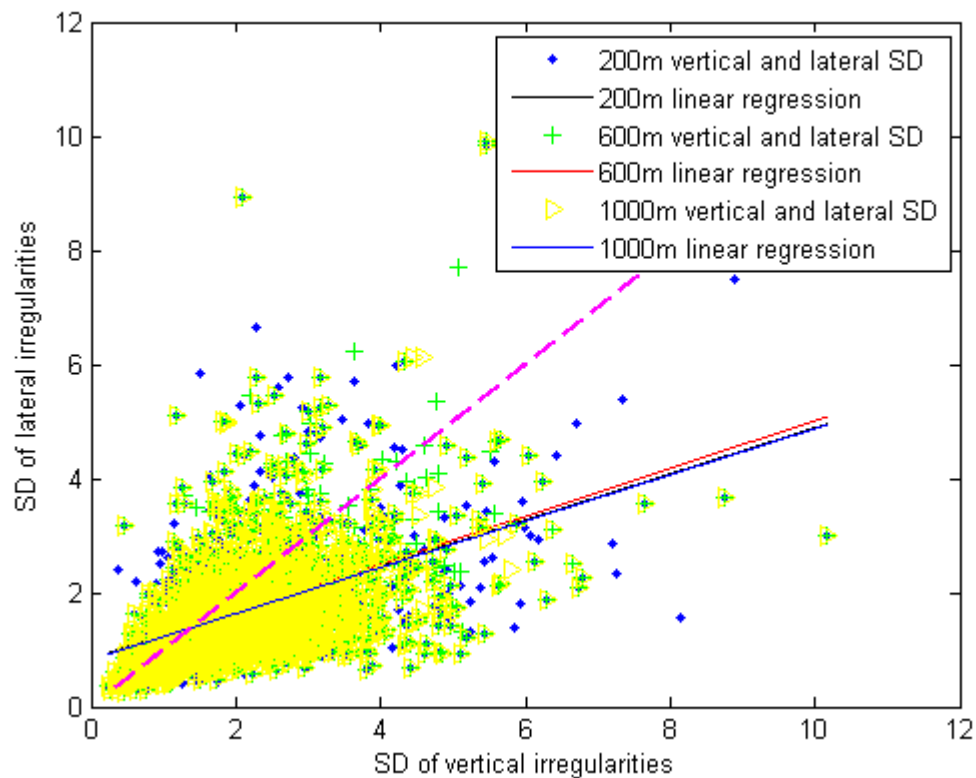


Figure 9-15 Vertical and lateral SD values in regional lines of Network B

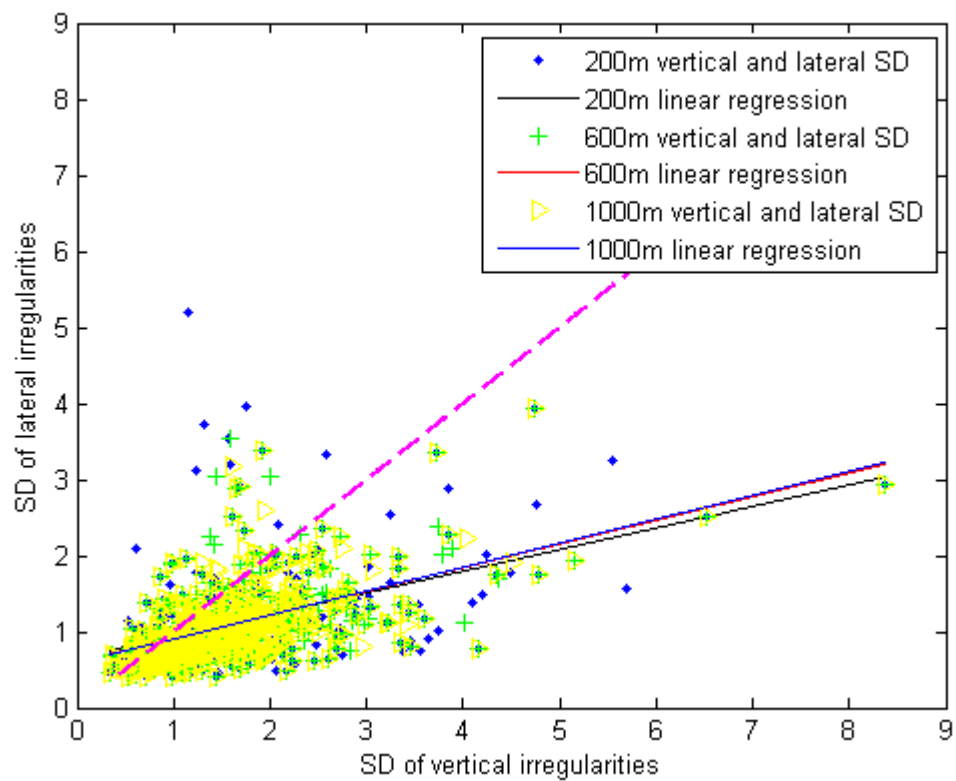


Figure 9-16 Vertical and lateral SD values in upgraded lines of Network B

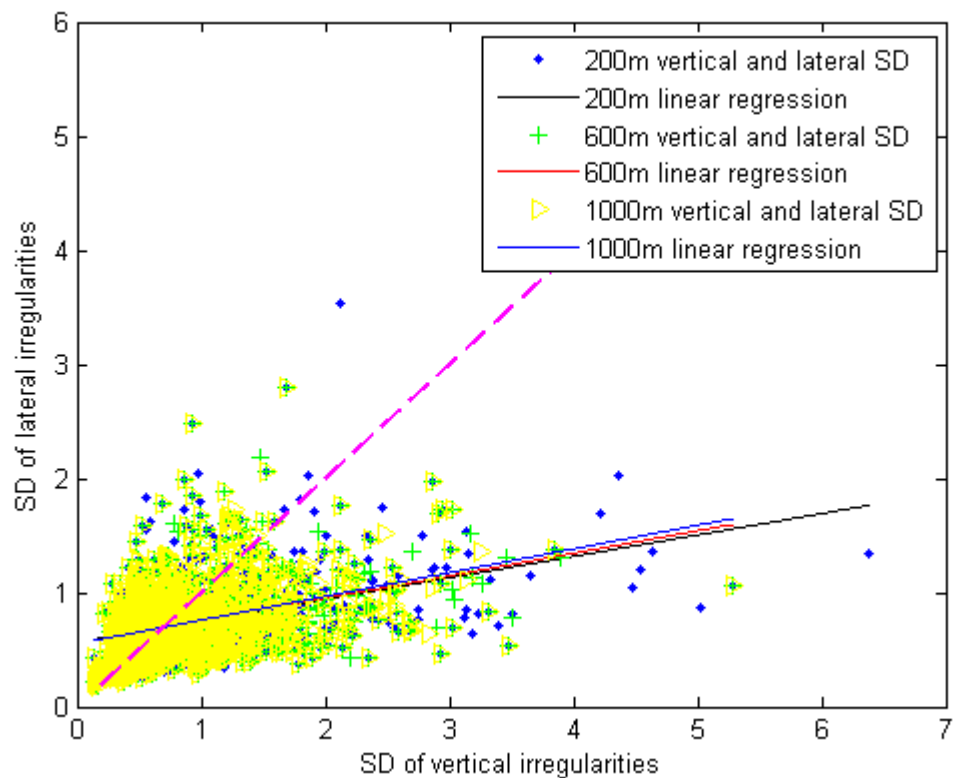


Figure 9-17 Vertical and lateral SD values in high speed lines of Network B

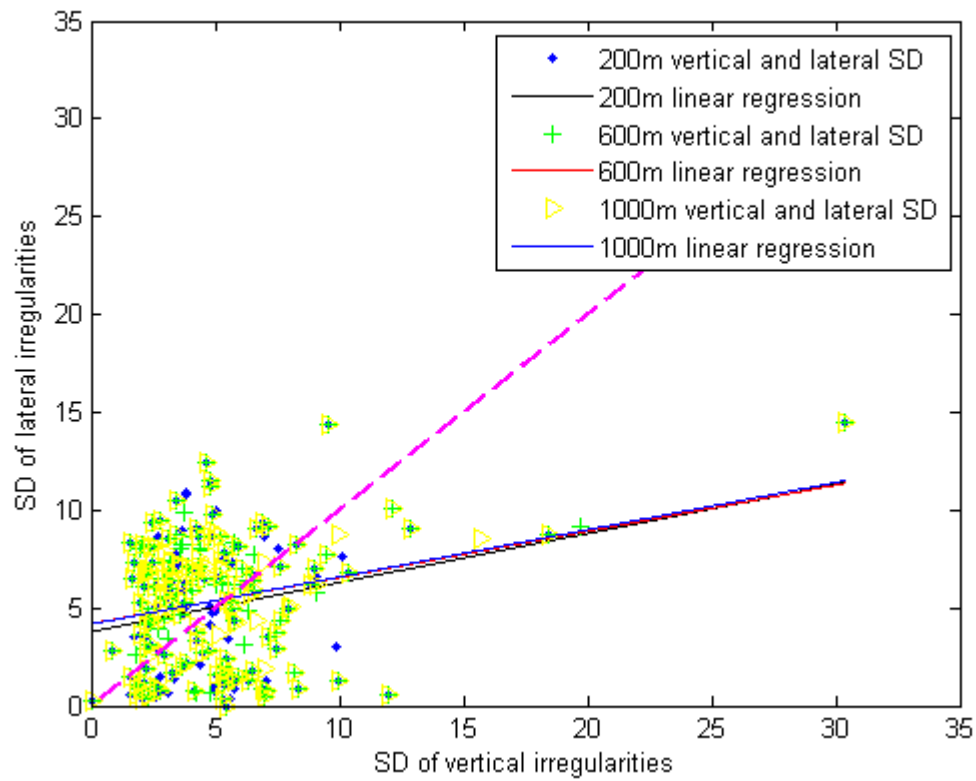


Figure 9-18 Vertical and lateral SD values in freight lines of Network C

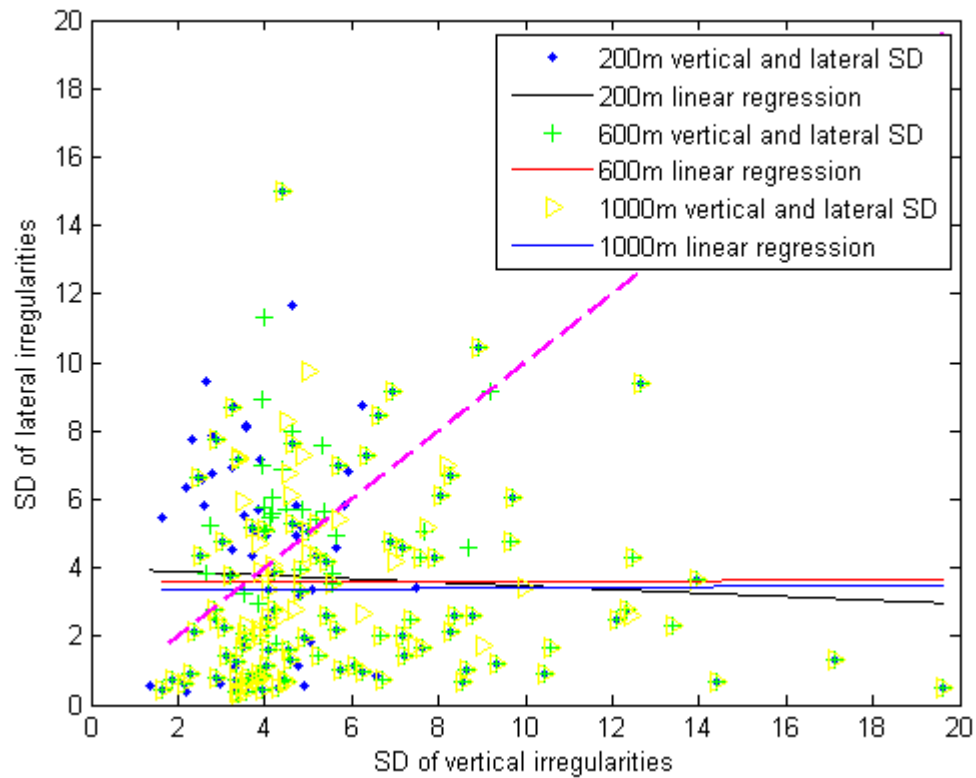


Figure 9-19 Vertical and lateral SD values in regional lines of Network C

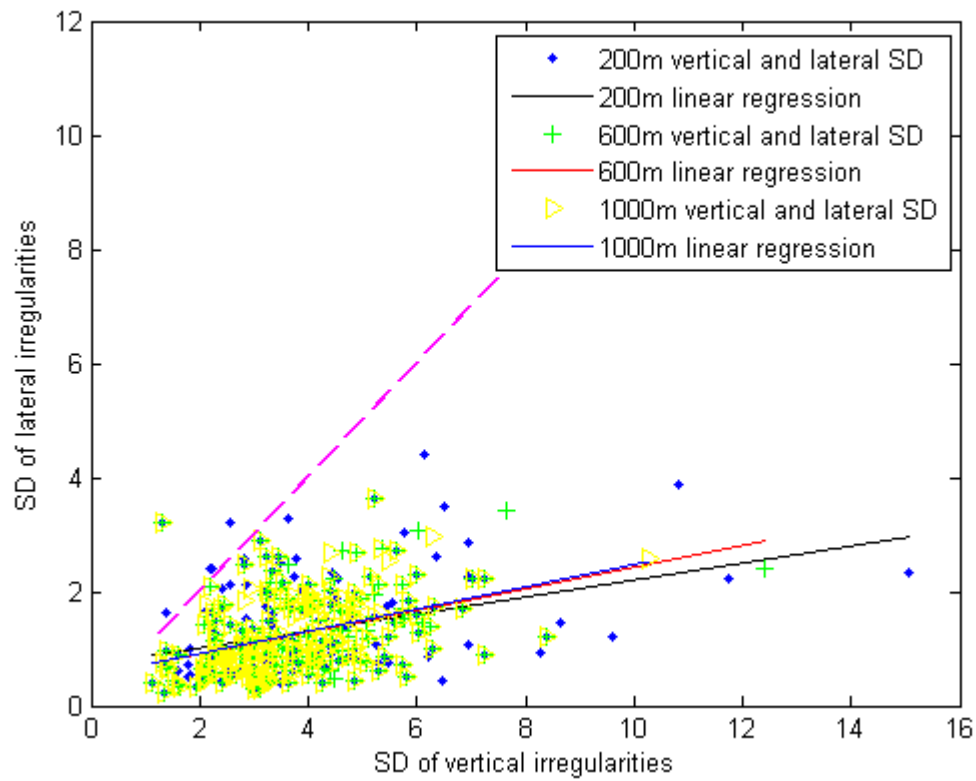
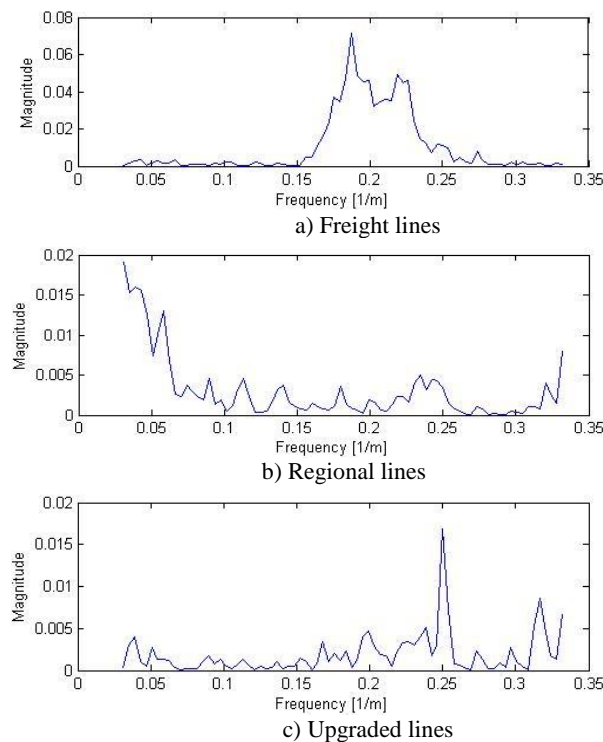


Figure 9-20 Vertical and lateral SD values in upgraded lines of Network C

A.2 MSC results between track lateral and vertical irregularities

The MSC results of all three railway networks are shown below.



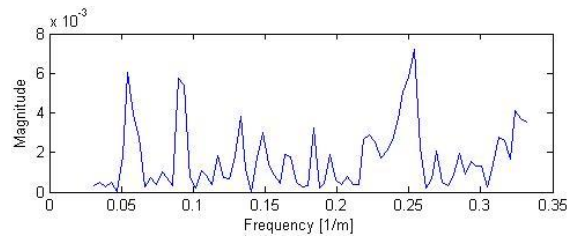


Figure 9-21 MSC between track lateral and vertical irregularities of Network A

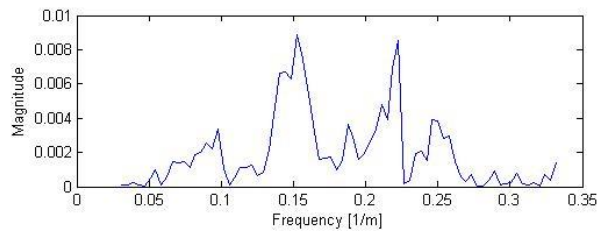
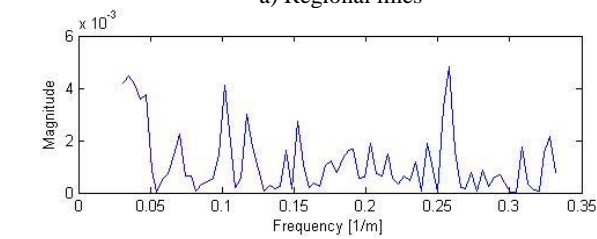
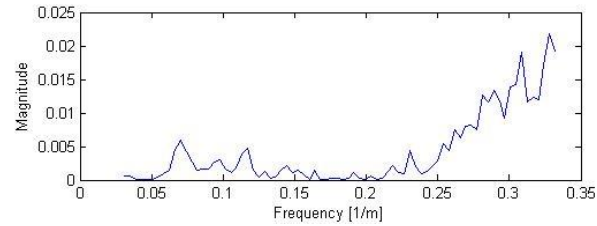
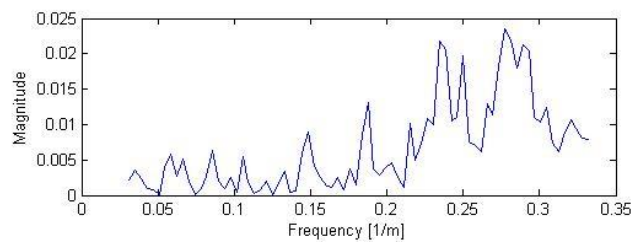
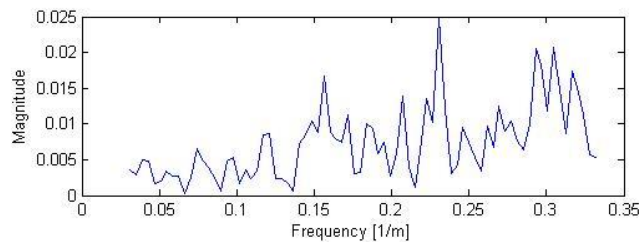


Figure 9-22 MSC between track lateral and vertical irregularities of Network B



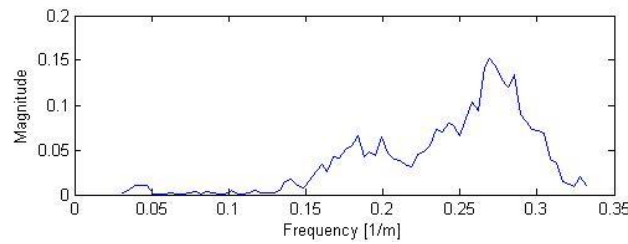


Figure 9-23 MSC between track lateral and vertical irregularities of Network C

A.3 Box-plot of track irregularities against track curvature

The meaning of numbers 1 to 6 on x axis is shown in Table 9-1. Where r is the curve radius expressed by versine with the unit of 1/km, and $\max(r)$ is the maximum value of the track versine. Therefore, 1 is the tangent track data group and 6 is the track data group with sharpest curve radius.

Table 9-1 Meaning of the numbers on x axis in box-plot figures

1	Tangent track
2	$0 \sim \frac{\max(r)}{5}$
3	$\frac{\max(r)}{5} \sim \frac{2 \cdot \max(r)}{5}$
4	$\frac{2 \cdot \max(r)}{5} \sim \frac{3 \cdot \max(r)}{5}$
5	$\frac{3 \cdot \max(r)}{5} \sim \frac{4 \cdot \max(r)}{5}$
6	$\frac{4 \cdot \max(r)}{5} \sim \max(r)$

The box plot results of all networks are shown below.

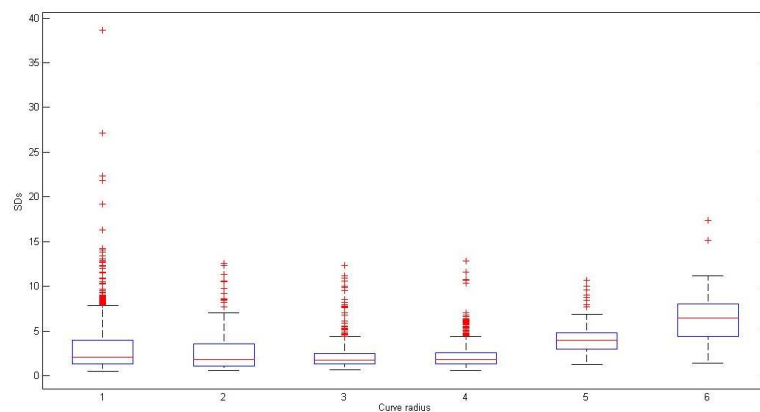


Figure 9-24 SD value box plot result of freight lines in Network A

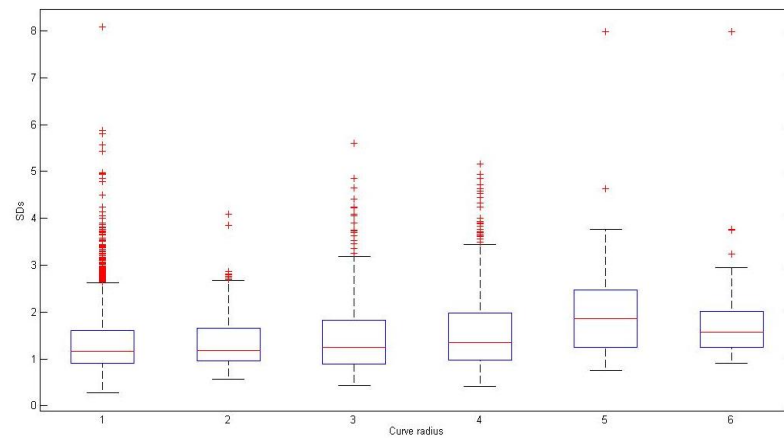


Figure 9-25 SD value box plot result of regional lines in Network A

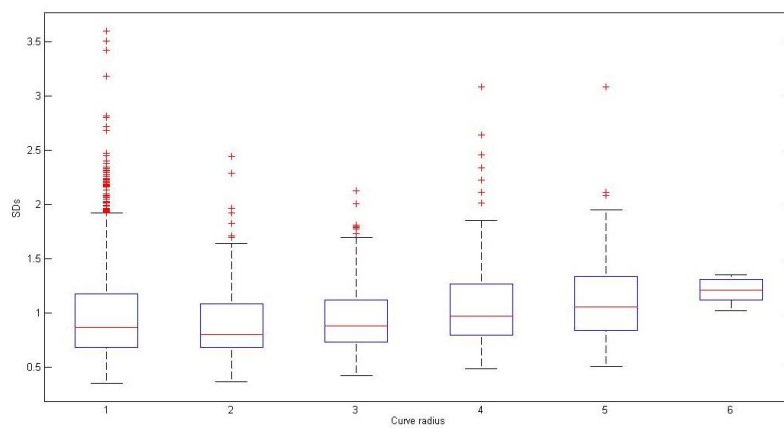


Figure 9-26 SD value box plot result of upgraded lines in Network A

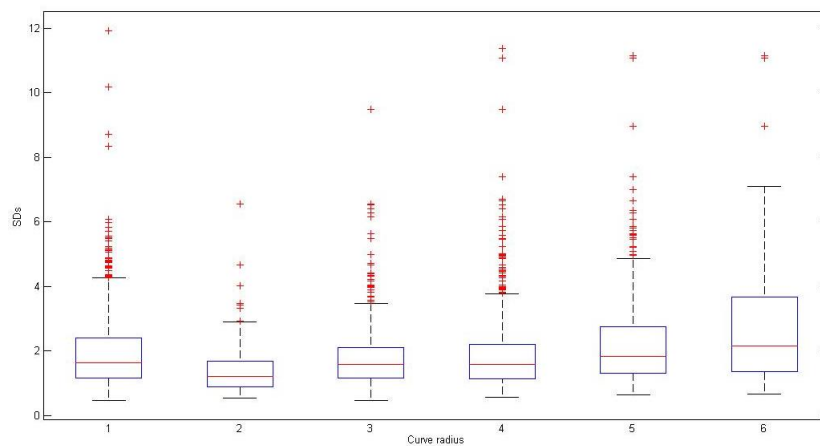


Figure 9-27 SD value box plot result of high speed lines in Network A

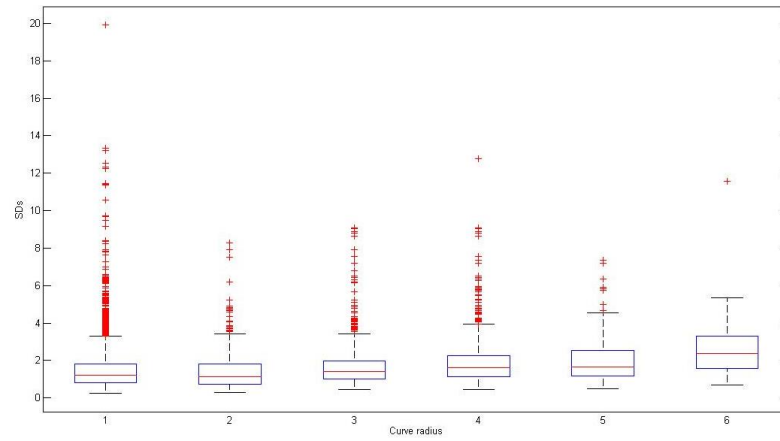


Figure 9-28 SD value box plot result of regional lines in Network B

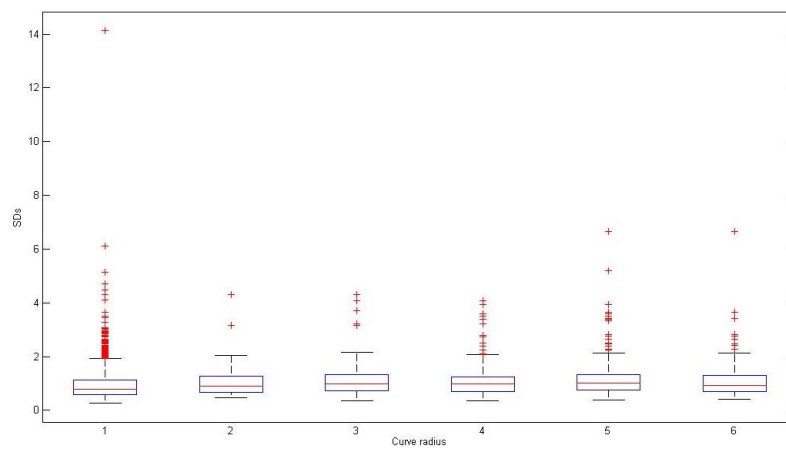


Figure 9-29 SD value box plot result of upgraded lines in Network B

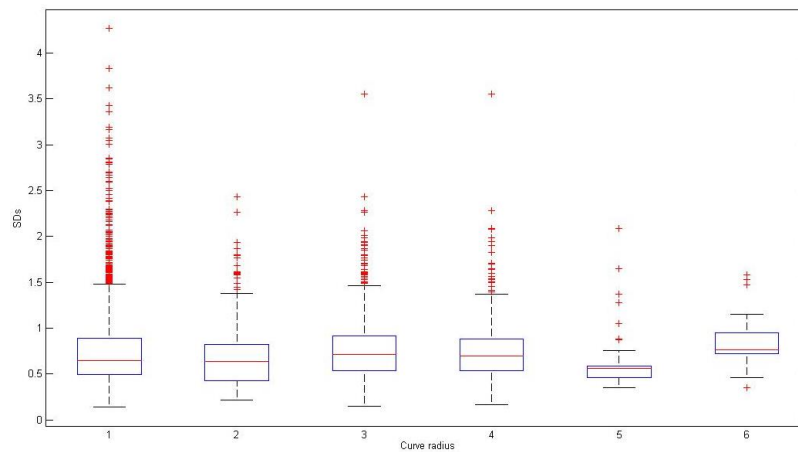


Figure 9-30 SD value box plot result of high speed lines in Network B

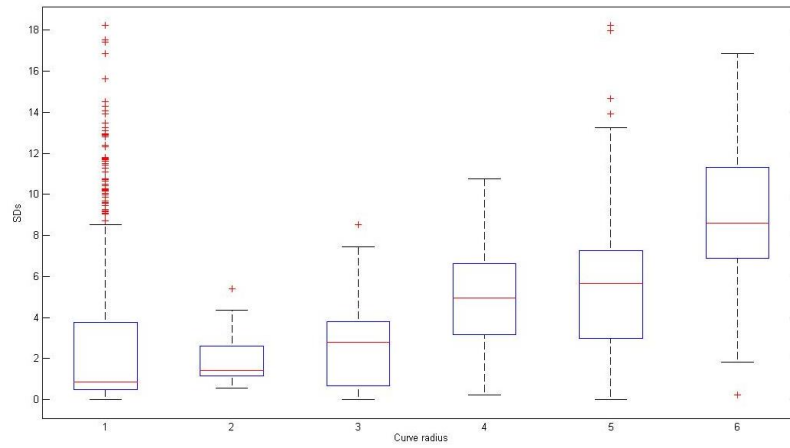


Figure 9-31 SD value box plot result of freight lines in Network C

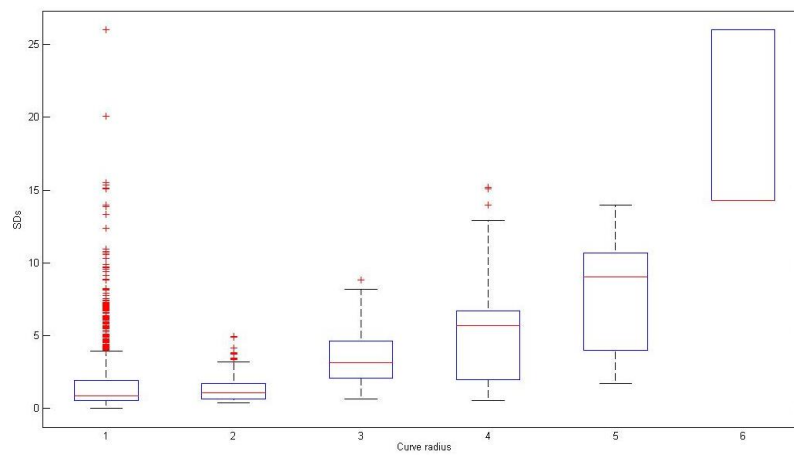


Figure 9-32 SD value box plot result of regional lines in Network C

The result of 6th track data group in Figure 9-32 is different because there may not be enough data in curve radius range $\frac{4 \cdot \max(r)}{5} \sim \max(r)$.

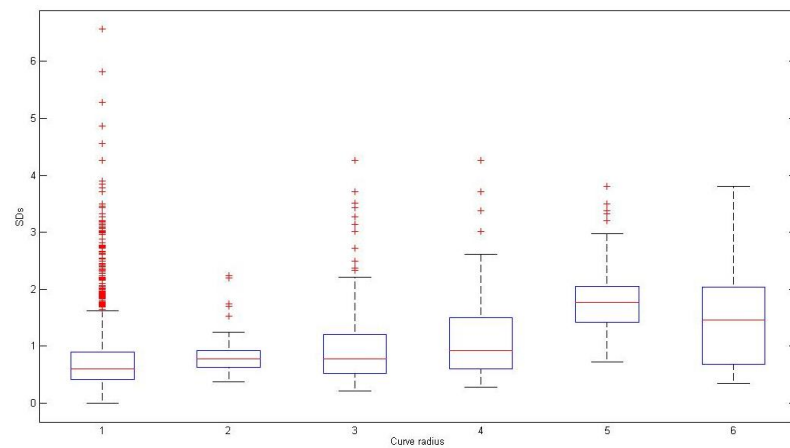


Figure 9-33 SD value box plot result of upgraded lines in Network C

A.4 Fractal analysis results

From Figure 9-34 to Figure 9-43, the upper figure shows the fractal dimensions for each 1km long track along the whole DynoTrain recorded track data from Network A to C, and the lower figures show the corresponded linear relationship between the vertical and lateral track irregularity fractal dimensions. In all figures the blue lines represents vertical data and black lines represents lateral data.

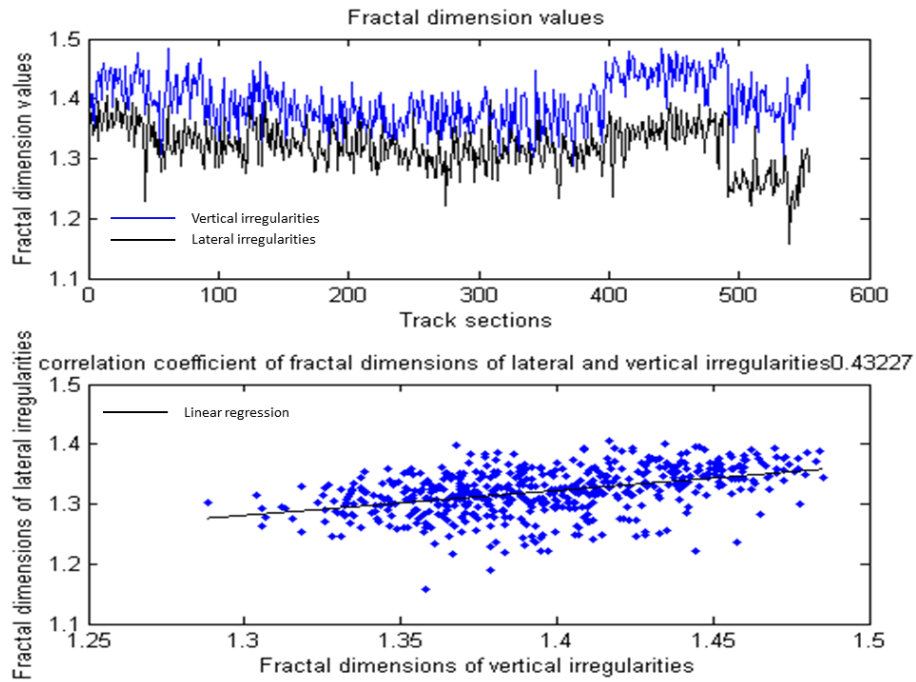


Figure 9-34 Vertical and lateral fractal dimension values in freight lines of Network A

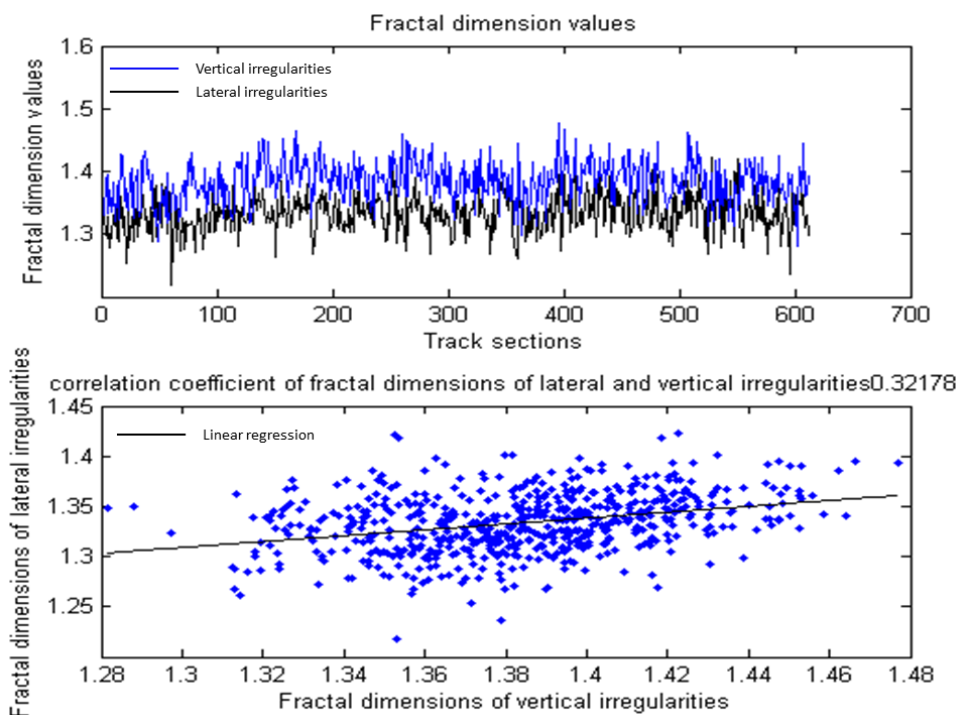


Figure 9-35 Vertical and lateral fractal dimension values in regional lines of Network A

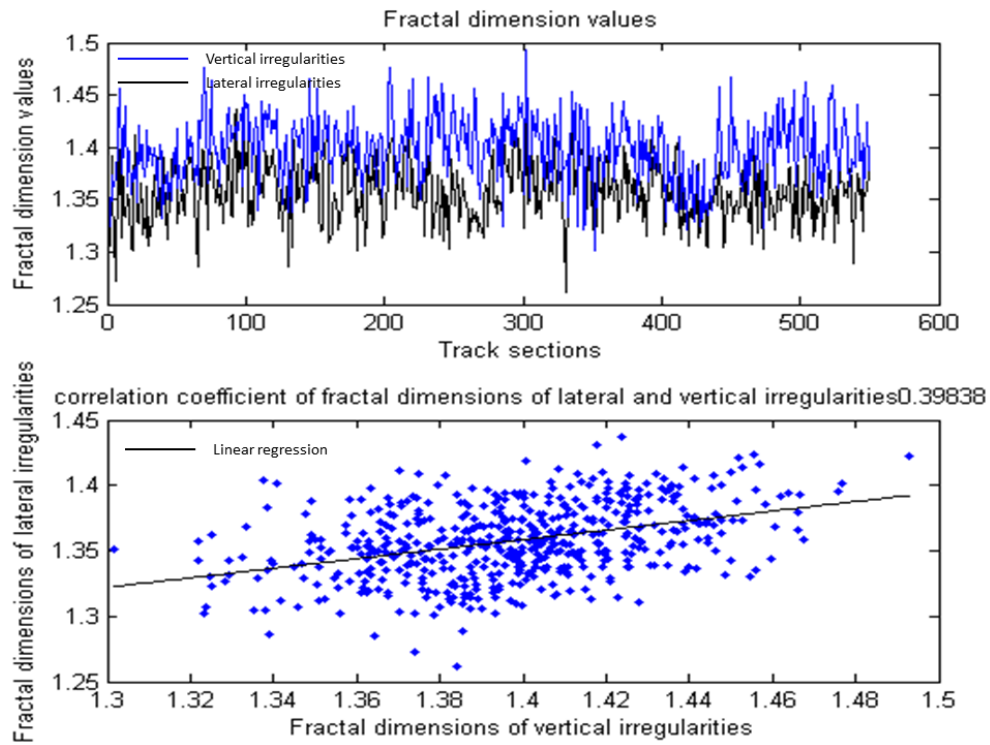


Figure 9-36 Vertical and lateral fractal dimension values in upgraded lines of Network A

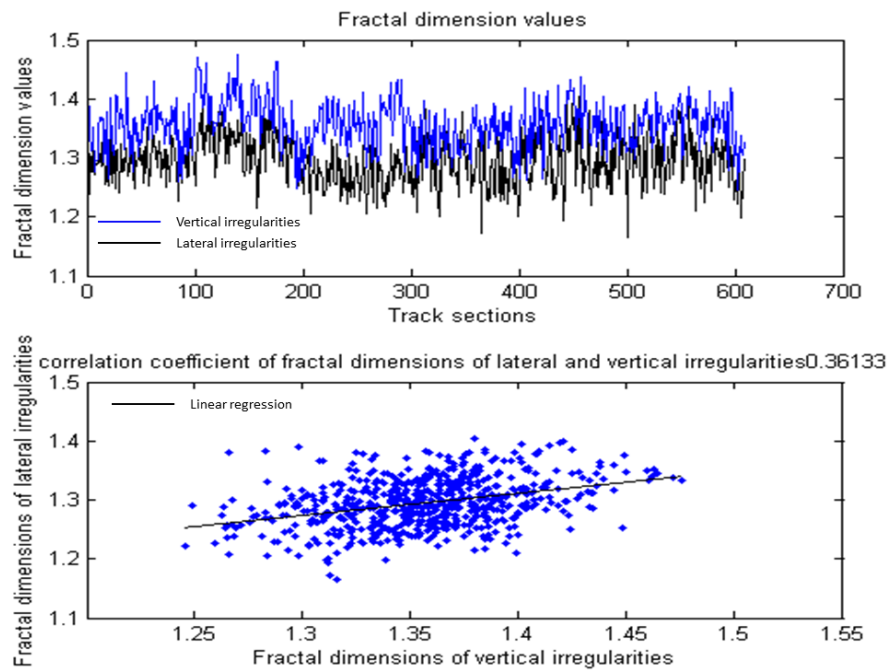


Figure 9-37 Vertical and lateral fractal dimension values in high speed lines of Network A

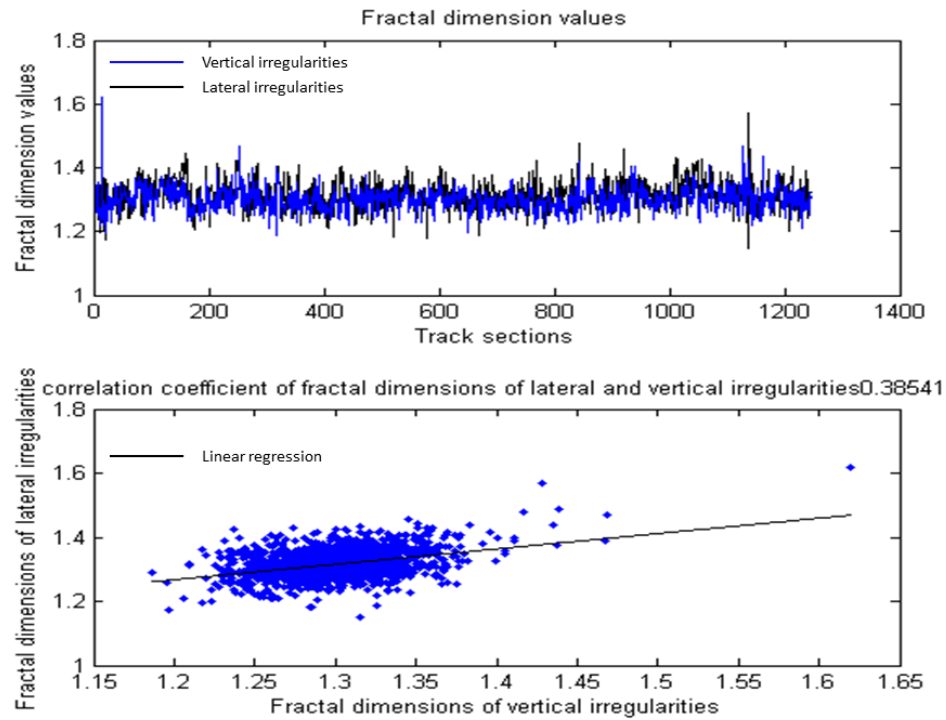


Figure 9-38 Vertical and lateral fractal dimension values in regional lines of Network B

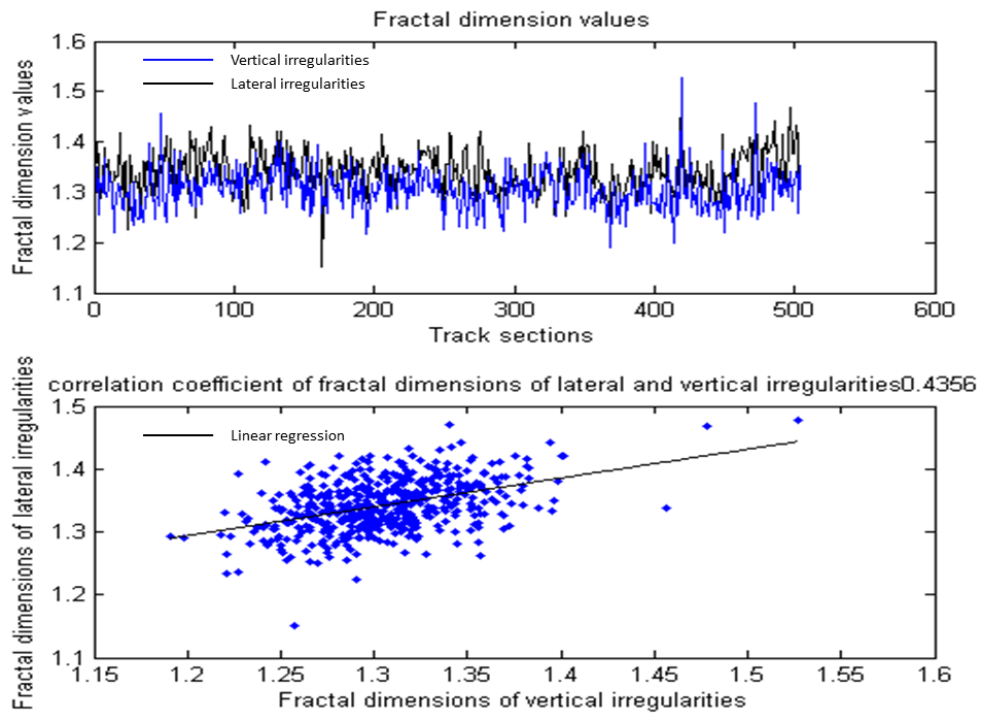


Figure 9-39 Vertical and lateral fractal dimension values in upgraded lines of Network B

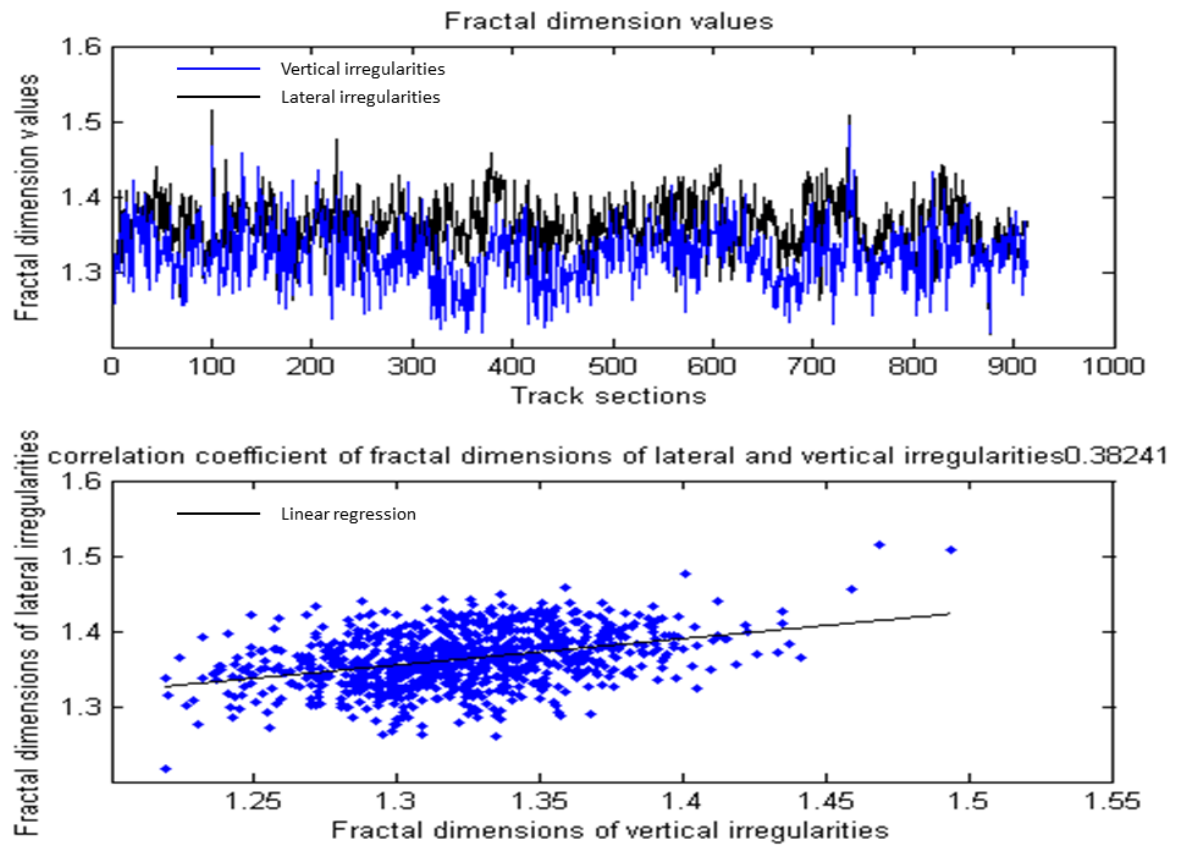


Figure 9-40 Vertical and lateral fractal dimension values in high speed lines of Network B

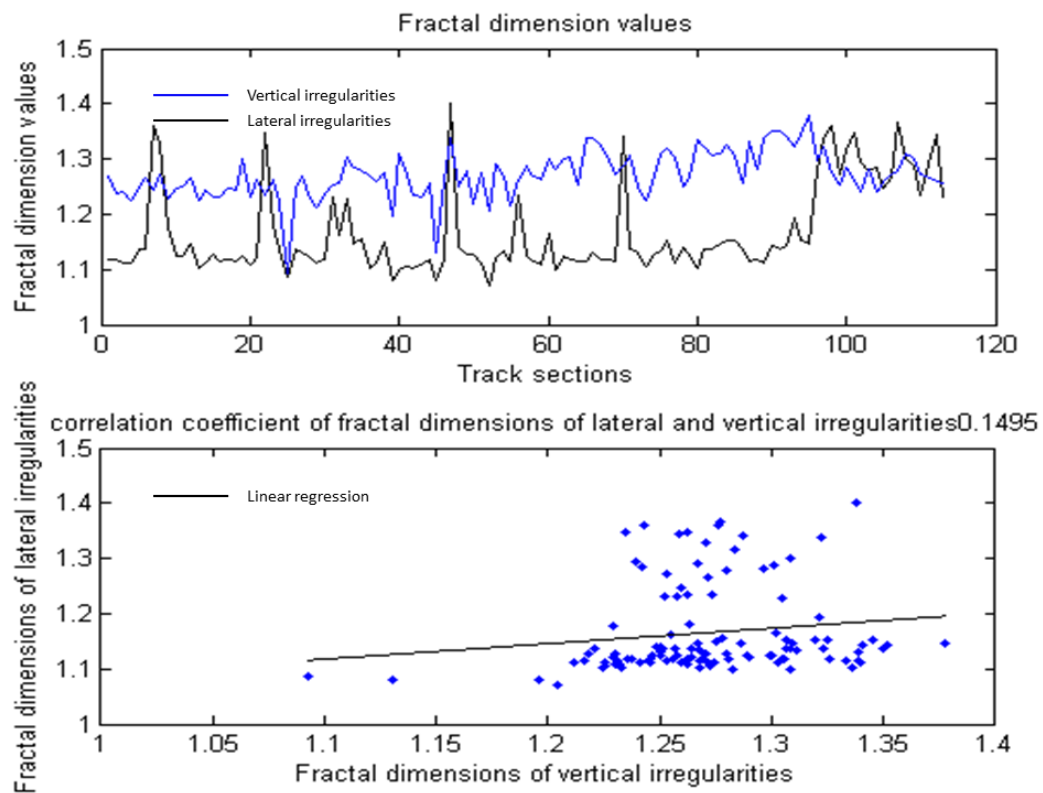


Figure 9-41 Vertical and lateral fractal dimension values in freight lines of Network C

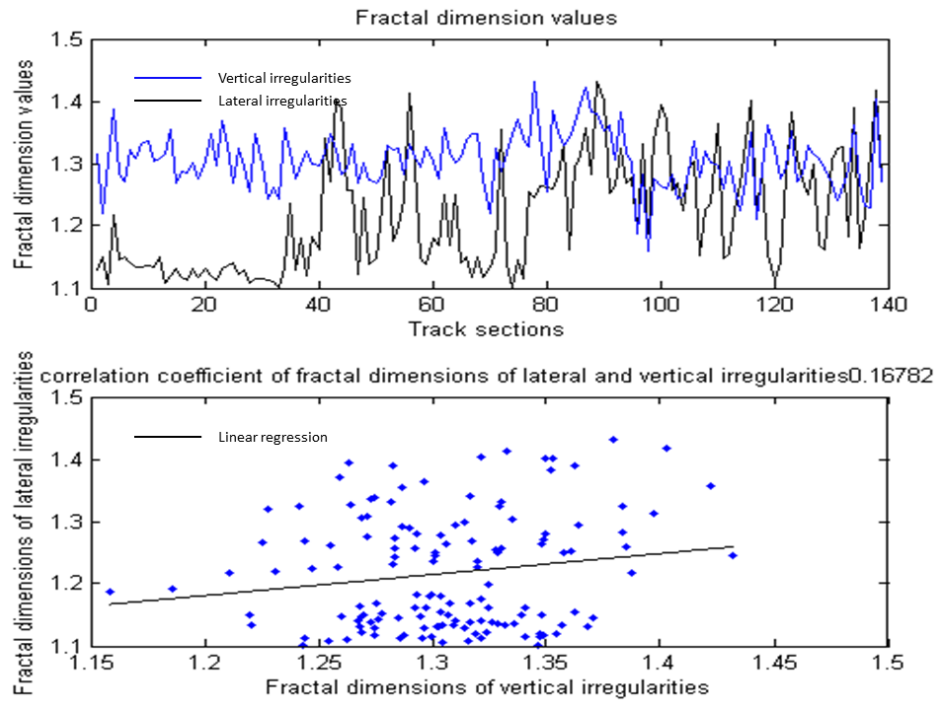


Figure 9-42 Vertical and lateral fractal dimension values in regional lines of Network C

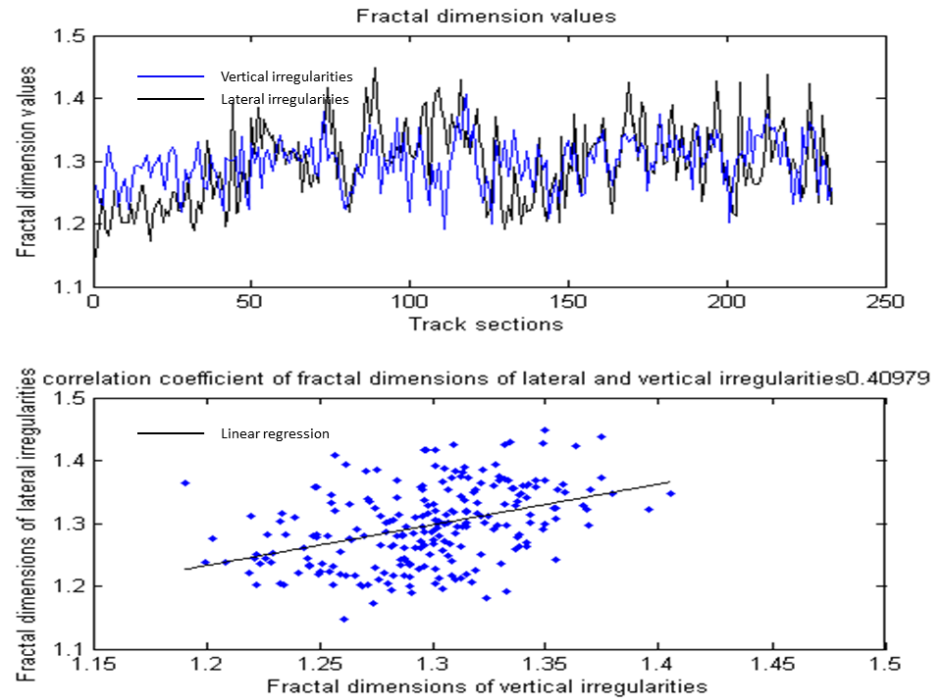


Figure 9-43 Vertical and lateral fractal dimension values in upgraded lines of Network C

Appendix B GOVERNING EQUATIONS FOR BOEF TRACK MODEL

From Figure 6-1, the movement at the point x can be analysed as the beam element model is shown in Figure 9-44. The method of Euler-Bernoulli beam model is used here.

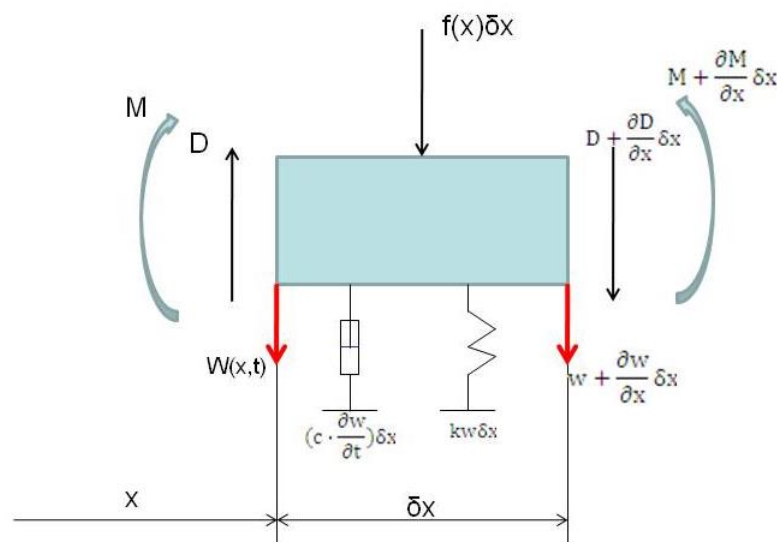


Figure 9-44 Beam Element Model

$F(t)$... input load that evaluated at the level the axle and summed for the passage of the vehicles

M ...beam bending moment

D ...shear force

EI ...the bending stiffness of the beam

k ...vertical stiffness assuming a linear lateral response to load

c ...vertical damping assuming a linear response to velocity

$w(x, t)$... beam deflection

x ...the longitudinal distance from the load

$f(x, t)$...assumed distributed load on the beam

ρ ...mass density of the beam

A ...cross section area of the beam.

From the diagram resolve vertically,

$$f(x, t) \cdot \delta x - D + \left(D + \frac{\partial D}{\partial x} \delta x \right) - c \cdot \frac{\partial w}{\partial t} \delta x - kw \delta x$$

$$= \rho A \frac{\partial^2 w}{\partial t^2} \delta x$$
Equation 72

$$f(x, t) + \frac{\partial D}{\partial x} - c \cdot \frac{\partial w}{\partial t} - kw = \rho A \frac{\partial^2 w}{\partial t^2}$$
Equation 73

Take moment about the element,

$$M + \left(D + \frac{\partial D}{\partial x} \delta x \right) \delta x = M + \frac{\partial M}{\partial x} \delta x$$
Equation 74

Neglect δx^2 terms, simplify:

$$D = \frac{\partial M}{\partial x}$$
Equation 75

From structures elastic theory it can be found:

$$M = -EI \frac{\partial^2 w}{\partial x^2}$$
Equation 76

Substituting the Equation 75 and Equation 76,

$$D = -EI \frac{\partial^3 w}{\partial x^3}$$
Equation 77

Therefore, substituting Equation 77 into Equation 73,

$$f(x, t) - EI \frac{\partial^4 w}{\partial x^4} - c \cdot \frac{\partial w}{\partial t} - kw = \rho A \frac{\partial^2 w}{\partial t^2}$$
Equation 78

Rearrange,

$$f(x, t) = EI \frac{\partial^4 w}{\partial x^4} + c \cdot \frac{\partial w}{\partial t} + kw + \rho A \frac{\partial^2 w}{\partial t^2}$$
Equation 79

Because there is no distributed load f , only a constant point load F for $x > 0$ this equation can be equated to 0. The governing PDE is

$$EI \frac{\partial^4 w(x, t)}{\partial x^4} + kw(x, t) + c \frac{\partial w(x, t)}{\partial t} + \rho A \frac{\partial^2 w(x, t)}{\partial t^2} = 0$$
Equation 80

Appendix C MASS, STIFFNESS AND DAMPING MATRIX CREATION FOR TRACK MODEL

C.1 Mass, stiffness and damping matrix of FE track lateral model

The overall mass and stiffness matrix of the system can be formed by putting the coefficient of each term in the first variation of Equation 54 and Equation 55.

Consequently, the complete mass matrix for the system is a $5N \times 5N$ symmetric matrix as shown in Equation 81.

$$[M] = \begin{bmatrix} M_1 & & \\ & M_2 & \\ & & M_s \end{bmatrix} \quad \text{Equation 81}$$

Where,

$[M_1], [M_2]$...mass matrix of the left and right rails, which is a $2N \times 2N$ regular symmetric matrix as shown below. The parts in the same colour duplicate in the matrix.

$$[M_1] = [M_2] = \frac{m_r L}{420} \begin{bmatrix} 156 & 22L & 54 & -13 & 0 & 0 & 0 & 0 & 0 & 0 & 0 & 0 \\ 22L & 4L^2 & 13L & -3L^2 & 0 & 0 & 0 & 0 & 0 & 0 & 0 & 0 \\ 54 & 13L & 312 & 0 & 54 & -13 & 0 & 0 & 0 & 0 & 0 & 0 \\ -13L & -3L^2 & 0 & 8L^2 & 13L & -3L^2 & 0 & 0 & 0 & 0 & 0 & 0 \\ 0 & 0 & 54 & 13L & 312 & 0 & \ddots & 0 & 0 & 0 & 0 & 0 \\ 0 & 0 & -13L & -3L^2 & 0 & 8L^2 & \ddots & 54 & -13 & 0 & 0 & 0 \\ 0 & 0 & 0 & 0 & \ddots & \ddots & \ddots & 13L & -3L^2 & 0 & 0 & 0 \\ 0 & 0 & 0 & 0 & 0 & 54 & 13L & 312 & 0 & 54 & -13 & 0 \\ 0 & 0 & 0 & 0 & 0 & -13L & -3L^2 & 0 & 8L^2 & 13L & -3L^2 & 0 \\ 0 & 0 & 0 & 0 & 0 & 0 & 0 & 54 & 13L & 156 & -22 & 0 \\ 0 & 0 & 0 & 0 & 0 & 0 & 0 & -13L & -3L^2 & -22 & 4L^2 \end{bmatrix}$$

$[M_s]$... mass matrix for the sleepers, which is a $N \times N$ symmetric matrix as shown below.

$$[M_s] = \begin{bmatrix} m_s & & \\ & \ddots & \\ & & m_s \end{bmatrix}$$

The stiffness matrix is in the similar form as the mass matrix, which is a $5N \times 5N$ symmetric matrix:

$$[K] = \begin{bmatrix} K_1 & & K_{s1} \\ & K_2 & K_{s2} \\ K_{1s} & K_{2s} & K_s \end{bmatrix} \quad \text{Equation 82}$$

Where,

$[K_1], [K_2] \dots 2N \times 2N$ symmetric matrix:

$$[K_1] = [K_2] = \frac{EI}{L^3} \begin{bmatrix} 12 + k_r & 6L & -12 & 6L & 0 & 0 & 0 & 0 & 0 & 0 & 0 & 0 \\ 6L & 4L^2 & -6L & 2L^2 & 0 & 0 & 0 & 0 & 0 & 0 & 0 & 0 \\ -12 & -6L & 24 + k_r & 0 & -12 & 6L & 0 & 0 & 0 & 0 & 0 & 0 \\ 6L & 2L^2 & 0 & 8L^2 & -6L & 2L^2 & 0 & 0 & 0 & 0 & 0 & 0 \\ 0 & 0 & -12 & -6L & 24 + k_r & 0 & \ddots & 0 & 0 & 0 & 0 & 0 \\ 0 & 0 & 6L & 2L^2 & 0 & 8L^2 & \ddots & -12 & 6L & 0 & 0 & 0 \\ 0 & 0 & 0 & 0 & \ddots & \ddots & \ddots & -6L & 2L^2 & 0 & 0 & 0 \\ 0 & 0 & 0 & 0 & 0 & -12 & -6L & 24 + k_r & 0 & -12 & 6L & 0 \\ 0 & 0 & 0 & 0 & 0 & 6L & 2L^2 & 0 & 8L^2 & -6L & 2L^2 & 0 \\ 0 & 0 & 0 & 0 & 0 & 0 & 0 & -12 & -6L & 12 + k_r & -6L & 0 \\ 0 & 0 & 0 & 0 & 0 & 0 & 0 & 6L & 2L^2 & -6L & 4L^2 & 0 \end{bmatrix}$$

$[K_{1s}], [K_{2s}] \dots N \times 2N$ symmetric matrix:

$$[K_{1s}] = [K_{2s}] = \begin{bmatrix} -k_r & 0 & & \\ & \ddots & & \\ & & -k_r & 0 \end{bmatrix}$$

$[K_{s1}], [K_{s2}] \dots 2N \times N$ symmetric matrix:

$$[K_{s1}] = [K_{s2}] = \begin{bmatrix} -k_r & & \\ 0 & \ddots & \\ & & -k_r \\ & & & 0 \end{bmatrix}$$

$[K_s] \dots N \times N$ Symmetric matrix:

$$[K_s] = \begin{bmatrix} 2k_r + k_s & & \\ & \ddots & \\ & & 2k_r + k_s \end{bmatrix}$$

From the virtual work expression, the damping stiffness matrix can be found as a $5N \times 5N$ symmetric matrix:

$$[K] = \begin{bmatrix} C_1 & & C_{s1} \\ & C_2 & C_{s2} \\ C & C_{2s} & C_s \end{bmatrix} \quad \text{Equation 83}$$

Where,

$[C_1], [C_2] \dots 2N \times 2N$ symmetric matrix:

$$[C_1] = [C_2] = \begin{bmatrix} c_r & 0 & & & \\ 0 & 0 & & & \\ & & \ddots & & \\ & & & c_r & 0 \\ & & & 0 & 0 \end{bmatrix}$$

$[C_{1s}], [C_{2s}] \dots N \times 2N$ symmetric matrix:

$$[C_{1s}] = [C_{2s}] = \begin{bmatrix} -c_r & 0 & & & \\ & & \ddots & & \\ & & & -c_r & 0 \end{bmatrix}$$

$[C_{s1}], [C_{s2}] \dots 2N \times N$ symmetric matrix:

$$[C_{s1}] = [C_{s2}] = \begin{bmatrix} -c_r & & & \\ 0 & & & \\ & \ddots & & \\ & & -c_r & \\ & & 0 & \end{bmatrix}$$

$[C_s] \dots N \times N$ Symmetric matrix:

$$[C_s] = \begin{bmatrix} 2c_r + c_s & & & \\ & \ddots & & \\ & & 2c_r + c_s & \end{bmatrix}$$

Appendix D TRACK MODEL PARAMETER SELECTION

D.1 Traffic information on WCML

Table 9-2 shows the fleet composition information Actraff data found for the route on WCML, which is split into three separate sections and taken for one period 13 x 4 week periods in a year. The ‘name’ column actually contains the number of wheelsets for all vehicles through that section, including other vehicles which are not listed in the table as individually they each represent a small percentage of the traffic. In this case the traffic levels are constant through all three sections, though they might not have been if there was some S&C in the site and traffic had come onto or left the route.

Table 9-2 ACTRAFF data for the route

ELR	Track Id	Start Mi.Mi	End Mi.Mi	Code	Name	ID #	Extra1	Extra2	Legnth	Mgntd	St Dist	End Dist
LEC1	2100	68.625	69.7	Veh	8180	221M	TBC	135980	1892	8180	4610	6514
LEC1	2100	69.7	70.45	Veh	8180	221M	TBC	135988	1320	8180	6514	7841
LEC1	2100	70.45	76.7875	Veh	8180	221M	TBC	135988	11154	8180	7841	12349
LEC1	2100	68.625	69.7	Veh	73272	390M	TBC	135980	1892	73272	4610	6514
LEC1	2100	69.7	70.45	Veh	73272	390M	TBC	135988	1320	73272	6514	7841
LEC1	2100	70.45	76.7875	Veh	73272	390M	TBC	135988	11154	73272	7841	12349
LEC1	2100	68.625	69.7	Veh	36636	390T	TBC	135980	1892	36636	4610	6514
LEC1	2100	69.7	70.45	Veh	36636	390T	TBC	135988	1320	36636	6514	7841
LEC1	2100	70.45	76.7875	Veh	36636	390T	TBC	135988	11154	36636	7841	12349
LEC1	2100	68.625	69.7	Veh	504	66/5	TBC	135980	1892	504	4610	6514
LEC1	2100	69.7	70.45	Veh	504	66/5	TBC	135988	1320	504	6514	7841
LEC1	2100	70.45	76.7875	Veh	504	66/5	TBC	135988	11154	504	7841	12349
LEC1	2100	68.625	69.7	Veh	4264	FEAB	TBC	135980	1892	4264	4610	6514
LEC1	2100	69.7	70.45	Veh	4264	FEAB	TBC	135988	1320	4264	6514	7841
LEC1	2100	70.45	76.7875	Veh	4264	FEAB	TBC	135988	11154	4264	7841	12349
LEC1	2100	68.625	69.7	Veh	648	FIAB	TBC	135980	1892	648	4610	6514
LEC1	2100	69.7	70.45	Veh	648	FIAB	TBC	135988	1320	648	6514	7841
LEC1	2100	70.45	76.7875	Veh	648	FIAB	TBC	135988	11154	648	7841	12349
LEC1	2100	68.625	69.7	Veh	4232	FSAO	TBC	135980	1892	4232	4610	6514
LEC1	2100	69.7	70.45	Veh	4232	FSAO	TBC	135988	1320	4232	6514	7841
LEC1	2100	70.45	76.7875	Veh	4232	FSAO	TBC	135988	11154	4232	7841	12349
LEC1	2100	68.625	69.7	Veh	1048	FTAI	TBC	135980	1892	1048	4610	6514
LEC1	2100	69.7	70.45	Veh	1048	FTAI	TBC	135988	1320	1048	6514	7841
LEC1	2100	70.45	76.7875	Veh	1048	FTAI	TBC	135988	11154	1048	7841	12349
LEC1	2100	68.625	69.7	Veh	1016	IPAV	TBC	135980	1892	1016	4610	6514
LEC1	2100	69.7	70.45	Veh	1016	IPAV	TBC	135988	1320	1016	6514	7841
LEC1	2100	70.45	76.7875	Veh	1016	IPAV	TBC	135988	11154	1016	7841	12349
LEC1	2100	68.625	69.7	Veh	876	KFAF	TBC	135980	1892	876	4610	6514
LEC1	2100	69.7	70.45	Veh	876	KFAF	TBC	135988	1320	876	6514	7841
LEC1	2100	70.45	76.7875	Veh	876	KFAF	TBC	135988	11154	876	7841	12349
LEC1	2100	68.625	69.7	Veh	520	Mkil	TBC	135980	1892	520	4610	6514
LEC1	2100	69.7	70.45	Veh	520	Mkil	TBC	135988	1320	520	6514	7841
LEC1	2100	70.45	76.7875	Veh	520	Mkil	TBC	135988	11154	520	7841	12349
LEC1	2100	68.625	69.7	Veh	1480	Mkil	TBC	135980	1892	1480	4610	6514
LEC1	2100	69.7	70.45	Veh	1480	Mkil	TBC	135988	1320	1480	6514	7841
LEC1	2100	70.45	76.7875	Veh	1480	Mkil	TBC	135988	11154	1480	7841	12349

D.2 Lateral resistance parameters

Kish et al. [2] studied the track residual deflection in detail and summarised the track lateral resistance parameters in Table 9-3. The lateral elastic breaking resistance F_e depends on the peak lateral resistance F_p , and typically on the order of $F_p/4$.

Table 9-3 Track lateral resistance parameters

	Elastic resistance F_e (kN)	Elastic displacement w_e (mm)	Peak resistance F_p (kN)	Peak displacement w_p (mm)
Weak, tamped track	2 – 2.5	0.6 – 0.7	8 – 9.8	3 – 3.5
Good quality track	3.3 – 4.5	1 – 1.3	13.3 – 17.8	4.8 – 6.4

Esvelde [80] summarised the lateral resistance parameter from many test programmes and it is shown in Table 9-4. These values are relatively lower than the values for typical track system because the worst design case is considered.

Table 9-4 Lateral resistance characteristic values per sleeper

	Peak resistance F_p (kN)	Peak displacement w_p (mm)	Min. resistance F_l (kN)	Displacement w_l (mm)
Loose Tamped/Relay (Weak)	5.2	15	5.2	40
Just Tamped (Medium)	7.1	10	6.2	40
Trafficked (Strong)	8.1	5	6.7	40

Le Pen [77] did a single sleeper push test and found the lateral resistance on unloaded track for concrete sleepers are shown in the table below.

Table 9-5 Summary of lateral resistance test on unloaded track, concrete sleepers

Ballast category	Lateral resistance/sleeper(kN)-peak within a deflection of 20mm			
	Minimum	20% less than	50% less than	Maximum
Loose tamped/relay	4.2	5.2	5.9	6.9
Just tamped/undisturbed	5.9	7.1	8.3	11.8
Trafficked	5.4	8.1	10.3	15.7